Towards the implementation of fundamental knowledge in Oxidation Catalysis: Perovskites as dataset for Artificial Intelligence analysis

vorgelegt von

M. Sc.

Giulia Bellini

an der Fakultät II – Mathematik und Naturwissenschaften

der Technischen Universität Berlin

zur Erlangung des akademischen Grades

Doktorin der Naturwissenschaften

Dr. rer. nat.

genehmigte Dissertation

Promotionsausschuss:

Vorsitzender: Prof. Dr. Franziska Hess

Gutachter: Prof. Dr. Robert Schlögl

Gutachter: Prof. Dr. Arne Thomas

Gutachter: Prof. Dr. Malte Behrens

Tag der wissenschaftlichen Aussprache: 16. September 2022

Berlin 2022

Towards the implementation of fundamental knowledge in Oxidation Catalysis: Perovskites as dataset for Artificial Intelligence analysis

M. Sc. Giulia Bellini

Berlin 2022

„Thoughts without content are empty, intuitions without concepts are blind... The understanding can intuit nothing, the senses can think nothing. Only through their union can knowledge arise"

- Immanuel Kant

Acknowledgement

First and foremost, I want to express my gratitude to Prof. Dr. Robert Schlögl who offered me the opportunity to perform my PhD studies at the Inorganic Department of the Fritz-Haber-Institute of the Max-Planck-Society. I have been delighted by the honor to have the chance to work under his guidance and to learn from such a savant and professional deontological scientific environment, surrounded by passionate and inspiring scientists. Prof. Schlögl has always pushed my work forward with numerous inspiring suggestions and remarks by guiding my PhD and I will be always grateful for that.

A very sincere gratitude goes to my scientific supervisor, Dr. Annette Trunschke, who supervised and guided me through this journey. She has always been a precious source of support and especially motivation during these years, being always able to transmit her passion for heterogeneous catalysis to her students and co-workers and thus embodying a source of professional inspiration for the future career. In this regard, I am very thankful as well for her criticism, which contributed positively to the outcome of the project and also to my scientific and personal growth.

I gratefully acknowledge Prof. Dr. Arne Thomas and Prof. Dr. Malte Behrens for having invested their valuable time to review this Thesis. In addition, I greatly thank Prof. Dr. Franziska Hess for acting as the chairperson of the examination board.

I would also like to express my gratitude to the colleagues involved in the Perovskite project: Gregor Koch and Jinhu Dong, to Gregor Koch in particular. Thank you very much for the scientific discussion, the material support and for establishing a magic synergy of team feeling.

Many thanks go in particular to Frank Girgsdies and to Olaf Timpe for your help, material support and guidance to my project.

I would like to thank also all the other scientists who gave a scientific contribution to my project: Spencer James Carey, Peter Kraus, Michael Havecker, Detre Teschner, Sven Richter, Rania Hanna, Thomas Götsch, Franz Schmidt, Pierre Kube, Andrey Tarasov, Jutta Kröhnert, Maike Hashagen and Jasmin Allan.

I want to thank especially Lucas Foppa, my theoretical “counterpart” in the following Thesis project. It has been a really pleasure to collaborate with you. Thank you for your expertise contribution, for the discussion and for the great support.

Great appreciation goes out to all the other PhD students who worked with me and to those I had the pleasure to know, even if only for a short period of time, Leon, Maximillian, Marie, Hamideh, Anna, Elisabeth, Lorenz, Samuel, Frederic, Ezgi, Julia and Liseth.

I would like to thank also Cryriac for the personal support during this path and Clara, Matus and Daniel for having shared with me the work environment in these last months during the pandemic.

Finally, I want to thank all my family members, my parents in particular, and friends for their unconditional love and encouragements.

Last but not least, my gratitude goes to Edoardo, for his patience, love and support and most of all for being able of taking out the best of my self.

Abstract

In the context of the impending oil shortage in the near future, it is vital to find an economical and environmental-friendly route to produce alternative building blocks for chemical industry, such as propene and acrylic acid. Many attempts have been done in the past decades in order to implement an efficient and suitable catalyst for alkane oxidation. However, no real breakthrough has been achieved in the catalytic community since the discovery of MoVTeNb M1 phase-pure catalyst patented by Mitsubishi Corp. in the early 1990s. The lack of homogeneity of data presented in the literature, regarding the many proposed catalytic systems, addresses the new oxidation catalysis research back to fundamental roots, since only a deep understanding and a systematic study of the intrinsic nature of the catalyst may constitute the key for the future. To this latter extent, the implementation of a catalyst requires the study of relative simple and flexible system, such as perovskites, since these bulk oxide catalysts present a high level of flexibility without destroying their structure. Mathematical tools, such as high-throughput DFT calculations, machine learning (ML) and artificial intelligence, have already been widely employed for accelerating the discovery of possible new perovskite-like structures [1-5] and for searching for key-descriptors for the catalytic performance. The present project deals with the synthesis, characterization and catalytic testing of twenty-three phase-pure perovskite-like catalysts (two of them are 97% phase-pure perovskite-like catalysts) in order to serve as basis for artificial intelligence analysis. For this purpose, Mn has been chosen as B-site cation combined with an other metal belonging to the 3d or 4d row of the periodic table (the synergistic effect is claimed to be beneficial to the catalytic performance). The selected element at the B-site have similar ionic radius among each other (ionic radii in six coordination: Co^{2+} = 0.65 Å, Zn^{2+}= 0.74 Å, Ni^{2+}=0.69 Å, Fe^{2+}=0.61 Å, Cr^{2+}=0.73 Å, Pd^{2+}=0.86 Å, Cu^{2+}= 0.73 Å and $Mn^{3+/4+}$=0.53-0.64 Å). The A-site cation has been changed between La^{3+}, Pr^{3+}, Nd^{3+} and Sm^{3+} to tune the structural and electronic properties. Therefore, twenty-one purely phase-pure perovskites, among which fourteen present the general formula $(La,Pr)Mn_{(1-x)}Cu_xO_3$ (with x=0-0.4) and other five the general formula $AMn_{0.7}B'_{0.3}O_3$ (with A=Pr, Nd and Sm and B'=Co, Zn, Ni, Fe, Cr) and $(La,Pr)_2CuO_4$ perovskite-related structures have been synthesized, tested in CO and propane oxidation and subjected to different characterization methods in order to obtain numerical values of some properties (also known as basic descriptors) for artificial intelligence analysis. As first step, the $(La,Pr)Mn_{(1-x)}Cu_xO_3$ series has been investigated in detail. From the combined analysis of the characterization data with those of catalysis, it emerges the high complexity generated by the synergistic effect of a double B-site into the catalytic dynamic. Furthermore, the catalytic results highlight that also the A-site indirectly influences the catalytic scenario, in particular in CO oxidation. This is in contrast to what is generally reported in the literature, where it is claimed that the B-site is the responsible element for the catalytic performance. The Artificial Intelligence

analysis performed over the (La,Pr)$Mn_{(1-x)}Cu_xO_3$ series have highlighted how a single primary feature based on chemical intuition is not sufficient to fully describe the properties linked to the catalytic performance in CO oxidation. Additionally, the found optimal model has confirmed the hypothesis and expectations formulated for the (La,Pr)-based series, where the A-site is indirectly involved in the catalytic performance in CO oxidation. Also the AI performed over the whole perovskite matrix ((La,Pr)$Mn_{(1-x)}Cu_xO_3$ series + $AMn_{0.7}B'_{0.3}O_3$ series) confirms the results discussed for the (La,Pr)-series in CO oxidation. Many different conclusions can be drawn from the AI analysis results of the data deriving from propane oxidation. For instance, they highlight how the addition of steam into the reaction feed could affect the catalytic scenario to different extents depending on the involved samples. A detailed summary and the final overview of the herein presented project are reported in the conclusion part of this work.

Zusammenfassung

Vor dem Hintergrund der in naher Zukunft drohenden Ölknappheit, gilt es, einen wirtschaftlichen und umweltfreundlichen Weg zu finden, um alternative Bausteine, wie Propen und Acrylsäure, für die chemische Industrie herzustellen. In den letzten Jahrzehnten wurden viele Versuche unternommen, einen effizienten und geeigneten Katalysator für die Alkanoxidation zu entwickeln. Seit der Entdeckung des phasenreinen MoVTeNb-M1-Katalysators, der von Mitsubishi Corp. in den frühen 1990er Jahren patentiert wurde, wurde jedoch kein weiterer Durchbruch mehr in der katalytischen Gemeinschaft erzielt. Der Mangel an Homogenität der in der Literatur präsentierten Daten, zu den vielen vorgeschlagenen Katalysatoren, führt die heutige Oxidationskatalyseforschung zu ihren grundlegenden Wurzeln zurück, da nur ein tiefes Verständnis und eine systematische Untersuchung der intrinsischen Natur des Katalysators der Schlüssel für die Zukunft ist. Daher erfordert die Implementierung eines Katalysators die Untersuchung relativ einfacher und flexibler Systeme wie Perowskite, da diese Bulk-Oxidkatalysatoren ein hohes Maß an Flexibilität aufweisen, ohne ihre Struktur zu verlieren. Mathematische Werkzeuge wie high-throughput-DFT-Rechnungen, Machine Learning (ML) und künstliche Intelligenz (KI) wurden bereits häufig eingesetzt, um die Entdeckung möglicher neuer Perowskit-ähnlicher Strukturen zu beschleunigen und nach Schlüsseldeskriptoren für die katalytische Performance zu suchen. Die vorliegende der Arbeit beschäftigt sich mit der Synthese, Charakterisierung und katalytischen Testung von dreiundzwanzig phasenreinen perowskitähnlichen Katalysatoren (zwei davon sind 97% phasenreine perowskitähnliche Katalysatoren) als Grundlage für die weiterführende Analyse mittels künstlicher Intelligenz. Zu diesem Zweck wurde Mn als Kation der B-Site in Kombination mit einem zweiten Metall aus der 3. oder 4. Reihe des Periodensystems gewählt (der synergistische Effekt soll der katalytischen Performance zugute kommen). Die ausgewählten Elemente an der B-Site haben dabei ähnliche Ionenradien (Ionenradien in sechsfacher Koordination: Co^{2+}= 0.65 Å, Zn^{2+}= 0.74 Å, Ni^{2+}=0.69 Å, Fe^{2+}=0.61 Å, Cr^{2+}=0.73 Å, Pd^{2+}=0.86 Å, Cu^{2+}= 0.73 Å und $Mn^{3+/4+}$=0.53-0.64). Das Kation der A-Site wurde zwischen La^{3+}, Pr^{3+}, Nd^{3+} und Sm^{3+} variiert, um die strukturellen und elektronischen Eigenschaften zu modifizieren. Um das zu realisieren, wurden einundzwanzig phasenreine Perowskite synthetisiert, in CO- und Propanoxidation getestet und standardmäßigen Strukturcharakterisierungen unterzogen, um numerische Werte bestimmte Eigenschaften (auch als grundlegende Deskriptoren bekannt) für die Analyse der künstlichen Intelligenz zu erhalten. Von den einundzwanzig vollständig phasenreinen Katalysatoren, weisen vierzehn die allgemeine Formel $(La,Pr)Mn_{(1-x)}Cu_xO_3$ (mit x=0-0.4) auf, weitere fünf Perowskite besitzen die allgemeine Formel $AMn_{0.7}B'_{0.3}O_3$ (mit A=Pr, Nd und Sm und B'=Co, Zn, Ni, Fe, Cr) und zwei Perowskit-ähnliche Strukturen lassen sich durch die Formel $(La,Pr)_2CuO_4$ beschreiben. Als erster Schritt wurde die $(La,Pr)Mn_{(1-x)}Cu_xO_3$-Reihe im Detail untersucht. Aus der kombinierten

Analyse der Charakterisierungsdaten und der Katalyse zeigt sich eine hohe Komplexität, die durch den synergistischen Effekt einer doppelten B-Site während der Katalyse erzeugt wird. Weiters zeigen die katalytischen Ergebnisse, dass auch die A-Site die katalytische Performance indirekt beeinflusst, insbesondere bei der CO Oxidation. Das steht im Gegensatz zu den allgemein in der Literatur berichteten Behauptungen, dass (ausschließlich) die B-Site das verantwortliche Element für die katalytische Performance ist. Die durchgeführte Analyse mittels künstlicher Intelligenz über die (La,Pr)$Mn_{(1-x)}Cu_xO_3$-Reihe hat gezeigt, dass ein einzelnes primäres Merkmal, das auf chemischer Intuition basiert, nicht ausreicht, um die katalytische Performance vollständig zu beschreiben. Darüber hinaus hat das gefundene optimale Modell, die formulierten Hypothesen und Erwartungen für die (La,Pr)-basierte Reihe bestätigt, bei der auch die A-Site indirekt an der katalytischen Performance bei der CO Oxidation beteiligt ist. Auch die KI-Analyse über die gesamte Perowskitmatrix ((La,Pr)$Mn_{(1-x)}Cu_xO_3$-Reihe + $AMn_{0.7}B'_{0.3}O_3$-Reihe) bestätigt die (La,Pr)-Reihe diskutierten Ergebnisse in der CO-Oxidation. Im Fall der Propanoxidation, ergibt sich eine Vielzahl an Schlussfolgerungen, die aus der KI-Analyse gezogen werden können. Zum Beispiel zeigen sie auf, wie die Zugabe von Wasserdampf die Katalyse in Abhängigkeit von den beteiligten Proben unterschiedlich stark beeinflussen kann. Eine detaillierte Zusammenfassung und ein abschließender Überblick über das hier vorgestellte Projekt werden im Schlussteil dieser Arbeit berichtet.

Contents

List of Figures

List of Tables

List of Figures and Tables of the Appendices

List of Abbreviations

AA	Acrylic Acid
AI	Artificial Intelligence
CHFS	Continuous hydrothermal flow synthesis
CV-RMSE	Cross validation root mean squared error
D	Dimension of the SISSO model
DFT	Density function theory
EDX	Energy Dispersive X-Ray
ER	Eley Rideal mechanism
FCC	Fluid catalytic cracking
FSP	Flame spray pyrolysis
ICP-OES	Inductively coupled plasma – optical emission spectrometry
LH	Langmuir-Hinselwood mechanism
MA	Maleic anhydride
MCPT	Microwave cavity perturbation technique
ML	Machine learning
MvK	Mars van Krevelen
NAP-XPS	Near ambient pressure – photoelectron spectroscopy
ODH	Oxidative dehydrogenation
ODP	Oxidative dehydrogenation of propane
ORR	Oxygen reduction reaction
POMs	Polyoxometalates
q	Rung of SISSO model
RSD	Relative standard deviation
SEM	Scanning electron microscopy
STEM-EDX	Scanning electron transition microscopy – energy dispersive microscopy
TCD	Thermal conductivity detector
T_c	Critical temperature
TPO	Temperature programmed oxidation
TPR	Temperature programmed reduction
VB	Valence band
XPS	X-Ray photoelectron spectroscopy

XRD	X-Ray diffraction

1. Introduction

The objective of this introduction is to endow first an overview on the industrial and environmental motivations, which encompass the presented research question (chapter 1.1), followed by the basic concepts of heterogenous catalysis (chapter 1.2.1) together with the pillars and correlations, which have been developed in selective oxidation so far (chapter 1.2.2). Secondly, perovskites, the tested, analysed and discussed system in the present doctoral project, are described in detail (chapter 1.3.1), together with their most common industrial applications and academical research topics (chapter 1.3.3) and with their embryonic structural potentiality to serve as basis for fundamental insights into oxidation catalysis to study structure-function relationships and as conceivably promising low-cost alternative catalyst for many selective oxidation reactions (chapter 1.3.4). Then, the catalytic systems, which have been mostly studied, tested and employed in academia and in industry for the selective oxidation of alkanes in the last 40 years are presented (chapter 1.4). Finally, a brief summary (chapter 1.5) will point out the research question of the herein presented work.

1.1 Industrial and environmental perspective for the oxidative dehydrogenation of light alkanes

In the past decades the proximate worldwide oil shortage has directed the chemical research towards the changeover from oil-based feedstock. Since olefins constitute the key building blocks for the (petro)chemical industry, their manufacture process plays a fundamental economical and environmental role. [6, 7] Nowadays, olefins are mainly generated by high–temperature processes, such as steam cracking, fluid catalytic cracking (FCC) or catalytic dehydrogenation of the corresponding alkane. These methods present several limitations, within these the most important are: ethylene is the preferred product from steam cracking, while propylene has a current higher demand and catalytic dehydrogenation can lead to catalyst deactivation due to cocking. [8]

In particular, selective heterogeneous catalysis is essential for the well-being of a society, because it produces about the 25% of the organic chemicals and intermediates employed by the manufacturing processes of industrial products and material goods. [9] Propylene is used for example in the production of polypropylene, but it is employed also to produce acrylic acid, acrylonitrile and propylene oxide. Acrylic acid constitutes one of the most important intermediates for the production of acrylates (mainly used to produce coatings, sealants, adhesives and textile fibers) and polyacrylic acid (mainly used to produce superabsorbents) and the economical increasing demand requires a yearly enhancement of 4-5% of its production (that currently lies in the range of 6 million tons per year). Historically, until the mid-1990s, acrylic acid was manufactured by C-C coupling reactions

in processes based on Reppe chemistry. While today, acrylic acid is mainly produced by acrolein oxidation derived from propylene oxidation in two stages-processes, which are performed over promoted bismuth molybdate and mixed Mo-V-W oxides, respectively, at the reaction temperature of approximately 600 K and 523 K, respectively (Figure 1.1). [10] Hence, due to the multistep technology and other disadvantages explained above, the alternative way for the oxidation of light alkanes to olefins and then to further oxygenates in an environmentally benign integrated route has become a key issue in oxidation catalysis research. [11]

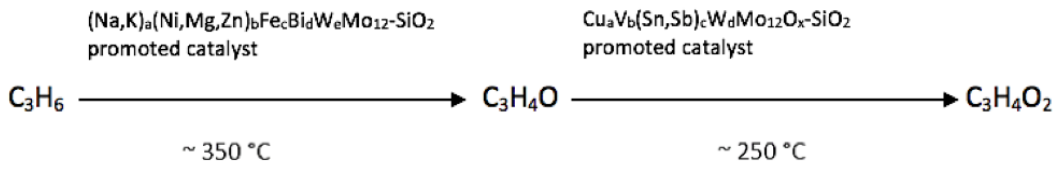

Figure 1.1. *Schematic illustration of the two stages processes for the production of acrylic acid from propene over promoted bismuth molybdate and promoted mixed Mo-V-W oxide catalysts. From Reference [10]*

1.2 Fundamental concepts in selective heterogeneous oxidation catalysis

1.2.1 Basic principles

The term "Catalysis" was coined by Berzelius in 1863 and it derives etymologically from ancient Greek, literally meaning "loosing down". Afterwards, the introduction of dehydrogenation in catalysis started with the French scientist Sabatier, who formulated the so-called Sabatier's principle, which states as follows: "the interaction between the catalyst and the substrate molecule, should be neither too strong or neither too weak." Finally, a landmark in the history of heterogeneous catalysis was signed by Fritz Haber with the discovery of ammonia synthesis starting from gaseous N_2 and H_2 catalysed by F_3O_4 under high-pressure condition. A catalyst is intrinsically defined as a substance, which is able to enhance the rate of realization of a chemical equilibrium without itself undergoing into chemical change [12] and the heterogeneous catalysis process is believed to occur on the surface, whose chemical properties may deviate significantly from those of the bulk. Therefore, the necessity of the surface's characterization becomes vital in order to encode the catalytic properties of the system, being the major obstacle in this regard constituted by the so-called "pressure gap" between the real working conditions and the near-working conditions, which are established in the in-situ characterization apparatus. To this extent, simplified and well-defined models, such as single crystals surfaces, can simplify the challenge. [13] The elementary steps in heterogenous catalysed reactions can be summarized in: a) molecular chemisorption of substrate, which can occur either through a non-dissociative or through a dissociative path, where a bond rupture of the substrate molecule occurs b) the formed product desorbs as a result of the

thermal activation in case of non-dissociative chemisorption or occurs via recombination of the fragments on the surface. Since the catalyst´s surface is a dynamic system, the study of the energetics of the interactions between the substrate molecules and the surface becomes essential. For this purpose, the formulation and determination of microscopic reaction mechanisms, which are able to individualize the elementary steps become indispensable.

Different reaction mechanisms have been postulated in heterogeneous catalysis, the more regularly discussed in ODH is the Mars-van-Krevelen (MvK) model, which assumes that the substrate molecule is oxidized by the oxygen of the metal oxide catalyst and that the formed oxygen vacancy is then refilled by the oxygen from the gas-phase.

A second approach to describe the reaction mechanism in ODH is the Langmuir-Hinshelwood mechanism, which assumes that the oxygen of the metal oxide does not take part in the reaction mechanism and the reaction proceed through the activated absorbed oxygen deriving from the gas-phase and the absorbed substrate molecules on the catalyst's surface. Such model is based on the assumption that every elementary reaction step can be the rate determining one and all the reaction stages are close to the thermodynamic equilibrium. A special case of this latter model is the Eley Rideal (ER) model, in which one species reacts directly in the gas-phase without being prior absorbed on the catalyst's surface.

The reaction mechanism is not unique for each type of reaction or each class of catalyst, it may vary both with the surface's composition, as well with the alkane.

1.2.2 Concepts, pillars and correlations in selective oxidation

In the past, there have been made many attempts to determine key-factors, which aim to gain control over the activity and selectivity of catalytic systems. [9, 14-24] The investigated features could be divided into three main groups: structural aspects, surface and the electronic structure properties. It is generally accepted that the characterization of some of the properties mentioned above for a given catalyst and their further correlation with catalysis could lead to a significant breakthrough in the knowledge of the reaction process. Nevertheless, in gathering data reported in the literature, a lack of homogeneity in these latter ones is evident and hence they cannot really serve as basis for a comparison to extrapolate general rules. For this reason, the simplest system which presents the potential to fulfill to the most required criteria to be a good oxidation catalyst is unavoidable. Recently, Schlögl, Trunschke et al. tried to solve this "selective oxidation labyrinth" addressing several efforts to study and characterize the well-defined, phase-pure M1 catalyst. [25-30]

From some pioneering experiments on propane oxidation over copper oxide, Grasselli and co-workers found that the selectivity changes with depletion in abundance of lattice oxygen. [9] From this observation, they presented a general design principle for all selective oxidation catalysts: controlling the abundance of lattice oxygen through the structure-design can lead to the control over the selectivity. The target is to limit the lattice oxygen presence at the surface to avoid over-stoichiometric oxidations. In order to make this, the isolation between the active sites becomes necessary. Grasselli et al. stated that the site isolation should be designed in order to satisfy the required abundance of lattice oxygen in a structure which should be chemically isolated from other active sites such that no exchange between them can occur. [9]

Based on this work, Grasselli and co-workers have reported seven important pillars as structural key-factors: (1) Lattice oxygen mobility, (2) Multifunctionality of the active sites, (3) Site isolation, (4) Phase cooperation (which are independent between each other) and (5) Strength of metal-oxygen bond (which depends on lattice oxygen, motif of the host structure and the redox properties of the cations respectively), (6) Motif of the host structure (which determines lattice oxygen mobility, strength of the metal-oxygen bond, redox properties of the cation and site isolation respectively) and (7) Redox properties of the cations (which is related to lattice oxygen mobility, strength of the metal-oxygen bond and motif of the host structure respectively). These latter interdependent "pillars" can be summarized into a unique concept of selecting the best electronic structure. [9] The seven "pillars" link the catalytic properties with the material science part of them. [31] However, the dynamic nature of the catalyst is not included. Therefore, the seven "pillars" still remains a rather formal concept to design a new catalyst, because they are not universally applicable, for instance, although the structure complexity generally provides the site isolation, for the $Mo_xW_{1-x}O_3$ catalyst the increase of shear planes leads to a decrease of selectivity. [32] Also the motif of the host structure is not universally valid as reported for butane oxidation. [33]

Alternative concepts, such as the role of thermodynamic stability of reactants and products in oxidation reactions were investigated by Hodnett et al. [16, 34] They mainly gathered literature data into a series of selectivity-conversion plots. They used on purpose data from different catalyst and operating conditions in order to define benchmarks of performance for every selective oxidation reactions. [16] The analysis shows that if the difference between the bond dissociation enthalpy of the weakest C-H bond in the reactant and the bond dissociation enthalpy of the weakest C-C or C-H bond in the selective oxidation product is less than 30 kJ/mol, a very high selectivity is achievable at all conversions, whereas for differences greater than 70 kJ/mol, low selectivity is always observed. However, unfortunately, this valuable work does not lead to a deeper understanding of the reason for different selectivities. Based on this concept, it is, for example, not understandable, why maleic anhydride is formed in oxidation of *n*-butane over $(VO)_2P_2O_7$ with high selectivity, but on MoVTeNb oxide with low one.

Also many combinatorial efforts and the design of libraries are reported for the optimization of the M1 phase, [35-38] but they seem to constitute purely statistical concepts rather than chemical insights. [31] Any new perspective in chemical reactivity of the surface is opened, as well in the theoretical calculations reported by Nørskov and co-workers [18, 21, 22, 39-44] and similar theoretical data reported in the literature. [17, 45, 46] They are generally suitable for very simple reaction mechanisms and the found correlation among parameters are not useful to understand the chemical selectivity, but only the activity (Figure 1.2).

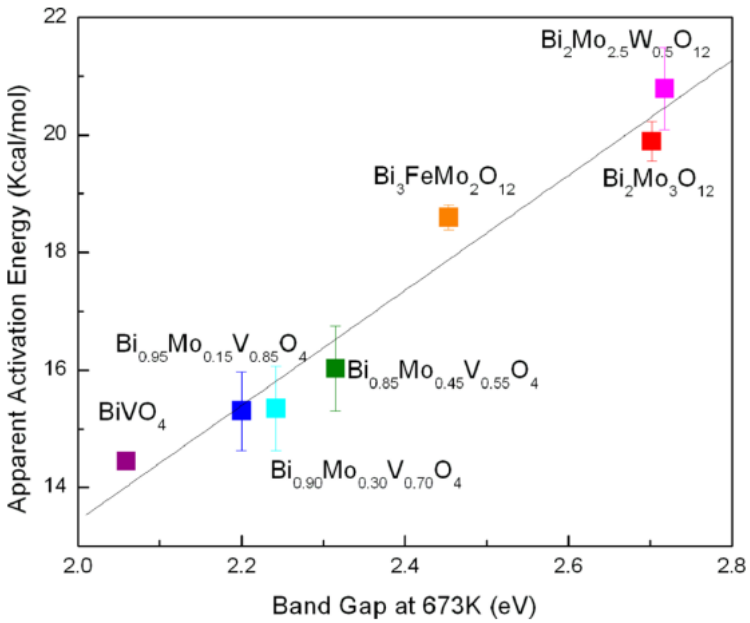

Figure 1.2. *Linear correlation found plotting the apparent activation energies for propylene oxidation to acrolein over bismuth molybdates vs their Band Gap. From Reference [17]*

1.3 Perovskites

1.3.1. The structure. From Reference [47]

Perovskite are originated from $CaTiO_3$, [48] and their name originates from the Russian mineralogist Count Lev Aleksevich von Petovski, although this class of minerals was earlier discovered in 1839 by the Prussian mineralogist Gustav Rose. Perovskite present the general formula ABX_3, where the A cation is a large-size cation, generally a lanthanide, an alkaline or alkaline-earth cation and B is a medium-size cation, generally a metal element belonging to the 3d, 4d or 5d configuration. While, X is constituted by an anion, typically O, N or an halogen. The overall structure should maintain the electrical neutrality. The idealized (aristotype) perovskite structure is represented by the cubic $SrTiO_3$, wherein the larger A cations are coordinated in a cuboctahedral cage-site (12-fold coordination), while the smaller B cations present six coordination and are located in the center of

octahedral polyhedrons (Figure 1.3). [47] One of most important features of perovskites is their structure flexibility, indeed they could accommodate around 90% of the metallic elements of the periodic table without destroying the structure. [49] From a crystallographic perspective the ideal perovskite is inflexible, meaning that a change in the composition should be accommodated by a change in the lattice parameters, due to the fact that the position of the atomic parameter cannot be varied. Starting from the crystallographic relations of the ideal cubic structure ($\frac{(A-X)}{\sqrt{(B-x)}}$ =1), Goldschmidt formulated in 1926 the so-called tolerance factor "t" , which limits the degree of A- and/or B-sites substitution lying in the range of $0.75 \leq t \leq 1$ and it is expressed by the following equation $t = (r_A+r_x)/(\sqrt{2}(r_B+r_x))$, where r_A, r_B and r_x are the radii of the A cation, B cation and X anion respectively. [50] Despite the simplicity of its formula, the tolerance factor has a reasonable predictable power for perovskites structures, especially of the oxides, where ionic radii are known with highest precision. Ideally, the t factor is equal to 1, indeed, when it lies in the range between 0.9 and 1, the cubic perovskite is a reasonable possibility. While, when "t" is larger than 1, it means that B is much smaller with respect to the A-site cation and the hexagonal packing of ABX_3 layers is preferred. Finally, when "t" is smaller than 1, the octahedral frameworks of the B-sites are distorted and close down the cuboctahedral cage of the A-site cations, resulting in a crystal structure with lower symmetry than the cubic one. Ionic radii have been employed also by Muller and Roy in order to predict in which structure the perovskite evolves with the changing of its chemical composition. For this purpose they invented Structure-Field maps, which can be considered as the graphical equivalent of the tolerance factor (Figure 1.4). [51]

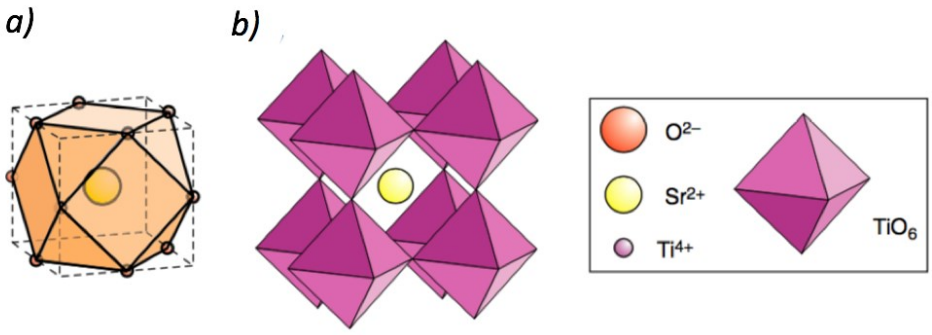

***Figure 1.3**. **a)** Cuboctahedral cage for the A-site; **b)** BO_6 octahedral polyhedron framework with the A-site (Sr^{2+}) at the center of the cubic cell for $SrTiO_3$. From Reference [47]*

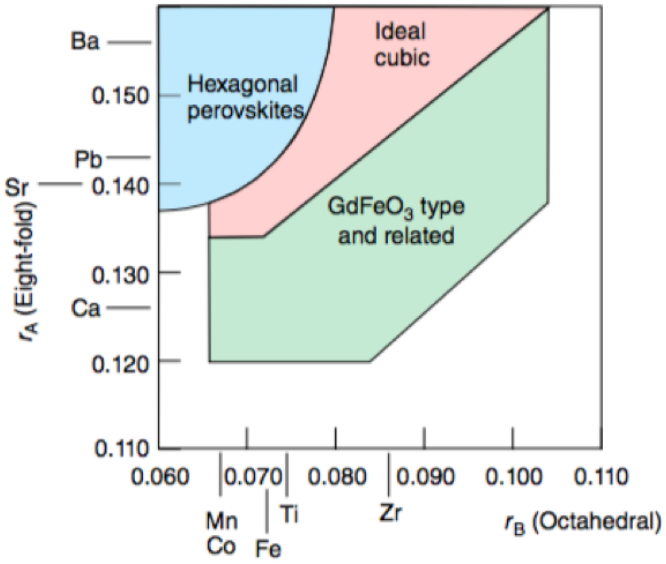

Figure 1.4. *Structure-Field map for $A^{2+}B^{4+}O_3$. From Reference [51]*

The BX_6 octhaedra are the roots of the many structure variants, which can be envisaged for perovskite-like structures. This is because the structural/chemical manipulation is mediated by the electronic configuration of the B-sites, which can be modified themselves by the surrounding geometry of the six anions (X). Although their influence cannot be considered negligible, the A-site cations tend to present a close-shelled structure with fixed valency, thus being less susceptible to chemical manipulation. There are three main factors which can lead to structural variations in perovskite-like compounds : a) the cation displacement, b) the octahedra tilt or rotation and c) the Jahn-Teller-induced distortion of the B-sites.

The cation displacement is the most elementary change which can be envisaged to maintain the BX_6 octahedra perfect (or nearly perfect), the B cation simply displace away from the octahedra's centers. This structural adaptation generally occurs when the B-site cations are too small ($t<1$). From an electronic perspective, this mechanism occurs for nonlinear molecules with a nondegenerate ground state and a low-energy-lying excited state. In such a situation, the distortion (caused by the displacement) occurs because it lowers the ground-state energy by mixing the ground state and the excited state. Additionally, it is important to notice that the preservation of the maximum degree of the symmetry has the highest priority during the transformation, therefore cation displacement has to be along one of the symmetry axes of the octahedra, such as twofold, threefold or fourfold axes (Figure 1.5).

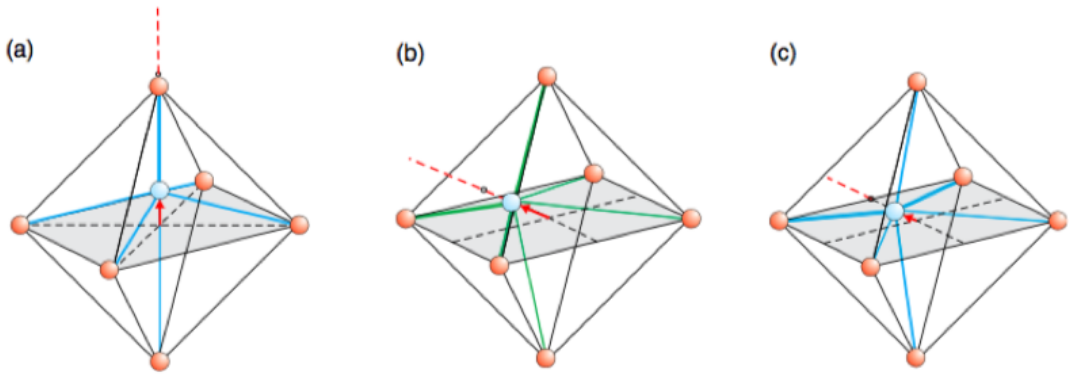

Figure 1.5. *Cation displacement in BX3 octahedra along* ***a)*** *the fourfold axis;* ***b)*** *threefold axis;* ***c)*** *the twofold axis. From Reference* [47]

The second structural compensation which can occur in order to preserve the perfect (or nearly so) BX_6 geometry is the tilt or rotation of the octahedra. This change is generally associated with the presence of a too small A-site cation for the cuboctahedra cage, in such a case, the BX_6 octahedra consequently twist so as to adequately reduce the cavity's dimension in order to maintain the symmetry, accommodating in this way t values <1. As for the cation displacement mechanism, the tilt can occur around the twofold, threefold and fourfold axes (Figure 1.6) and can be envisaged also as rotation around the x-,y- and z-axes of the parent ideal perovskite structure (Glazer notation). [52] The chemical substitution of A- and B-site may alter the tilt or rotation, for instance the degree of octahedral tilting in lanthanoids nickalates ($LnNiO_3$) is directly proportional to the size of the lanthanoid cation. [47] Moreover, the tilt or rotation is extremely responsive to the external conditions, such as temperature, pressure and strain.

Finally, the BX_6 octahedra themselves can give rise to elongated or flattened octahedra, eventually leading to square planar or square pyramidal coordination in some extreme cases. This is the result of the interaction of the electronic orbitals of the B-site cation with the surrounding anions. According to the crystalline-field theory, in an ideal octahedron the d-orbitals split into t_{2g} (at lower energy, a triple degenerate orbitals : d_{xy}, d_{xz} and d_{yz}) and into e_g (at higher energy, a double degenerate orbitals : d_{x2-y2} and d_{z2}). When a d-metal ion posses an odd number of electrons in the e_g orbital, such as Mn^{3+} (d^4, $t^3_{2g}e^1_g$) or Cu^{2+} (d^9, $t^6_{2g}e^3_g$), their e_g electrons will have the choice of two possible energetically equivalent distribution, leading in this way to a degenerate groundstate. The degeneracy is removed by the further splitting of the d levels (t_{2g} and e_g) and this electronic modification is accompanied by a significant structural change stabilization effect, which is expressed by an elongation or a compression along the z axis, the so-called "Jahn-Teller distortion". The splitting of t_{2g} orbitals is rather small and does not produce any important change for the perovskite structure, while the e_g splitting is the responsible factor for octahedra distortion in perosvkites, although very frequently happens that the A and B cations are able to remain in the

center of the polyhedra despite the distortion and only the crystal symmetry is lowered. Moreover, since the Jahn-Teller effect is temperature and pressure sensitive, the structure is generally able to return to the ideal cubic symmetry at elevated temperatures and pressures.

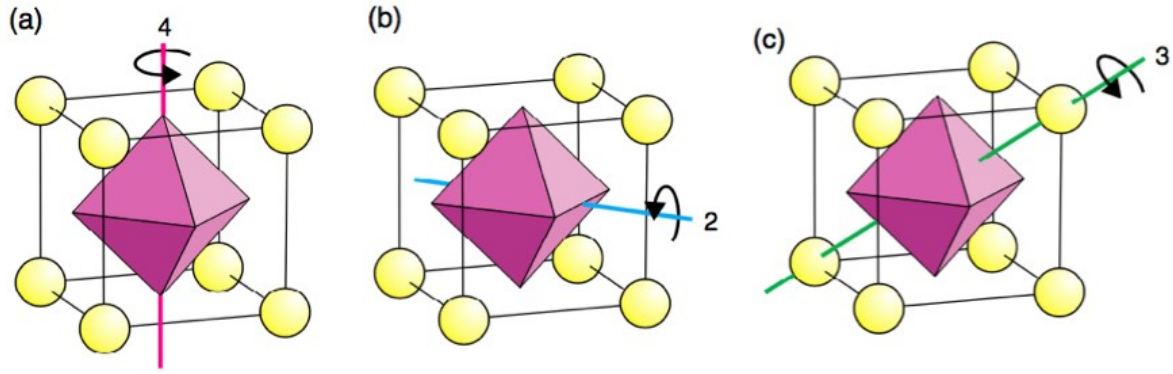

Figure 1.6. *Tilt in BX_3 octahedra along* ***a)*** *the fourfold axis;* ***b)*** *threefold axis;* ***c)*** *the twofold axis. From Reference* [47]

It is important to emphasize that these three listed above structural modifications are not mutually exclusive and they can occur individually or be combined. When the resulting changes affect all the octahedra in a similar way, that is a cooperative effect. While, when a non-cooperative effect is established, the distortion may cancel out some macroscopic functions, although they are still present at microscopic level.

In the earliest theory of the solid state, it was perceived that all d-electron-containing perovskite oxides have metallic behavior, because electrons were considered as a free and non-interacting electron gas. But, not all B cations which present partially filled d orbital generate metallic perovskites, being many of them antiferromagnetic insulators. The issue was solved in the middle of the XX century assuming that the partly filled 3d band, due to the Coulombic repulsion between electrons, splits into two sub-bands, a filled and an empty one with a band gap in between, being named valence band and conduction band, respectively. Many perovskites in the insulating state are semiconductors, because itinerant electrons can be promoted by thermal energy to the empty conduction bands and holes are left in the valence band. This loss of conducting state in perovskites can occur also because of different factors from the Coulombic repulsion, such as octahedra tilting or distortion, particularly Jahn-Teller distortion, cation ordering or cation displacement ordering and cooperative ordering of cation orbitals. [53]

Changes in the oxygen content of the perovskites are generally linked to changes in the ionic and electronic conductivity of these latter ones. Indeed, the conductivity is proportional to the number of electrons and to the partial pressure of oxygen as follows : $\Omega \propto [e'] \propto p^{1/4}_{O2}$. This is true when, under certain circumstances (during the synthesis, vacuum annealing et cetera), no variation of the

valence of the A cation is possible and oxygen poor composition is accompanied by the formation of oxygen vacancies. While, when the valency change of the cations is possible, the incorporation of free electrons or holes can give rise to electronic conductivity by electron hoping mechanism from cation to cation. However, it should not be forgotten that the formation of oxygen vacancies may also encourage oxygen ion conduction and the total conductivity of the material is the result of multiple components, oxide ion and electron or hole contribution.

The perovskite structure presents a broad multicolored fan of variegated structure-types, which could be subdivided into three main groups: a) ABX_3 related structures, b) hexagonal structures and c) modular phases.

The ABX_3 class is extended to more chemically complex phases, in which chemical defects play a fundamental role. The cation and anions can be distributed randomly over the available site, but they can also be ordered in double or even triple perovskite-type unit cells. The distribution and valence of these ordered or partly ordered ions is generally clarified by the employment of bond valence sums derived empirically from the determination of bond valence distance. Seldomly they are clearly apparent in diffraction studies. Among these structures, one of the most common is represented by the Rock-salt ordered double perovskite structure, with formula $A_2(BB')O_6$. In the double B-site perovskite, the ordering can be seen as a consequence on the energetic level of the different sizes and charges of the ions in order to reduce the lattice energy.

Moreover, the A-site cation can affect the B-site ordering, like in the case of La_2CoRuO_6-$La_{0.4}Sr_{1.6}CoRuO_6$ and $La_{0.8}Sr_{1.8}CoRuO_6$-Sr_2CoRuO_6 where the B-sites are ordered and disordered, respectively. Additionally, B-B' and A-A' ordering can coexist in the same structure, as in the case of $NaLaMgWO_6$ perovskite (Figure 1.7). Differently from the B ions, the A ions ordering takes form of layers, presenting non-stoichiometric oxygen deficient structures. In some cases, even the oxygen vacancies are ordered, like in the case of $BaYMn_2O_{5+\delta}$. In some rare cases the B cations, instead of coordinating into octahedra, can be also arranged in sheets, which are perpendicular to the cubic and/or pseudocubic axes or even at a diagonal of these latter ones.

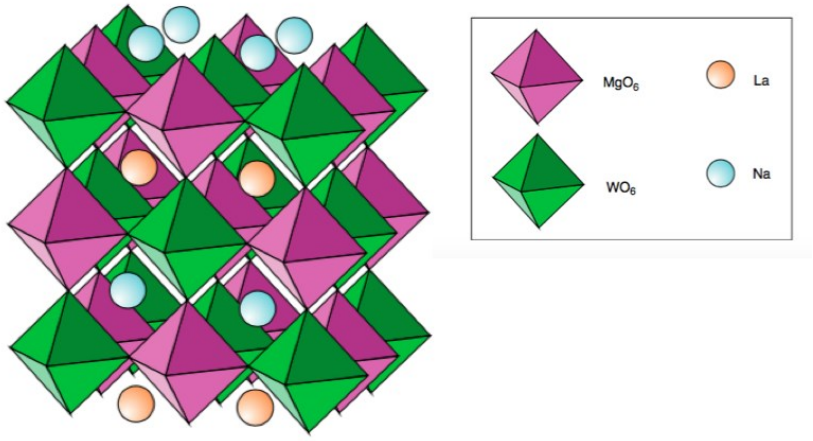

Figure 1.7. *$NaLaMgWO_6$ structure with double ordered A- and B-site cations. From Reference [47]*

A further class of A-site ordered perovskites is constituted by the oxides group with general formula $AA_3'B_4O_{12}$, where A is an alkali, alkaline earth or a lanthanoid metal and A' is a 3d metal ion, which should show a high Jahn-Teller distortion tendency in order to be included into the large A cage. Indeed, the $AA_3'B_4O_{12}$ compounds reported in the literature present Mn^{3+} and Cu^{2+} as A' site and the synthesis can occur only under high oxygen pressure (in the GPa range), which is necessary to stabilize the small cation in the twelvefold position of the perovskite. [54] However, recent studies have revealed that not only Jahn-Teller active ions can be stabilized at the A'-site, but also cation with other ionic states, in which the electrons can be delocalized into both A' and B-site. [55]

Regarding the cation deficient phases, it is important to emphasize the the A-site deficient perovskites, including in particular the ReO_3, WO_3 and related structures, where the A-site can be empty if the B-site presents a charge of +6. A_xWO_3 is a class of compound named tungsten "bronzes", in which foreign atoms can fill the A-site vacancy in the WO_3 structure. While, the anion-deficient phases can be divided into two main groups: the brownmillerites and the manganites. The first ones present the general formula $A_2B_2O_5$, within which the B cations are coordinated in tetrahedra and the oxygen stoichiometry is achieved by arranging rows of oxygen vacancies along the [110] direction in order to emulate an ideal perovskite. Altough they present the same composition of the brownmillerites, the B atoms of the manganites are coordinated into BO_5 square pyramids.

Despite of the ideal cubic close packing of the AX_3 layers, the hexagonal perovskites are constituted by hexagonal close packing of AX_3 layers, or by mixed sequence of hexagonal and cubic AX_3 close-packed layers. $BaNiO_3$ (or 2H-$BaNiO_3$) can be considered as the hexagonal analogue of the cubic perovskite structure and can be envisaged as a column of face-sharing octahedra parallel to the c axis, among which are interleaved chains of Ba^{2+} ions (Figure 1.8 a).

Finally, the so-called modular phases present the peculiarity to be able to accommodate the composition variation simply by changing the thickness of the perovskite units. Homologous species of the phase are produced when the components are ordered, while when these latter ones are disordered, planar-faults are formed, giving rise in this way to non-stoichiometric structures. Among these structures, the most frequently studied is the Ruddlesden-Popper phase structure, with general formula $A_{(n+1)}B_nO_{(3n+2)}$, where the B cation occupies the octahedra units and the A cation is located at the center of 4 apical oxygen ions, deriving from the four nearest octahedra, and it is also placed directly below the apical oxygen of the nearest octahedra belonging to neighboring layer (Figure 1.8 b). This layer structure presents quite often the tilting of the octahedra, lowering so the symmetry and influencing the physical properties, and non-stoichiometry, especially when Co, Fe or Mn constitute the B cation. Moreover, the Ruddlesden-Popper perovskites can be structured according to the T, T' or T^* geometry. The classical T (or T/O) structure is the one described previously, while the T' structure differs from the T one basically from the disposition of the oxygen atoms. In this latter one, the B cation sheets are no any longer octahedrally coordinated, but occupy the center of square planar pyramids (BO_2 layers). Whereas, the T^* structure is composed by a 1:1 intergrowth of the T and T' geometries.

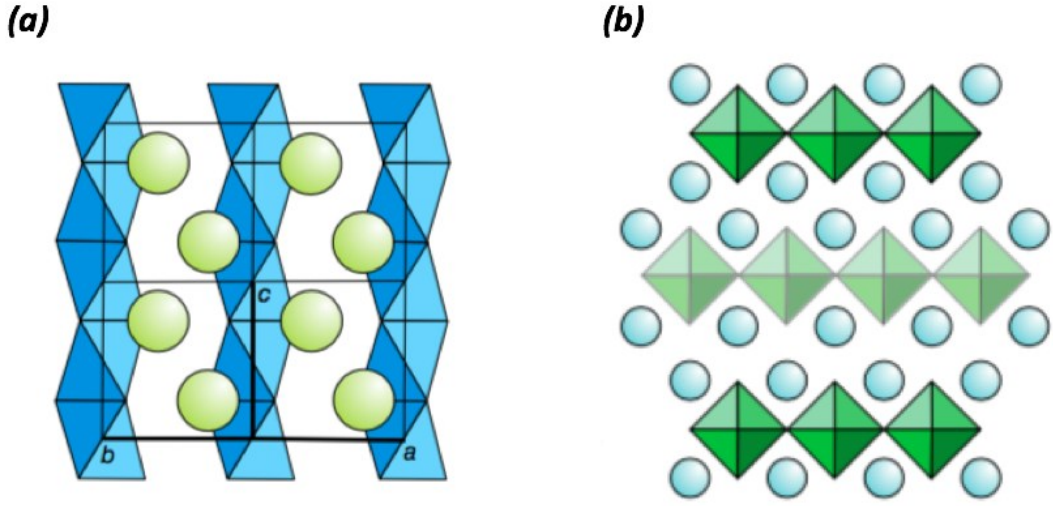

Figure 1.8. a)*2H-$BaNiO_3$ hexagonal structure in the [110] projection. Colours: green: Ba^{2+} ions and blue: NiO_6 hexagonal close-packed octahedra.* ***b)*** *Idealized Ruddlesden-Popper phase in the [110] projection. Colours: blue: A cations and green: BO_6 octahedra. From Reference [47]*

Other layered perovskites phases which deserve to be mentioned are the Dion-Jacobson phase and the Aurivillius phase. They can both be defined as variants of the Ruddlesden-Popper phase, with the first one presenting the replacement of an A cation ($A'A_{(n-1)}B_nO_{(3n+1)}$). Whereas, in the Aurivillius phase, one of the A cation is substituted by Bi_2O_2 layers, with the resulting formula unit being $(BiO_2)(A_{n-1}B_nO_{3n+1})$.

Many cuprate oxides layered perovskites are superconductors. For instance, the Jahn-Teller distorted La_2CuO_4 can be transformed from a room temperature insulator into a superconductor by replacement of some La^{3+} ions with alkaline earth cations, in this way some oxygen vacancies are formed upon the replacement in order to maintain the charge neutrality. The most studied oxygen-deficient cuprate superconductor is $YBa_2Cu_3O_{(7-\delta)}$ ($0 \leq \delta \leq 1$), which has been discovered as the first compound presenting a T_c above the boiling point of liquid N_2. Its structure consists of three perovskite unit cells stacked on top of the other. In the middle unit cell Y is the A cation, while Ba is located in the A-site in the upper and lower unit cells. Cu is the B cation, arranged into two different coordination: the square pyramidal and square planar one (Figure 1.9)

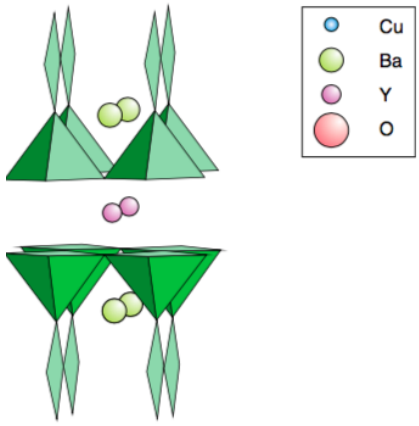

***Figure 1.9**. Idealized $YBa_2Cu_3O_7$ structure, presenting the CuO_5 square pyramids and the CuO_4 square planar polyhedra. From Reference [47]*

1.3.2. Synthesis of nanostructured perovskites

The commonly used proposed preparation method for perovskites was the ceramic one in the 1970s. [56] It consists in mixing the starting oxide powders, which react through solid-state diffusion resulting then in the desired product. Since the diffusion process in the solid-state is quite slow, these routes usually require high reaction temperatures (usually higher than 1000 °C) and long reaction time to complete the reaction and to obtain a phase-pure perovskite. [56-59] Due to the high synthesis temperature, the specific surface area of the resulting materials is rather low. Moreover, although this method can be considered environmentally friendly as the perovskite is synthesized directly from oxides without releasing toxic gases, it is necessary to homogenize the metal oxide precursors in order to make them react with each other through ion-diffusion. In this respect, different homogenization techniques can be employed, being the so-called "ball mill technique" the most popular one and most suitable for materials with catalytic properties, due to the fact that the resulting materials present an increased surface area. This mechanochemical activation is one of the most effective method to obtain highly disperse systems. It consists in grinding the precursors

though mechanical shaking in a closed volume employing high grinding bodies (generally it is constituted by agate balls into an agate vessel, but depending on the target material, the vessel and the balls can be constituted also of zirconia or alumina). [60] The process can be explained on the energetic level in occurring of energy accumulation, which proceeds in material destruction, due to the appearance of cracks and changing at the boundaries between the phases, resulting in the formation of new surfaces with increased energy and corresponding increased surface areas. Therefore, the starting materials are transformed into a new material presenting physical and, in some cases, even chemical changes with respect to its precursors. [61] This mechanochemical activation has preceded the synthesis though ceramic route or has been employed as self-sustaining synthesis route for mostly ABO_3, A_2BO_4 and $A_2B_2O_6$ perovskite- and double-perovskite-like structures. [62-67] Additionally, the class of double A-site perovskites presenting general formula $A_3A'B_4O_{12}$ (see above) can be synthesized only through high-pressure solid-state synthesis route. [54, 68-70] The reason lies in the nature of A' ion, which is a Jahn-Teller distorted metallic ion belonging to the 3d electronic configuration, which therefore requires high oxygen pressure and high temperature in order to be stabilized into the twelvefold coordination position of the large A-cage. [54]

However, in order to be applied in catalysis, the synthesis route should aim to produce a material with increased surface area and/or decreased particles size of the perovskite oxides, since catalysis belongs to a class of surface reaction. To this extent, an efficient way is represented by soluble metal nitrates-based synthesis routes, where the preparation of the perovskite oxides is conducted in presence of an organic component (such as glycine or citric acid) able to coordinate, combust and disperse the metal oxides formed particles. [71-76] Although the sol-gel and self-combustion method can be considered rather advantageous due to their simple preparation process as well the considerable catalytic performance, the surface area of the perovskite oxides prepared by these routes is still not totally satisfactory. [77]

Apart from the sol-gel synthesis, other solution-mediated methods which are frequently employed for perovskites synthesis are coprecipitation, [78, 79] and complexation. [80, 81] The coprecipitation process is one of the oldest technique for the preparation of mixed oxides and consists in simply dissolving the desired cations in an aqueous solution, which is subsequently mixed with a second solution containing the precipitating agent. The mixing rate, the pH, the temperature and the concentration can be considered as the parameters which exert most dominating influence over the synthesis control. [82] These soft-chemistry methods are based on dissolving precursors in liquid media followed by drying and evaporating the solvent and subsequent calcinations. [83] Since these methods make use of liquid media, the phase formation temperature decreases by hundreds of degrees with respect to the solid-state reactions because precursors become more homogeneous, thus suppressing grain growth and loss of surface areas. [84, 85]

The hydrothermal method is a potentially superior route for low cost production of advanced mixed oxides, such as perovskites, because the complex oxides powders can be formed directly. [82] It can be differentiated by the other solution-mediated processes, such as sol-gel method and coprecipitation, by the temperatures and pressures involved. The temperature is between the boiling point of water and its critical temperature (374 °C), [86] while the pressure can go as high as 15 MPa. [87] The reaction mechanism follows the nucleation model [88] and allows the control over particles size, surface areas and phase composition of the target material. [86] Moreover, despite of the other solution-mediated methods, the hydrothermal route permits the preparation of nanocrystalline metastable phases. [89, 90] The hydrothermal synthesis of perovskites are generally carried out between 200-300°C, at autogenous pressure, employing metal nitrates, acetates, metal hydroxides or organometallic precursors and in with a pH major than 8. [91-97]

A novel extension of the hydrothermal synthesis method, which is able to produce nanomaterials with high surface area and controlled morphologies, is the so-called "Continuous Hydrothermal Flow Synthesis" (CHFS). Despite of the batch-based processes, this continuous flow-based method is able to produce inorganic NPs presenting unique structures or combination of particle properties, [98] which can lead to metastable or kinetic compositions, characteristics which render this synthesis method the most suitable for the synthesis of materials addressed to catalytic application. [99, 100] The employed medium is Supercritical water, which is formed when water is heated above 374 °C and subject to a pressure, which lies above 22.1 MPa. [101] Once the critical point (374°C, 22.1 MPa) is reached, the infinite percolating network of hydrogen bonds breaks apart [102] and consequently the dielectric constant decreases drastically, as much as supercritical water can be treated as a non-polar organic solvent (its dielectric constant approaches the value of six). [103] Together with the dielectric constant, also the density and the ionic product of water decrease significantly (Figure 1.10), giving rise to a much broader pH range. [86] The reaction mechanism can be divided into the two classical steps which define the hydrothermal process: a) $M(NO_3)_x + xH_2O \rightarrow M(OH)_x + xHNO_3$ and b) $M(OH)_x \rightarrow MO_{x/2} + \frac{x}{2} H_2O$, named hydrolysis and oxalation, respectively. The driving force of this hydrothermal flow synthesis with respect to the traditional batch-based ones is constituted by the fact that the dehydration step takes place before large hydrous oxide particles are grown. Indeed, the smaller the hydrous oxide particles ($M(OH)_x$), the higher the dehydration's rate, which is translated into the formation of fine metal oxides particles with high surface areas. [104]

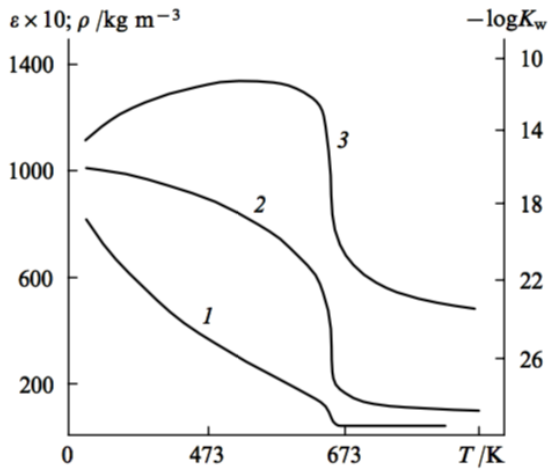

Figure 1.10. *Temperature dependence of the (1) dielectric constant, (2) density and (3) ionic product of water at 24 MPa. From Reference* [86]

Two different reactor geometries are reported for the CHFS method : the counter-current reactor [105-107] and the co-current one, [108] being the last one the most recent (Figure 1.11). Many ABO_3 and layered perovskites, addressed to catalysis and presenting very well-defined morphology and high surface areas, have been synthesized with this cutting-edge synthesis method employing both reactor configurations. [109-117]

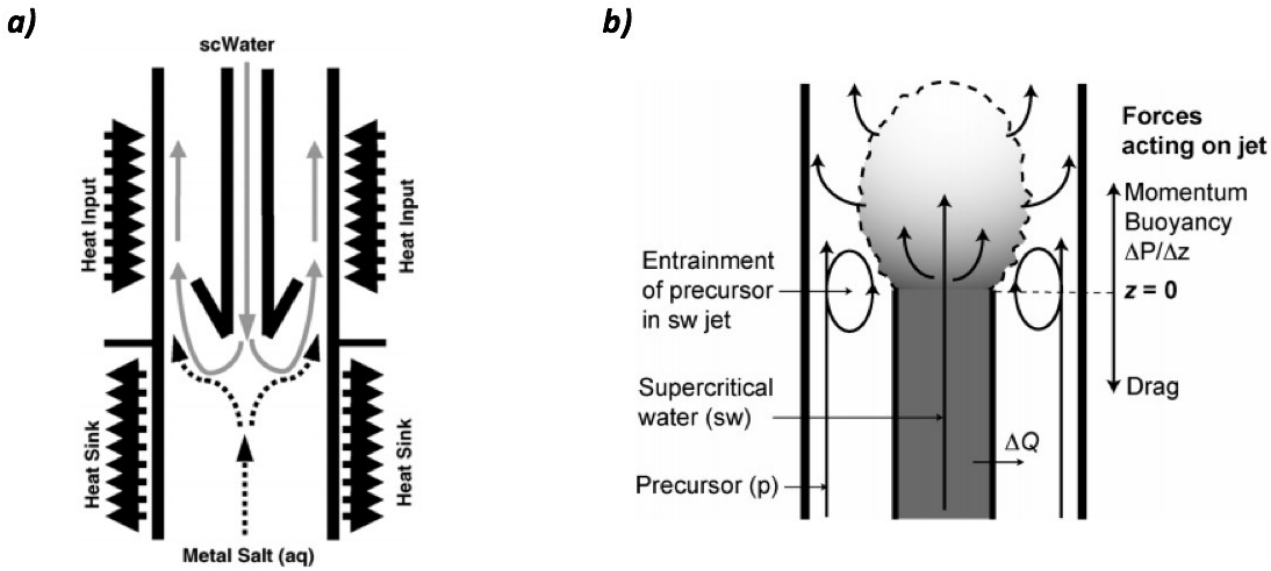

Figure 1.11. *Configuration of* ***a)*** *the counter-current reactor (Nozzle reactor), from Reference*[106] ***b)*** *the co-current reactor, from Reference* [108]

An additional promising, versatile and relatively easy bottom-up synthesis technique employable for the production of perovskites addressed to catalysis is the Flame Spray Pyrolysis (FSP) method.

This route allows the production of very fine nanoparticles with homogeneous morphology and size, being the right combination of precursors and solvents the key-issue of a successful synthesis. Indeed, the most important parameters are the solubility of the precursors into the solvent and the combustion enthalpy of the solvents and precursors. [118] The synthesis set-up is basically composed by a syringe-pump, which flows the precursors solution into a flame burner and the powders produced by the combustion are generally collected by a filter attached to a vacuum pump or by an electrostatic precipitator (Figure 1.12). The reaction mechanism follows the gas-to-particle route, where the precursors evaporate at the tip of the needle of the flame burner forming a metal vapour, consequently, the gasified metal oxide precursors start to nucleate as result of supersaturation and grow by coalescence or sintering. Finally, the particles can create aggregates by hard chemical bonds or agglomerates by soft physical interactions.

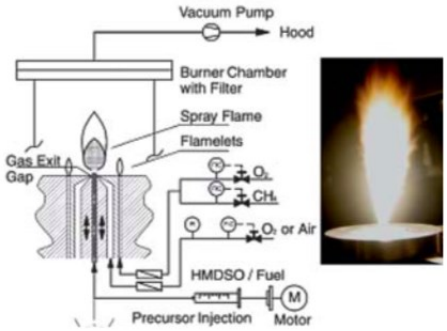

***Figure 1.12**. Schematic flow chart diagram oft he FSP set-up. From Reference [118]*

Many perovskites have been synthesized by FSP method mainly starting from nitrates, acetates and acetylacetonates, propoxides precursors dissolved in organic mixture mostly composed by ethanol, methanol, 2-ETA, propionic acid, toluene, xylene and water. [119-131]

1.3.3. Applications

Ceramics are by far the most widely produced and employed materials by the humankind and there are only a half of a dozen phases that dominate the human use, especially in terms of technological significance. [132] Among these phases, ABX_3, A_2BX_4 and spinel structures emerge, being the perovskite-related structure far ahead of the spinel one, due to its flexible composition. Indeed, perovskite could accommodate around the 90% of the metallic elements without destroying their structure, thus giving rise to a wide fan of different compounds with uncountable material properties. The first useful property discovered in perovskites was the high dielectric constant (k), which was found in $BaTiO_3$ during WWII and links perovskites to ferroelectricity. Some perovskites exhibit electronic conduction, while others are insulator. The mechanism of electric

conduction can be either electronic, ionic or mixed conduction of electrons, protons [133] or oxide ions. [134] In particular, "relaxors" are a family of substituted perovskites with extraordinary high dielectric constants as result of their order-disorder behavior [135] and their symmetry is generally the rhombohedral one, due to the slightly distorted lattice parameters. Furthermore, due to their high dielectric constant, perovskites are employed to produce dielectric resonator for microwave applications. The dielectric constant correlates with the tolerance factor (Figure 1.13 a), which also correlates with the peak width and frequency of A_{1g} Raman scattering (Figure 1.13 b), because of the dielectric losses of perovskite-like compounds in the microwave frequency region. Moreover, some perovskites, such as $SrTiO_3$, [136] $CaTiO_3$ and (RE,Na)TiO_3 (RE: La, Nd, Sm, Gd) present a quantum paraelectrics behavior, [132] which is a tendency of the material to show an impending phase-transition at low temperature, but at such low temperatures, quantum effects are activated blocking the impeding phase-transition. The transition between an electronic conductor and a semiconductor can occur when the RE cation (RE: rare earth) in $RETiO_3$ is properly substituted. [134] Indeed, after having dominated the world of dielectrics for almost 30 years, perovskites have conquered also the world of superconductors. Indeed, it was noted that the combination of 4*f* cations in the A-site and 3*d* cation in the B-site gives rise to rather conducting phases at room temperature. Sleight and co-workers developed the highest T_c oxide superconductor in $BaBiPbO_x$ in 1975, [137] while the first perovskite with a Tc above 30 K was $BaLaCuO_x$. Afterwards, it was the turn of cuprates perovskites in superconductor field with the discovery of YBC superconductor by Ashburn [138] and the following identification of $YBa_2Cu_3O_{(7-\delta)}$ ($0 \leq \delta \leq 1$) as a perovskite which presents a T_C above the boiling point of liquid N_2 (77 K). [139] Unfortunately, the magnetic property of this latter material can not be studied in combination with ist catalytic properties, because of the high T at which catalysis is generally performed. Additionally, some perovskite-related structure with general formula $RE_{(1-x)}A_xMnO_{(3+\delta)}$ (with RE: rear-earth cation and A: alkaline-earth cation) exhibit giant magnetoresistance effect (GMR), [140] which consists in a change in the material resistance in presence of a magnetic field by more than a factor of ten. GMR oxides find various important applications, such as high-pressure pumps, underwater sonar, active vibration control and potential applications in magnetic storage technologies. Moreover, superconductivity and high mobility in a 2D electron gas have been discovered at the atomically interface between two insulating materials, such as $SrTiO_3$ and $LaAlO_3$. [141, 142]

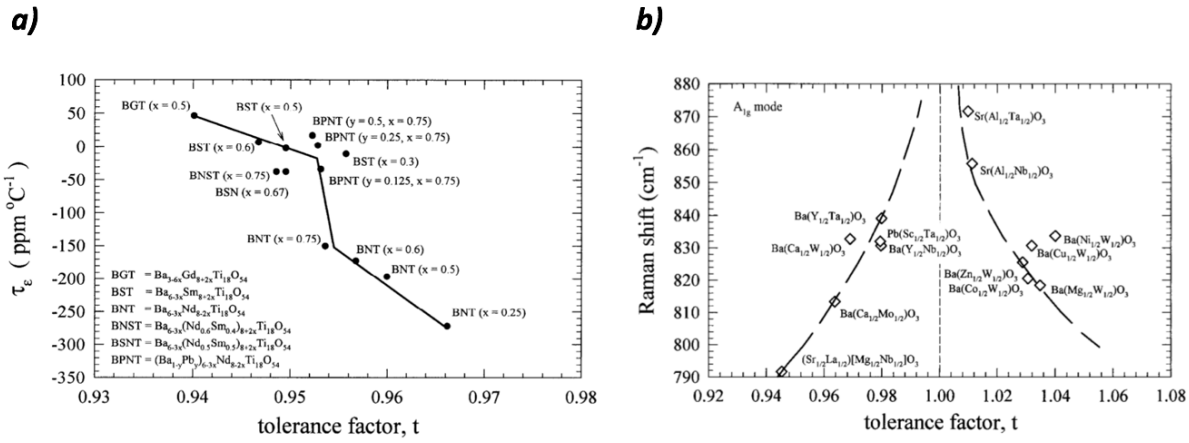

Figure 1.13. a) *Temperature coefficient versus tollerance factor for BNT compounds;* ***b)*** *A_{1g} Raman mode shift versus tollerance factor in perovskite structure. From Reference* [132]

Starting form the 80s, perovskites have been widely tested in catalysis, mainly in (photo)electrocatalysis. [143-145] Perovskites have been discovered to be efficient and low-cost alterantive catalysts for OER snd ORR reactions , [146] which play a central role in the effeciencies of solar cells (halide perovskites in particular), [147-152] fuel cells, [153-157] metal-air batteries [158-160] and (photo)electrochemical water-splitting devices. [161-163] Shao-Horn and co-workers have highligthed the importance of the control over the electronic structure of perovskites in order to modulate the catalytic activity in ORR reactions, showing the critical influence of σ^* orbital and metal-oxygen covalency on the competition of different reaction steps as the rate-determining one though a descriptor-based approach. They have found a volcano-relationship between the ORR activity of 15 A- or B-site substituted perovskites and the e_g electrons (Figure 14). [143]

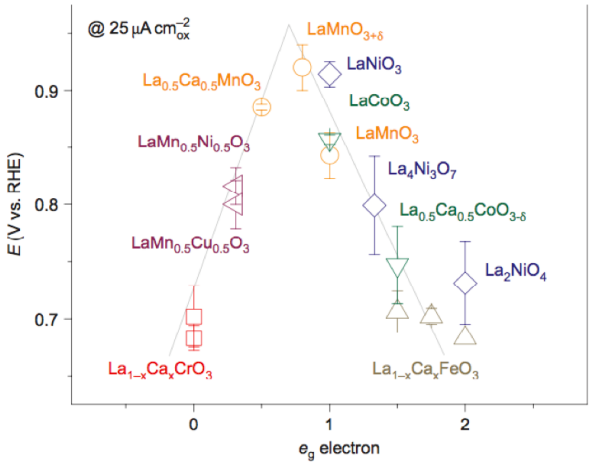

Figure 1.14. *Potential at 25 $\mu A cm^{-2}_{ox}$ as a function of e_g orbital in perovskite oxides. From Reference* [143]

Furthermore, perovskites can be employed for air purification, due to their the capability to catalyze several reactions, such as CO oxidation [164-167] and NO_x [168, 169] and CO_2 [170] reduction. A huge variety of other reactions can be catalyzed by perovskite oxides, in particular oxidation reactions, which will be discussed in detail in the next chapter (1.3.3.). The most common catalytic applications of perovskite oxides are summarized in Table 1.1.

Table 1.1. Table summarizing the catalytic applications for a given compound and the corresponding oxidation state of the B-site cation.

Compound	**Catalytic application**	**Oxidation state of the B-site**
$LaVO_3$ [171]	Isopropanol decomposition	+3
$LaVO_4$ [171]		+5
$SrMnO_3$ [172, 173]	Hydrocarbon combustion	+4
$La(Nd)MnO_3$ [72]		+3
$Bi_2Sr_2CuO_6$ [174]	N_xO decomposition	+2
$Bi_2Sr_2CaCu_2O_8$ [174]		+2
$BaMnO_3$ [175]		+4
Nd_2CuO_4 [176]		+2
$BaMnO_3$ [177]	Oxygen reduction and oxygen evolution	+4
$YBa_2Cu_3O_7$ [178]	CO_2 hydrogenation	+2/+3
$YBa_2Cu_3O_7$ [97]	Methane oxidation	+2/+3
$LaVO_4$ [179]	Selective oxidation of H_2S to S	+5
$LaMnO_3$ [180]	VOCs degradation	+3
$SmMn_2O_5$ [167]	CO oxidation	+3/+4
$SmMn_2O_5$ [181]	NO oxidation	+3/+4
$LaVO_4$ [182]	Oxidative dehydrogenation of propane	+5
$PrVO_4$ [183]		+5
$NdVO_4$ [71]		+5
$SmVO_4$ [184]		+5
$YBa_2Cu_3O_{7-\delta}$ [185]	Partial oxidation of ethanol to acetaldehyde	+2.23
$LaMnO_3$ [186]	Tartrazine oxidation	+3
La_2CuO_4 [187]	Oxidation of aldehydes to corresponding carboxylic acid	+2
$PrMnO_3$ [188]	CO and Soot oxidation	+3

Table 1.1 (cont.)

RE_2CuO_4 [189] $RE_2Cu_2O_5$ [189]	Soot oxidation	+2 +2
$LaVO_4$ [190]	Ammoxidation of 2-methylpyrazine to 2-cyanopyrazine	+5

1.3.4. Perovskite oxides in Oxidation Catalysis

Many fundamental as well as application studies have been carried out on the oxidative catalytic properties of perovskite oxides, since high catalytic performance of these latter materials for CO oxidation were reported in 1970s. [191] Although the perovskites have most frequently been applied in total combustion catalysis, it is reported in the literature that some of the perovskites and related structures are utilized for selective oxidation reactions, such as oxidative dehydrogenation of propane [71, 182, 184, 192-197] or the partial oxidation of ethanol to acetaldehyde. [185] For example, when the oxidative dehydrogenation of propane is performed over phase-pure rare-earth orthovanadates catalysts at the temperature of 500 ° C, the selectivity towards propene achieves up to 75.8% at the conversion of 2.86%, 78.3% at the conversion of 2.17%, 47.8% at the conversion of 5.10%, 45.7% at the conversion of 16.6% values when $LaVO_4$, $PrVO_4$, $NdVO_4$ and $SmVO_4$ are employed respectively. [71, 197] Nonetheless, the only products detected in propane oxidation over perovskite-like catalysts are propene and CO_2.

Due to the potential capacity to include several metals within the perovskite structure and the stability, perovskites offer a way to link solid state chemistry with catalytic properties. [198] Indeed, some basic strategies for designing perovskite-type materials for catalytic applications were proposed by Tanaka and Misono in 2001, where they presented five advantages and design parameters perovskite-type catalysts: [199]

1. Selection of the B-site allows control of reactivity
2. Stabilization of unusual oxidation states is possible
3. Synergistic effects when two the different B sites are used in one structure
4. Enhancement of surface area by forming fine particles is often necessary
5. Perovskites can be used to support precious metals

Concerning the choice of the B-site element, this latter one is known to influence the catalytic activity while the A-site element was discovered to play a secondary role with respect to that (especially when A is a rare-earth ions and B belongs to the 3d configuration). [200] Some studies reported that the activity for propane and CO oxidation changes with the B-site or with the synergistic effect of a double B-site, while the synergistic effect of a double A-site seems to not

influence the catalytic performance [166, 199, 201] because the introduction of cation on the B-site increases the O_{ads}/O_{latt} ratio and oxygen vacancies concentration on the surface. [201]

However, these attempts to define a structural-function relationship in perovskite oxides present a lack of systematicity in the studies. In some cases, CO the activity has been correlated with a nominal descriptor, such as the nominal Cu content in $LaMn_{(1-x)}Cu_xO_3$ (with X=0-0.5), instead of an experimental derived one. Since catalysis belongs to a class of surface reaction, the elemental surface concentration is far ahead more significant descriptor and in such a case the proposed structure-function relationship would not be any longer valid. [166] In other cases, the reported rates have been calculated at very high temperature, where the system is no longer in the kinetic regime for CO oxidation, which render the presented data unreliable and the B-site substitution has been tested on a single A-site within the series, neglecting the possible effect of optimal synergistic combination between A and B-site. [166, 201] Indeed, a systematic study on an extended matrix where A and B have been individually substituted within the same series is missing. Optimum substituted catalysts such as $La_xSr_{(1-x)}Fe_yCo_{(1-y)}O_3$ have been tested in toluene oxidation after a three layer perceptron neural network has been employed for modeling and simulating the catalytic performance and material descriptors. [166, 202] Regarding the reaction mechanism of CO and propane combustion/oxidation over perovskite-like catalysts, different mechanism have been considered, being the interfacial (MvK) one the most reported, [203-209] although the efficiency of interfacial mechanism critically depends from the formation energy of oxygen vacancies. [210] In some cases also suprafacial mechanisms, such as L-H and E-R have been proposed. [211-213]

1.4 Classical oxidation catalysts

A high number of multi-metal oxide catalysts has been claimed to be active in selective oxidation reactions. They are generally composed by early-transition metal oxides, such as Mo, V, Mn which can be mixed with hetero atoms, i.e. non-metals such as P, Bi, Sb, Nb , W or Te, and/or with alkaline and alkaline earth ions such as Na^+ or Mg^{2+}. [214-225] For the selective oxidation of propane several multi-metal oxide systems are reported in the literature and with respect of their chemical composition they can be classified into (a) molybdenum-based mixed oxides, (b) heteropoly acids and their salts and (c) phosphates.

Ni-Co-molybdates catalysts offer a stable catalytic system for oxidative dehydrogenation of alkanes and present the possibility to add further elements into the ternary molybdate structure with formula $Ni_{0.45}Co_{0.45}X_{0.066}MoO_4$, where X = P, Bi, Fe, Cr, V and Ce. [226]

MoV-based catalysts show the ability to catalyse several oxidation reactions, like (amm)oxidation of propane, [227] oxidation of acrolein to acrylic acid, [228] oxidation of ethane to ethylene or to acetic

acid [229, 230] and the ODH of n-butane to maleic acid or anhydride. [228] They differ in composition and in crystalline phases, among these the most studied are the tetragonal, the pseudo-hexagonal and the orthorhombic structure. Thorsteinson et al. were pioneers to work with molybdenum-vanadium oxide based catalysts for selective oxidation reactions and nowadays MoV-based M1 phase-pure catalysts are the preferred ones for selective oxidation of propane, in particular, The Mo, V, Te, Nb multi-metal oxide shows the best performance for propane oxidation to acrylic acid (50-70 wt%). [26, 230, 231] In fact, Thorsteinson et al. indicated niobium as the responsible element for the stability of the catalyst bulk against oxidation and reduction. [232] Regarding Te, it is reported in the literature that it has a beneficial effect on the selectivity to acrylic acid. [233] Afterwards, Tellurium was mentioned to play a role in the active ensemble, [234, 235] even if subsequently was probed that a significant amount of acrylic acid is produced also over a Te-free M1 catalyst where the hexagonal channel is partially filled with vanadium which migrates through the channel to the surface. This could explain the major selectivity of MoVTeNb M1 oxide with respect to MoV M1 oxide: the enrichment of Te at the catalyst surface limits the enrichment of V^{5+}species which in accumulation of more than 50 % are cause for the post-combustion of acrylic acid. [30]

12-Molybdophosphoric acid shows some activity in the formation of acrylic acid which becomes enhanced when the protons are exchanged by counterions like Cs^{+}, Fe^{3+} or Ni^{2+}. [236-238] Also Ga^{3+} seems to be another counterion that affects positively the formation of acrylic acid over Kegging-type heteropoly oxometalates. [239] However, heteropoly compounds are usually not stable under reaction conditions and generally transform into mixed oxide or phosphates. [231]

The VPO system is mainly employed for n-butane oxidation to maleic anhydride, but can be also employed for ODP reaction and presents different crystal phases, within these the VPP seems to be the best compromise between activity and MA selectivity. [240-243]

Although some claim that vanadium is not necessarily required to activate the alkane, [8, 244] vanadium has been discussed so far as the key element for selective oxidation of alkane.

For the selective oxidation of propane a MoVTeNb catalyst was patented by Mitsubishi Corp. in the early 1990s. [227] This catalyst shows high yields with respect to the previous employed catalysts in propane oxidation, but its productivity is not yet sufficient to compete with the established industrial processes. This nanostructured multimetal-oxide catalyst composed of Mo, V, Te and Nb presents a selectivity that seldom exceeds the 80% at maximum conversion of 60%, thus the yield of 50 % yield has been rarely surpassed. The benchmark yield for applications depends on the raw materials prices and the economic situation, but it is usually considered to be above 60%.

In spite of the considerable efforts reported in the last 20 years literature in order to raise MoVTeNb catalytic performance, no breakthrough has really been achieved with respect to the original MoVTeNb catalyst patented by Mitsubishi. [227, 231]

In the MoVTeNb mixed oxide, like in POMs [245-247] which are its synthesis precursors, the structural motif $\{(M)M_5\}$, where M= Mo, V, Nb is composed of a pentagonal bypiramidal unit MO_7 which shares the five edges with five MO_6 octahedra units. Keplerates $\{(Mo^{VI})Mo^{VI}_5\}_{12}(linker)_{30}$ and Lindqvsit anions $(Mo_6O_{19})^{2-}$ can be considered as donor of $\{(M)M_5\}$ building blocks in the hydrothermal synthesis of MoVTeNb mixed oxide with M1 structure. [248]

Several crystallographic analyses aimed to solve the structure of MoVTeNb oxide [249] and to identify the active centers were performed in the past, among these the majority by Grasselli et al [45, 234, 250-257] (Figure 1.15).

It is reported that MoVTeNb M1 oxide exhibits an orthorhombic phase characterized by the length of the cell edges in the following ranges: a= 21.1035(1)-21.208 (5) Å, b= 26.5798(19)-26.741 (6) Å, c= 4.0016 (6)-4.0189(2) Å, [25, 28, 227, 250, 251, 253, 256, 258, 259] by a cell volume of 2260.3(3)-2261.89(78) $Å^3$ [255, 260] and by a crystallographic density of 4.4 g/cm^3. [261] The pentagonal bipyramidal units are occupied by Nb^{5+} and the distorted squared pyramids around the pentagonal center are occupied by $Mo^{5+/6+}$and the linker sites are occupied by a mixture of $Mo^{5+/6+}$ and $V^{4+/5+}$. The hexagonal channel is partially filled with Te^{4+} and the heptagonal channel is usually reported to be empty, [249-252, 256] with the exception for two studies within which traces of Te^{4+} were considered to be located also into the heptagonal channels of the M1 structure. [255, 256]

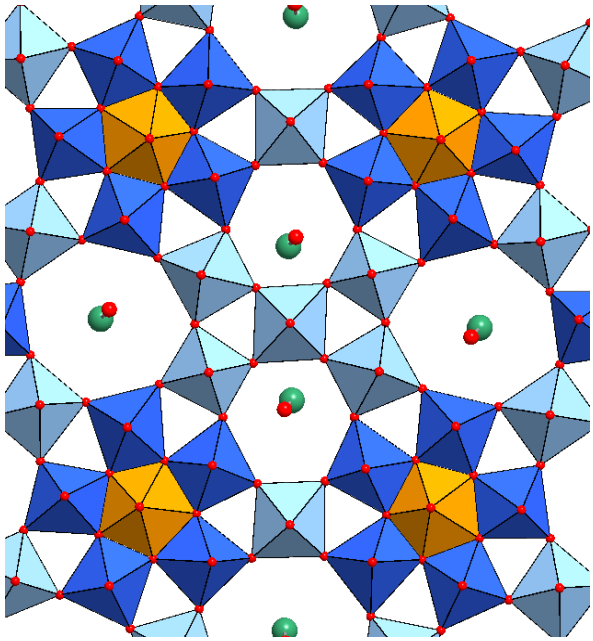

Figure 1.15. *Catalytically active plane of $Mo_{7.8}V_{1.2}Te_{0.94}NbO_{29}$ M1 phase in [001] projection.*

The morphology is mainly needle-like [25, 252, 256] or prismatic, found for the following stoichiometry range $MoV_{0.23-0.35}Te_{0.08-0.28}Nb_{0.14-0.45}$. [26]

Grasselli and co-workers also claimed that "the key paraffin activation phase is M1". They assumed that the catalytically active sites are located on the surface of the M1 basal plane (001) (Figure 1.15) and proposed a propane oxidation mechanism where the methylene hydrogen of propane is activated and abstracted by $V^{5+}=O$ $^{4+}V\cdot\text{-}O\cdot$ sites at the crystallographic positions M3 and M7 (Figure 1.15). Then, once the chemisorbed propylene is formed, the adjacent Te^{4+}-O sites abstract the α-H from this latter one and the adjacent $O=Mo^{6+}=O$ centers insert the surface lattice O into the chemisorbed π-allylic intermediate. Afterwards, the formed species could desorb as acrolein or react with water molecule, further oxidize and desorb as acrylic acid. [262]

Ueda et al. attribute the activity of the M1 phase to the strain generated by the heptagonal rings. The octahedra become distorted or even puckered when the heptagonal ring is introduced. Due to of this structural distortion, the probability that the Mo and V octahedra may give rise to active oxygen species becomes higher. [263]

While, by studying the electronic properties of the M1 phase, Schlögl et al. claimed that the surface state, which could be simplified as the V^{5+}/V^{4+} redox couple, affects the band banding of the crystalline M1 structure, thus it could become possible to decouple in time the reaction steps of alkane oxidation and oxygen activation. [264]

1.5 Motivation and scope of research

As reported in chapter 1.1.1., due to impending oil shortage in the near future, it is vital to find an economical and environmental-friendly route to produce alternative building blocks for chemical industry, such as propene and acrylic acid. Many attempts have been done in the past decades in order to implement an efficient and suitable catalyst for alkane oxidation. However, no real breakthrough has been achieved in the catalytic community from the discovery of MoVTeNb M1 phase-pure catalyst patented by Mitsubishi Corp. in the early 1990s. The lack of homogeneity of data presented in the literature, regarding the many proposed catalytic systems, addresses the new oxidation catalysis research back to fundamental roots, since only a deep understanding and a systematic study of the intrinsic nature of the catalyst may constitute the key for the future. To this latter extent, the implementation of a catalyst requires the study of relative simple and flexible system, such as perovskites. Designing a new catalyst is a challenging task, particularly when it is addressed to the selective oxidation of alkanes. This is because of the numerous consecutive/parallel reaction steps which compose the complex reaction network. [25, 265] Anyway, some design parameters, such as: (a) phase purity of the bulk which confer structural stability, (b)

multifunctionality in order to satisfy the required various reaction steps, (c) semiconducting properties of the bulk beneficial to the transfer of a high number of electrons and (d) balanced oxygen activation to avoid the total combustion to carbon dioxide are considered to be important. [20, 266] Looking into this direction, perovskite-like oxide phase-pure catalyst seems to be the most suitable candidate as "starting" catalyst to be improved because it fulfills the most of criteria cited above. These bulk oxide catalysts present a high level of flexibility without destroying their structure, due to the tolerance factor [50] and their crystal structure can present lattice distortion, due to the tilting of the octahedra, which depends on the temperature and affects bulk and surface electronic properties by influencing the charge-carrier dynamics of the bulk. Indeed, perovskites act as a chemiresistor where it becomes possible to modulate the electronic structure of the surface by tuning the conductivity of the bulk. [267-272] They can be either n-type or p-type semiconductors, behaving mostly as p-type semiconductors under oxidative feed. [270, 271] Furthermore, the defect chemistry of perovskites, beside of providing a high number of oxygen vacancies, which is beneficial to control the oxygen activation during reaction process, [273] can equilibrate with changes in the electric conductivity under various temperatures and oxygen activities. A competition between the electronic or ionic compensation can be established when structural defects are present, for instance, it is reported that if the valences of the ions are lowered, the substitution is compensated by the formation of oxygen vacancies and no contribution to the electronic conductivity occurs for $LaCrO_3$ and $LaMnO_3$. [270] Furthermore, also valence and vacancy control are considered to be extremely important strategies, particularly when the designed perovskites are addressed to oxidation catalysis, due to the fact that the reduction of a metal oxide produces the release of lattice oxygen. Withal, because of the tolerance factor, lattice defects are usually generated and can affect the catalytic performance. For instance, it was found that the enhancement of the catalytic activity in CO oxidation could be attributed to the ease of oxygen removal from hole-doped perovskites. [274] Additionally, a lack of knowledge concerning the electronic structure of perovskites under near-working-condition is unfortunately present in the literature. Surface operando characterization techniques have the potential to encode the active sites present on the surface and the interconnection between the surface's electronic structure with that of the bulk. In this regard, a study of the surface electronic structure of $(La,Sm)MnO_3$ perovskites under reaction condition in propane oxidation has been reported by Koch et al, where new descriptors with respect to the "classical" ones deriving from ex-situ characterization, can be associated to the selectivity to propene in wet feed, such as the Mn^{2+} surface species and OH-absorbed oxygen species. [275] Nevertheless, the so-called "pressure-gap" may constitutes an obstacle in the correct examination under actual reaction conditions [13] and therefore the most simplified model systems with well defined surfaces and variable chemical composition is required for an integrated experimental-computational research. Indeed, high-throughput DFT calculations, [276-278] machine learning (ML) [279, 280] and artificial intelligence [281, 282] have already been widely used for accelerating materials

and catalyst discovery. Machine learning helps to generate new knowledge and to understand catalysis better. [283] Machine learning is used for example

- to develop atomistic potentials that are learned from DFT calculations to be able to probe reaction trajectories under realistic reaction conditions,
- to identify the most likely reaction pathway to a desired product in complex reaction networks, [44]
- for spectra interpretation and image analysis.

These mathematical tools are already employed for accelerating the discovery of possible new perovskite-like structures [1-5] and for searching for key-descriptors for the catalytic performance. [143, 146] The main idea of this project is to synthesize many perovskites, perovskite-like structures and other structures composed by Mn as B-site cation combined with an other metal belonging to the 3d or 4d row of the periodic table (the synergistic effect is claimed to be beneficial to the catalytic performance) and explore their potential in oxidation catalysis, in the oxidation of propane and in CO oxidation. The selected element at the B-site have similar ionic radius between each other (ionic radii in six coordination: Co^{2+} = 0.65 Å, Zn^{2+}= 0.74 Å, Ni^{2+}=0.69 Å, Fe^{2+}=0.61 Å, Cr^{2+}=0.73 Å, Pd^{2+}=0.86 Å, Cu^{2+}= 0.73 Å and $Mn^{3+/4+}$=0.53-0.64 Å,). The most utilized metals as B-site have been Cu and Mn, where Cu is reported to be a promoter in oxidation reaction [10, 284-286] and finally Mn is a well-known element in oxidation catalysis [287] and it was also found to be selective in alkane oxidation. [288, 289] The A-site cation has been changed between La^{3+}, Pr^{3+}, Nd^{3+} and Sm^{3+} to tune the structural and electronic properties. Therefore, twenty-one purely phase-pure perovskites, among which fourteen present the general formula $(La,Pr)Mn_{(1-x)}Cu_xO_3$ (with x=0-0.4), have been synthesized, characterized and tested in CO and propane oxidation. Additionally, the two series have been subjected to operando characterization such as NAP-XPS measurements and operando MCPT. Other 6 perovskite presenting the general formula $AMn_{0.7}B'_{0.3}O_3$ (with A=Pr, Nd and Sm and B'=Co, Zn, Ni, Fe, Cr, Ru) together with $PrMn_{0.95}Pd_{0.05}O_3$ and $(La,Pr)_2CuO_4$ perovskite-related structures have been synthesized, tested in CO and propane oxidation and subjected to standard structural characterizations in order to obtain numerical values of some properties (also known as basic descriptors), for instance: crystallographic parameters, M-O distances and surface composition. Finally, thanks to a collaboration with the Theory department of the FHI der Max-Plank-Gesellschaft, the structural descriptors deriving from catalysts´ characterization will be examined and combined with reactivity data employing mathematical tools and methods to identify new key descriptors and correlations among them (on the basis of the (dis)similarities between data they are grouped in families) in order to rationalize the catalytic activity and selectivity and to predict new possible perovskite-type structures. In the current project, artificial intelligence will be used in terms of developing models for predicting properties

of catalysts or for elucidating, which properties of perovskites might be important for activity and selectivity in oxidation catalysis. This requires the input of knowledge that has been acquired in the field of oxidation catalysis to identify descriptors that are linked to the catalytic properties.

2. Experimental Section

Catalyst Preparation. [290] *Materials.* For the synthesis of the catalysts $La(NO_3)_3 \cdot 6H_2O$ (Alpha Aesar, purity 99.9%, LOT: 61800314) , $Pr(NO_3)_3 \cdot 6H_2O$ (Alpha Aesar, purity 99.9%, LOT: 61300461), $Nd(NO_3)_3 \cdot 6H_2O$ (Sigma Aldrich, purity 99.9%), $Sm(NO_3)_3 \cdot 6H_2O$ (Across Organic, purity 99.9%, LOT: AO413123) $Mn(NO_3)_2 \cdot 4H_2O$ (Roth, purity ≥98%) $Cu(NO_3)_2 \cdot 6H_2O$ (Acros Organics, purity 99%, LOT: AO374996), $Fe(NO_3)_3 \cdot 9H_2O$ (Sigma Aldrich, purity 98%), $Cr(NO_3)_3 \cdot 9H_2O$ (Alpha Aesar, purity 98,5%), $Ni(NO_3)_2 \cdot 6H_2O$, $Co(NO_3)_2 \cdot 6H_2O$ (Merck), $Zn(NO_3)_2 \cdot 6H_2O$, $Pd(NO_3)_2$ solution in diluited HNO_3, ruthenium nitrosyl nitrate sol in diluited nitric acid (Sigma Aldrich, Ru 1,5 wt%), glycine (TCI, purity ≥99%) and deionized water, which was obtained from a laboratory purification system, were employed.

Synthesis. [290] The perovskite catalysts were synthesized via self-combustion route, [291] where the glycine served both as fuel and as complexing agent. Stoichiometric amounts to obtain 10 g of final products of the metal nitrates were dissolved in distillated water together with glycine, being the ratio between the glycine and metal nitrates was fixed to 2.66, in order to reach the equal oxygen balance. The clear solution was stirred for 30 min, quantitively transferred into an evaporation basin and the solvent was evaporated on a hot plate at 95 °C. The obtained foam-like resin was self-ignited on the hot plate set at 460°C. The produced black powders (yields from 37% until 84%) were collected and calcined in a flow consisting of 20% O_2 and 80% of Ar at 800°C, with a heating ramp of $3°C min^{-1}$, for 6 hours (the amount of sample lost during the calcination process varies from 3% until 35%). $PrMn_{0.65}Cu_{0.35}O_3$ and $(La,Pr)Mn_{0.6}Cu_{0.4}O_3$ were washed with acetic acid sol (5% w/w) after the calcination in order to remove traces of $(La,Pr)_2CuO_4$ by-phases and, finally, they have been subjected to a second calcination process.

Catalysts Characterization. *X-Ray Diffraction* (*XRD).* The phase identification of the samples was performed using X-ray diffraction (XRD) measurements on a Bruker AXS D8 Advance II θ/θ diffractometer using Ni-filtered Cu Kα radiation and a position sensitive energy dispersive LynxEye silicon strip detector. The employed geometry was Bragg−Brentano. The sample powder was filled into the recess of a cup-shaped sample holder, the surface of the powder bed being flush with the sample holder edge (front loading). The powder XRD data were analyzed and the lattice parameters calculated using a full pattern fitting, according to the Rietveld method as implemented in the TOPAS software (TOPAS version 5, copyright 1999−2014 Bruker AXS).

Chemical analysis. The metal content of the perovskites was determined by Inductively Coupled Plasma Emission Spectroscopy (ICP-OES) analysis employing an ICP-OES Optima 8300 spectrometer (Perkin Elmer) equipped with a Zyklon nebulizer. The samples were dissolved employing distillated water with conductivity 0.05 μS/cm from ELGA pure water system (VEOLIA) and acids in supra-pure quality into PTFE liners in a Multiwave Pr autoclave (Anton Paar), which operates maximum at 200°C and 6MPa. Certified standard solutions, single and multi-element standards have been employed as calibration standards, being each calibration based on minimum of two points and forced through zero. The measurements have been recorder in axial mode, using water as spectral blank and a sample solution without sample as reagent blank. Spectral evaluation is based on three point per peak. Every measurement was repeated at least three times for each sample in order to calculate the RSD of metal values. The oxygen content determination was repeated three times per sample using a TCH600 setup from LECO by applying the inert gas fusion technique and employing 10 mg of each catalyst, which was heated to 3000 °C in a He stream in a graphite crucible. CO and CO_2 formed by reaction of the oxygen in the sample with the crucible were detected by an IR cell. Y_2O_3 was used for the machine calibration, prior to the analysis.

Laboratory X-ray Photoelectron Spectroscopy (XPS). XPS spectra were recorded at room temperature, using non- monochromatized Al Kα (1486.6 eV) or Mg Kα (1253.6 eV) excitation and a hemispherical analyzer (Phoibos 150, SPECS). The binding energy scale was calibrated by the standard Au $4f_{7/2}$ and Cu $2p_{3/2}$ procedure. To calculate the elemental composition, the theoretical cross sections from Yeh and Lindau, [292] the inelastic free path of the electrons from Tanuma, Powell and Penn [293] and the transmission function of the analyser were used. These fits for Cu2p, Mn3s, La3d and Pr3d were based on [294-297]. Gaussian-Lorentzian line shapes with Shirley backgrounds were used for all peaks. To analyze the Cu2p and Pr3d, a Pr3d clean spectra was acquired measuring $PrMnO_3$, while several Cu2p spectra were recorded measuring La-based series with the same filament employed for the Pr-based one. Finally, the spectra for the Pr-based series were fitted by scaling the two individual fits for Pr3d and Cu2p with some allowance for energy position. Mn oxidation states were estimated from the Mn3s splitting. [298] C1s fits were based on standard C-C, C-O, and C=O binding energies. [299] The O1s species have been fitted according to the model reported by Koch et al., modified by fixing O1s carbonates species intensity to those of C-O and C=O species in C1s fitting and by fixing the Guassian/Lorentian ration to 75.[275]

Thermogravimetric Mass Spectrometry analysis (TG-MS). Thermoanalyses were performed on a NEZTSCH TG 209 F1 Libra analyzer and on NETZSCH STA 449C Jupiter thermoanalyzer equipped with an electromagnetic microbalance with top loading and using 10−15 mg of sample placed into an alumina crucible (85 μL) without a lid. Evolution of the gas phase during reaction was monitored with a calibrated quadrupole mass spectrometer (QMS200 Omnista, Balzers)

coupled to STA via a quartz capillary heated to 393K. The experiments were performed with an electron ionization energy of 70 eV and a dwell time per mass of 0.2s and thermal decomposition was measured from room temperature to 1000 °C, with a heating ramp of 5 °K/min in Ar atmosphere (100 mL·min^{-1}) and dwell time of 1 h.

Morphological studies through Scanning Electron Microscopy (SEM) and Energy Dispersive X-ray (EDX) Mapping. SEM images were conducted using a Hitachi S-4800 microscope equipped with a cold filed emission gun. For imaging 1.5 kV acceleration voltage and 4 mm working distance was set to display the image by using both, upper and lower secondary electron detector. Additionally, EDX mapping was done setting the acceleration voltage to 15 kV and working distance to 10 mm. The energy dispersive QUANTAX 800 EDX spectrometer working with the XFlash®6 | 30 detector has been used to map the elemental distribution. Usually, mapping was done for 2 min when sufficient counts were gained (>10 kps). Recorded spectra were analyzed considering all found peaks and corresponding elemental ratios were calculated for each map/spectrum. Standard deviations were calculated on results of all maps.

Surface Area Determination. N_2 adsorption was performed at −196 °C using the Autosorb-6B analyzer (Quantachrome) after outgassing the catalysts under vacuum for 2 h at 150 °C. All data treatments were performed using the Quantachrome Autosorb software package. The specific surface area was calculated according to the multipoint Brunauer−Emmett− Teller method (BET) in the range $0.05 < p/p_0 < 0.15$ assuming a N_2 cross sectional area of 16.2 Å^2.

Temperature-Programmed Oxidation (TPO) and Temperature-Programmed Reduction (TPR). TPO/TPR cycles was performed in a fixed-bed quartz reactor using 180 mg of the catalyst. The catalysts were first subjected to in-situ calcination at 800°C in synthetic air (20/80=O_2/He), followed by a pre-treatment in He and by cycles of TPO and TPR performed at 300°C for 2 h applying a heating rate of 5 °C min^{-1} with a concentration of 0.25% O_2 and 5%H_2, respectively (flow rate 50 mL min^{-1}). O_2 consumption was monitored with a paramagnetic detector, while H_2 consumption with a thermal conductivity one. The averaged oxygen capacity has been calculated starting from the average of the oxygen atoms which have been transferred during TPO and TPR cycles with the following formula:

$$\Delta x = (n\ of\ O\ atoms\ transferred\ during\ the\ cycle\ (\mu mol))/(n\ of\ ABO_3\ (\mu mol))$$

Being the number of O atoms transferred during the cycle equal to the integrated area of the signal multiplied by a factor of 2 for TPO cycles and by a factor of 1 for TPR cycle, given the reaction

$$H_2 + \frac{1}{2}O_2 \longrightarrow H_2O.$$

Near-Ambient-Pressure X-Ray Photoelectron Spectroscopy (NAP-XPS). Near-Ambient-Pressure X-Ray Photoelectron Spectroscopy measurements have been performed at BELChem facility at the synchrotron radiation source BESSY II in Berlin, Germany. Pressed pellets of 15 mg were measured under vacuum at room temperature at then heated in $C_3H_8/O_2/N_2/H_2O$=0/20/80/0 mixture to 300°C (heating rate 5°C·min^{-1}). At 300°C the reaction feed was switched to $C_3H_8/O_2/N_2/H_2O$=5/10/85/0 and finally to wet feed $C_3H_8/O_2/N_2/H_2O$=5/10/45/40. The total gas pressure under all reaction conditions was 2500 Pa. The gas-phase products were monitored by a Thermoscientific 13000 gas chromatograph. The measurements were carried out at photoelectron kinetic energy of 143-157 eV for all core levels with a corrected electron inelastic mean free path (IMFP) of λ = 1 nm (λ were estimated using the predictive TPP-2M formula by Tanuma, Powell and Penn [293]) by setting the photon energies to 790 eV (Mn 2p), 680 eV (O 1s), 455 eV (C 1s), 1100 eV (Pr 3d) and 1110eV (Cu2p). The atomic subshell photoionization cross sections and asymmetry parameters from numerical calculations by Yeh and Lindau [292] were used for the quantitative analysis of the core level intensities, taking the monochromatic photon energy dependent photon flux into account. Gaussian-Lorentzian line shapes with Shirley backgrounds were used for all peaks. The same fitting procedure described in the XPS chapter has been applied to resolve the overlap of Pr3d and Cu2p peaks. The contribution of carbonates has been explicitly included in the O 1s fit based on the C1s carbonates XPS intensity. The sensitivity factor, calculated from theoretical cross sections, has been applied to calculate the O 1s carbonate from the C 1s intensity. An upper/lower intensity margin has been considered to take into account uncertainties of the C 1s intensity assigned to carbonate species.

Microwave Cavity Perturbation Technique (MCPT). [290] MCPT measurements were performed using as a resonator a cylindrical using transverse magnetic TM_{010} mode at 5 GHz with a height of 20 mm and a diameter of 68 mm. In order to obtain the quality factor from vacuum experiments (Q), which varied between 0,847 and 1,279, the sample was placed in the electric field antinode at the resonator's center. While the employed sample's mass varied between 12,5 and 42,8 mg. The perturbation was related to the relative complex permittivity $\tilde{\varepsilon} = \varepsilon' - i\varepsilon''$ and the electrical conductivity σ was determined from the imaginary part of the permittivity ε″ and the angular resonant frequency ω according to $\sigma = \varepsilon\omega\varepsilon''$, where ε_0 denotes the vacuum permittivity. The measurements were performed in propane oxidation by pre-treating the catalyst at 300°C in lean air (O_2/N_2=10/90) at 300°C (5 K/min) for 3 hours (where the reference conductivity σr has been measured) , afterwards the sample was cooled down to 260°C, temperature at which the feed was switch to propane feed $C_3H_8/O_2/N_2$=5/10/85 , then the catalyst was heated up until 300°C (steady-state condition each 10°C) in order to study the temperature dependence of the conductivity. At

300°C in propane feed three contact time has been varied and finally the feed was switch to lean air again in order to detect the change in conductivity. The simultaneous analysis of reaction product was monitored by online gas chromatography (Agilent 7890).

Catalytic studies. CO oxidation. The catalytic tests were performed into a self-made setup employing a quartz plug-flow U-tube reactor, which was loaded with 30 mg (sieved particles, 250-350 μm) of catalyst diluted with inert SiC of the same sieved fraction of the catalyst (catalyst/SiC ratio: 1/9) employing a flow rate of 50 mL·min^{-1}. The reactant and product concentrations were detected with an online gas analyzer (X-STREAM XE, Emerson/Rosemount) which was equipped with an infrared and a paramagnetic sensor, for the simultaneous quantification of carbon monoxide, carbon dioxide, water and oxygen, respectively. CO gas was purified using a carbonyl remover consisting of a tube filled with inert silicon carbide heated up to 300 °C. All catalysts have been dwelled in inert atmosphere a T= 150°C prior to the cycling experiments. The CO consumption rates in mmol h^{-1} g^{-1} have been determined by derivating the linear function :

$$X_{CO} = f\left(\frac{W}{F}\right): \; r_{CO\ consumption} = \frac{dXco}{d\left(\frac{W}{F}\right)}$$

Where W is the weight of the catalyst (g) and F is the flow rate of the reactants (mL·h^{-1}).

Propane oxidation. The catalytic tests were carried out using a setup for partial oxidation (Integrated Lab Solutions) with 10 fixed-bed tubular reactors (2 mm inner diameter) in parallel employing 100 mg (sieved particles, 100-200 μm) of catalyst with a flow rate varying from 5 to 30 mL·min^{-1}. An online gas chromatographer was used for gas analysis (Agilent 7890A). The permanent gases CO, CO_2, O_2 and N_2 have been analyzed by a combination of Plot Q (length 30 m, 0.53 mm internal diameter, 40 μm film thickness) and Plot-MoleSieve 5A columns (30 m length, 0.53 mm internal diameter, 50 μm film thickness) connected to a TCD detector. While, propane and propene have been analyzed by a combination of FFAP (length 30 m, 0.53 mm internal diameter, 1 μm film thickness) and a Plot-Q column (length 30 m, 0.53 mm internal diameter, 40 μm film thickness) connected to a FID detector. Additionally, a methanizer has been installed in order to detect CO and CO_2 amount also at the FID detector, with higher precision and accuracy with respect to the concentrations revealed by the TCD detector. The conversion of propane ($X_{C3H8)}$ and the selectivity to products *i* (*Si)* in percentages was determined with the following equation based on the total amount of carbon atoms in the product and the sum of all products

formed:

$$X_{C3H8} = \frac{\sum_{i=1}^{n} Nici}{\sum_{i=1}^{n} Nici + 3cC3H8\ out} \text{ x } 100$$

$$S_i = \frac{Nici}{\sum_{i=1}^{n} Nici.} \text{ x } 100$$

Where N_i is the number of carbon atoms in the products, c_i is the concentration of the products in the gas exiting from the reactor.

The rates of C_3H_8 consumption, C_3H_6 and CO_2 formation have been calculated using the following equation:

$$X_{C3H8,C3H6,CO2} = f\left(\frac{W}{F}\right): \ r_{C3H8\ consumption/\ C3H6\ or\ CO2\ formation} = \frac{dX\ or\ S}{d\left(\frac{W}{F}\right)}$$

The initial rates of C_3H_8 consumption and C_3H_6 or CO_2 formation have been calculated by extrapolating the rates to the contact time (W/F)=0 and allows us to compare all catalysts among each other at the same temperature, decoupled from the contact time.

3. Catalysts' synthesis and characterization

3.1 Self-Ignition Synthesis

All the catalysts have been synthesized starting from metal nitrates and water employing glycine both as fuel and as chelating agent. Following the work published by Chyi-Ching et al.[300] where the stoichiometric amount of glycine (ψ) was calculated in order to reach the equal oxygen balance as shown in the following general equation for the $AB_{(1-x)}B'_xO_3$ structure (Equation 3.1):

$$A(NO_3)_y \cdot aH_2O + (1-x)B(NO_3)_z \cdot bH_2O + xB'(NO_3)_w \cdot cH_2O\ \psi NH_2CH_2COOH$$

$$\rightarrow AB_{(1-x)}B'_xC_{2\psi}H_{5\psi}N_{[y+(1-x)z+xw]+\psi}O_{[3y+3(1-x)z+3xw]+2\psi}$$

$$\rightarrow AB_{(1-x)}B'_xO_3 + \{[y+\ (1-x)z+\ xw]/2+\ (\psi/2)\} \cdot N_2 + 2\psi \cdot CO_2 + 2.5\psi \cdot H_2O + [3y\ +3(1-x)z\ +3xw - 3+\ 2\psi - 2.5\psi - 4\psi]/2O_2$$

$$\rightarrow AB_{(1-x)}B'_xO_3 + \{[y+\ (1-x)z+\ xw]/2+\ (\psi/2)\} \cdot N_2 + 2\psi \cdot CO_2 + 2.5\psi \cdot H_2O + [3y+3(1-x)z+3xw - 3 - 4.5\psi]/2O_2$$

$\rightarrow 0 = [3y+3(1-x)z+3xw] - 3 - 4.5\psi$

$\rightarrow \psi = [3y+3(1-x)z+3xw - 3]/4.5$ (Eq. 3.1)

Being x the amount of B' dopant, y, z and w the stoichiometric coefficient of the of the NO_3^- group in the corresponding nitrates precursors.

In the self-ignition method, the heating and the evaporation of the solution containing metal nitrates and glycine can result in a very exothermic process which leads to self-firing of the starting materials. The ignition of the resin intermediate at relatively low temperature leads to the removal of the organic material and to the formation of metal oxides, resulting in a fine powder and thus representing an efficient synthesis method for catalytic application. Indeed, the synthesis of materials addressed to catalysis aims to produce samples with increased surface areas and/or decreased particle size, since catalysis belongs to a class of surface reaction. Moreover, together with the advantage of the fine particles size, this bottom-up synthesis technique presents several advantages, such as the quick, efficient and straightforward preparation process and relative low cost of the employed precursors. [291, 300] These are the main reasons of why it is a preferred synthesis route for perovskites with respect to the sol-gel/citrate route or the classical solid-state one, where the specific surface area of the resulting material is rather low, due to the high required temperatures and although this latter route can be considered environmentally friendly, since the perovskite is synthesized directly from the starting oxides without the release of toxic gases, it is always necessary to homogenize the metal oxide precursors in order to make them react with each other through ion-diffusion and, for this latter reason, it becomes rather challenging to produce the perovskite in large batches with solid-state synthesis technique. While, the main drawback of self-ignition synthesis method is the lack of control over the synthesis parameters, such as the reaction temperature, which might be different for each synthesized material, since it depends on type of nitrate which are employed and on their amount, making also the scaling up and down of the perovskite batch not always reproducible.

Many perovskite-type oxides have been reported to be synthesized with the self-ignition method due to the advantages cited above for catalytic purpose [301-306] and given the frequently discussed importance of the B-site element [200] and particularly of the beneficial effect of the synergy established with a double B-site on the catalytic performance, [166, 199, 201] which could be advantageous also because the introduction of a second metal in the B-site introduces structural distortion which in turn leads to the creation of defects and vacancies, [307] the presented PhD project has started from the self-combustion synthesis of the $(La,Pr)Mn_{(1-x)}Cu_xO_3$ series (with $0 \leq x \geq 0.4$), taking inspiration from some catalysis studies over the $LaMn_{(1-x)}Cu_xO_3$ series, where the samples have been synthesized either by Pechini method, [308] or citrate method or freeze-drying sol starting

from metal acetates, [73, 201, 309-312] with the addition of the systematic substitution of the A-site to study also its influence over the bulk and electronic structure of the catalysts and to enable a comparison between La- and Pr-based series. Prior to the synthesis of the described batches for $(La,Pr)Mn_{(1-x)}Cu_xO_3$ series, a preliminary screening over the most suitable calcination T (1000, 800 and 500 °C) has been performed over the stoichiometry with x=0.1, 0.2 and 0.3 , starting from the same batch of sample. Based on this preliminary screening, in which phase-purity and surface areas have been evaluated (Table 3.1 and 3.2) in order to decide the optimal calcination temperature for the reproduction of larger batches of $(La,Pr)Mn_{(1-x)}Cu_xO_3$. 800° has been selected as calcination temperature for all the samples presented in the Thesis, since it was the best compromise between the achievement of the phase-purity of the materials and a feasible surface area in order to employ the samples in catalysis (Table 3.1 and 3.2).

Table 3.1. Table with listed: the crystallographic phase from Rietveld Refinement. Being R-3cH: rhombohedral symmetry and Pbnm : orthorhombic symmetry. Color-code: orange: La-based samples; green: Pr-based samples.

T calcination	*1000°C*		*800°C*		*500°C*	
X_{Cu}	*La*	*Pr*	*La*	*Pr*	*La*	*Pr*
0.1	*R-3cH*	*Pbnm*	*R-3cH*	*Pbnm*	*R-3cH*	*Pbnm*
0.2	*Pbnm*	*Pbnm*	*R3cH/Pbnm*	*Pbnm*	*R-3cH*	*Pbnm*
0.3	*Pbnm*	*Pbnm*	*Pbnm*	*Pbnm*	*Pbnm* + La_2O_3 + *CuO*	*Pbnm* + Pr_2O_3 + PrO_2 + *CuO*

Table 3.2. Table with listed: the BET areas. Color-code: orange: La-based samples; green: Pr-based samples.

T calcination	*1000°C*		*800°C*		*500°C*	
X_{Cu}	*La*	*Pr*	*La*	*Pr*	*La*	*Pr*
0.1	*3.0*	*2.6*	*6.3*	*6.6*	*15.1*	*11.8*
0.2	*3.7*	*1.7*	*6.0*	*7.2*	*16.5*	*12.7*
0.3	*2.8*	*3.4*	*7.0*	*3.2*	*10.6*	*n.a.*

By comparing the data derived from Rietveld refinement of this preliminary screening of samples, it becomes evident how the calcination temperature, the A-site and Cu loading amount affect the formation of the thermodynamically stable crystallographic phase. The first deduced information is that the lower the Cu loading amount, the higher the crystallographic symmetry (Table 3.1). Secondly, $LaMn_{0.9}Cu_{0.1}O_3$ presents rhombohedral symmetry at all the three different calcination temperatures, while $PrMn_{0.9}Cu_{0.1}O_3$ is the orthorhombic, due to the fact that Pr has a smaller size of La and therefore the crystallographic strain is enhanced in Pr-series, leading to lower symmetry.[313]

Although La-based materials present higher symmetry with respect to the corresponding Pr-based ones at low Cu content, when the Cu loading is increased within the series, the scenario changes. Indeed, $LaMn_{0.8}Cu_{0.2}O_3$ clearly shows the thermodynamic metastable character of the perovskite-like materials, being orthorhombic at the highest calcination T (1000°C), a phase-mixture of orthorhombic and rhombohedral at the medium calcination T (800°C) and rhombohedral at the lowest calcination T (500°C) as shown in Figure 1. In this latter specific case, it is evident that also the temperature and not only the amount of Cu or the A-site size has an influence on the crystallographic strain. [306] Indeed, the increasing of the temperature leads to the stabilization of structure with lower symmetry, such as orthorhombic, probably because thermal treatment at this calcination temperature (1000°C) provides sufficient energy to the migration of Mn and Cu cations into the orthorhombic structure to create crystalline well defined perovskite phase.

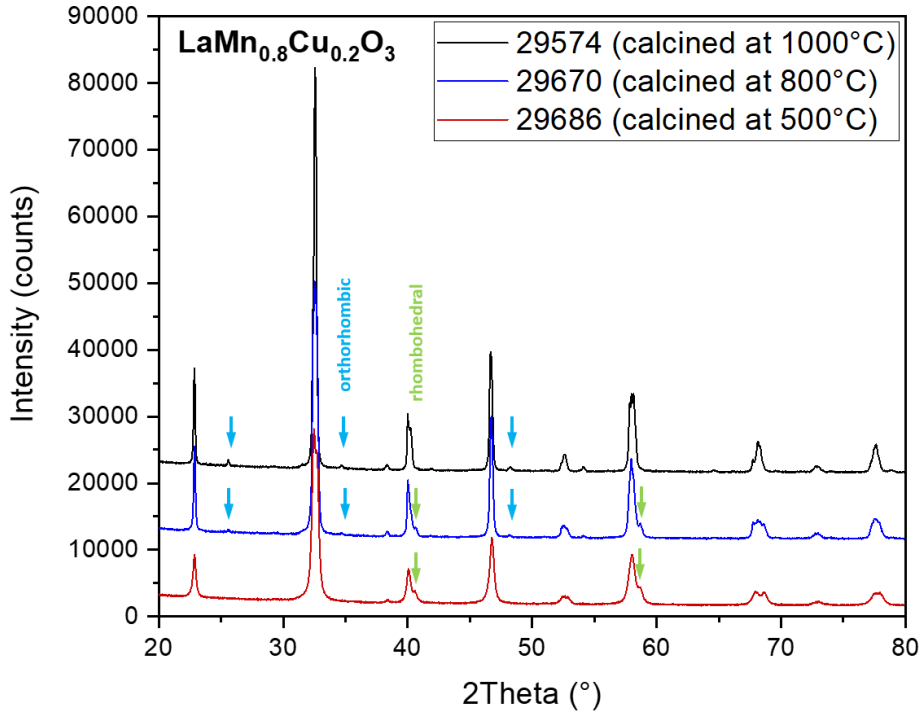

Figure 3.1. *Graph showing the XRD diffractogram for $LaMn_{0.8}Cu_{0.2}O_3$ calcined at 1000°C (#29574), at 800°C (#29670) and at 500°C (#29686). Color code: black: #29574; blue: #29670; red: #29686; light blue: orthorhombic features and green: rhombohedral features.*

Finally, the samples $(La,Pr)Mn_{0.7}Cu_{0.3}O_3$ are orthorhombic even at the highest calcination temperature (1000°C) and the ones calcined at 500°C are not phase-pure, indicating that 500°C for 8 h is not a sufficient temperature to form phase-pure perovskite compounds when the Cu loading is increased. Interestingly, the calcination temperature has basically no impact on the values the <B-O> sigma and <A-O> sigma, which are always higher for Pr-based sample with respect to the corresponding La-based ones (since Pr-based series present a higher degree of orthorhombic distortion), meaning that the thermal treatment is able to have an impact on the phase-transition and

phase stabilization, but not directly on the distortion parameters, which are dominated mostly by conformational structural phenomena (such es. A-size cation and amount of B´ loading) (Table 3.3).

Table 3.3. Table with listed: the crystallographic data from Rietveld Refinement for 0.1≤x≤0.3 stoichiometry at 1000 and 800°C. Being R-3cH: rhombohedral symmetry and Pbnm : orthorhombic symmetry, a,b,c: lattice constants; V: normalized volume of the unit cell; <B-O> and <A-O>: mean of the interatomic distances and<B-O> sigma and <A-O sigma the standard deviations of interatomic distances. Color-code: orange: La-based samples; green: Pr-based samples.

x_{Cu}	*A-site*	Calcination T(°C)	Lattice symmetry	*a* (Å)	*b* (Å)	*c* (Å)	*V/Z* (Å^3)	<B-O> (Å)	<B-O>sigma (Å)	<A-O> (Å)	<A-O>sigma (Å)
0.1	La	1000	R-3cH	5.525	5.525	13.325	58.719	1.965	0.000	2.756	0.204
		800	R-3cH	5.520	5.520	13.329	58.615	1.963	0.000	2.754	0.200
	Pr	1000	Pbnm	5.461	5.543	7.699	58.262	1.987	0.044	2.767	0.343
		800	Pbnm	5.460	5.538	7.703	58.240	1.986	0.061	2.766	0.340
0.2	La	1000	Pbnm	5.531	5.486	7.775	58.976	1.975	0.006	2.764	0.247
		800	R-3cH	5.528	5.528	13.321	58.761	1.968	0.000	2.758	0.218
			Pbnm	5.530	5.484	7.774	58.938	1.974	0.051	2.764	0.241
	Pr	1000	Pbnm	5.463	5.576	7.681	58.507	1.994	0.040	2.774	0.363
		800	Pbnm	5.463	5.547	7.697	58.317	1.989	0.049	2.796	0.349
0.3	La	1000	Pbnm	5.530	5.495	7.786	59.144	1.982	0.006	2.769	0.267
		800	Pbnm	5.526	5.485	7.777	58.928	1.976	0.019	2.764	0.252
	Pr	1000	Pbnm	5.468	5.549	7.697	58.384	1.993	0.038	2.771	0.258
		800	Pbnm	5.465	5.540	7.694	58.230	1.989	0.040	2.768	0.350

In summary, a preliminary screening of the calcination temperatures has been performed among 1000°C, 800°C and 500°C in order to select the optimal one as a compromise between surface area and crystallinity. From the preliminary screening it emerges that the lower the Cu content, the higher the symmetry. Additionally, also the A cation size plays a role on the symmetry. Indeed, all Pr-based samples, even those with low Cu content (0≤x≤0.1), present the orthorhombic symmetry, while the La-based samples with x=0-0.1 show the rhombohedral one. This phenomenon is probably ascribable to the smaller size of Pr cation with respect to the La one and thus on the consequent enhanced crystallographic strain, which leads to octahedral distorsion. [313] Moreover, also the calcination temperature influences the crystallographic strain, [306] as, the higher the calcination temperature, the lower the symmetry. Indeed, $LaMn_{0.8}Cu_{0.2}O_3$ compound represents the thermodynamic metastable character of the perovskite-like materials (Figure 1), highlighting that the thermal treatment at high temperature provides sufficient energy for the migration of Mn and Cu cations into the orthorhombic structure to create crystalline well defined perovskite phase. The best compromise between phase-purity and surface area is achieved by calcining the perovskites at

800°C. Moreover, the two corresponding Ruddlesden-Popper phase structures $(La,Pr)_2CuO_4$ have been added to the last cited series to explore materials with similar composition, but very different structures in catalysis. Finally, the project has been completed with the synthesis of $(Pr,Nd,Sm)Mn_{0.7}B'_{0.3}O_3$ series with B´=Ni, Zn, Co, Fe, Cr, Pd and Ru, in order to focus on double B-site perovskites and study the variation of different B´elements belonging to 3 and 4 d configuration into the catalyst´s nanostructures and their influences on the catalytic performance.

3.2 Analysis of the structural and electronic properties of the $(La,Pr)Mn_{(1-x)}Cu_xO_3$ series

3.2.1 Crystal symmetry

Fourteen catalysts of the $(La,Pr)Mn_{(1-x)}Cu_xO_3$ series has been synthesized by self-ignition route and calcined at 800°C, being this latter temperature the best compromise between crystallinity and surface area. As evidenced by Rietveld refinement of powder X-ray diffractograms (Figure SI 1), all the synthesis products are phase-pure perovskite-like samples, which present either rhombohedral or orthorhombic symmetry, being the orthorhombic phase the dominant one among the synthesized perovskites (Table 3.4 and 3.5). Generally, the XRD pattern of the $LaMn_{(1-x)}Cu_xO_3$ series reported in the literature [166, 309] present rhombohedral symmetry for $0 \leq x \leq 0.2$ stoichiometry, as it is the case for the presented samples and the samples with stoichiometry with $0.3 \leq x \leq 0.5$ show cubic symmetry, while those synthesized in the specific project starting from $x \geq 0.25$ are orthorhombic (Table 3.4 and 3.5). The replacement of a certain percentage of Cu atoms instead of Mn atoms into the octahedral sites should increase the crystallographic strain, leading to lower crystallographic symmetry. [307] In this regard, it becomes more intuitive to understand a phase-transition from rhombohedral to orthorhombic (i.e. where the crystallographic symmetry is lowered), as it is found in the presented project, instead of a phase-transition from rhombohedral to cubic (i.e. a symmetry enhancement), as reported in some literature. [166, 309] Indeed, some other authors report that the introduction of a second B-site (Cu,Fe) into the octahedron of the $LaMnO_3$, does not change significantly the intensity or peak shape, but it causes a 2Theta shift, which is reflected in a change of the cell unit size. [201] Additionally, the calculated tolerance factor for La-based perovskite with $x>0.2$ is more distant to 1 (which is the t_{obs} value for the ideal cubic perovskite) with respect to the other La-based samples with lower Cu content loading ($x \leq 0.2$), indicating that the crystallographic distortion for these latter samples with Cu loading >0.2 is higher (Figure 3.2).

Finally, due to the lanthanide contraction, the Pr-based perovskites present a higher degree of orthorhombic distortion with respect to the corresponding La-based ones, because the perovskite has to undergo to higher strain in order to maintain the symmetry by having a smaller A-size cation in the large cuboctahedral A-cage. [313] The lowered crystallographic symmetry of Pr-based samples is also reflected in the higher distance of their calculated t_{obs} (observed tolerance factor) from the one of the ideal cubic perovskite (where t=1), since the higher the distance from the ideal value of 1 for t_{obs}, the higher the crystallographic distortion (Figure 3.2). While, La-based perovskites present a t_{obs} which is closer to 1. The crystallographic stain might also be evaluated in <B-O> sigma and <A-O> sigma, being this latter one the standard deviation of the interatomic distance A-O able to reflect the amount of the cuboctahedral distortion, while <B-O> sigma reflects that of the octahedral with Jahn-Teller one within the structure, being in these specific series dominated from the ratio of the two Jahn-Teller ions, such as Mn^{3+} and Cu^{2+} (Table 3.4 and 3.5). Indeed, <A-O> sigma and <B-O> sigma are always higher for Pr-based samples with respect to La-series. Finally, <A-O> sigma increases linearly with <B-O> distances, which in turn linearly depends on Cu loading only for La-based series, indicating that the Jahn-Teller and octahedral distortion is strongly influenced by the Cu amount, while it is not the case for Pr-based series. This is probably because in Pr case, the Cu induced effect is smeared by the already present crystallographic strain due to the smaller size of Pr and therefore, since multiple strain inducing parameters are present simultaneously in the Pr-based series, it becomes difficult to evidence a clear correlation with Cu loading content and the consequent increase in cuboctahedra distortion.

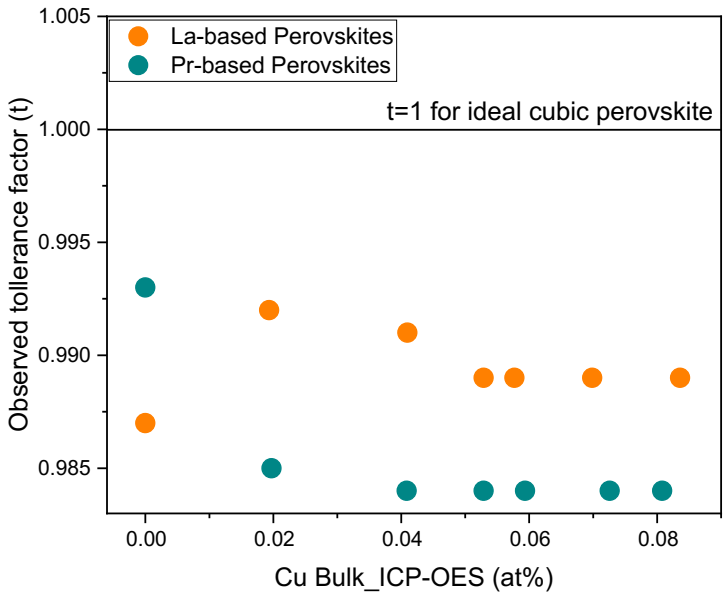

Figure 3.2. *Graph showing the observed tolerance factor as calculated from the distances determined by Rietveld Refinement over the Cu content determined by ICP-OES analysis. Orange: La-based samples and green:Pr-based samples.*

Table 3.4. Crystallographic data from Rietveld Refinement for the $LaMn_{(1-x)}Cu_xO_3$ series. Being R-3cH: rhombohedral symmetry and Pbnm : orthorhombic symmetry, a,b,c: lattice constants; V/Z:normalized volume of the unit cell; <B-O> and <A-O>:mean of the interatomic distances and <B-O> sigma and <A-O> sigma the standard deviations of interatomic distances.

x_{Cu}	Lattice symmetry	*a* (Å)	*b* (Å)	*c* (Å)	*V/Z* (Å^3)	<B-O> (Å)	<B-O>sigma (Å)	<A-O> (Å)	<A-O>sigma (Å)
0	*R-3cH*	5.507	5.507	13.340	58.395	1.957	0.000	2.750	0.184
0.1	*R-3cH*	5.520	5.520	13.326	58.613	1.964	0.003	2.755	0.204
0.2	*R-3cH*	5.526	5.526	13.326	58.741	1.969	0.011	2.759	0.224
	Pbnm	5.526	5.485	7.770					
0.25	*Pbnm*	5.529	5.486	7.777	58.972	1.976	0.039	2.765	0.249
0.3	*Pbnm*	5.526	5.483	7.773	58.890	1.976	0.031	2.764	0.252
0.35	*Pbnm*	5.526	5.487	7.779	58.969	1.978	0.064	2.766	0.256
0.4	*Pbnm*	5.527	5.488	7.779	58.991	1.979	0.057	2.767	0.260

Table 3.5. Crystallographic data from Rietveld Refinement for the PrMn(1-x)CuxO3 series. Being R-3cH: rhombohedral symmetry and Pbnm : orthorhombic symmetry, a,b,c: lattice constants; V/Z:normalized volume of the unit cell; <B-O> and <A-O>:mean of the interatomic distances and <B-O> sigma and <A-O> sigma the standard deviations of interatomic distances.

x_{Cu}	Lattice symmetry	*a* (Å)	*b* (Å)	*c* (Å)	*V/Z* (Å^3)	<B-O> (Å)	<B-O>sigma (Å)	<A-O> (Å)	<A-O>sigma (Å)
0	*Pbnm*	*5.460*	*5.490*	*7.713*	*57.805*	*1.973*	*0.044*	*2.754*	*0.303*
0.1	*Pbnm*	*5.460*	*5.510*	*7.703*	*58.171*	*1.984*	*0.064*	*2.765*	*0.334*
0.2	*Pbnm*	*5.463*	*5.548*	*7.696*	*58.319*	*1.990*	*0.041*	*2.769*	*0.353*
0.25	*Pbnm*	*5.464*	*5.544*	*7.696*	*58.286*	*1.990*	*0.044*	*0.353*	*0.353*
0.3	*Pbnm*	*5.466*	*5.544*	*7.695*	*58.296*	*1.991*	*0.041*	*2.769*	*0.354*
0.35	*Pbnm*	*5.465*	*5.532*	*7.695*	*58.161*	*1.988*	*0.049*	*2.769*	*0.347*
0.4	*Pbnm*	*5.465*	*5.530*	*7.691*	*58.109*	*1.988*	*0.043*	*2.766*	*0.352*

In summary, the Rietveld Refinement analysis has evidenced how the crystallographic strain is affected by the Cu loading and in particular by the A-site. Indeed, a phase-change from rhombohedral to orthorhombic occurs in the La-based series with x=0.2 and Pr-based catalysts present a higher degree of crystallographic distorsion compared to the corresponding ones of the La-based series, due to the fact that the perovskite has to undergo to higher strain in order to maintain the structure by having a smaller A-size cation in the large cuboctahedral A-cage.

3.2.2. Chemical composition, nanostructure and porosity of the catalysts

The bulk and the surface stoichiometry have been determined by ICP-OES (Table 3.6) and XPS (Table 3.7), respectively, confirming that the Mn:Cu ratios were very close to the nominal ones both for the bulk and the surface within the series. However, some differences in the bulk´s elemental distribution are visible within the two series. Indeed, the La-based samples present a higher B/A bulk´s content with respect to the corresponding Pr-based ones (Figure 3.3), which might be due to the fact that the octahedra of Mn and Cu are better stabilized into the bulk by the larger cuboctahedron of La.

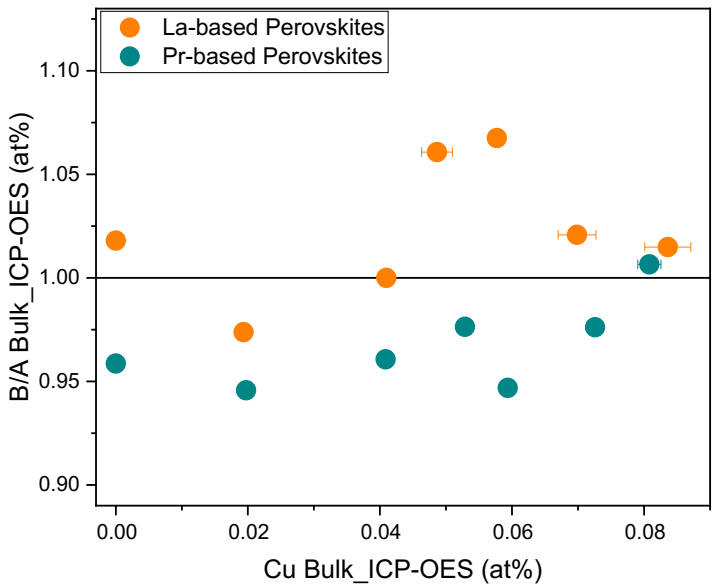

Figure 3.3. *Graph indicating the bulk´s B/A ratio. Orange: La-based samples, green: Pr-based samples.*

This A-site bulk enrichment in Pr-series, is visible also when the stoichiometry are normalized on (A+B)=2 or (B+B´)=1 in Table 3.6 and Table 3.7. Indeed, the stoichiometry have been reported in three different normalizations, such as (A+B)=2, A=1 and (B+B´)=1, in order to highlight and

compare different aspects of the metal composition simultaneously. From the comparison, it emerges that the La-samples do not present A-site enrichment, neither in (A+B)=2 formula or in (B+B´)=1, while for the Pr-based samples it is always the case for each Cu loading. Concerning the B-site, it is evident that the Cu is very close to the nominal value in all the three different stoichiometry normalizations, indicating that the real Cu content in the two series is effectively almost coincident with the nominal loading. While, Mn bulk detected content generally presents a deviation from the nominal one, which becomes evident in (A+B)=2 and A=1 normalized stoichiometry, especially for Pr-based samples. Moreover, the ICP-OES bulk analysis, as the oxygen content determination ones, have been repeated three times for each sample in order to determine the relative standard deviations for the value of each detected element in the measurements, which range from 0.7 to maximum 4.8 %, indicating that no elements present bulk segregation within the series.

Table 3.6. Table with listed: CO2 mass loss determined by TG-MS, the stoichiometry determined by ICP-OES combined with oxygen content determination analysis and the BET surface areas for the $LaMn_{(1-x)}Cu_xO_3$ series. Purple stoichiometry is calculated on the basis of the combined metal chemical analysis (ICP-OES) and oxygen content determination. Oxygen content determined values have been corrected by subtraction of O_2 amount contained into CO_2 molecules. The CO_2 amount has been measured by TG-MS analysis.

x_{Cu}	CO_2 (wt%)	(A+B) = 2[a]	A = 1[b]	(B+B´) = 1[c]	BET surface area ($m^2 \cdot g^{-1}$)
0	1.88	$La_{0.99}Mn_{1.01}O_{3.00}$	$La_{1.00}Mn_{1.02}O_{3.03}$	$La_{0.98}Mn_{1.00}O_{2.98}$	11.7
		$La_{0.99}Mn_{1.01}O_{2.80}$	$La_{1.00}Mn_{1.02}O_{2.82}$	$La_{0.98}Mn_{1.00}O_{2.77}$	
0.1	0.61	$La_{1.01}Mn_{0.89}Cu_{0.1}O_{3.27}$	$La_{1.00}Mn_{0.87}Cu_{0.1}O_{3.23}$	$La_{1.03}Mn_{0.90}Cu_{0.1}O_{3.32}$	6.2
		$La_{1.01}Mn_{0.89}Cu_{0.1}O_{3.17}$	$La_{1.00}Mn_{0.87}Cu_{0.1}O_{3.13}$	$La_{1.03}Mn_{0.90}Cu_{0.1}O_{3.21}$	
0.2	1.04	$La_{1.00}Mn_{0.8}Cu_{0.2}O_{3.01}$	$La_{1.00}Mn_{0.8}Cu_{0.2}O_{3.01}$	$La_{1.00}Mn_{0.8}Cu_{0.2}O_{3.01}$	6.0
		$La_{1.00}Mn_{0.8}Cu_{0.2}O_{2.87}$	$La_{1.00}Mn_{0.8}Cu_{0.2}O_{2.87}$	$La_{1.00}Mn_{0.8}Cu_{0.2}O_{2.87}$	
0.25	0.86	$La_{0.97}Mn_{0.79}Cu_{0.24}O_{3.14}$	$La_{1.00}Mn_{0.81}Cu_{0.25}O_{3.24}$	$La_{0.94}Mn_{0.76}Cu_{0.24}O_{3.05}$	5.5
		$La_{0.97}Mn_{0.79}Cu_{0.24}O_{3.01}$	$La_{1.00}Mn_{0.81}Cu_{0.25}O_{3.10}$	$La_{0.94}Mn_{0.76}Cu_{0.24}O_{2.92}$	
0.3	0.74	$La_{0.97}Mn_{0.75}Cu_{0.28}O_{2.95}$	$La_{1.00}Mn_{0.77}Cu_{0.29}O_{3.05}$	$La_{0.94}Mn_{0.72}Cu_{0.28}O_{2.86}$	4.2
		$La_{0.97}Mn_{0.75}Cu_{0.28}O_{2.84}$	$La_{1.00}Mn_{0.77}Cu_{0.29}O_{2.94}$	$La_{0.94}Mn_{0.72}Cu_{0.28}O_{2.75}$	
0.35	0.85	$La_{0.99}Mn_{0.66}Cu_{0.36}O_{3.12}$	$La_{1.00}Mn_{0.66}Cu_{0.36}O_{3.16}$	$La_{0.98}Mn_{0.65}Cu_{0.35}O_{3.09}$	9.6
		$La_{0.99}Mn_{0.66}Cu_{0.36}O_{3.00}$	$La_{1.00}Mn_{0.66}Cu_{0.36}O_{3.03}$	$La_{0.98}Mn_{0.65}Cu_{0.35}O_{2.97}$	
0.4	0.49	$La_{0.99}Mn_{0.59}Cu_{0.41}O_{2.99}$	$La_{1.00}Mn_{0.60}Cu_{0.42}O_{3.01}$	$La_{0.99}Mn_{0.59}Cu_{0.41}O_{2.97}$	5.9
		$La_{0.99}Mn_{0.59}Cu_{0.41}O_{2.89}$	$La_{1.00}Mn_{0.60}Cu_{0.42}O_{2.91}$	$La_{0.99}Mn_{0.59}Cu_{0.41}O_{2.87}$	

[a] Stoichiometry calculated on the sum of metals equal to two.

[b] Stoichiometry calculated by fixing the amount of A to one.

[c] Stoichiometry calculated by fixing the amount of (B+B´) to one.

Table 3.7. Table with listed: CO2 mass loss determined by TG-MS, the stoichiometry determined by ICP-OES combined with oxygen content determination analysis and the BET surface areas for the $PrMn_{(1-x)}Cu_xO_3$ series. Purple stoichiometry is calculated on the basis of the combined metal chemical analysis (ICP-OES) and oxygen content determination. Oxygen content determined values have been corrected by subtraction of O_2 amount contained into CO_2 molecules. The CO_2 amount has been measured by TG-MS analysis.

x_{Cu}	CO_2 (wt%)	(A+B) = 2[a]	A = 1[b]	(B+B´) = 1[c]	BET surface area ($m^2 \cdot g^{-1}$)
0	1.36	$Pr_{1.03}Mn_{0.97}O_{2.74}$	$Pr_{1.00}Mn_{0.95}O_{2.66}$	$Pr_{1.06}Mn_{1.00}O_{2.82}$	9.4
		$Pr_{1.03}Mn_{0.97}O_{2.58}$	$Pr_{1.00}Mn_{0.95}O_{2.51}$	$Pr_{1.06}Mn_{1.00}O_{2.66}$	
0.1	0.39	$Pr_{1.04}Mn_{0.86}Cu_{0.10}O_{3.15}$	$Pr_{1.00}Mn_{0.83}Cu_{0.1}O_{3.05}$	$Pr_{1.07}Mn_{0.89}Cu_{0.11}O_{3.27}$	5.4
		$Pr_{1.04}Mn_{0.86}Cu_{0.10}O_{3.08}$	$Pr_{1.00}Mn_{0.83}Cu_{0.1}O_{2.98}$	$Pr_{1.07}Mn_{0.89}Cu_{0.11}O_{3.19}$	
0.2	0.45	$Pr_{1.03}Mn_{0.77}Cu_{0.20}O_{3.01}$	$Pr_{1.00}Mn_{0.75}Cu_{0.2}O_{2.93}$	$Pr_{1.06}Mn_{0.79}Cu_{0.21}O_{3.10}$	4.2
		$Pr_{1.03}Mn_{0.77}Cu_{0.20}O_{2.85}$	$Pr_{1.00}Mn_{0.75}Cu_{0.2}O_{2.78}$	$Pr_{1.06}Mn_{0.79}Cu_{0.21}O_{2.93}$	
0.25	0.47	$Pr_{1.02}Mn_{0.73}Cu_{0.25}O_{2.77}$	$Pr_{1.00}Mn_{0.72}Cu_{0.25}O_{2.72}$	$Pr_{1.04}Mn_{0.74}Cu_{0.26}O_{2.82}$	9.0
		$Pr_{1.02}Mn_{0.73}Cu_{0.25}O_{2.48}$	$Pr_{1.00}Mn_{0.72}Cu_{0.25}O_{2.44}$	$Pr_{1.04}Mn_{0.74}Cu_{0.26}O_{2.53}$	
0.3	0.94	$Pr_{1.03}Mn_{0.68}Cu_{0.29}O_{2.83}$	$Pr_{1.00}Mn_{0.66}Cu_{0.28}O_{2.73}$	$Pr_{1.07}Mn_{0.70}Cu_{0.30}O_{2.93}$	6.1
		$Pr_{1.03}Mn_{0.68}Cu_{0.29}O_{2.58}$	$Pr_{1.00}Mn_{0.66}Cu_{0.28}O_{2.50}$	$Pr_{1.07}Mn_{0.70}Cu_{0.30}O_{2.68}$	
0.35	0.59	$Pr_{1.02}Mn_{0.64}Cu_{0.34}O_{2.70}$	$Pr_{1.00}Mn_{0.63}Cu_{0.33}O_{2.65}$	$Pr_{1.04}Mn_{0.65}Cu_{0.35}O_{2.76}$	3.0
		$Pr_{1.02}Mn_{0.64}Cu_{0.34}O_{2.70}$	$Pr_{1.00}Mn_{0.63}Cu_{0.33}O_{2.65}$	$Pr_{1.04}Mn_{0.65}Cu_{0.35}O_{2.76}$	
0.4	0.68	$Pr_{1.00}Mn_{0.60}Cu_{0.39}O_{2.85}$	$Pr_{1.00}Mn_{0.60}Cu_{0.39}O_{2.84}$	$Pr_{1.01}Mn_{0.61}Cu_{0.39}O_{2.87}$	2.4
		$Pr_{1.00}Mn_{0.60}Cu_{0.39}O_{2.58}$	$Pr_{1.00}Mn_{0.60}Cu_{0.39}O_{2.59}$	$Pr_{1.01}Mn_{0.61}Cu_{0.39}O_{2.59}$	

[a] Stoichiometry calculated on the sum of metals equal to two.
[b] Stoichiometry calculated by fixing the amount of A to one.
[c] Stoichiometry calculated by fixing the amount of (B+B´) to one.

Additionally, also the stoichiometry corrected with the subtraction of oxygen content contained in CO_2 mass loss detected by TG-MS are reported (stoichiometry colored in purple in Table 3.6 and Table 3.7) (see TG-MS mass loss plots in Figure 4SI). The metal amount is not affected for any sample in each of the three employed normalization by this correction, while a decrease in oxygen amount is always resulting, being the highest -7% of oxygen content for $LaMnO_3$ and the lowest -2% for $PrMn_{0.9}Cu_{0.1}O_3$. Interestingly, the oxygen content only of Pr-based samples is higher when the stoichiometry is normalized on (B+B´)=1, followed by (A+B)=2 and finally by A=1, while it is not the case for La-based catalysts. The correction of the oxygen values with the subtraction of O_2 content as detected by TG-MS should be possible because the detected mass loss might be estimated to be due only to CO_2 (m/z=44) mass loss for all the samples, since the other detected species, such as O_2 (m/z=32), CO (m/z=28), N_2(m/z=28) and H_2O (m/z=18), do not show a MS peak or if shown, it is presented at the same temperature of that of CO_2 (see TG-MS mass loss plots in Figure 6SI).

Only $PrMnO_3$, $LaMn_{0.75}Cu_{0.25}O_3$ and $LaMn_{0.7}Cu_{0.3}O_3$ present an O_2 peak in the mass spectrometer (m/z=32) at different temperatures of the CO_2 peak. However, the difference between the oxygen bulk amount without CO_2 correction and those presenting the CO_2 corrections do not fit linearly with the mass loss for Pr-based catalysts (Figure 3.4). This indicates that the stoichiometry reported for Pr-based catalysts with the CO_2 correction of oxygen bulk content should not be taken into consideration, since the mass loss is probably due to the desorption of further species (release of bulk oxygen or N_2 deriving probably from glycine residuals which are not fully combusted during the synthesis and calcination process), although these latter ones have not been detected by TG-MS analysis. Finally, the measured BET surface areas vary from 2.5 until 12 $m^2 \cdot g^{-1}$ (Table 3.6 and Table 3.7) and are in a similar order of magnitude of $LaMn_{(1-x)}Cu_xO_3$ compounds synthesized with similar synthesis methods. [166, 311, 314] Finally, in contrast with some findings reported in the literature, in both the oxygen stoichiometry (with or without CO_2 correction) the oxygen content does not decrease with Cu loading increasing, reflecting the oxidation of Mn^{3+} to Mn^{4+} as a function of Cu^{2+} content. [312]

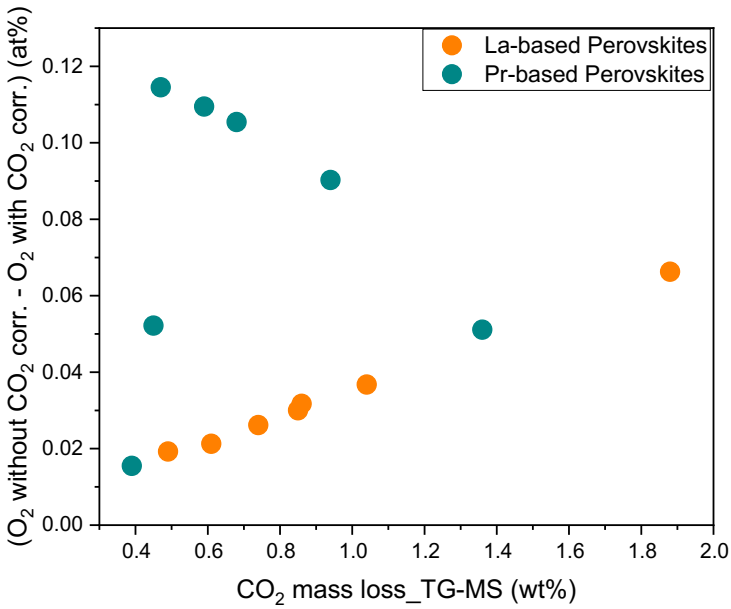

Figure 3.4. *Plot reporting the difference between the not corrected O bulk content and those with CO_2 correction over the CO_2 mass loss detected by TG. Orange: La-based samples, green: Pr-based samples*

In summary, ICP-OES analysis have evidenced that the La-based series present a higher B/A bulk´s ratio in comparison with the corresponding Pr-based ones, which might be due to the fact that the octahedral of Mn and Cu are better embedded into the larger cuboctahedron of La. The difference between the oxygen bulk amounts without CO_2 corrections and those reporting CO_2 corrections fits linearly with the mass loss for La-based series, while it is not the case for the Pr-based ones,

(Figure 4). This indicates that the stoichiometry reported for Pr-based catalysts with CO_2 correction of the oxygen bulk content should not be taken into consideration, since the mass loss is probably due to the desorption of further species (release of bulk oxygen or N_2 deriving probably from glycine residuals which are not fully combusted during the synthesis and calcination process).

3.2.3. Surface composition and surface oxidation state

The surface elemental composition has been calculated employing the core levels of La3d, Pr3d, Mn2p and Cu2p, the theoretical cross sections from Yeh and Lindau, [292] the inelastic free path of the electrons from Tanuma, Powell and Penn [293] and the transmission function of the analyser . The core levels of La, Pr, Mn, Cu and O are shown in Figure SI 3. The oxidation state of Mn has been calculated from the Mn3s splitting based on the work published by Galakhov et al [298] (Table 3.8) and the Mn^{4+}/Mn^{3+} ratio should increase with Cu loading. [201, 315-317] While, in the analyzed catalysts it seems not be the case neither for La- or Pr-series, presenting this latter one higher Mn ox state in comparison with La, probably due to the higher amount of surface Cu fraction in Pr-based samples, which causes an increment in Mn surface oxidation state. Since the Cu2p and Pr3d spectra have very similar binding energies, in order to analyze the spectra of the $PrMn_{(1-x)}Cu_xO_3$ series a Pr3d clean spectra was acquired measuring $PrMnO_3$ (Figure 3.5 a), while several Cu2p spectra were recorded measuring La-based series with the same filament employed for the Pr-based one. Finally, the spectra for the Pr-based series were fitted by scaling the two individual fits for Pr3d according to the literature [297, 318] and Cu2p [296] with some allowance for energy position (Figure 5). The Cu2p region of XPS spectra of all the perovskites display shake-up satellites peaks around 10 eV above the major lines in the Cu2p region, revealing the presence of Cu^{+2} (Figure 3.5 b). [294] The presence of Cu^0 or Cu^{1+} has generally not been detected by laboratory photoelectron spectroscopy, although the NEXAFS experiments over $LaMn_{0.75}Cu_{0.25}O_3$ and $LaMn_{0.7}Cu_{0.3}O_3$ show a feature a 3.5 eV higher than the main peak (resonance position of Cu^{2+} has been fixed at 930.4 eV), which might be attributable to different oxidation state of Cu or to a feature of Cu^{2+} contribution in the perovskite-like structure (Figure 3.6). The contribution of Cu^{3+} is reported to display a feature at + 2eV and not 3.5 eV for perovskite samples, [319, 320] while this feature is generally present in the Cu L-edges spectra of perovskite-like samples presenting Cu^{2+}, although no different oxidation state from Cu^{2+} has been discussed. [321-323] Interestingly, a second XPS band in Cu2p spectra around 4eV below the major line, typical of the electron donation of Cu with lanthana, which should result in more electronegative Cu species shifted to lower BE, [312] is not present in La-based samples with highest Cu loading in comparison with those with the lower one. Finally La or Pr display always oxidation state 3+. [295, 297]

Table 3.8. Table with listed the VB onset averaged on the values measured with Al (Al Kα =1486.6 eV) and Mg (Mg Kα =1253.6 eV) filament, Mn3s splitting and Mn ox state calculated from the Mn3s splitting [298] for the (La,Pr)-series.

Catalyst	VB Onset (eV)	Mn3s Splitting (eV)	Mn Ox State	Catalyst	VB Onset (eV)	Mn3s Splitting (eV)	Mn Ox State
$LaMnO_3$	0.82	6.10	2.2	$PrMnO_3$	0.51	5.49	2.8
$LaMn_{0.9}Cu_{0.1}O_3$	0.78	5.42	2.9	$PrMn_{0.9}Cu_{0.1}O_3$	0.63	5.51	2.8
$LaMn_{0.8}Cu_{0.2}O_3$	0.44	5.71	2.6	$PrMn_{0.8}Cu_{0.2}O_3$	0.77	5.33	3.0-3.3
$LaMn_{0.75}Cu_{0.25}O_3$	0.51	5.95	2.3	$PrMn_{0.75}Cu_{0.25}O_3$	0.79	5.29	3.0-3.3
$LaMn_{0.7}Cu_{0.3}O_3$	0.75	6.10	2.1	$PrMn_{0.7}Cu_{0.3}O_3$	0.72	5.30	3.0-3.3
$LaMn_{0.65}Cu_{0.35}O_3$	0.61	5.89	2.4	$PrMn_{0.65}Cu_{0.35}O_3$	0.72	5.52	2.8
$LaMn_{0.6}Cu_{0.4}O_3$	0.60	5.38	2.9	$PrMn_{0.6}Cu_{0.4}O_3$	0.67	4.93	3.5

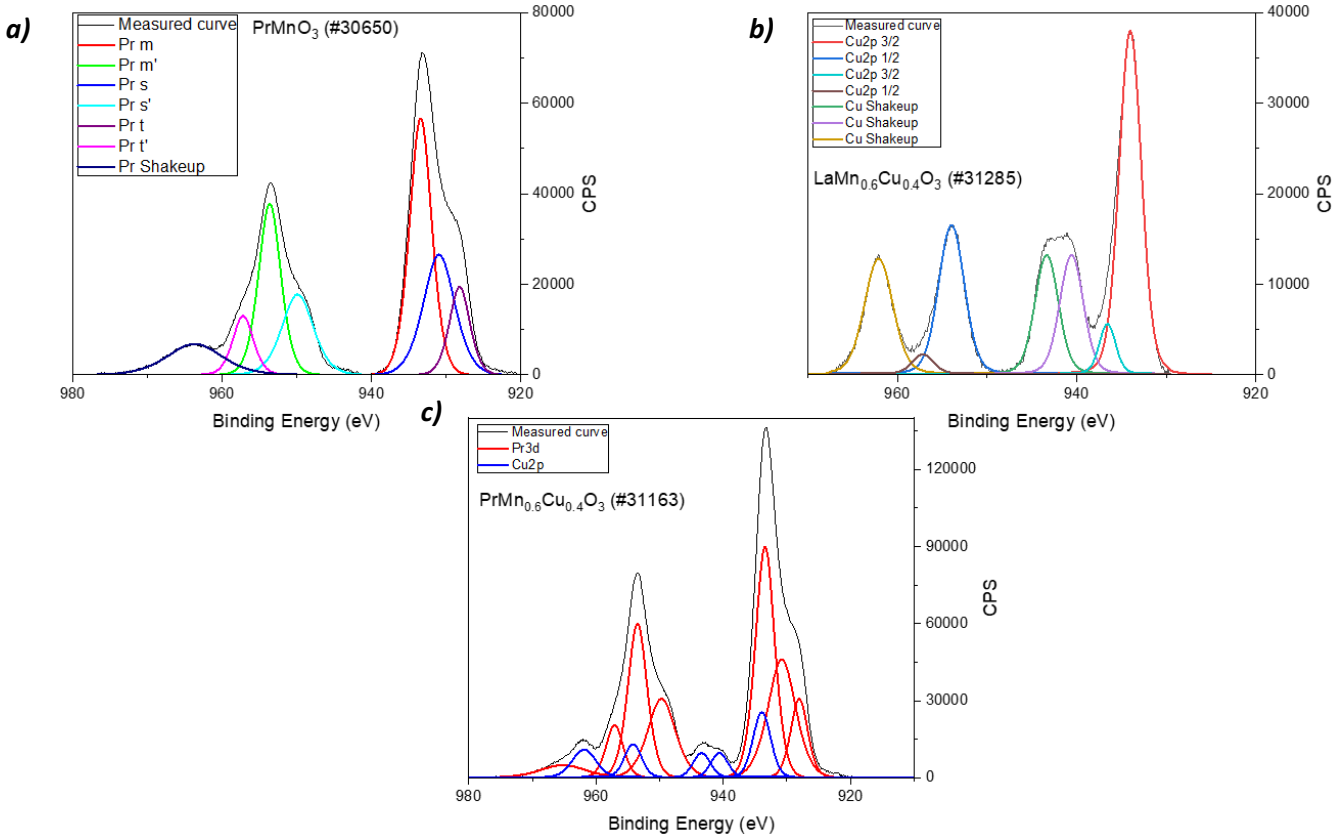

Figure 3.5. *XPS fitted spectra for* ***a)*** *Pr3d* ***b)*** *Cu2p and* ***c)*** *resolving of Pr3d and Cu2p overlapped spectra.*

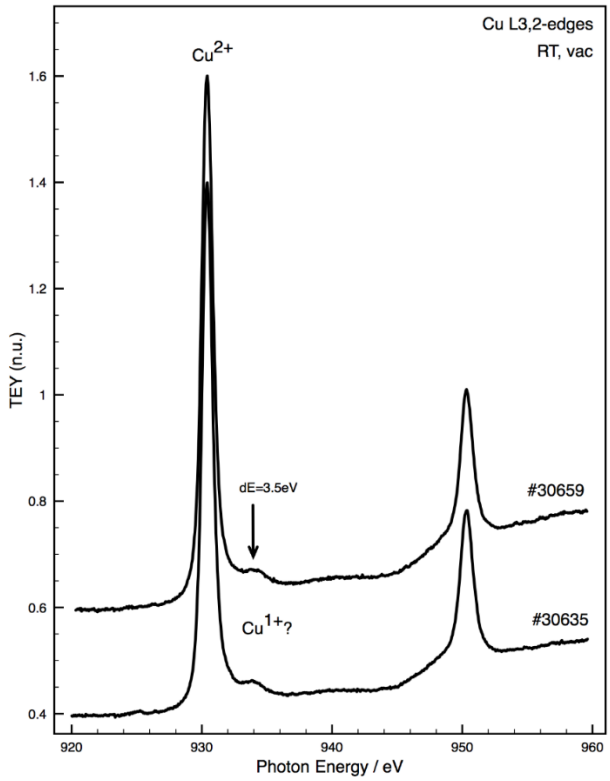

Figure 3.6. *Cu L-edges for #30635 ($LaMn_{0.75}Cu_{0.25}O_3$) and #30659 ($LaMn_{0.7}Cu_{0.3}O_3$) recorded in ultra high vacuum at room temperature.*

The surface composition of (La,Pr)$Mn_{(1-x)}Cu_xO_3$ series determined by XPS are summarized in Table 3.9. The surface elemental ratio B:A is rather close to one and in agreement with the surface elemental analysis reported in the literature for $LaMn_{(1-x)}Cu_xO_3$ series, [310] although there are some differences between the La- and Pr-series. Indeed, the Pr-based catalysts present always a higher B:A ratio in comparison with the corresponding La-based ones (except for x_{Cu}=0.4 and 1), which is probably attributable to the enhanced crystallographic strain discussed above in Pr-based samples, which leads to B-site surface enrichment/segregation. Indeed, although La-based perovskites present higher Mn/A and Cu/A ratios than the same perovskites reported in the literature synthesized by citrate route, [312] the Mn/A and Cu/A ratio is always higher for Pr-based catalysts in comparison to the corresponding La-ones. This makes Pr-based series more interesting in catalysis with respect to La-based ones, since the B-site has generally been considered the responsible element for the catalytic performance. [200] The Mn/A and Cu/A ratio presents a linear dependence, decreases and increases, respectively, with the nominal loading of Mn and Cu, with the exception of $PrMn_{0.9}Cu_{0.1}O_3$ which shows a higher Mn/A ratio with respect to $PrMnO_3$.

Table 3.9. Table with listed the elemental atomic composition on the surface, the B/A surface ratio, the Mn/A surface ratio and Cu/A surface ratio as determined by X-Ray Photoelectron Spectroscopy.

x_{Cu}	*A-site*	*A surface (at%)*	*Mn surface (at%)*	*Cu surface (at%)*	*B/A surface (at%)*	*Mn/A surface (at%)*	*Cu/A surface (at%)*
0	La	23.05%	17.59%	0.00%	0.76	0.76	0.00
	Pr	21.17%	19.22%	0.00%	0.91	0.91	0.00
0.1	La	22.70%	14.42%	3.07%	0.77	0.64	0.14
	Pr	19.70%	18.85%	3.37%	1.13	0.96	0.17
0.2	La	19.74%	12.16%	4.45%	0.84	0.62	0.23
	Pr	20.87%	16.89%	6.18%	1.11	0.81	0.30
0.25	La	20.95%	11.30%	6.08%	0.83	0.54	0.29
	Pr	23.41%	14.64%	6.98%	0.92	0.63	0.30
0.3	La	22.21%	11.43%	6.88%	0.82	0.51	0.31
	Pr	23.26%	13.83%	7.34%	0.91	0.59	0.32
0.35	La	24.58%	10.76%	6.58%	0.71	0.44	0.27
	Pr	24.62%	10.87%	8.45%	0.78	0.44	0.34
0.4	La	20.78%	9.78%	11.56%	1.03	0.47	0.56
	Pr	23.70%	10.47%	11.00%	0.91	0.44	0.46

Regarding the distribution of each single metal between the bulk and the surface has revealed that the A-site (La or Pr) is more enriched on the surface (with the exception of Pr-based samples x= 0, 0.1, 0.2) (Figure 3.7 a). Concerning the double B-site, Mn shows a depletion on the surface respect to the bulk, although Pr-based samples present generally a higher Mn content in comparison with the corresponding La-based samples (Figure 3.7 b). Differently from Mn, Cu is distributed more towards the surface than the bulk for almost each sample, with the La-based series presenting a higher Cu surface content with respect to the corresponding Pr-based one (except La-based sample with x=0.35) (Figure 3.7 c).

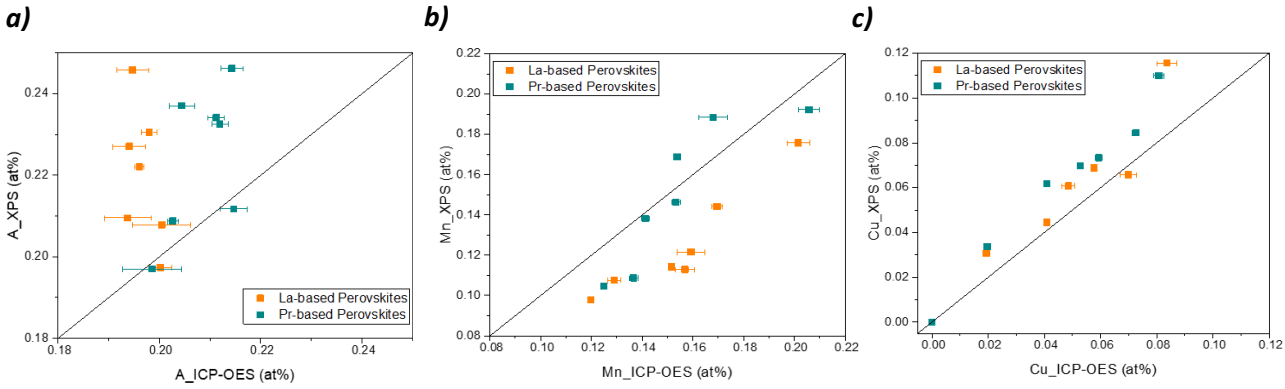

Figure 3.7. *Graphs showing the surface Vs the bulk content for* ***a)*** *the A-site,* ***b)*** *Mn and* ***c)*** *Cu. Orange: La-based samples and green: Pr-based samples.*

3.2.4 Morphology and elemental homogeneity

Scanning electron microscopy (SEM) imaging reveals that all the samples of the (La,Pr)$Mn_{(1-x)}Cu_xO_3$ series present a macroporous coral-like morphology composed by agglomerates of nanocrystallytes, which form hollow tubes in some samples. No by-phases are detected by SEM within the series and no particular morphological difference is visible between the La and Pr-based corresponding catalysts with the same Cu loading content. While, the presence of the Cu dopant seems to increase the tendency to form thinner and more ramified networks (Figure 3.8 c-f) with respect to the $AMnO_3$ catalysts (Figure 3.8 a and b). The SEM picture of the remaining catalysts are shown in Figure 4SI. The homogeneous distribution of all elements in the μm range has been confirmed by EDX mapping (Figure SI 5). The morphology of the $LaMn_{(1-x)}Cu_xO_3$ series seem to present a more regular shape distinguished also by smaller hollow cavity with respect to those reported in the literature for the same catalysts (always at 1 μm). [201]

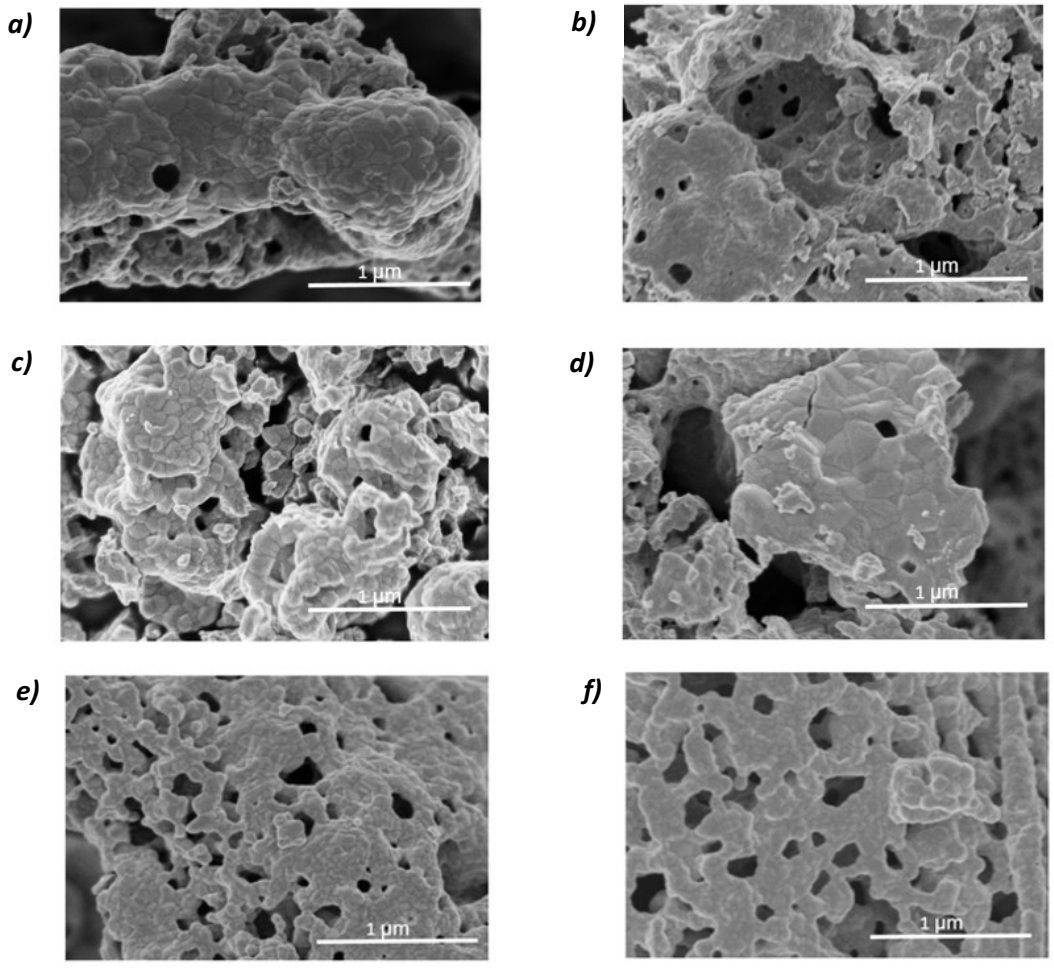

Figure 3.8. *SEM images at 1 μm of* ***a)*** *$LaMnO_3$;* ***b)*** *$PrMnO_3$,;* ***c)*** *$LaMn_{0.75}Cu_{0.25}O_3$;* ***d)*** *$PrMn_{0.75}Cu_{0.25}O_3$;* ***e)*** *$LaMn_{0.6}Cu_{0.4}O_3$ and* ***f)*** *$PrMn_{0.6}Cu_{0.4}O_3$.*

While, in order to investigate further the elemental homogeneous distribution in the nm range and to check for the presence of possible exsolution process in perovskites samples, occurring this latter phenomenon with higher probability in the catalysts with the highest Cu loading, Scanning Transmission Electron Microscopy – Energy Dispersive X-Ray Spectroscopy (STEM-EDX) analysis have been performed over (La,Pr)$Mn_{0.6}Cu_{0.4}O_3$ perovskites. The analysis has rarely revealed the presence of an exsolution process detecting CuO particles in $PrMn_{0.6}Cu_{0.4}O_3$ sample (#31163) (Figure 3.9 b, where a separate peak for Cu and O signal is highlighted in pink within the spectrum), while the investigation of $LaMn_{0.6}Cu_{0.4}O_3$ has not detected the presence of elemental ununiform distribution within the sample (Figure 3.9 a). The fact that segregated CuO has been found only in the Pr-based perovskite with the highest Cu loading and not also in the corresponding La-based one, might indicate that the homogeneous embedding of the elements on the surface's structure might be partially influenced by the higher lattice distortion induced by the smaller size of Pr with respect to La. In addition, the High Resolution Scanning Transmission Electron Microscopy analysis (HR-STEM) performed on $PrMn_{0.6}Cu_{0.4}O_3$ has revealed the presence of a layered structure, where three rows of brighter atoms (in this case Pr, since it is the heaviest element and thus strongest scatterer) separated by a row of lighter element (probably Cu) were visible (Figure 3.10). This structure is similar to the known layered Pr_2CuO_4 Ruddlesden-Popper phase, but it appears to contain 3 layers of cubically coordinated Pr instead of two. Thus, a different structure was proposed containing an additional layer of $[PrO_8]$ cubes, generated based on the Pr_2CuO_4 phase. This results in a composition of Pr_3CuO_6, indicating that the layered by-phase is not the classical Ruddlesden-Popper-Phase (The comparison between the two structures is shown in Figure 3.11). However, in order to fit the measured data, the unit cell of Pr_3CuO_6 had to be shrinked isotropically to 80%, leading to smaller bond lengths than for Pr_2CuO_4. Simulated HAADF images of Pr_3CuO_6 in [110] zone axis are shown in Figure 12 for different probe sizes. Despite of the detected by-phases with STEM-EDX and HR-STEM (CuO and Pr_3CuO_4, respectively), $PrMn_{0.6}Cu_{0.4}O_3$ has never behaved as outlier in propane oxidation under tested condition, while in CO oxidation, it seems to be an outlier with respect to the Pr-series trend.

a)

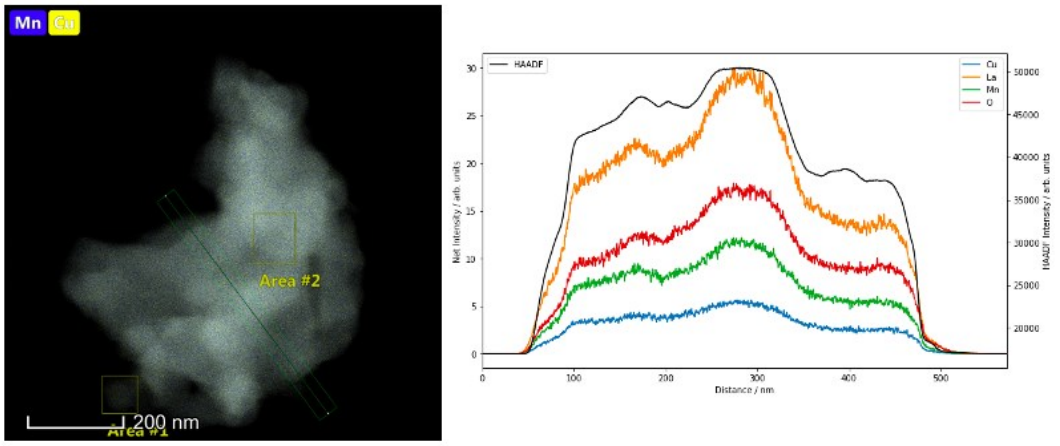

b)

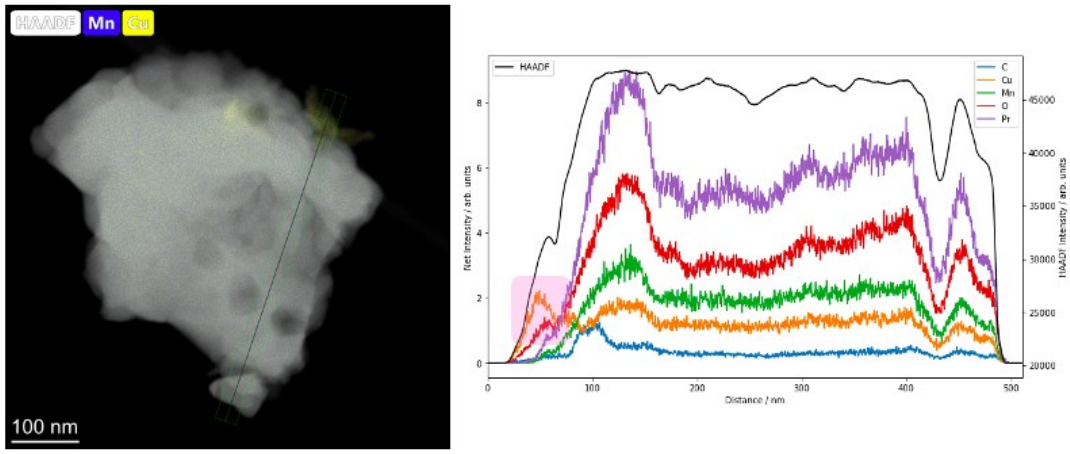

Figure 3.9. *STEM-EDX images and spectra for* ***a)*** *$LaMn_{0.6}Cu_{0.4}O_3$ and* ***b)*** *$PrMn_{0.6}Cu_{0.4}O_3$.*

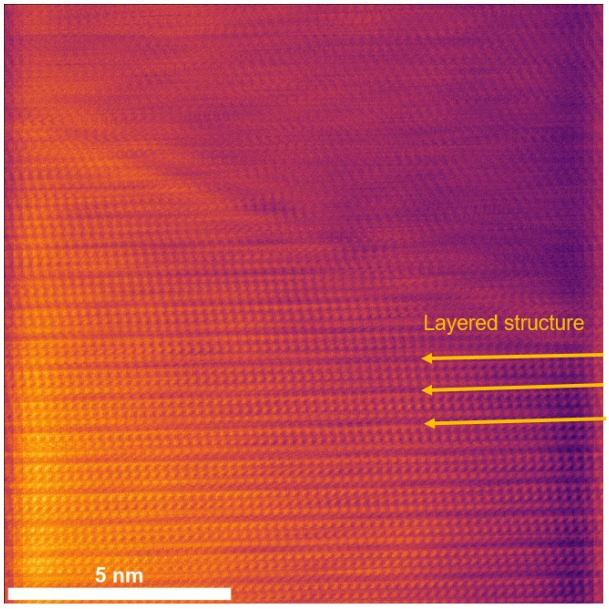

Figure 3.10. *Inverted Bright Field STEM image of a by-phase in $PrMn_{0.6}Cu_{0.4}O_3$. The image was Fourier-filtered and the contrast inverted in order to improve the visibility of the atomic features.*

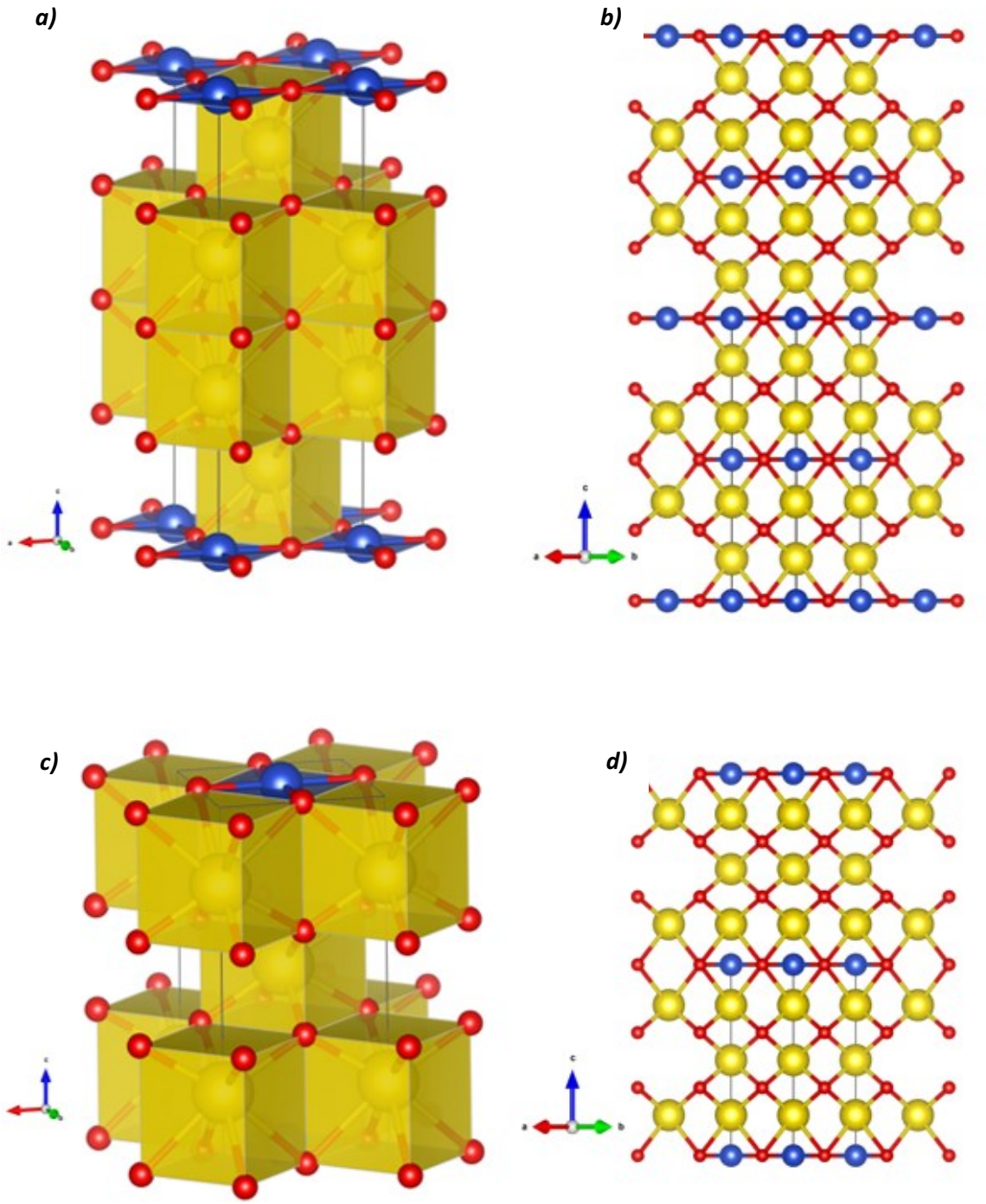

Figure 3.11. *Structures of* ***a)*** *Pr_2CuO_4 in 3D view;* ***b)*** *Pr_2CuO_4 in [110] zone axis;* ***c)*** *Pr_3CuO_6 in 3D view and d)) Pr_3CuO_6 in [110] zone axis.*

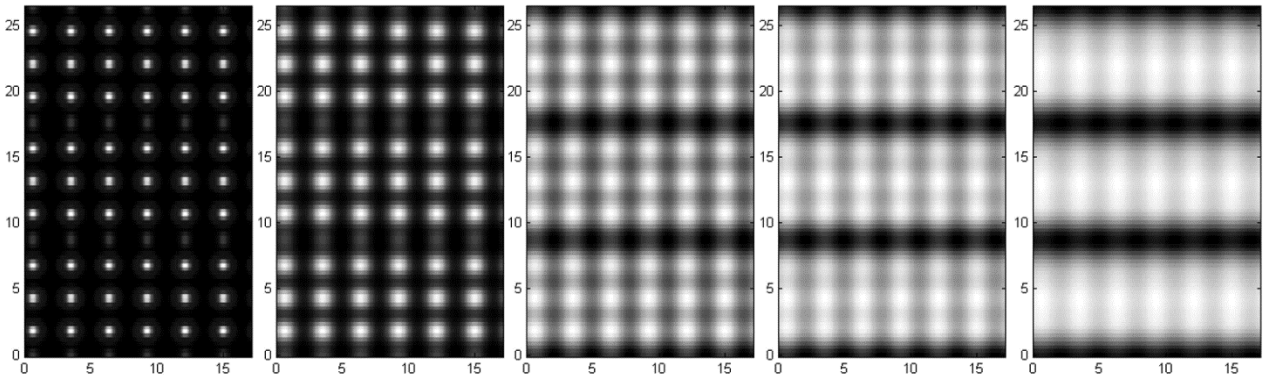

Figure 3.12. *QSTEM simulated HR-STEM images for Pr_3CuO_6 in [110] zone axis for different probe sizes, corresponding to different resolutions (from left to right: 0 Å, 1 Å, 2 Å, 2.5 Å, 3 Å).*

3.2.5 Redox Properties

The redox behavior of the catalysts has been investigated through TPO/TPR cycles in order to probe the oxygen capacity of the catalysts at 300°C with a heating ramp of 5 K/min, which is the reaction temperature employed in propane oxidation. After an in-situ calcination in synthetic air (O_2/He=20/80) at 800°C for 6 h with a heating ramp of 10 K/min (same calcination performed for each sample after the synthesis) in order to remove the presence of adsorbed water and carbonates species, an inert pre-treatment (He) at 300°C for 2 h is performed in order to simulate a reducing atmosphere at the same reaction temperature of propane oxidation. However, the first TPO signal (TPO1 shown by the blue curves in Figure SI 7) for all samples is always zero, indicating that the perovskites are saturated with oxygen during the in-situ calcination and that the pre-treatment with inert at 300°C does not create oxygen vacancies. In some cases, the cycles are not reversible (Figure 3.13) but, generally, the first TPR occurs a different temperature and presents a different shape from the second and the third ones, which are almost coincident for all samples (TPRs shown by the blue curves in Figure SI 7). Usually, the curves display a small peak between 140 and 220°C for La-based series and between 135 and 200°C for Pr-based one, which could be ascribable to the excess oxygen due to cationic defects [324] and since the cationic defects could cause the partial oxidation of Mn^{3+} to Mn^{4+}, the first reduction peak was could also be related to the reduction of Mn^{4+} to Mn^{3+}. [325] A peak indicating the reduction of Cu^{2+} has never been observed in the curve profiles. As mentioned above, the second and third TPR cycles are almost coincident, with the exception of $PrMn_{0.9}Cu_{0.1}O_3$ (Figure 3.13), in which, although the difference between the second and the third TPR profile for this latter catalyst might be considered moderate, some solid-state diffusion mechanism could have played a significant role.

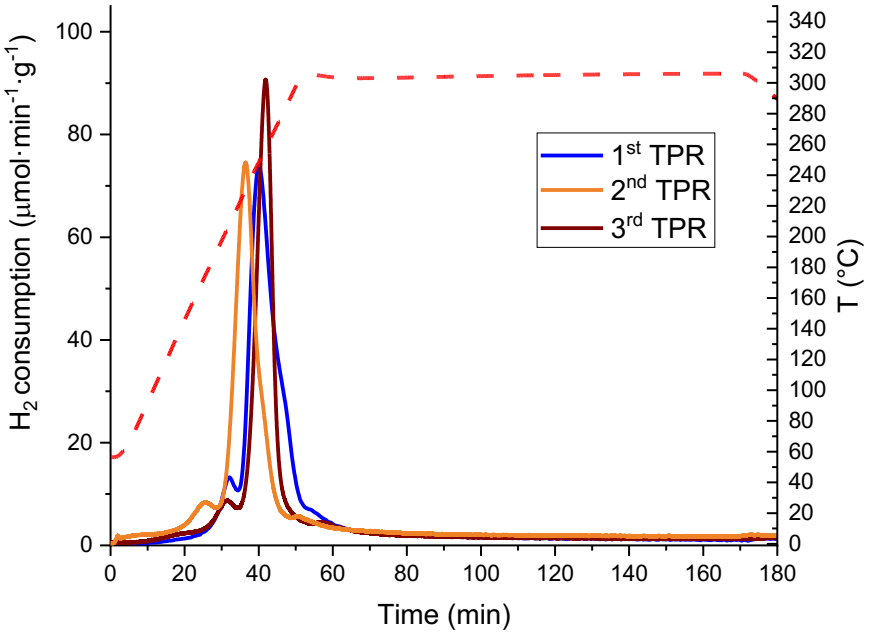

Figure 3.13. *TPR cycles performed at 300° for $PrMn_{0.9}Cu_{0.1}O_3$. Color-code: blue: 1st cycle; orange: 2nd cycle; brown: 3rd cycle and red dotted line: temperature profile.*

Additionally, in order to investigate whether the oxygen content of the catalysts probed at 300°C through TPO/TPR cycles could be considered bulk oxygen, a full TPR up to 1000°C has been performed for the catalysts showing the highest redox capacity, $PrMn_{0.6}Cu_{0.4}O_3$ (Figure 3.14). The integrated area of the TPR experiment performed at 300°C represents the 56% of the area of the TPR performed up to 1000°C, clearly indicating that the TPO/TPR experiments performed at 300°C probe the bulk oxygen of the catalysts. Concerning the difference displayed by the Cu loading in the TPOs and TPRs profile, it seems that the catalysts with lower Cu content show a more smeared peak profile than those with the highest loading (Figure 3.15) and that the main peak occurs generally at the same time for all the samples, except the TPR profiles of $PrMn_{0.9}Cu_{0.1}O_3$ and $PrMn_{0.8}Cu_{0.2}O_3$, which present a different peak profile from all the other catalysts (brown and orange curves in Figure 3.15 d, respectively).

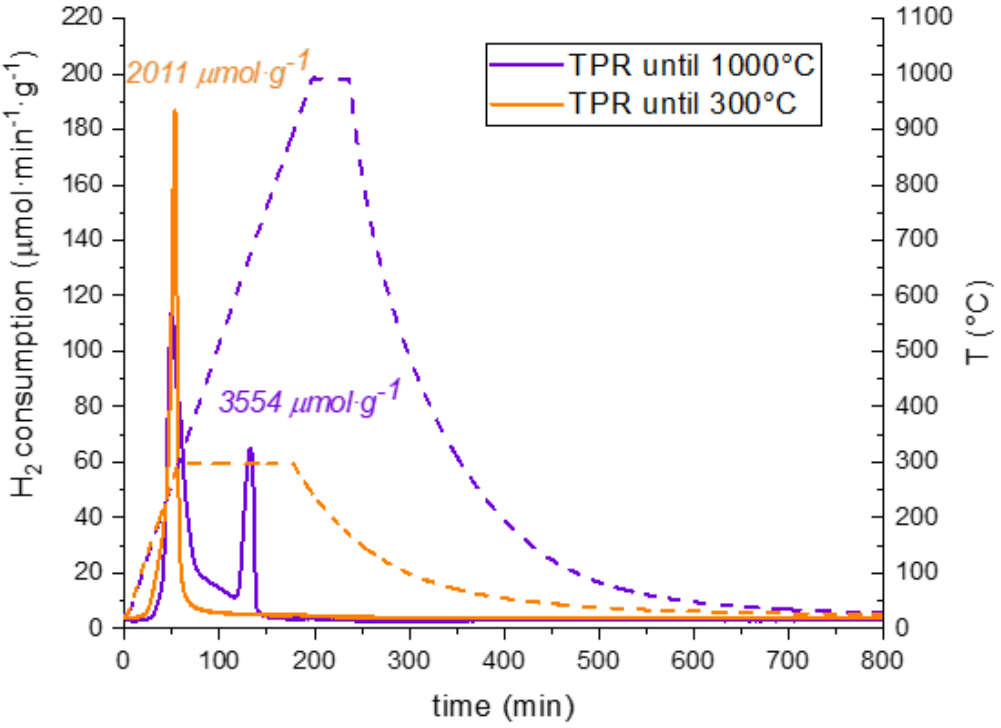

Figure 3.14. *TPR cycles for $PrMn_{0.6}Cu_{0.4}O_3$ performed at 300° (orange curve) and 1000°C (purple curve).Color-code: orange: TPR performed util 300°C and purple: TPR performed until 1000°C. Dotted-lines: temperature profiles.*

a)

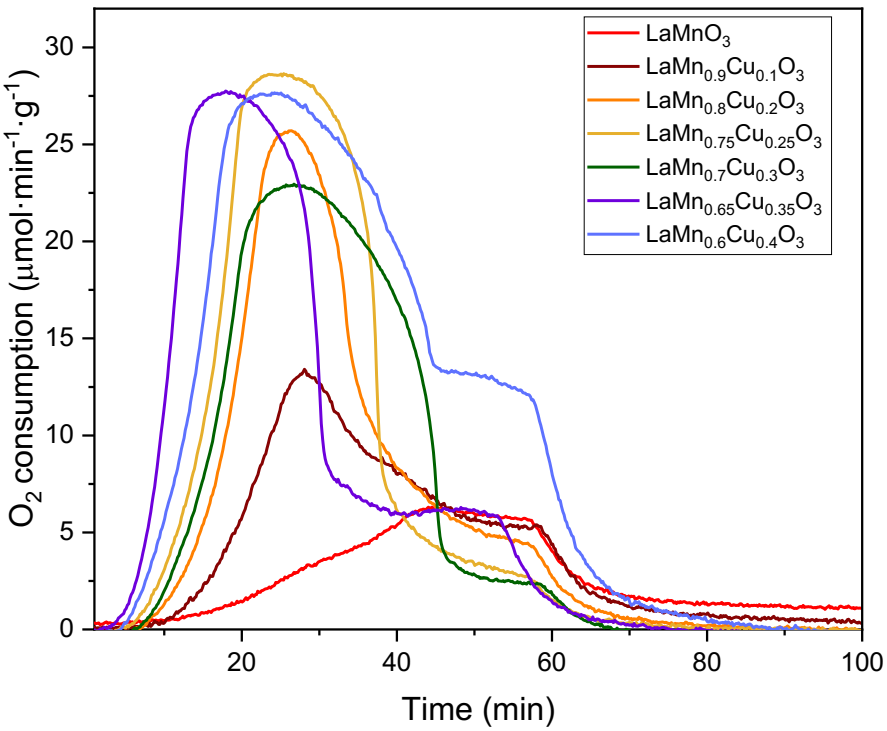

b)

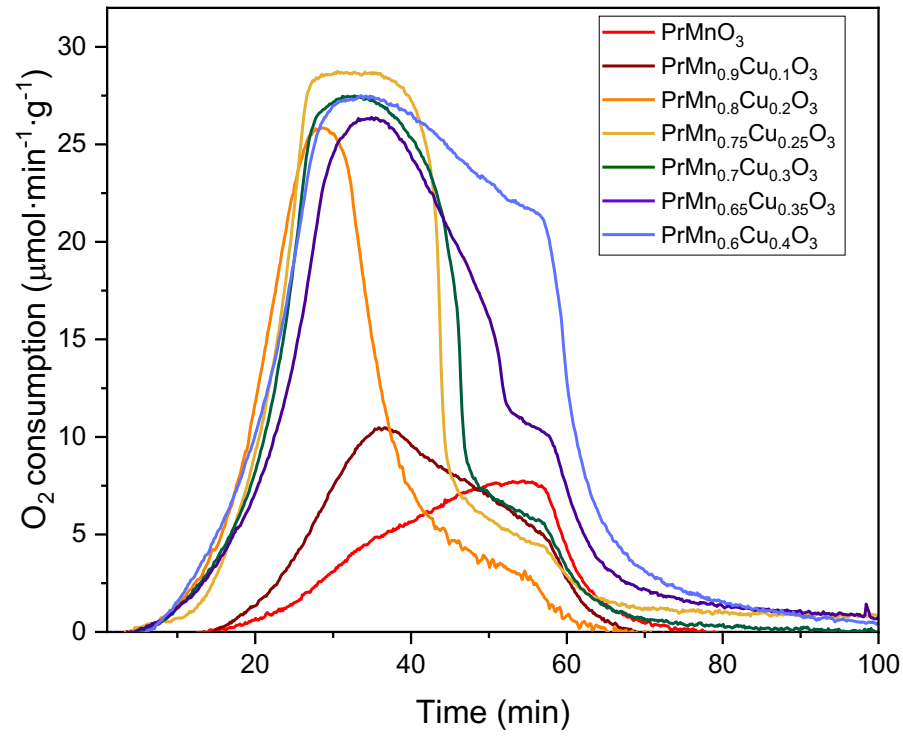
PrMnO3
PrMn0.9Cu0.1O3
PrMn0.8Cu0.2O3
PrMn0.75Cu0.25O3
PrMn0.7Cu0.3O3
PrMn0.65Cu0.35O3
PrMn0.6Cu0.4O3
O2 consumption (µmol·min-1·g-1)
Time (min)

c)

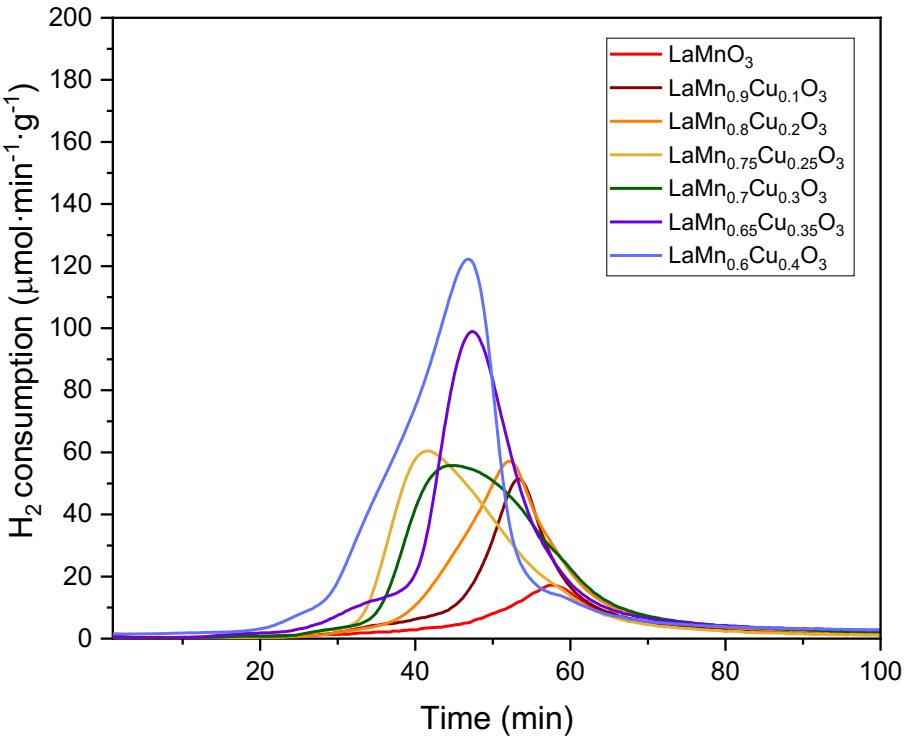
LaMnO3
LaMn0.9Cu0.1O3
LaMn0.8Cu0.2O3
LaMn0.75Cu0.25O3
LaMn0.7Cu0.3O3
LaMn0.65Cu0.35O3
LaMn0.6Cu0.4O3
H2 consumption (µmol·min-1·g-1)
Time (min)

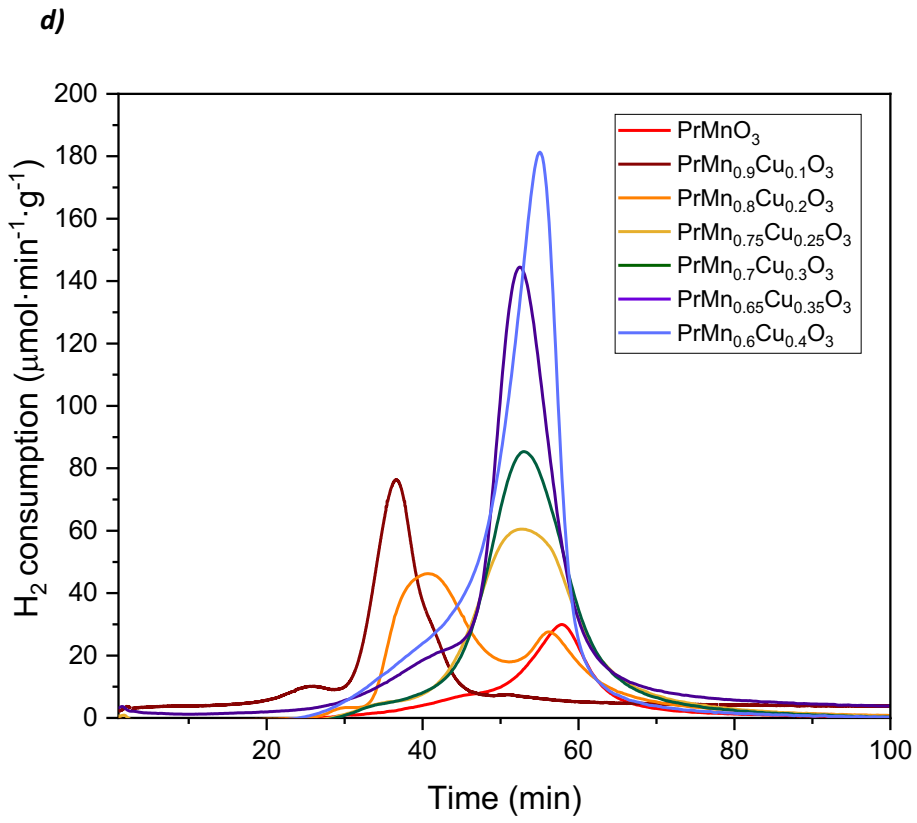

Figure 3.15. *Curves of the 2nd TPO cycle for* ***a)*** *La-based series and* ***b)*** *Pr -based series. Curves of the 2nd TPR cycle for* ***c)*** *La-based series and* ***d)*** *Pr -based series. Color-code: red: x=0; brown: x=0.1; orange: x=0.2; yellow: x=0.25; green: x=0.3; purple: x=0.35 and light blue: x=0.4.*

As evidenced by TPO/TPR cycles, the bulk´s oxygen capacity which is calculated as the amount of oxygen atoms which are transferred during either a TPO or a TPR cycle (delta x detailed calculation in Section 2) is rather constant for all cycles (except TPO2 for $LaMnO_3$), although it generally shows the tendency to slightly decrease over the cycles, especially for the catalysts with x<0.2 (Figure 3.16). The values of the amount of O_2 and H_2 consumed during each cycle, from which the delta x has been calculated is listed in Table 3.10. Moreover, the higher the Cu content within the series, the higher the delta x (i.e. the oxygen capacity), being this latter one even higher for the Pr-based samples with respect to the corresponding La-ones (except of $(La,Pr)Mn_{0.9}Cu_{0.1}O_3$.) (Figure 3.16). Indeed, the averaged delta x, which is a value calculated by averaging the individual delta x shown in Figure 3.16, by excluding the delta x of TPR1, since it occurs immediately after TPO1 which always displays no oxygen absorption by the catalysts and therefore it seems more reasonable to not include it into the "redox equilibrium" of the sample (indeed in Figure 3.16 TPR1 shows always higher delta x than the rest of the cycles), increases linearly with the Cu bulk content and it is always slightly higher for Pr-based sample with respect to the La-based ones (except of $(La,Pr)Mn_{0.9}Cu_{0.1}O_3$) as shown in Figure 3.17. This latter mentioned phenomenon could probably

be explained by the capacity of Cu^{1+}, presumably the major Cu^{n+} species after reduction, to form a linear coordination sphere [326] and to consequently stabilize the formed oxygen vacancies.

Table 3.10. Amounts of O_2 or H_2 consumed (µmol) during each TPO/TPR cycle and the averaged delta x calculated by averaging the individual delta x for each TPO/TPR cycle for the $(La,Pr)Mn_{(1-x)}Cu_xO_3$ series.

x_{Cu}	*A*-site	TPR1-H_2 consumed (µmol)	TPO2-O_2 consumed (µmol)	TPR2-H_2 consumed (µmol)	TPO3-O_2 consumed (µmol)	TPR3-H_2 consumed (µmol)	Averaged $\|\Delta x\|$
0	La	122.7	32.4	79.4	36.9	73.1	0.10
	Pr	137.0	54.9	104.7	51.2	89.8	0.14
0.1	La	n.a.*	73.2	144.6	67.3	133.1	0.18
	Pr	154.4	63.4	127.2	59.0	119.9	0.17
0.2	La	240.4	107.5	195.1	111.7	190.9	0.28
	Pr	211.0	102.0	204.3	96.7	207.0	0.28
0.25	La	243.4	121.1	230.5	116.7	219.7	0.32
	Pr	255.1	129.8	244.0	136.0	238.8	0.35
0.3	La	261.5	129.9	254.7	141.1	254.3	0.36
	Pr	282.5	132.5	288.3	145.7	274.2	0.38
0.35	La	291.7	136.3	290.9	142.0	290.5	0.39
	Pr	328.1	155.1	330.2	161.6	317.9	0.44
0.4	La	368.0	189.0	356.0	169.1	354.6	0.48
	Pr	412.2	201.0	375.5	201.1	370.2	0.53

*During TPR1 a recording problem of the detector occurred, however, the cycle has been performed correctly and therefore the following cycles can be considered valid experiments.

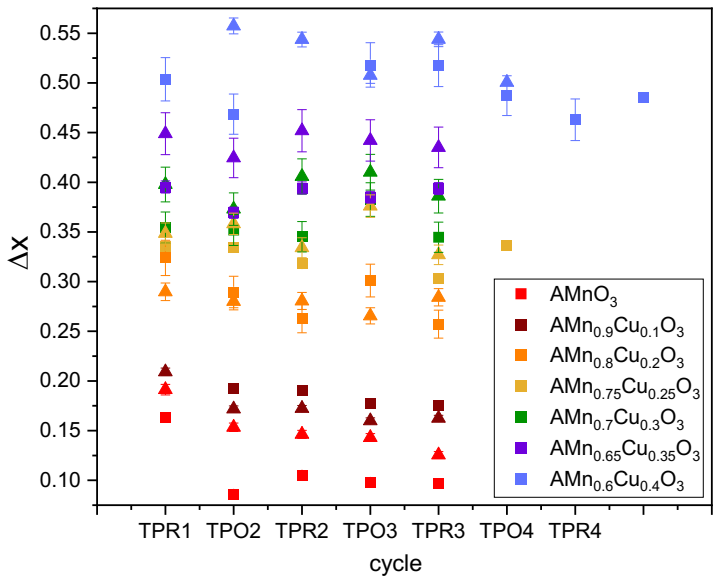

Figure 3.16. *Plot showing the oxygen capacity (delta x) for each sample at each TPO/TPR cycle. Squares: La-based samples and triangles: Pr-based samples. Color-code: red: x=0; brown: x=0.1; orange: x=0.2; yellow: x=0.25; green: x=0.3; purple: x=0.35 and light blue: x=0.4*

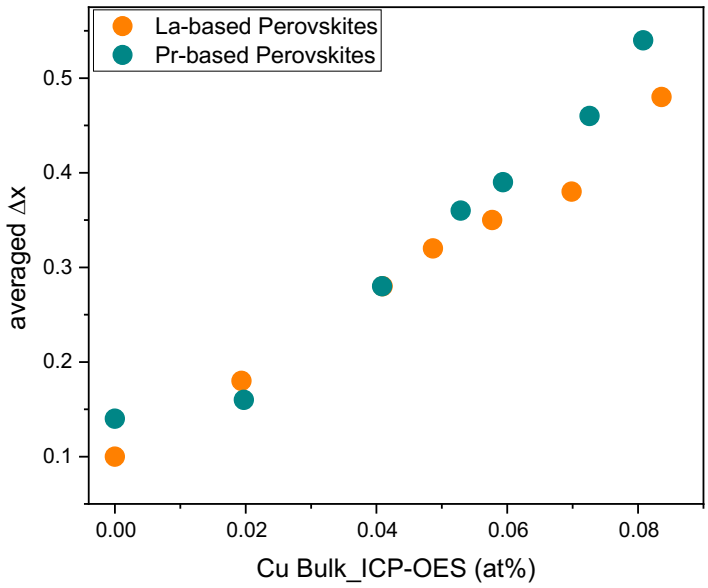

Figure 3.17. *Plot showing the oxygen capacity (averaged delta x) calculated averaging all the oxygen capacities calculated from each TPO and TPR cycle over the Cu bulk content. Orange: La-based samples, green: Pr-based samples.*

TPR post-mortem samples have been subjected to XRD in order to investigate the crystallographic change upon reduction. The XRD analysis have evidenced that the most of the catalysts have maintained the same crystallographic phase upon reduction at 300°C, in agreement with the literature [311], while La-based catalysts until x≤0.2 have decreased their symmetry from rhombohedral to pure orthorhombic and all the catalysts show a shrinking of the c axis, which leads to a volume expansion, in agreement to what is reported in the literature [327] (Table 3.11 and 3.12).

Table 3.11. Table containing the lattice constants and the normalized volume from Rietveld-Refinement for the $LaMn_{(1-x)}Cu_xO_3$ series.

xCu	***Catalyst´s status***	***Lattice symmetry***	***a (Å)***	***b (Å)***	***c (Å)***	***V/Z (Å^3)***
0	Fresh	R-3cH	5.507	5.507	13.340	58.395
	Post TPR	Pbnm	5.541	5.596	7.783	60.341
0.1	Fresh	R-3cH	5.520	5.520	13.326	58.613
	Post TPR	*Pbnm*	5.553	5.582	7.815	60.556
0.2	Fresh	R-3cH	5.526	5.526	13.326	58.741
		Pbnm	5.526	5.485	7.770	
	Post TPR	Pbnm	5.563	5.546	7.851	60.550
0.25	Fresh	Pbnm	5.529	5.486	7.777	58.972

Table 3.11 (cont.)

	Post TPR	Pbnm	5.535	5.499	7.788	59.261
0.3	Fresh	Pbnm	5.526	5.483	7.773	58.890
	Post TPR	Pbnm	5.563	5.536	7.838	60.347
0.35	Fresh	Pbnm	5.526	5.487	7.779	58.969
	Post TPR	Pbnm	5.563	5.545	7.840	60.465
0.4	Fresh	Pbnm	5.527	5.488	7.779	58.991
	Post TPR	Pbnm	5.569	5.551	7.862	60.762

Table 3.12. Table containing the lattice constants and the normalized volume from Rietveld-Refinement for the $PrMn_{(1-x)}Cu_xO_3$ series.

xCu	***Catalyst´s status***	***Lattice symmetry***	***a (Å)***	***b (Å)***	***c (Å)***	***V/Z (Å³)***
0	Fresh	Pbnm	*5.460*	*5.490*	*7.713*	57.805
	Post TPR	Pbnm	5.453	5.805	7.610	60.219
0.1	Fresh	Pbnm	*5.460*	*5.510*	*7.703*	58.171
	Post TPR	Pbnm	5.449	5.826	7.601	60.324
0.2	Fresh	Pbnm	*5.463*	*5.548*	*7.696*	58.319
	Post TPR	Pbnm	5.482	5.696	7.691	60.048
0.25	Fresh	Pbnm	*5.464*	*5.544*	*7.696*	58.286
	Post TPR	Pbnm	5.515	5.580	7.751	59.631
0.3	Fresh	Pbnm	*5.466*	*5.544*	*7.695*	58.296
	Post TPR	Pbnm	5.520	5.588	7.761	59.848
0.35	Fresh	Pbnm	*5.465*	*5.532*	*7.695*	58.161
	Post TPR	Pbnm	5.517	5.612	7.759	60.058
0.4	Fresh	Pbnm	*5.465*	*5.530*	*7.691*	58.109
	Post TPR	Pbnm	5.497	5.629	7.724	59.748

In summary, the TPO/TPR cycles performed at 300°C have evidenced that the cycle reversibility is generally achieved after the first TPR for almost all catalysts (see the integrated areas listed in Table 3.10), being the calculated bulk´s oxygen capacity from the cycle (delta x) rather constant for all cycles, although it generally shows the tendency to slightly decreases over the cycles, especially for the catalysts with x<0.2 (Figure 3.16). The averaged delta x, which is the value calculated by

averaging the individual delta x excluding those of TPO1 and TPR1 (since the first TPO always show no oxygen absorption for all catalysts), increases linearly with the Cu bulk content and it is always slightly higher for Pr-based sample with respect to the La-based ones (Figure 3.17). This latter mentioned phenomenon is probably ascribable to the tendency of Cu^{1+}, presumably the major Cu^{n+} species after reduction, to form a linear coordination sphere [326] and to consequently stabilize the formed oxygen vacancies. No trend is observed between the Cu loading and the peak profiles feature of TPO/TPR cycles. The perovskite structure is maintained for all samples upon reduction, without the segregation of by-phases, as evidenced by XRD post-mortem analysis.

3.3 Analysis of the structural and electronic properties of the $(La,Pr)_2CuO_4$ perovskite-related structures

3.3.1 *Crystal symmetry*

The $(La,Pr)_2CuO_4$ catalysts have been treated independently because of their different structure-type with respect to the $(La,Pr)Mn_{(1-x)}Cu_xO_3$ series. The two perovskite-related structure catalysts have been synthesized by the self-ignition method and calcined at 800°C in synair (O_2/Ar=20/80), as all the other catalysts presented in the herein project. As evidenced by Rietveld refinement of powder X-ray diffractograms (Figure SI 2), La_2CuO_4 is 99% phase-pure (1% of La_2O_3) and Pr_2CuO_4 is 100% phase-pure according to XRD detection limit. These perovskite-related structures are named Ruddlesden-Popper-Phase, which are layered structures that present the general formula $A_{(n+1)}B_nO_{(3n+2)}$ (see Section 1.3.1. for the detailed description of the structure). La_2CuO_4 (#33018) presents the tetragonal symmetry with orthorhombic distortion, while Pr_2CuO_4 (#33343) presents the tetragonal symmetry with T´geometry. In the T geometry, the B cation occupies the octahedra units and the A cation is located at the center of 4 apical oxygen ions, deriving from the four nearest octahedra, and it is also placed directly below the apical oxygen of the nearest octahedra belonging to neighboring layer. Therefore, the A-site has coordination number 9 in La_2CuO_4. While, in the T´ geometry differs from the T one basically from the disposition of the oxygen atoms. In this latter one, the B cation sheets are no any longer octahedrally coordinated, but occupy the center of square planar pyramids (BO_2 layers) and the A-site has coordination of 8 in Pr_2CuO_4 structure. The XRD results are in agreement with those presented in the literature for Pr_2CuO_4, reported to be K_2NiF_4 structure-type (T´), [305, 328] while La_2CuO_4 is generally reported to be orthorhombic instead of T structure. [166, 309, 329] In the case of the La_2CuO_4 catalyst presented in this Thesis project, the orthorhombic distortion to the T structure might be due to an excess of oxygen between the B octahedral and the A-O layers, which could induce the tilting of the octahedra. The calculated lattice

constants and the V1 volume (2d-perovskite volume) are in agreement to those reported in the literature for the same compounds. [305, 329] The <B-O> sigma value for La_2CuO_4 is higher than that for the corresponding Pr-based sample, indicating that the octahedral Jahn-Teller distortion is higher for #33018, as it is reflected in the crystallographic symmetry which is tetragonal with orthorhombic distortion. While the <A-O> sigma values can not be compared for these two materials, due to the different symmetry with respect to the A-ion (Table 3.13).

Table 3.13. Table with listed: the crystallographic data from Rietveld Refinement. Being Bmab: orthorhombic symmetry and I4/mmm: tetragonal symmetry; a,b,c: lattice constants; V:normalized volume of the unit cell; <B-O> and <A-O>: mean of interatomic distances and <B-O> sigma and <A-O> sigma the standard deviations of interatomic distances for the A_2CuO_4 samples.

A-site	Lattice symmetry	*a* (Å)	*b* (Å)	*c* (Å)	*V/Z 1* (Å^3)[a]	*V/Z 2* (Å^3)[b]	<B-O> (Å)	<B-O>sigma (Å)	<A-O> (Å)	<A-O>sigma (Å)
La	*Bmab*	5.358	5.400	13.152	95.139	63.426	2.073	0.236	2.658	0.165
Pr	*I*4/*mmm*	3.960	3.960	12.222	95.819	63.879	1.980	0.000	2.511	0.173

a Normalized volume calculated by dividing the cell volume by the number of formula units.

b Normalized volume calculated by estimation of the partition of the c axis, i.e. $\frac{2}{3}$ of the volume belong to the ABO_3 motif and $\frac{1}{3}$ belongs to the AO rock salt motif.

3.3.2 Chemical composition, nanostructure, porosity and morphology of the catalysts

The bulk and the surface stoichiometry have been determined by ICP-OES (Table 3.14) and XPS (Table 3.15), respectively, confirming that the A:Cu ratios were very close to the nominal ones both for the bulk and the surface within the series. However, in contrast to La_2CuO_4 which shows a B/A ratio almost coincident with the nominal one (ideal B/A for A_2BO_4=0.5), the Pr_2CuO_4 catalyst shows a slight bulk B-site enrichment (Figure 3.18).

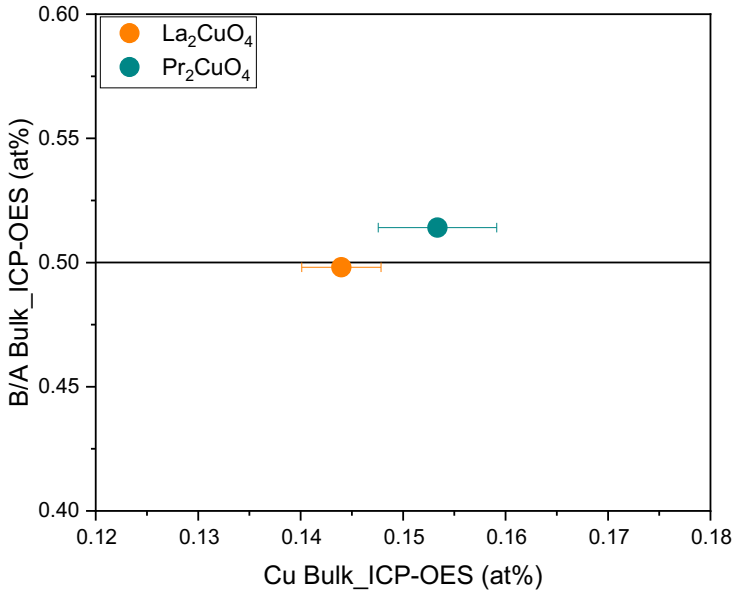

Figure 3.18. *Graph indicating the bulk's B/A ratio. Orange: La_2CuO_4 , green: Pr_2CuO_4.*

This B-site enrichment is visible also in the three normalized stoichiometry listed in Table 3.14, where Pr is always minor than 2 and Cu slightly higher than 1 for #33343. Both samples seem to present oxygen deficiency in all the three normalizations, being the oxygen content higher for the La-based catalyst in comparison to the Pr-based one and this could ascribable to the excess of oxygen between the B octahedra and the A-O layers in La_2CuO_4, which could induce the tilting of the octahedra. Moreover, the ICP-OES bulk analysis have been repeated three times for each sample in order to determine the relative standard deviations for the value of each metals, which range from 0.04 to maximum 2.28 %, indicating that no elements present bulk segregation in the two analyzed compounds. Also oxygen content determination analysis have been repeated three times for each material. The surface areas reported in Table 3.14 for the two Ruddlesden-Popper phase catalysts are rather low and in agreement with those reported in the literature for La_2CuO_4 synthesized freeze-drying solutions. [166]

Table 3.14. Table with listed: the stoichiometry determined by ICP-OES combined with oxygen content determination analysis and the BET surface areas. Color-code: orange: La_2CuO_4 , green: Pr_2CuO_4.

A-site	*Space group*	*(A+B) = 2*[a]	*A = 1*[b]	*(B+B') = 1*[c]	*BET surface area ($m^2 \cdot g^{-1}$)*
La	*Bmab*	$La_2CuO_{3.93}$	$La_2CuO_{3.92}$	$La_{2.01}CuO_{3.94}$	1.7
Pr	*I4/mmm*	$Pr_{1.98}Cu_{1.02}O_{3.64}$	$Pr_2Cu_{1.03}O_{3.68}$	$Pr_{1.95}CuO_{3.58}$	1.6

[a] *Stoichiometry calculated on the sum of metals equal to two (three for A_2CuO_4 structures).* [b] *Stoichiometry calculated by fixing the amount of A to one (two for A_2CuO_4 structures).* [c] *Stoichiometry calculated by fixing the amount of (B+B') to one.*

The surface composition of the A_2CuO_4 catalysts determined by XPS are summarized in Table 3.15. The elemental ratio B:A is rather close to 0.5 and in agreement with the surface elemental analysis reported in the literature for the same compounds. [310] As it is the case for the bulk, the La-based sample presents a B/A surface ratio which is almost the ideal one, while Pr-based sample presents an A-site enrichment. While, regarding the distribution of each single metal between the bulk and the surface both A and Cu seem to be enriched in the bulk for both samples, in particular the La-based one (Figure 3.19).

Table 3.15. Table with listed the elemental atomic composition on the surface and the B/A surface ratio as determined by X-Ray Photoelectron Spectroscopy. Color-code: orange: La_2CuO_4 , green: Pr_2CuO_4.

A-site	*A surface (at%)*	*Cu surface (at%)*	*B/A surface (at%)*
La	18.87	9.25	0.49
Pr	25.21	11.48	0.46

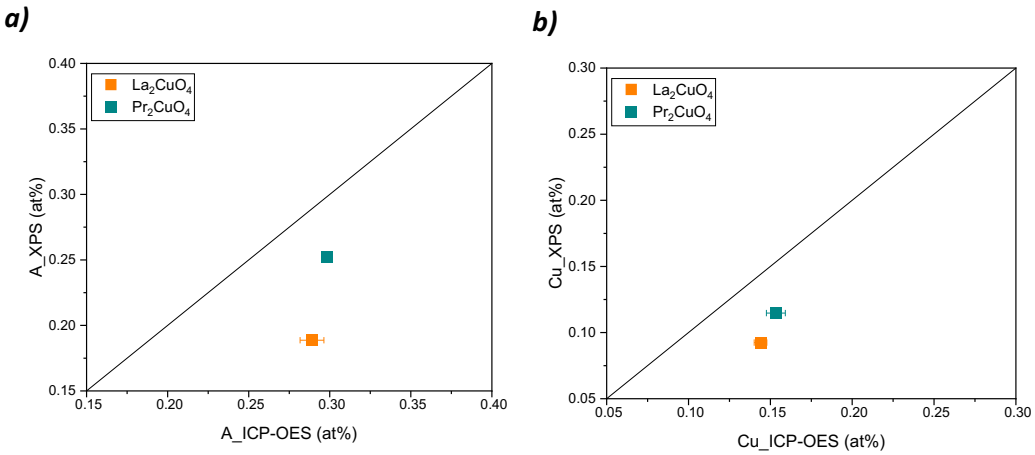

Figure 3.19. *Graphs showing the surface Vs the bulk content for* ***a)*** *the A-site and* ***b)*** *Cu. Orange: La_2CuO_4 , green: Pr_2CuO_4.*

By analyzing the XPS spectra the Cu2p region displays shake-up satellites peaks around 10 eV above the major lines in the Cu2p region, revealing the presence of Cu^{+2} [294] (Figure 3.20).

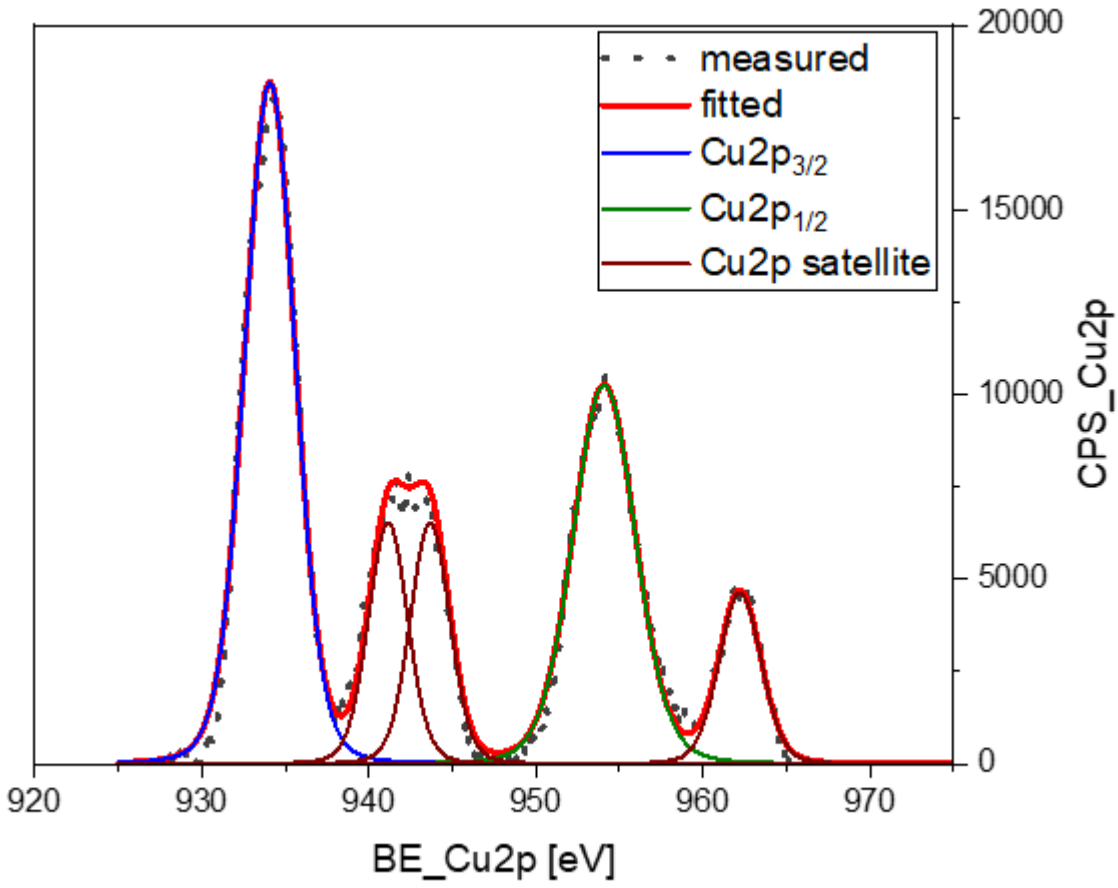

Figure 3.20. *Graphs showing the Cu2p spectrum for La_2CuO_4. Color-code: grey : measured curve; red :enveloped curve; blue: $Cu2p_{3/2}$; green: $Cu2p_{1/2}$ and brown: Cu2p satellites.*

Scanning electron microscopy (SEM) imaging reveals that the two Ruddlesden-Popper Phase perovskites (Figure 3.21) present bigger crystals and defined structured networks in comparison with the (La,Pr)$Mn_{(1-x)}Cu_xO_3$ series (Figure 3.6). Also spherical agglomeration of particles are displayed the lower magnification SEM images (Figure 3.21 a and b). The morphology is very similar from that presented in literature for Pr_2CuO_4 synthesized with glycine-nitrate combustion method, [305] while it differs significantly from that reported for La_2CuO_4 synthesized by hydrothermal route, where either cubes with size distribution of 45-180 nm, or spherical particles or even square rods are produced after calcination at 800°C depending on the precursors combination. [330]

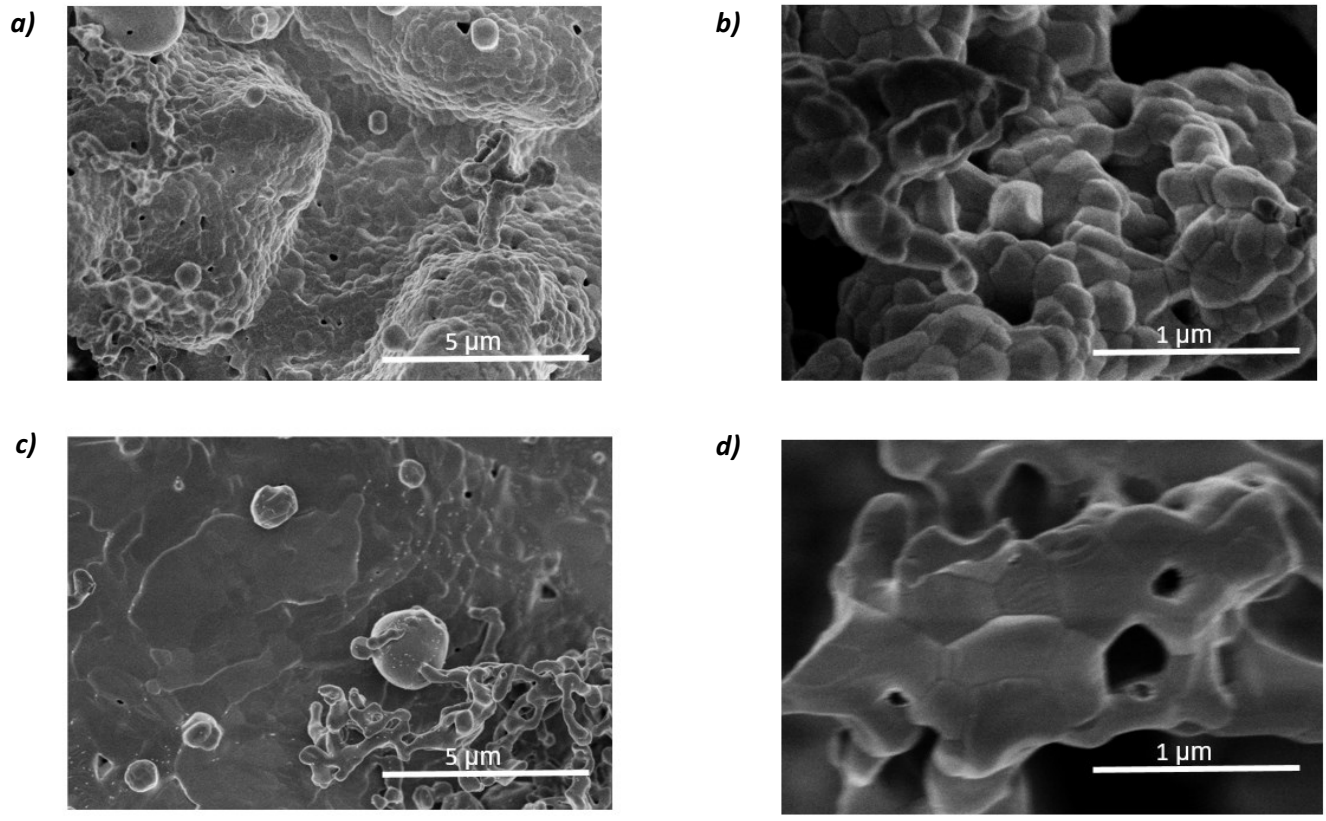

Figure 3.21. *SEM images at 1 µm of* ***a)*** *La_2CuO_4 at 5 µm;* ***b)*** *La_2CuO_4 at 1 µm;* ***c)*** *Pr_2CuO_4 at 5 µm and* ***d)*** *Pr_2CuO_4 at 1 µm.*

In summary, $(La,Pr)_2CuO_4$ Ruddlesden-Popper phase catalysts have been synthesized by self-ignition method and calcined at 800°C in synair (O_2/Ar=20/80). As evidenced by Rietveld refinement of powder X-ray diffractograms (Figure 2SI), La_2CuO_4 is 99% phase-pure (1% of La_2O_3) and Pr_2CuO_4 is 100% phase-pure according to XRD detection limit. La_2CuO_4 presents the tetragonal symmetry with orthorhombic distortion, which is also reflected in the higer <B-O> sigma value, while Pr_2CuO_4 presents the tetragonal symmetry with T´geometry. As evidenced by ICP-OES analysis combined with oxygen determination analysis, both samples seem to present oxygen deficiency, being the oxygen content higher for the La-based catalyst in comparison to the Pr-based one and this could explain the octahedral distortion adopted by La_2CuO_4, which could be related to the excess of oxygen between the B octahedra and the A-O layers. Concerning the bulk and surface elemental composition, La_2CuO_4 presents an ideal B/A bulk and surface ratio in agreement with the nominal one, while Pr_2CuO_4 shows an A-site enrichment on the surface and a B-site one on the bulk. Finally, scanning electron microscopy (SEM) imaging reveals that the two Ruddlesden-Popper Phase perovskites (Figure 3.21) present bigger crystals and defined structured networks in comparison with the $(La,Pr)Mn_{(1-x)}Cu_xO_3$ series (Figure 3.6).

3.4 Analysis of the structural and electronic properties of the (Pr,Nd,Sm)$Mn_{0.7}B'_{0.3}O_3$ Perovskites

3.4.1 Crystal symmetry

7 catalysts presenting the general formula (Pr,Nd,Sm)$Mn_{0.7}B'_{0.3}O_3$ (with B´=Zn, Ni, Co, Fe, Cr, Pd and Ru) have been synthesized by self-ignition route and calcined at 800°C, being this latter temperature the best compromise between crystallinity and surface area, as it was evidenced by the preliminary screening performed over the (La,Pr)$Mn_{(1-x)}Cu_xO_3$ series (Section 3.1). As evidenced by Rietveld refinement of powder X-ray diffractograms (Figure SI 8), all the synthesis products are phase-pure perovskite-like samples, which present orthorhombic symmetry, with the exception of $PrMn_{0.7}Ru_{0.3}O_3$ and $PrMn_{0.95}Pd_{0.05}O_3$, which present around 3% of RuO_2 and 2.5% of PdO, respectively (Table 3.16). This is probably ascribable to the fact that 4+ is a more common oxidation state for Ru with respect to 2+ and Pd is generally coordinated in a square planar geometry, instead of an octahedral one. [331, 332] As presented in Table 3.15, the standard deviations of the interatomic distances B-O (<B-O> sigma), which reflects the Jahn-Teller distortion, vary across the series in major extent with respect to <A-O> sigma (which reflects the cuboctahedral distortion). This is simply explainable by looking at the large folding fan of elemental variability for the B site in the series in comparison to the A one. Indeed, the only sample presenting an <A-O> sigma value which significantly differs from the others is $SmMn_{0.7}Cr_{0.3}O_3$ (#33622), since Sm is the smallest employed Lanthanoid. Additionally, $SmMn_{0.7}Cr_{0.3}O_3$ presents also one of the highest <B-O> sigma, due to the mismatch between the ionic radii of Mn and of Cr. $LaMn_{(1-x)}M_xO_3$ systems (M=Ni, Co) with $0.2 \leq x$ 0.4 have been reported to crystallize in the cubic symmetry after calcination at 700°C, while the catalysts calcined at 800°C presented in the following Thesis with B'=Ni and Co posses orthorhombic crystal structures. [333] The lower symmetry in comparison with similar structures reported in the literature might be attributable to the smaller size of Pr with respect to that of La cation, where the BO_6 octahedra tilt in order to maintain the perovskite-structure with the smaller cuboctahedral A-cage. [313] $PrMn_{0.7}Zn_{0.3}O_3$ presents orthorhombic crystal symmetry, being this latter result in agreement with the works found in the literature over the $LaMn_{(1-x)}Zn_xO_3$ system, where it is reported that when the Zn amount exceeds 0.1 of doping, the structural transition from rhombohedral to orthorhombic symmetry is observed. Moreover, it is claimed in this latter cited work that zinc doping is responsible for the tilting of MO_6 octahedra, influencing in this way the Jahn-Teller distortion of Mn^{3+}. [334] Indeed, the calculated <B-O> sigma value for $PrMn_{0.7}Zn_{0.3}O_3$ shows a higher Jahn-Teller distortion with respect to the materials with B'=Co and Ni. As in the cases of Co and Ni substituted perovskites, $LaMn_{0.7}Fe_{0.3}O_3$, it is reported in the literature with higher symmetry than the orthorhombic one [334] and, also in this case, the difference is ascribable to the

smaller size of Pr with respect to La. While, $LaMn_{(1-x)}Cr_xO_3$ system shows a phase transition from rhombohedral to orthorhombic when the doping amount of Cr exceeds 0.2. [335] Finally, as in the case of the material presented in the herein project (#33591), PdO by-phase formation has been detected by XRD for $LaMnO_3$ perovskites doped with 7% of Pd in the B-site a synthesized by sol-gel route. [336]

Table 3.16. Table with listed: the crystallographic data from Rietveld Refinement. Being R-3cH: rhombohedral symmetry and Pbnm : orthorhombic symmetry, a,b,c: lattice constants; V:normalized volume of the unit cell; <B-O> and <A-O>: mean of interatomic distances and <B-O> sigma and <A-O> sigma the standard deviations of interatomic distances for the (Pr,Nd,Sm)Mn0.7B'0.3O3 series.

A-site	B-site	Lattice symmetry	*a* (Å)	*b* (Å)	*c* (Å)	*V/Z* (Å^3)	<B-O> (Å)	<B-O>sigma (Å)	<A-O> (Å)	<A-O>sigma (Å)
Pr	Zn	Pbnm	5.462	5.526	7.731	58.336	1.991	0.041	2.769	0.350
Pr	Ni	Pbnm	5.451	5.488	7.711	57.659	1.978	0.027	2.755	0.331
Pr	Co	Pbnm	5.456	5.510	7.719	58.011	1.985	0.040	2.763	0.343
Nd	Fe	Pbnm	5.440	5.527	7.708	57.944	1.984	0.071	2.763	0.344
Sm	Cr	Pbnm	5.367	5.600	7.602	57.122	1.995	0.113	2.768	0.430
Pr	Pd	Pbnm + 2.5% PdO	5.455	5.528	7.706	58.102	1.985	0.051	2.764	0.342
Pr	Ru	Pbnm + 3% RuO_2	5.456	5.564	7.713	58.532	1.995	0.120	2.777	0.368

Due to the lanthanide contraction, the $SmMn_{0.7}Cr_{0.3}O_3$ present a higher degree of orthorhombic distortion with respect to the Pr-based samples, [313] However, $NdMn_{0.7}Fe_{0.3}O_3$ presents an observed tolerance factor which is in the same range of the ones of the Pr-based perovskites. Moreover, the B' site seems to not influence the crystallographic distortion, having all the Pr-based samples similar t_{obs} (Figure 3.22).

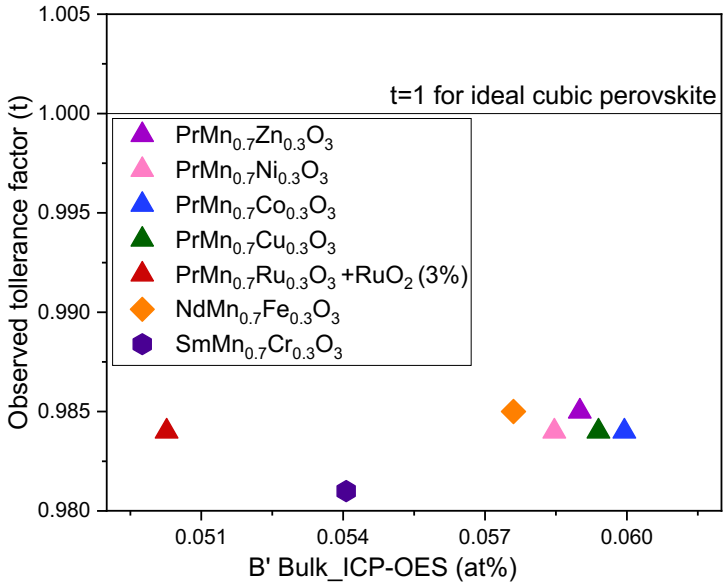

***Figure 3.22**. Graph showing the experimentally observed tolerance factor as calculated from the distances determined by Rietveld Refinement over the Mn bulk fraction. B' color-code: magenta: Zn; pink: Ni; light blue: Co; green: Cu; orange: Fe; violet: Cr; dull green: Pd and red: Ru. PrMn0.7Cu0.3O3 is inserted for comparison.*

3.4.2 Chemical composition, electronic structure and porosity of the catalysts

The bulk and the surface stoichiometries have been determined by ICP-OES (Table 3.17) and XPS (Table 3.18), respectively, confirming that the Mn:B' ratios were very close to the nominal ones both for the bulk and the surface. However, some differences in the bulk´s elemental distribution are visible within the $AMn_{0.7}B'_{0.3}O_3$ series. Indeed, the Ni, Zn, Co and Fe-based samples present a B-site enrichment, $SmMn_{0.7}Cr_{0.3}O_3$ sample's B/A bulk's ratio is almost coincident with the nominal one, while Ru, Cu, Pd-based sample present an B-site bulk depletion (Figure 3.23). This might indicate that Co, Zn, Ni, Fe and Cr render the stabilization of the (B+B')-site into the bulk of the perovskite structures more favorable with respect to the other employed B'-site metals, such as Cu, Pd and Ru. For $PrMn_{0.95}Pd_{0.05}O_3$ (#33591) and $PrMn_{0.7}Ru_{0.3}O_3$ (#33624) the (B+B')-site depletion in the bulk might be due also to the presence of the by-phases, which unbalance the elemental bulk distribution.

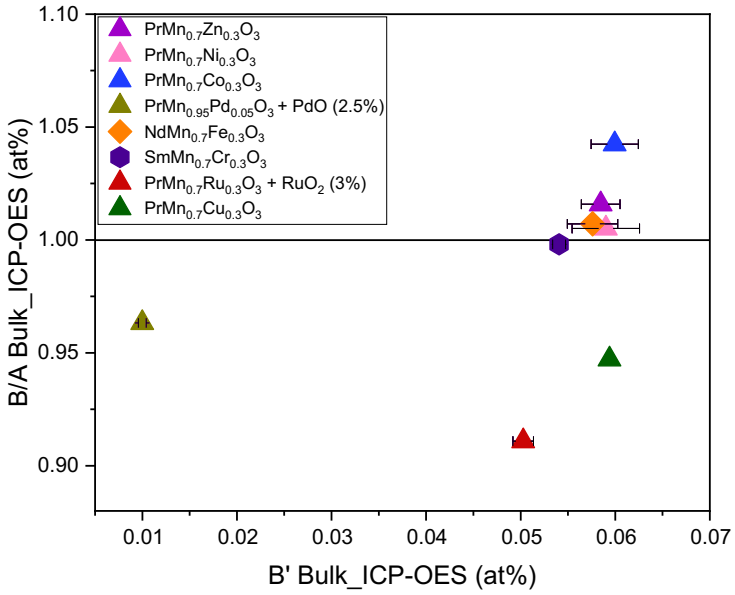

Figure 3.23. *Graph indicating the bulk's B/A ratio over the B' bulk content. B' color-code: magenta: Zn; pink: Ni; light blue: Co; green: Cu; orange: Fe; violet: Cr; dull green: Pd and red: Ru. PrMn0.7Cu0.3O3 is inserted for comparison.*

The depletion of the A-site in the bulk for the catalysts containing Co, Ni, Zn and Fe (#33454, 33366, 33380 and 33621) is visible also by comparing the normalized formulas (A+B)=2 and (B+B')=1 listed in Table 3.17. Indeed, as it was done for the (La,Pr)-series, the stoichiometry have been reported in three different normalizations, such as (A+B)=2, A=1 and (B+B′)=1, in order to highlight and compare different aspects of the metal composition simultaneously. As expected from the B/A ratio (Figure 3.23), all the three different normalizations show identical stoichiometry for the $SmMn_{0.7}Cr_{0.3}O_3$ catalyst (#33622), suggesting that Sm, Mn and Cr amounts are almost coincident with the nominal ones. The same might be true also for the B'-site in general, which is always very close to the nominal value of 0.3 for all the three different normalizations and for all the discussed materials, with the exception of the not-phase-pure sample $PrMn_{0.7}Ru_{0.3}O_3$ (#33624, red data point in Figure 3.23). Finally, by comparing the Mn content in the three different normalizations, it seems that the experimentally determined content is always slightly in excess with respect to the nominal one, except the not-phase pure material $PrMn_{0.95}Pd_{0.05}O_3$ (#33591). As it was performed also for the (La,Pr)-series, the ICP-OES bulk analysis has been repeated three times for each sample in order to determine the relative standard deviations for the value of each detected element in the measurements, which range from 0.47 to maximum 5.2 % for the phase-pure catalysts, (except the two not phase-pure materials #33591 and 33624). Also the oxygen content determination analysis has been repeated three times for each material. N_2 physiosorption analysis has been performed to determine the specific surface areas, being these latter ones between

1,6 and 12,7 $m^2 \cdot g^{-1}$ (Table 3.17) presenting values in the same order of magnitude of those of the (La,Pr)$Mn_{(1-x)}Cu_xO_3$ series and in a similar order of magnitude of $AMn_{0.7}B'_{0.3}O_3$ perovskites synthesized with close synthesis method. [166, 311, 314]

Table 3.17. Table with listed: the stoichiometries determined by ICP-OES and the BET surface areas for the (Pr,Nd,Sm)$Mn_{0.7}B'_{0.3}O_3$ series.

A-site	B'-site	(A+B) = 2[a]	A = 1[b]	(B+B´) = 1[c]	BET surface area ($m^2 \cdot g^{-1}$)
Pr	Ni	$Pr_{1.00}Mn_{0.70}Ni_{0.30}O_{3.08}$	$Pr_{1.00}Mn_{0.70}Ni_{0.30}O_{3.09}$	$Pr_{0.99}Mn_{0.70}Ni_{0.30}O_{3.07}$	7.0
Pr	Zn	$Pr_{0.99}Mn_{0.71}Zn_{0.30}O_{3.05}$	$Pr_{1.00}Mn_{0.72}Zn_{0.30}O_{3.07}$	$Pr_{0.98}Mn_{0.71}Zn_{0.29}O_{3.02}$	11.4
Pr	Co	$Pr_{0.98}Mn_{0.72}Co_{0.30}O_{3.02}$	$Pr_{1.00}Mn_{0.74}Co_{0.31}O_{3.08}$	$Pr_{0.96}Mn_{0.71}Co_{0.29}O_{2.96}$	9.4
Nd	Fe	$Nd_{1.00}Mn_{0.70}Fe_{0.30}O_{3.23}$	$Nd_{1.00}Mn_{0.70}Fe_{0.30}O_{3.24}$	$Nd_{0.99}Mn_{0.70}Fe_{0.30}O_{3.22}$	12.7
Sm	Cr	$Sm_{1.00}Mn_{0.71}Cr_{0.29}O_{3.30}$	$Sm_{1.00}Mn_{0.71}Cr_{0.29}O_{3.30}$	$Sm_{1.00}Mn_{0.71}Cr_{0.29}O_{3.30}$	10.4
Pr	Pd	$Pr_{1.02}Mn_{0.93}Pd_{0.05}O_{3.29}$	$Pr_{1.00}Mn_{0.91}Pd_{0.05}O_{3.23}$	$Pr_{1.04}Mn_{0.95}Pd_{0.05}O_{3.36}$	1.6
Pr	Ru	$Pr_{1.05}Mn_{0.69}Ru_{0.27}O_{3.28}$	$Pr_{1.00}Mn_{0.66}Ru_{0.25}O_{3.14}$	$Pr_{1.10}Mn_{0.72}Ru_{0.28}O_{3.44}$	4.1

[a] Stoichiometry calculated on the sum of metals equal to two (three for A_2CuO_4 structures)

[b] Stoichiometry calculated by fixing the amount of A to one (two for A_2CuO_4 structures)

[c] Stoichiometry calculated by fixing the amount of (B+B´) to one.

The surface elemental composition has been calculated employing the core levels of Pr3d, Nd3d, Sm3d, Mn2p, Zn2p, Ni2p, Co2p, Fe2p, Cr2p, Pd3d and Ru3d the theoretical cross sections from Yeh and Lindau, [292] the inelastic free path of the electrons from Tanuma, Powell and Penn [293] and the transmission function of the analyser . The Mn oxidation state, as evaluated from Mn3s splitting, [298] does not vary significantly among the series (Table 3.17) and the values are quite similar to the same stoichiometry with Cu as B´-site (Table 3.8), suggesting that all the B´-site element present a similar oxidation state. In the case of the Mn oxidation for $PrMn_{0.7}Zn_{0.3}O_3$, the error associated to the Mn3s value would be much higher than that reported for the other compounds. This is because, although Zn 3p has been fitted according to the literature, [337, 338] the Mn3s peak overlaps with that of Zn3p (Figure 3.24). After removing the Pr4d satellites, three clear peaks around 83, 89 and 92 eV were present. The middle larger peak around 89 eV is convoluted $Zn3p_{3/2}$ and half of Mn3s, since the two Mn3s peak were expected at 83 and 88 eV and the two of Zn3p at 89 and 92 eV.

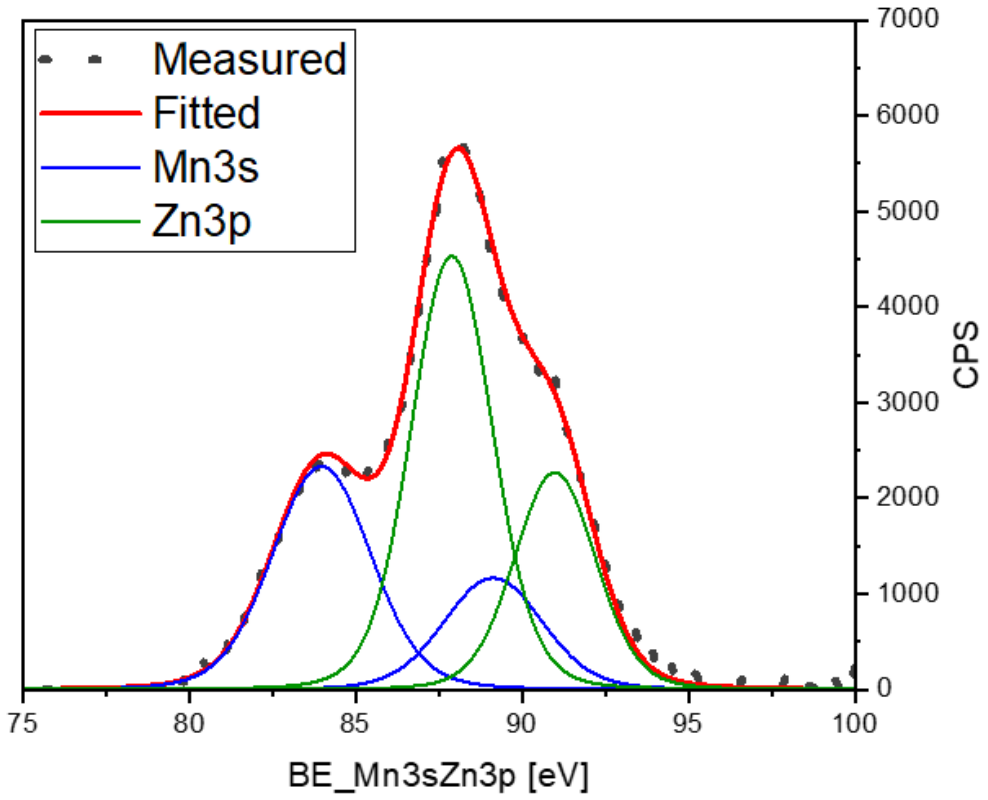

Figure 3.24. *Graphs showing the overlap between the Mn3s and Zn3p spectra. Color-code: grey : measured curve; red: enveloped curve; blue : Mn3s components and green: Zn3p components.*

The surface composition of (Pr,Nd,Sm)$Mn_{0.7}B'_{0.3}O_3$ series + $PrMn_{0.95}Pd_{0.05}O_3$ catalyst determined by XPS are reported in Table 3.18. The elemental B'/A ratios are rather different among each others depending on the B´-site metal and differ substantially also from the B'/A values listed for the (La,Pr)$Mn_{0.7}Cu_{0.3}O_3$ compounds listed in Table 3.9. In particular, the catalysts with B´ being Zn, Ni and Co show a very low B´/A ratio compared to the other phase-pure catalysts (B'= Fe and Cr), whose B'/A ratio is three time higher. Also $LaMn_{(1-x)}Ni_xO_3$ catalysts reported in the literature and synthesized by citric acid route show much higher Ni/A ratio, being between 0.28 and 0.37 for $0.25 \leq x \leq 0.4$. [339] This latter phenomenon might be also connected to the A-site. Indeed, the structural strain established by the smaller size of Nd and Sm might be a responsible factor for the surface enrichment of Fe and Cr. [313]

Table 3.18. Table with listed the elemental atomic composition on the surface, the B/A surface ratio, the Mn/A surface ratio, B′/A surface ratio and the Mn oxidation state from Mn3s splitting as determined by X-Ray Photoelectron Spectroscopy.

A-site	*B'-site*	*A surface (at%)*	*Mn surface (at%)*	*B' surface (at%)*	*B/A surface (at%)*	*Mn/A surface (at%)*	*B'/A surface (at%)*	*Mn ox state*
Pr	Ni	22.50	17.01	2.32	0.86	0.76	0.10	3.5
Pr	Zn	21.45	16.67	3.78	0.95	0.78	0.18	n.a.*
Pr	Co	18.09	11.78	2.09	0.77	0.65	0.12	3.4
Nd	Fe	14.44	11.79	6.19	1.24	0.82	0.43	3.2
Sm	Cr	14.37	7.86	6.14	0.97	0.55	0.43	3.5
Pr	Pd	19.11	13.47	2.16	0.82	0.70	0.11	3.4
Pr	Ru	19.50	8.80	3.35	0.62	0.45	0.17	3.1

* The calculation of the distance between the two peaks of Mn3s can not provide a reliable value, since Mn3s overlaps with Zn3p.

By analyzing the elemental distribution between surface and bulk of specifically only the $PrMn_{0.7}B'_{0.3}O_3$ series it becomes evident how the B' site may affect this latter one (Figure 3.25 a, b, c). Indeed, Co-based catalyst presents an A- site and Mn surface depletion in contrast to Zn- and Ni-based catalysts. Concerning the B'-site surface enrichment, it is present only for Pd, Fe and Cr. Interestingly, the two not phase-pure samples ($PrMn_{0.7}Ru_{0.3}O_3$ + 3% RuO_2 and $PrMn_{0.95}Pd_{0.05}O_3$ + 2.5% PdO) do not show an uneven distribution between the surface and bulk concentration of the A site (they perfectly fall on the line in Figure 3.25 a).

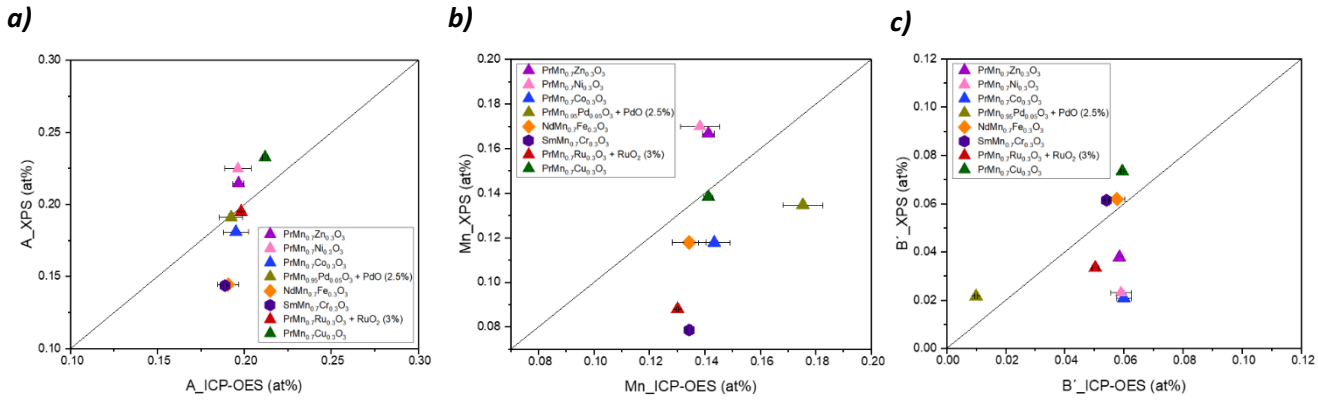

Figure 3.25. *Graphs showing the surface Vs the bulk content for* ***a)*** *the A-site,* ***b)*** *Mn and* ***c)*** *B'. B' color-code: magenta: Zn; pink: Ni; light blue: Co; green: Cu; orange: Fe; violet: Cr; dull green: Pd and red: Ru. PrMn0.7Cu0.3O3 is inserted for comparison.*

3.4.3 Morphology and elemental homogeneity

Scanning electron microscopy (SEM) imaging reveals that all the samples of the (Pr,Nd,Sm)$Mn_{0.7}B'_{0.3}O_3$ and $PrMn_{0.95}Pd_{0.05}O_3$ series present a macroporous network morphology composed by agglomerates of nanocrystallytes bridged-connected and presenting holes. The variation of the A and B' is reflected into morphological changes, indeed $PrMn_{0.7}B'_{0.3}O_3$ catalysts with B'=Ni and Fe present very similar morphology (Figure 3.26 a,b,c,d), Zn-based catalyst (Figure 3.26 a) shows the less ramified and most compacted structure, in the Co-based (Figure 3.26 c) one the tendency of the particles is to agglomerate in empty spherical like-particles, in agreement with the morphology reported in the literature for $LaMn_{(1-x)}M_xO_3$ materials, [333] while $SmMn_{0.7}Cr_{0.3}O_3$ show a thinner and more ramified coral-like macroporous structure with crystals not larger than 100 nm (Figure 3.26 e). $NdMn_{0.7}Fe_{0.3}O_3$ sample (Figure 3.26 d) shows holes of smaller dimension with respect to those reported in the literature for $LaMn_{0.7}Fe_{0.3}O_3$ synthesized by sol-gel method. [201] No by-phases are detected by SEM within the whole series, except for $PrMn_{0.95}Pd_{0.05}O_3$ (Figure 3.26 f and g) and $PrMn_{0.7}Ru_{0.3}O_3$ (Figure 3.26 h). $PrMn_{0.95}Pd_{0.05}O_3$ and $PrMn_{0.7}Ru_{0.3}O_3$ present crystals which correspond to PdO and RuO_2 [340] as detected by XRD, respectively. For these two latter catalysts presenting a considerable amount of by-phases, EDX mapping was performed in order to investigate the elemental homogenous distribution in the nm range. The samples present homogeneous distribution of all elements, being Pd and Ru segregated in the found crystals (Figure SI 9).

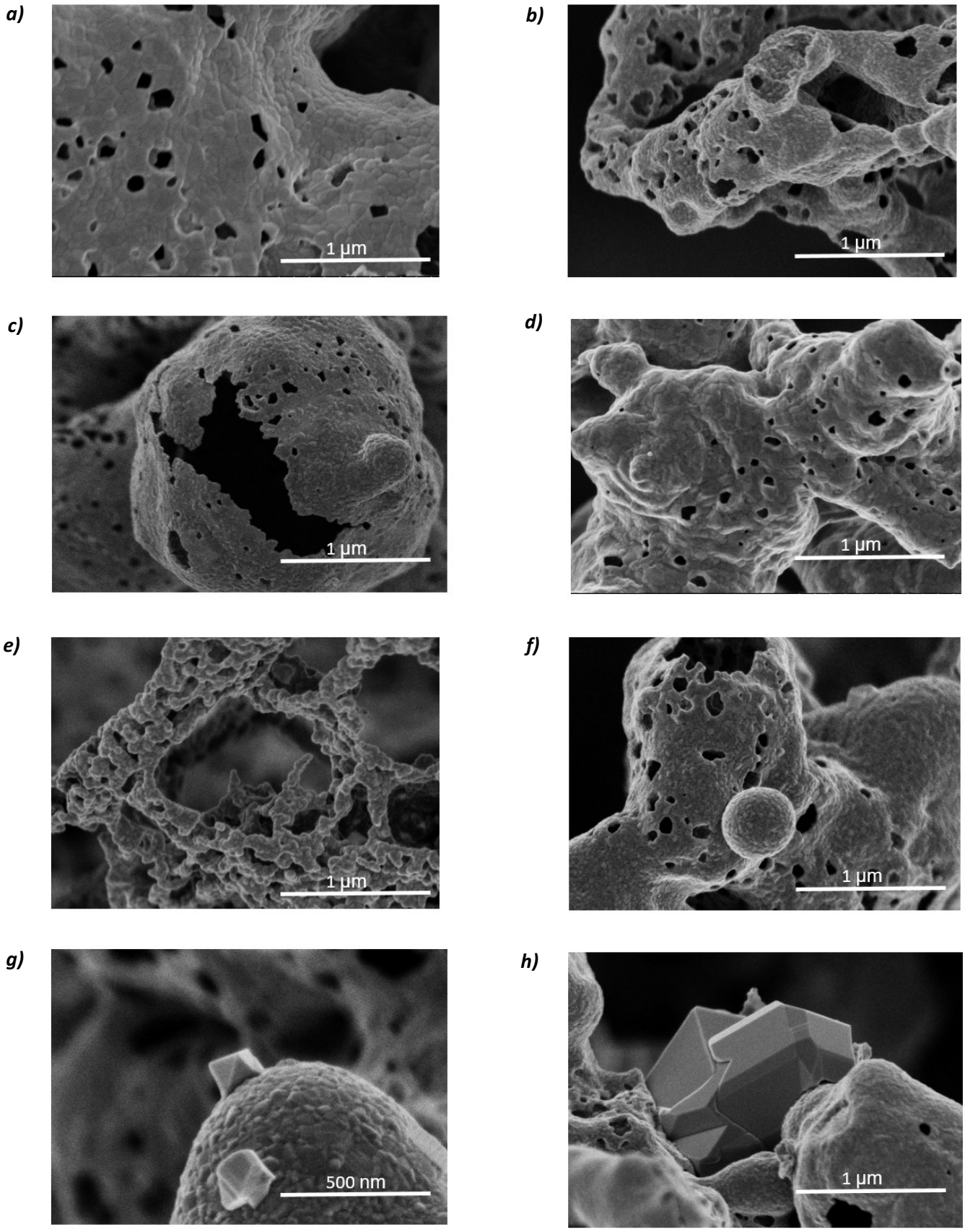

Figure 3.26. *SEM images at 1 µm of* ***a)*** *$PrMn_{0.7}Zn_{0.3}O_3$;* ***b)*** *$PrMn_{0.7}Ni_{.3}O_3$;* ***c)*** *$PrMn_{0.7}Co_{0.3}O_3$;* ***d)*** *$NdMn_{0.7}Fe_{0.3}O_3$ and* ***e)*** *$SmMn_{0.7}Cr_{0.3}O_3$;* ***f)*** *$PrMn_{0.95}Pd_{0.05}O_3$;* ***g)*** *$PrMn_{0.95}Pd_{0.05}O_3$ at 500 nm with visible PdO crystals and* ***h)*** *$PrMn_{0.7}Ru_{0.3}O_3$.*

In summary, seven catalysts presenting the general formula (Pr,Nd,Sm)$Mn_{0.7}B'_{0.3}O_3$ (with B´=Zn, Ni, Co, Fe, Cr, Pd and Ru) have been synthesized by self-ignition route and calcined at 800°C in order to expand the elemental folding fan from the (La,Pr)$Mn_{(1-x)}Cu_xO_3$ series for artificial intelligence analysis. As evidenced by Rietveld refinement of powder X-ray diffractograms (Figure 8SI), all the synthesis products are phase-pure perovskite-like samples, which present orthorhombic symmetry, with the exception of $PrMn_{0.7}Ru_{0.3}O_3$ and $PrMn_{0.95}Pd_{0.05}O_3$, which present around 3% of RuO_2 and 2.5% of PdO, respectively. Concerning the crystallographic distorsion, the standard deviations of the interatomic distances B-O (<B-O> sigma), which reflects the Jahn-Teller distortion, vary across the series in major extent with respect to <A-O> sigma (which reflects the cuboctahedral distortion) and this is ascribable to large folding fan of elemental variability for the B site in the series in comparison to the A one. Indeed, the only sample presenting an <A-O> sigma value which significantly differs from the others is $SmMn_{0.7}Cr_{0.3}O_3$ (#33622), since Sm is the smallest employed Lanthanoid. Additionally, $SmMn_{0.7}Cr_{0.3}O_3$ presents also one of the highest <B-O> sigma, due to the mismatch between the ionic radii of Mn and of Cr. The bulk and the surface stoichiometries determined by ICP-OES and laboratory XPS analyses have confirmed that the found elemental values are close to the nominal ones both for the bulk and the surface. However, some differences in the bulk´s elemental distribution are visible within the $AMn_{0.7}B'_{0.3}O_3$ series. Indeed, the Ni, Zn, Co and Fe-based samples present a B-site enrichment, $SmMn_{0.7}Cr_{0.3}O_3$ sample's B/A ratio is almost coincident with the nominal one, while Ru, Cu, Pd-based sample present a B-site depletion (Figure 3.23). This might indicate that Co, Zn, Ni, Fe and Cr render the stabilization of the (B+B')-site into the bulk of the perovskite structures more favorable with respect to the other employed B'-site metals, such as Cu, Pd and Ru. The elemental distribution between the bulk and the surface depends on the interplay between the B'-site nature and the A-site size. Finally, Scanning electron microscopy (SEM) imaging reveals that all the samples of the (Pr,Nd,Sm)$Mn_{0.7}B'_{0.3}O_3$ and $PrMn_{0.95}Pd_{0.05}O_3$ series present a macroporous network morphology composed by agglomerates of nanocrystallytes bridged-connected and presenting holes and that the variation of the A and B' is reflected into morphological changes.

4. Catalysis

4.1 CO oxidation

4.1.1 (La,Pr)$Mn_{(1-x)}Cu_xO_3$ series and $(La,Pr)_2CuO_4$ perovskite-related structures

CO oxidation over the two perovskite series has been performed measuring 3 cycles from 30-350°C (30-420 °C for (La,Pr)MnO_3 catalysts) with two different feeds, a more oxygen-rich feed (the typical exhaust feed) and a less-oxygen-rich feed, CO/O_2/inert = 1/20/79 and CO/O_2/inert = 1/2/97, respectively (Figure SI 10).

The results of the cycling experiments show that all the tested catalysts reach the total conversion to CO_2 within 350°C, with the exception of $LaMnO_3$ sample, which presents lower activity with 100% conversion at 371°C (Figure SI 10 c), indicating that the presence of Cu increases the catalytic activity for the La-based perovskites. Only the La_2CuO_4 catalyst is not able to reach 50% conversion although it has been tested from 30°C until 420°C in both feeds (Figure SI 10 i and l). For this latter catalyst the first cycle is significantly more active than the second and third one (which are coincident), indicating that the strong deactivation after the first cycle might be induced by crystallographic phase change during reaction condition. However, the Rietveld Refinement of the post-mortem CO oxidation La_2CuO_4 catalyst indicate that no phase change occurred during reaction condition (Figure SI 11). Additionally, all catalysts are generally more active in the first cycle compared to the second and the third one (except for CuO, Mn_2O_3 and $LaMnO_3$, Figure SI 10 a,b and c), being these latter ones completely identical in the most of the cases, suggesting that some surface carbonates, which are not completely decomposed during the pre-treatment and are still present during the first cycle, as evidenced by DRIFT Operando experiments (Figure 4.2), might be involved in the reaction process by sintering or surface changes which could induce the catalyst´s surface to undergo into a deactivation mechanism after the first cycle, presenting stable catalytic performance during the second and the third one.

Despite of what is generally reported in the literature for $LaMn_{(1-x)}Cu_xO_3$ series, where it is claimed that the B-site is the only element responsible for the catalytic performance , [200, 201] two different catalytic behaviours are visible for the La and Pr-based series when comparing their T_{10}, T_{50} and T_{90} from the second cycle. Indeed, according to a previous study,[308, 310] the La-based series shows a trend between the Cu surface fraction and the catalytic activity. The higher the Cu surface fraction, the higher the activity both for the oxygen-rich feed and the less-oxygen-rich one (Figure 4.1). Moreover, the T_{10}, T_{50} and T_{90} measured in the less-oxygen-rich feed are higher (less active) with respect to those measured in the oxygen-rich one for each sample of the La-based series (except the value of T_{90} for $LaMn_{0.8}Cu_{0.2}O_3$), indicating that a L-H mechanism may not be excluded. [341, 342]

The influence of the feed composition shows the same results also for the Pr-based series, being the catalysts measured in the oxygen-rich feed more active than those measured in the less-oxygen-rich one (with exception of $PrMn_{(1-x)}Cu_xO_3$ $0.25 \leq x \geq 0.35$). However, the T_{10}, T_{50} and T_{90} recorded for the Pr-based series do not show any particular trend depending on the surface metal composition (Figure 4.1).

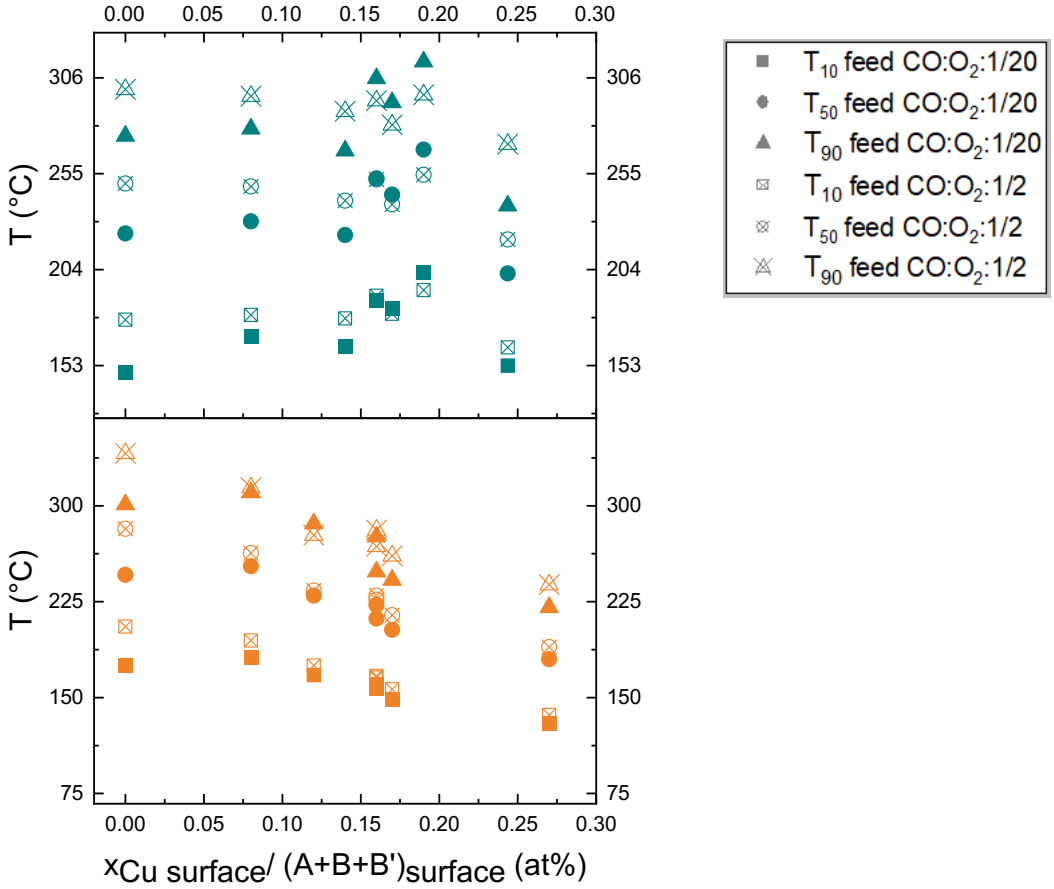

Figure 4.1. *Graphs showing the catalytic activity in CO oxidation over the Cu surface fraction. Color code: orange : La-based samples and green: Pr-based samples. Squares: T10, circles: T50 and triangles: T90. Filled symbols refer to the first feed, being CO/O₂/inert: 1/20/79 and half-filled symbols refer to the second feed, being CO/O₂/inert: 1/2/97.*

Finally, the rates of CO oxidation have been calculated from steady-state experiments performed at 130°C after one cycle to 420°C in feed CO/O_2/inert: 1/20/79 (Figure SI 12). From these experiments is clear that all the catalysts reach 100% conversion at a temperature which is lower than 420°C and present stable conversion at 130°C, being at this temperature in the kinetic regime before the heat and mass transport phenomena start to occur in the curve (below 10% CO conversion for all the catalysts of the series).

Previous operando DRIFT experiments in CO oxidation suggest the presence of monodentate carbonates since it is reported in the literature that CO adsorption bands over $LaMnO_3$ sample at room temperature appear around 1575, 1480 and 1410 cm^{-1}, [343] are decomposed after the first cycle at 420°C and therefore it could be assumed that the rates are derived from measurements performed in absence of carbonates (Figure 4.2).

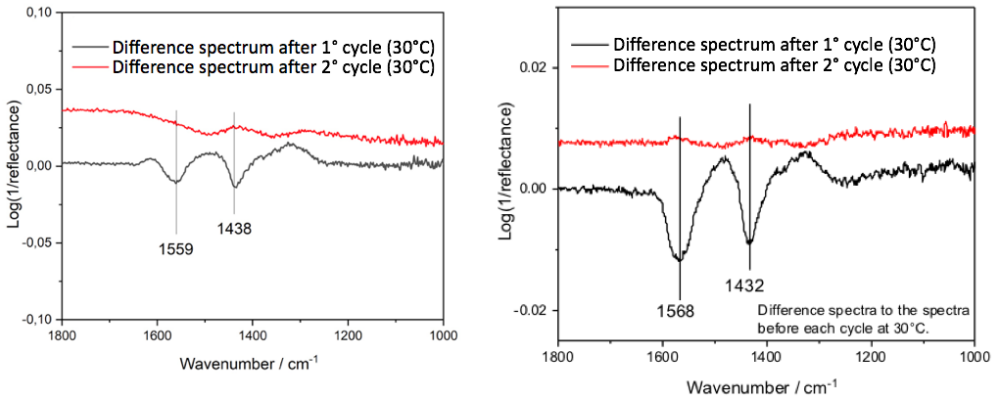

Figure 4.2. *Difference spectra between the one either after the first or the second cycle to the one before each cycle at RT for $PrMnO_3$ (left) and for $PrMn_{0.6}Cu_{0.4}O_3$ (right) from operando DRIFT experiments performed in CO oxidation with the first feed CO/O_2/inert : 1/20/79.*

The rate results shown in Figure 4.3 confirm the ones obtained by the cycling experiments for the La-based series: the lower the Mn surface fraction (which could also be read as: the higher the Cu surface fraction), the higher the rates, while the Pr-based one seems to show an opposite trend, with the exception of $PrMn_{0.6}Cu_{0.4}O_3$, probably due to the presence of segregated CuO on the surface, as revealed by STEM-EDX analysis (Figure 3.9 b in Section 3.2.3).

The CO oxidation results highlight the high complexity generated by the synergistic effect of a double B-site into the catalytic dynamics. [199, 309] Indeed, $PrMnO_3$ shows higher activity than $LaMnO_3$ in CO oxidation, but the catalysis picture changes drastically when Cu is inserted into the matrix, influencing the catalytic activity of (La,Pr)-based series in different extents, while it has been generally written that the B-site is the only responsible element for the catalytic performance in CO oxidation over perovskite-like catalysts. [200, 201, 310] This latter phenomenon is probably ascribable to the fact the structural modifications conferred by the different A-site [313] induce the generation of diverse active sites and different active oxygen species on the catalysts´ surface. [344-346] Moreover, it has been reported that the function of Mn is the oxygen activation and that of Cu is CO activation for $LaMn_{(1-x)}Cu_xO_3$ series. [310] In the case of Pr-based series, this functions´ combination could have been altered by the higher amount of surface Mn (Figure 3.7 b), generating

in this way a trend which may follow the oxygen activation step as the dominant one instead of the CO activation, like in the case of the La-based series. Finally, the two references $(La,Pr)_2CuO_4$ are almost inactive in CO oxidation, remarking how a different crystal structure-type from the ABO_3 perovskite one might change the catalytic scenario, irrespectively of the employed active sites (Figure 4.3). This latter result well correlates with those reported in the literature, where it is claimed that La_2CuO_4 presents a bad catalytic performance owed to its low activity for CO adsorption due to the inhibiting effect of the adsorbed CO_2, which is ascribable to the Cu ion. [310, 347]

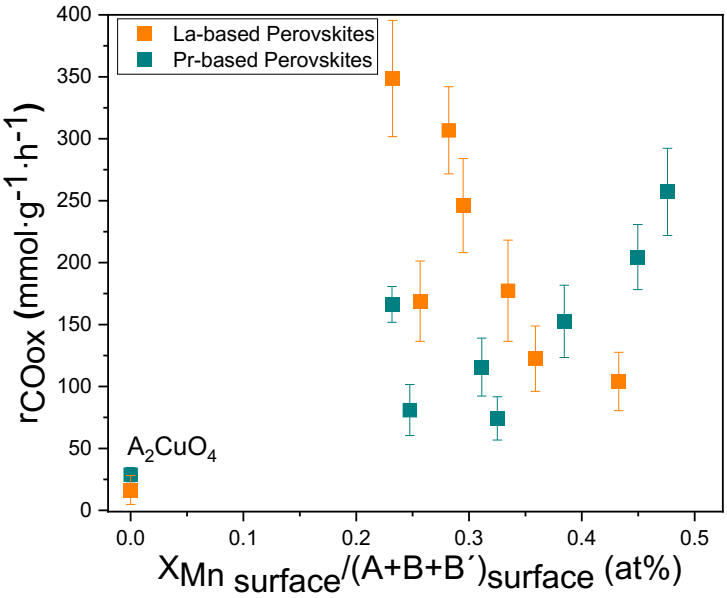

Figure 4.3. *Graphs showing the rates in CO oxidation over the Mn surface fraction. Orange: La-based samples, green: Pr-based samples.*

The conflicting correlations between the two series suggest that the surface B-metal composition is not a decisive factor for the catalytic performance, which is rather the result of synergistic relations between the multifactorial components of the dynamic system and therefore, a descriptor composed by a single parameter (for instance only by the metal surface´s composition) is definitely not sufficient to encode the catalytic performance of the studied system in CO oxidation.

4.1.2 $AMn_{0.7}B'_{0.3}O_3$ Perovskites

The same steady-state experiments reported for the $(La,Pr)Mn_{(1-x)}Cu_xO_3$ series to calculate the rate of CO consumption in absence of surface carbonates, have been performed over the $AMn_{0.7}B'_{0.3}O_3$ series. Indeed, the rates of CO oxidation have been calculated from steady-state experiments

performed at 130°C after one cycle to 420°C in feed CO/O_2/inert: 1/20/79 (Figure SI 13). Also all the catalysts of the (Pr,Nd)$Mn_{0.7}B'_{0.3}O_3$ series reach 100% conversion at a Temperature which is lower than 420°C and present stable conversion at 130°C, being at this temperature in the kinetic regime before the light off the curve starts (around 10% CO conversion for all the catalysts of the series).

The CO oxidation rates of these second series of catalysts emphasize the results already obtained for the (La,Pr)$Mn_{(1-x)}Cu_xO_3$ series on how the synergistic effect of a double B-site might chance the rules into the catalytic scenario. In detail, the highest CO consumption rate is presented by the Pd-based catalyst, as expected, [205, 348-351] followed then by Co and immediately afterwards by Fe, being Ni, Zn and Cu the less active ones. Generally, Fe-based perovskites present much lower activity in CO oxidation with respect to Ni- and Co-based ones for ABO_3 perovskite-structure. [350, 352, 353] While, as shown in Figure 4.4, the synergy established between Mn and Fe seems to be more beneficial to the catalytic performance in CO oxidation than those established between Mn and Ni, Zn or Cu. Also the role of the structural modifications induced by Nd smaller size with respect to Pr on the catalytic performance should not be neglected, because it could potentially generate different active sites on the surfaces, [344] although the lattice distortion of $NdMn_{0.7}Fe_{0.3}O_3$ is not higher than those of $PrMn_{0.7}B'_{0.3}O_3$ studied catalysts (Figure 3.22).

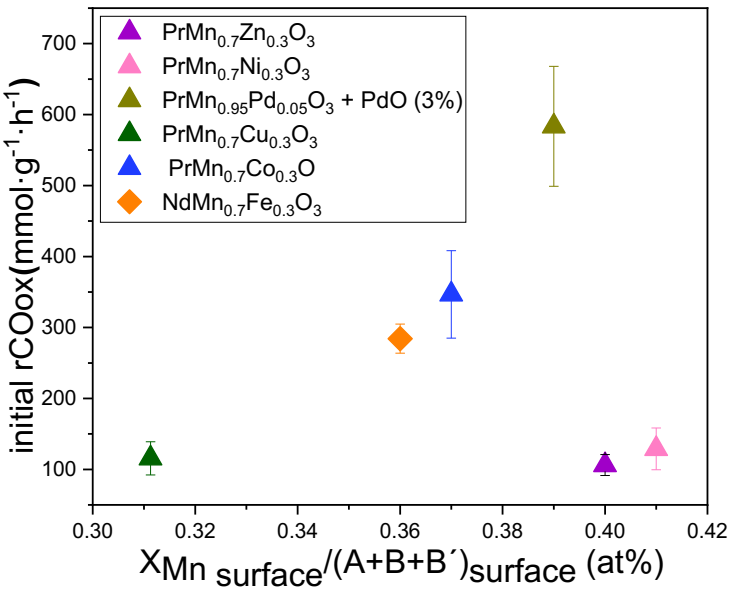

Figure 4.4. *Graphs showing the rates in CO oxidation over the Mn surface fraction. B' color-code: magenta: Zn; fuchsia: Ni; light blue: Co; green: Cu; orange: Fe and dull green: Pd.*

4.2 Propane oxidation

4.2.1 (La,Pr)$Mn_{(1-x)}Cu_xO_3$ series and $(La,Pr)_2CuO_4$ perovskite-related structures

The propane oxidation experiments have been performed from 260 until 300°C measuring in steady-state conditions at each 10 °C increment (Figure 4.5) and then applying four different contact times (W/F=0.18-1.2 $g \cdot s \cdot mL^{-1}$) in dry feed $C_3H_8/O_2/Ne/N_2$ = 5/10/2/83 (Figure 4.6) and three different contact times (W/F=0.3-1.2 $g \cdot s \cdot mL^{-1}$) in wet feed $C_3H_8/O_2/Ne/N_2/H_2O$ = 5/10/2/43/40 (Figure 4.7).

As evidenced from the temperature programmed reaction, the activity increases with temperature for La-based series, starting from 2% and achieving a maximum of 8%, for the most of the catalysts, with the exception of $(La,Pr)_2CuO_4$ and $LaMn_{0.75}Cu_{0.25}O_3$ (Figure 4.5).

Moreover, the higher the Mn content the higher the activity at each temperature for Pr-based perovskites (Figure 4.5), reflecting CO oxidation results (Figure 4.3). [354]

The only detectable products from propane oxidation are propene and CO_2, with the selectivity to propene presenting a minimum at 14% at 6% conversion for $PrMn_{0.8}Cu_{0.2}O_3$ and being able to reach about 45 % at 2.5% conversion in dry feed at W/F=0.18 $g \cdot s \cdot mL^{-1}$ for $LaMn_{0.75}Cu_{0.25}O_3$. Additionally, the selectivity to propene in dry feed for all the catalysts is higher with respect of those for the two reference materials, Mn_2O_3 and CuO, showing how a defective perovskite or perovskite-related structures, [201, 346] like in the case of A_2CuO_4 catalysts, and/or the synergy of a double-B site in perovskite-like structures may exert a beneficial effect on the catalytic performance (Figure 4.6). [199, 309]

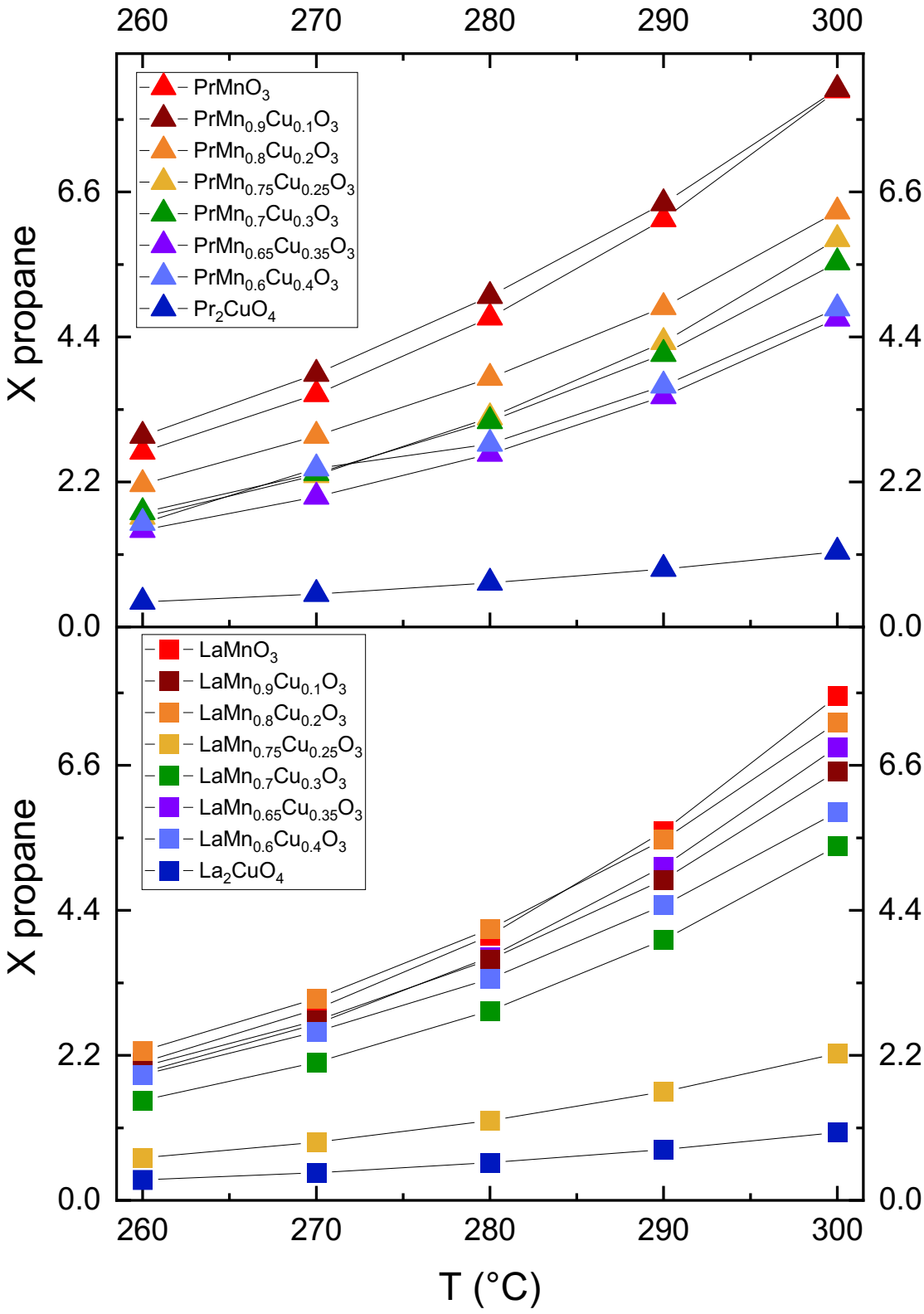

Figure 4.5. *Conversion of propane as a function of the temperature for all catalyst in dry feed C_3H_8/O_2/inert: 5/10/85 for the $AMn_{(1-x)}Cu_xO_3$ series.. Color-code: red: x=0; brawn: x=0.1; orange: x=0.2; yellow: x=0.25; green: x=0.3; purple: x=0.35; light blue: x=0.4 and blue: A_2CuO_4. Squares: La-based samples and triangles: Pr-based ones.*

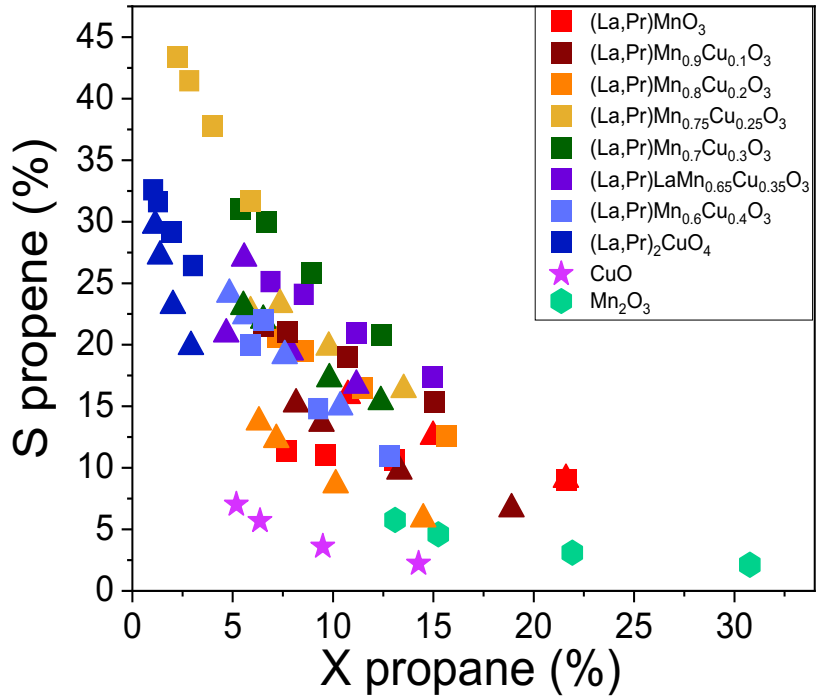

Figure 4.6. *Contact time variation (W/F = 0.18-1.2 g·s·mL^{-1}) for all catalysts at 300°C in dry feed. Color-code: red: x=0; brawn: x=0.1; orange: x=0.2; yellow: x=0.25; green: x=0.3; purple: x=0.35; light blue: x=0.4; blue: A2CuO$_4$; pink: CuO and light green: Mn$_2$O$_3$. Squares: La-based samples and triangles : Pr-based samples.*

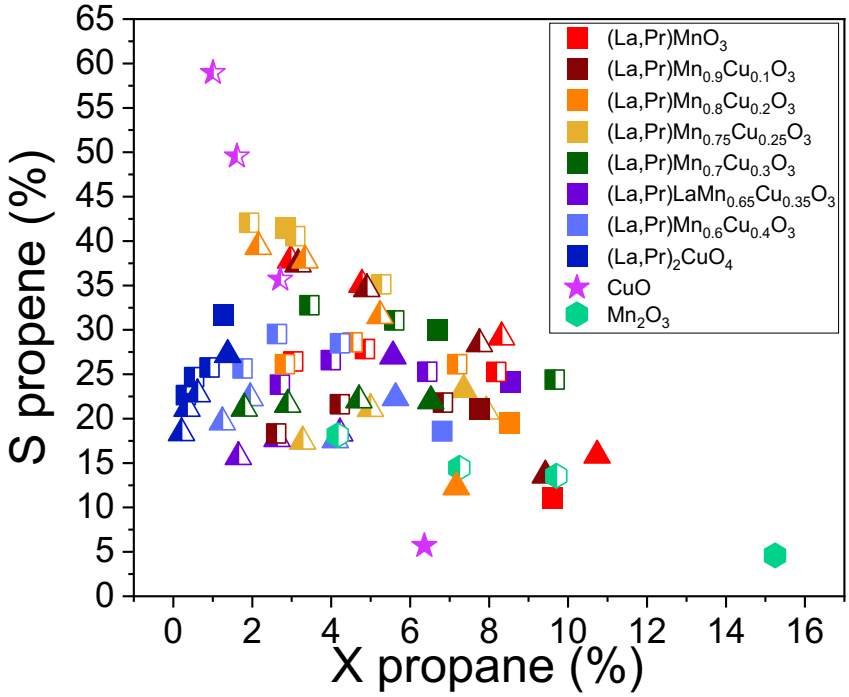

Figure 4.7. *Contact time variation (W/F = 0.3-1.2 g·s·mL^{-1}) for all catalysts at 300°C in wet feed (filled datapoints: dry feed, half-filled datapoints: wet feed). Color-code: red: x=0; brawn: x=0.1; orange: x=0.2; yellow: x=0.25; green: x=0.3; purple: x=0.35; light blue: x=0.4; blue: A$_2$CuO$_4$; pink: CuO and light green: Mn$_2$O$_3$. Squares: La-based samples and triangles : Pr-based samples.*

DRIFT experiments were performed to check the presence of carbonates during operation conditions. These experiments have shown that monodentate carbonates [343] disappear after the pre-treatment, while other product intermediates are generated during reaction conditions (Figure 4.8).

The initial rate of propane consumption or propene and CO_2 formation were employed to compare the catalysts (see Section 2 for initial rate calculation).

Not only in the case of CO oxidation, but also for propane oxidation the results seem to be in contrast with the reported literature, [200] highlighting how the perovskite-like system may response differently under catalytic conditions depending on the A-site. Indeed, from the results obtained in dry feed, it could be evidenced that only Pr-based samples show a trend with the Mn surface fraction, highlighting once again how CO oxidation might work as a probe reaction for propane oxidation (Figure 4.3). [354] Both the rates of propane consumption and CO_2 formation show a positive trend with the Mn surface content over the Pr-based catalysts (Figure 4.9 a and c), while the selectivity to propene is not affected by the surface Mn concentration in dry feed (Figure 4.9 b). On the other hand, no trend is observed for the La-based catalysts. The drawn conclusion based on the found experimental data for propane oxidation is that the reactivity of each target catalytic property seems to be controlled by the interacted interplay of different parameters and a descriptor based on a single physicochemical property is not sufficient to fully endcode the catalytic performance. Surprisingly and in contrast with the CO oxidation results, the Ruddlesden-Popper phase perovskites (A_2CuO_4), which show very low initial propane consumption and propene formation rate, present high CO_2 initial formation rate, being Pr_2CuO_4 the catalyst with the highest CO_2 initial formation rate among all the tested materials (Figure 4.9 c). This latter result might support the hypothesis proposed above (see *Section 4.1.1*), where it is suggested that the very low activity in CO oxidation for A_2CuO_4 perovskites is due to the inhibiting effect performed by the high amount of adsorbed CO_2. [310]

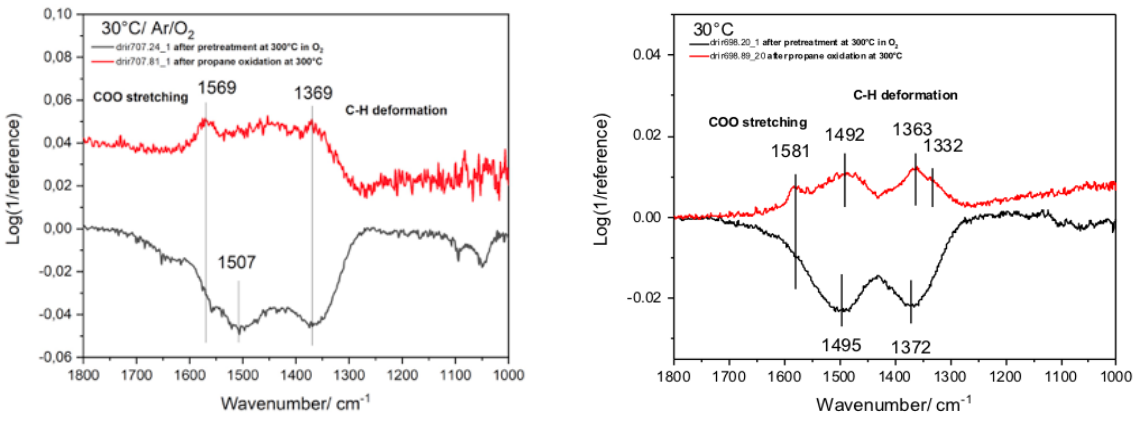

Figure 4.8. *Difference spectra to the one before each condition at room temperature for $PrMnO_3$ (left) and for $PrMn_{0.6}Cu_{0.4}O_3$ (right) from operando DRIFT experiments performed in propane oxidation with the feed C_3H_8/O_2/inert: 5/10/85.*

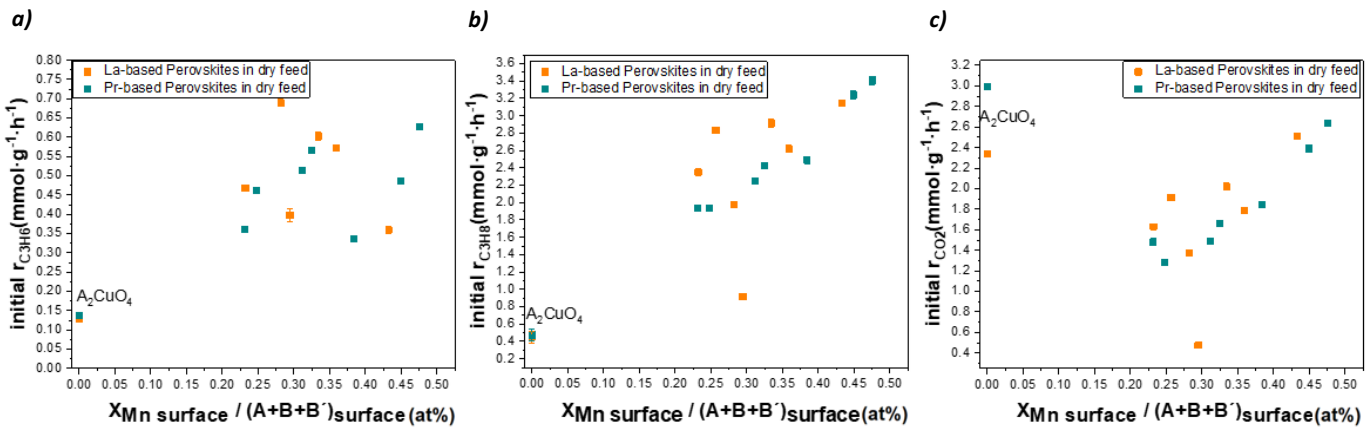

Figure 4.9. a) *Initial rate of propene formation,* ***b)*** *initial rates of propane consumption and* ***c)*** *initial rates of CO_2 formation over the Mn surface fraction in feed $C_3H_8/O_2/Ne/N_2$: 5/10/2/83. Orange: La-based samples, green: Pr-based samples.*

The catalytic scenario shows some interesting changes when steam is co-dosed into the feed (Figure 4.10). In this latter case, the conversion decreases and the selectivity increases almost for all the catalysts, in particular for those with higher Mn content (Fig. 4.10), [275, 355] although the reference material CuO is the most selective one. The catalytic data for dry and wet feed experiments are summarized in Table 4.1.

Table 4.1. Table with listed the activation energies calculated from the temperature programmed reaction performed from 260 until 300°C in dry feed at W/F=0.18-1.2 g·s·mL^{-1}, the products´ratio in dry feed at 300°C at W/F=0.18-1.2 g·s·mL^{-1} and the products´ratio in wet feed at 300°C at W/F=0.3-1.2 g·s·mL^{-1}.

x_{Cu}	*A-site*	*Activation Energy in dry feed (kJ mol^{-1})*	*Initial r_{C3H6}/initial r_{CO2} in dry feed*	*Initial r_{C3H6}/initial r_{CO2} in wet feed*
0	La	80.6	0.143	0.379
	Pr	71.2	0.237	0.665
0.1	La	73.9	0.320	0.227
	Pr	65.7	0.203	0.637
0.2	La	73.8	0.299	0.371
	Pr	67.4	0.183	0.694
0.25	La	78.8	0.837	0.773
	Pr	80.0	0.341	0.217
0.3	La	80.4	0.504	0.540
	Pr	73.3	0.345	0.266
0.35	La	80.4	0.373	0.325
	Pr	73.3	0.360	0.185
0.4	La	71.6	0.287	0.501
	Pr	67.5	0.244	0.242
1	La	77.0	0.055	0.034
	Pr	69.6	0.046	0.026

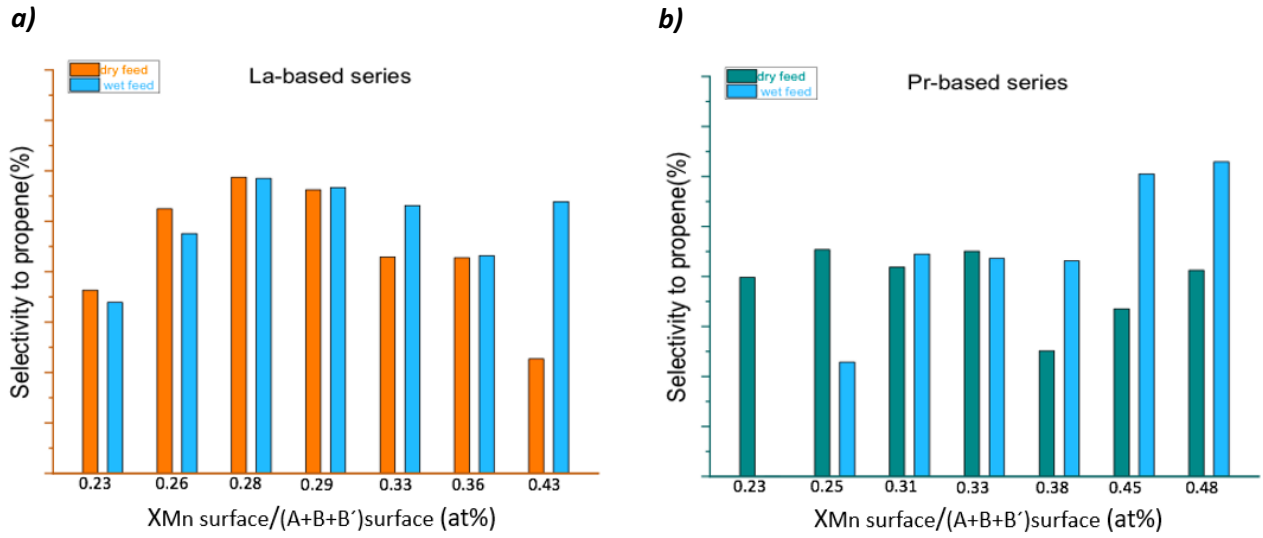

Figure 4.10. a) *Interpolated selectivity to propene at 7% conversion over the Mn surface fraction for La-based catalysts in dry feed (orange) and in wet feed (blue)* ***b)*** *Interpolated selectivity to propene at 7% conversion for Pr-based catalysts in dry feed (orange) and in wet feed (blue).*

Even more surprising, the addition of steam generates a positive catalytic trend between the Mn surface fraction and the selectivity only for Pr-based catalysts (Figure 4.11 b). This is likely due to the blockage of some active sites, avoiding so the total combustion to CO_2. [9] While, no trends are present between the Mn surface fraction and the initial rates of C_3H_8 consumption or CO_2 formation in wet feed (Figure 4.11 a and c).

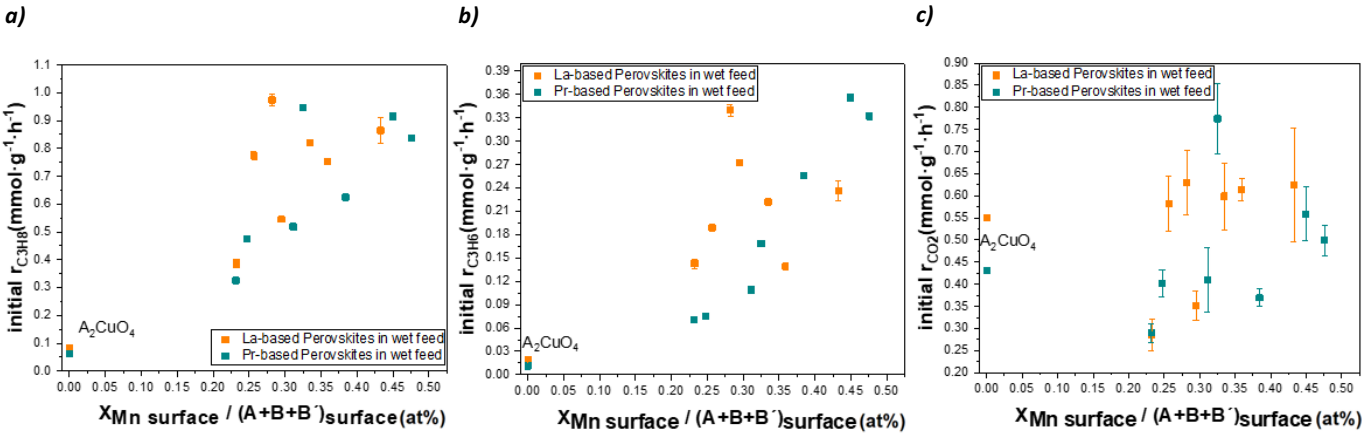

Figure 4.11. a) *Initial rate of propane consumption,* ***b)*** *initial rates of propene formation and* ***c)*** *initial rates of CO_2 formation over the Mn surface fraction in feed $C_3H_8/O_2/Ne/N_2/H_2O$: 5/10/2/43/40. Orange: La-based samples, green: Pr-based samples.*

4.2.1.1 NAP-XPS measurements in wet feed for Pr-based catalysts

Since the addition of steam generates a positive catalytic trend between the Mn surface fraction and the selectivity only for Pr-based catalysts (Figure 4.11 b), NAP-XPS measurements in wet feed have been performed over three Pr-based catalysts with different Mn content, such as

$PrMn_{0.9}Cu_{0.1}O_3$, $PrMn_{0.75}Cu_{0.25}O_3$ and $PrMn_{0.6}Cu_{0.4}O_3$. Three pressed pellets of 15 mg were tested in propane oxidation into the NAP-XPS cell under vacuum at room temperature for 1 and half hour and then heated in $C_3H_8/O_2/N_2/H_2O$=0/20/80/0 mixture to 300°C under the total gas pressure of 2500 Pa, then the reaction feed was switched to $C_3H_8/O_2/N_2/H_2O$=5/10/85/0 and kept for 1 and half hour and finally the feed was switched to wet feed $C_3H_8/O_2/N_2/H_2O$=5/10/45/40 always for one and half hour. The catalytic performance measured in the NAP-XPS cell is not directly comparable with that measured in the plug flow reactor for the three Pr-based catalysts. Indeed, the $PrMn_{0.75}Cu_{0.25}O_3$ catalyst, which shows the highest selectivity among the other catalysts in dry feed in the plug flow reactor measurements, is the less selective one in in the NAP-XPS cell. While, $PrMn_{0.6}Cu_{0.4}O_3$ shows the highest selectivity among the three tested catalysts in wet feed in the NAP-XPS cell, being this latter one the less selective one in the plug flow reactor experiments (Figure 4.12). The differences detected between the two measurements are probably due mostly to the pressure gap and different measuring conditions, such as the contact time of the plug flow reactor experiments, which cannot be reproduced in the NAP-XPS cell.

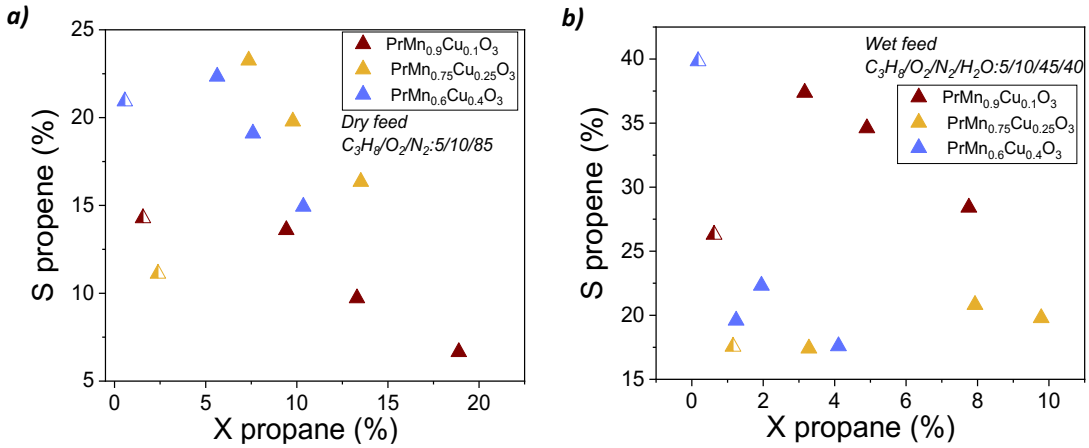

Figure 4.12. *Catalytic performance measured at 300°C* ***a)*** *in dry feed and* ***b)*** *in wet feed. Color-code: brown: $PrMn_{0.9}Cu_{0.1}O_3$; yellow: $PrMn_{0.75}Cu_{0.25}O_3$ and light blue: $PrMn_{0.6}Cu_{0.4}O_3$. Filled symbols: plug flow reactor measurements at ambient pressure with W/F=0.18-1.2 g·s·mL^{-1}. Half-filled symbols: NAP-XPS cell measurements at 0.25 mbar*

The surface elemental composition determined under working conditions switching from dry to wet feed shows an increase of Pr surface fraction for all samples, which is accompanied by a slight decrease of Mn surface fraction, while Cu amount remains mostly unvaried (Figure 4.13). Moreover, despite of what is reported in the literature for Cu-free catalysts, where the increase in selectivity in (La,Sm)MnO_3 perovskites has been attributed to the decrease of Mn oxidation state in wet feed, [275] the Mn3s splitting and oxidation states estimated from Mn3s spectra (Figure 4.14) shows an increase in Mn oxidation state in wet feed for all the catalysts, as follows : $PrM_{0.9}Cu_{0.1}O_3$ > $PrM_{0.75}Cu_{0.25}O_3$ > $PrM_{0.6}Cu_{0.4}O_3$ (Figure 4.15 and Table 4.2)**.** While, the Mn L-edges do not show any difference between dry and wet feed for all the samples (Figure 4.16). Changes in the local

structure in presence of steam for perovskite-like materials have also not been detected by other works, where it has been hypothesized that the high porosity of the studied materials ,might allow water to penetrate into the pores without affecting the surrounding electronic structure. [356] By fingerprint, the Mn oxidation state as evaluated by NEXAFS shows an opposite order for the three samples with respect to that evaluated from Mn3s splitting, being this discrepancy attributable to the fact that NEXAFS probes the 3d orbital population and splitting, while XPS probes the surface at lower depth and the oxidation state of Mn can differ between the sub-surface and the surface region.

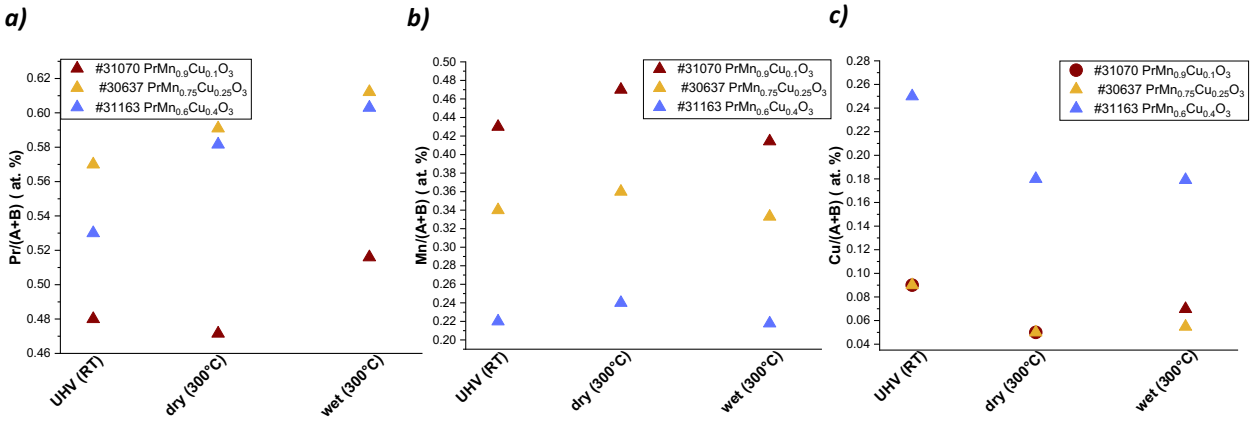

Figure 4.13. *Elemental composition under UHV (RT), dry feed ($C_3H_8/O_2/N_2$=5/10/85) at 300°C and wet feed ($C_3H_8/O_2/N_2/H_2O$ =5/10/45/40) for* ***a)*** *Pr;* ***b)*** *Mn and* ***c)*** *Cu. Color-code: brown: $PrMn_{0.9}Cu_{0.1}O_3$; yellow: $PrMn_{0.75}Cu_{0.25}O_3$ and light blue: $PrMn_{0.6}Cu_{0.4}O_3$.*

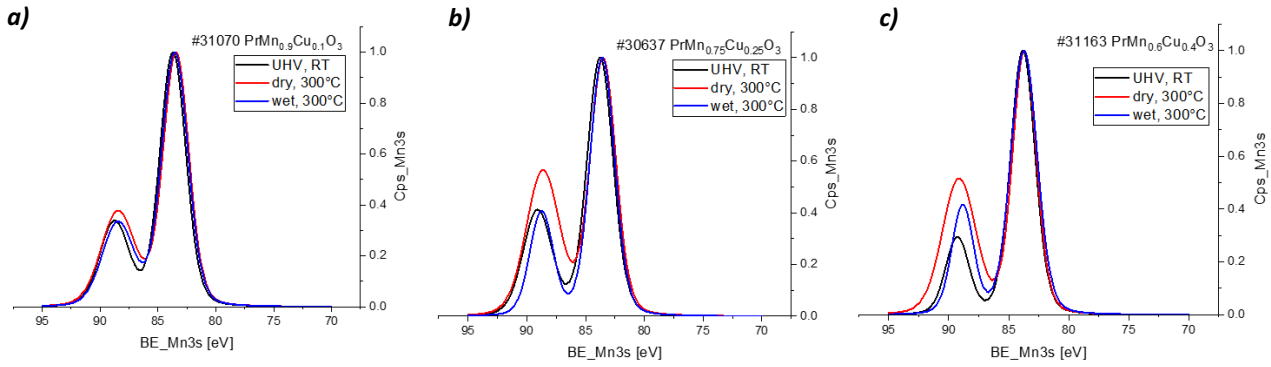

Figure 4.14. *Mn3s normalized spectra for* ***a)*** *$PrMn_{0.9}Cu_{0.1}O_3$;* ***b)*** *$PrMn_{0.75}Cu_{0.25}O_3$ and* ***c)*** *$PrMn_{0.6}Cu_{0.4}O_3$. Color-code: black: UHV (RT); red: dry feed ($C_3H_8/O_2/N_2$=5/10/85) at 300°C and blue: wet feed (($C_3H_8/O_2/N_2/H_2O$ =5/10/45/40).*

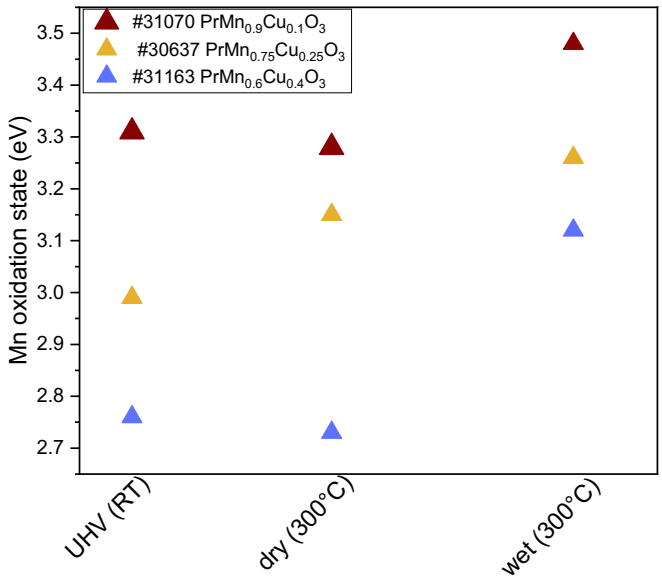

Figure 4.15. *Mn oxidation state as evaluated from Mn3s splitting for UHV (RT), dry feed ($C_3H_8/O_2/N_2$=5/10/85) at 300°C and wet feed ($C_3H_8/O_2/N_2/H_2O$ =5/10/45/40). Color-code: brown: $PrMn_{0.9}Cu_{0.1}O_3$; yellow: $PrMn_{0.75}Cu_{0.25}O_3$ and light blue: $PrMn_{0.6}Cu_{0.4}O_3$.*

Table 4.2. Exchange splitting and derived Mn ox state from Mn3s spectra for $PrMn_{0.9}Cu_{0.1}O_3$; $PrMn_{0.75}Cu_{0.25}O_3$ and $PrMn_{0.6}Cu_{0.4}O_3$

Sample		UHV (RT)	Dry feed (300°C)	Wet feed (300°C)
#31070 $PrMn_{0.9}Cu_{0.1}O_3$	Exchange splitting (eV)	5,07	5,09	4,92
	Averaged Mn3s ox state	3,31	3,28	3,48
#30637 $PrMn_{0.75}Cu_{0.25}O_3$	Exchange splitting (eV)	5,35	5,21	5,11
	Averaged Mn3s ox state	2,99	3,15	3,26
#31163 $PrMn_{0.6}Cu_{0.4}O_3$	Exchange splitting (eV)	5,55	5,58	5,23
	Averaged Mn3s ox state	2,76	2,73	3,12

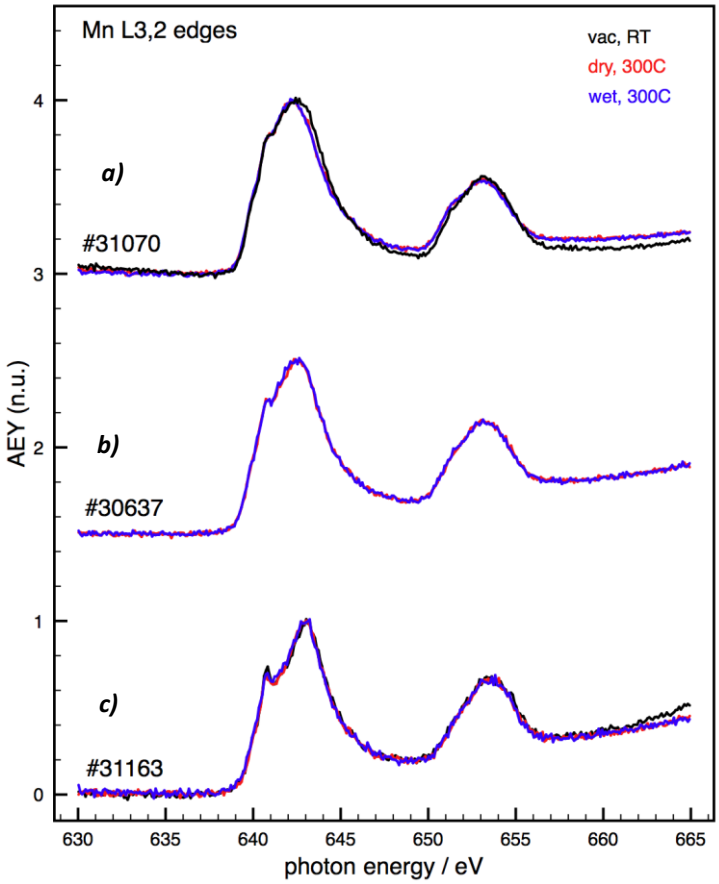

Figure 4.16. *Mn L-edges for* ***a)*** *$PrMn_{0.9}Cu_{0.1}O_3$;* ***b)*** *$PrMn_{0.75}Cu_{0.25}O_3$ and* ***c)*** *$PrMn_{0.6}Cu_{0.4}O_3$. Color-code: black: UHV (RT); red: dry feed ($C_3H_8/O_2/N_2$=5/10/85) at 300°C and blue: wet feed (($C_3H_8/O_2/N_2/H_2O$ =5/10/45/40).*

The O1s fit has revealed that the O1s species which change from dry to wet feed are only O lattice, O defects and OH, while O surface, O carbonates and O H_2O seem to be unvaried. The O1s OH species decrease, accompanied by an increase of O defect species and by a decrease of O lattice species (Figure 4.18). However, these three O1s components change in different extents for the three Pr-based tested catalysts in wet feed. Indeed, the O1s lattice to O1s defect ratio is higher for $PrM_{0.9}Cu_{0.1}O_3$, followed by $PrM_{0.75}Cu_{0.25}O_3$ and finally $PrM_{0.6}Cu_{0.4}O_3$, which presents the highest amount of defects species (Figure 4.18).

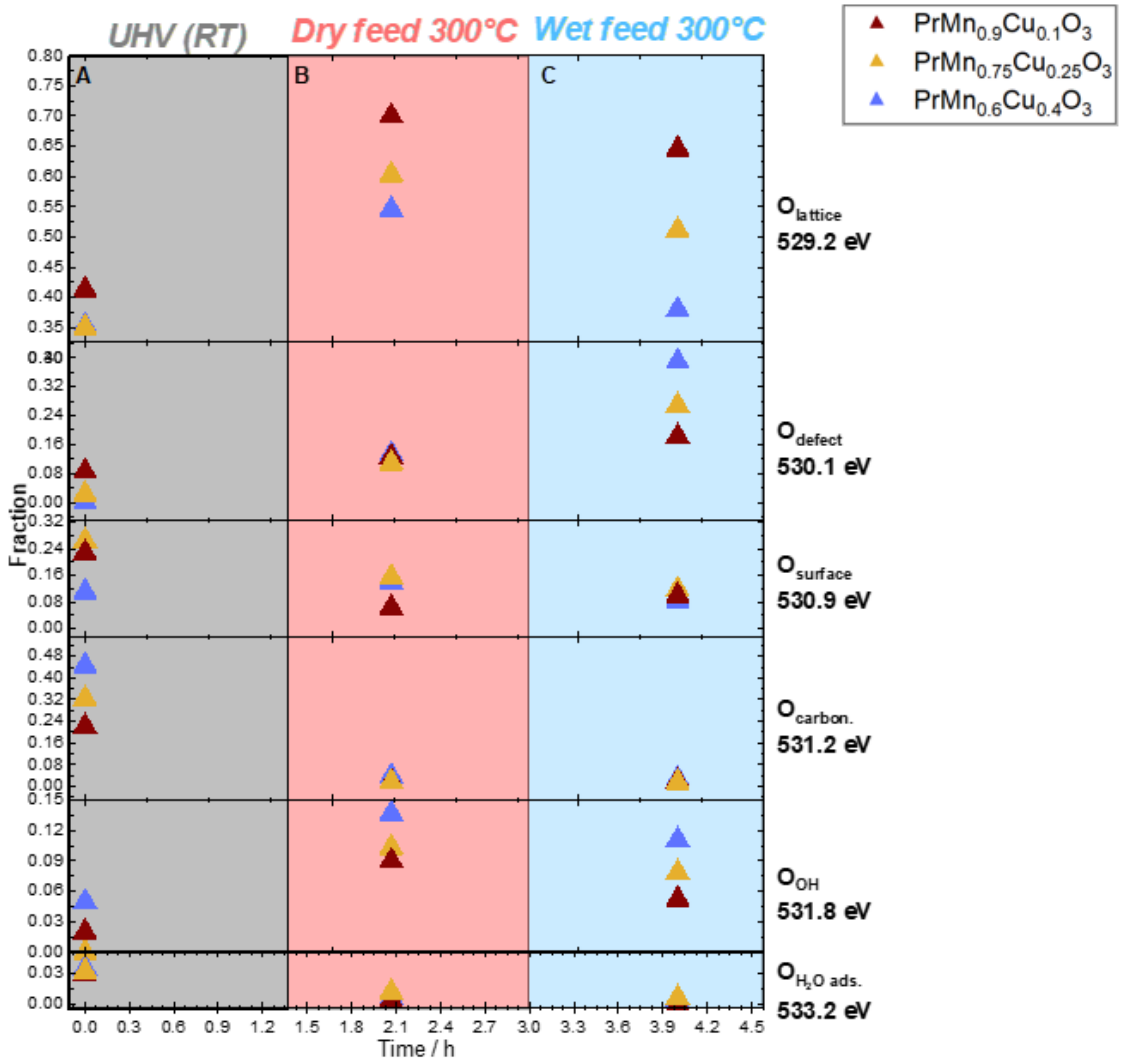

Figure 4.17. *Fraction of oxygen species obtained from O1s core level fitting of the NAP-XPS of $PrMn_{0.9}Cu_{0.1}O_3$ (brown datapoint), $PrMn_{0.75}Cu_{0.25}O_3$ (yellow datapoint) and $PrMn_{0.6}Cu_{0.4}O_3$ (light blue datapoint). The measurements were performed in UHV at RT (grey color), in dry feed $C_3H_8/O_2/N_2$= 5/10/85 at 300°C (pink color) and in wet feed $C_3H_8/O_2/N_2/H_2O$= 5/10/45/40*

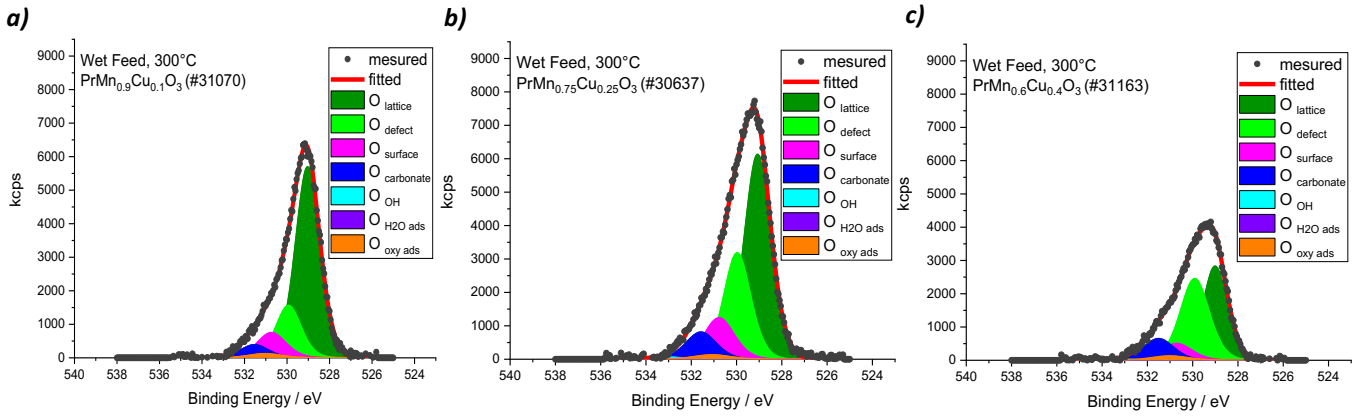

Figure 4.18. *O1s species distribution in wet feed for* ***a)*** *$PrMn_{0.9}Cu_{0.1}O_3$;* ***b)*** *$PrMn_{0.75}Cu_{0.25}O_3$ and* ***c)*** *$PrMn_{0.6}Cu_{0.4}O_3$.*

In particular, the enhancement in wet feed for O1s lattice species increases linearly with the increasing of Mn surface fraction measured in near working conditions, while the O1s defect and OH species show the opposite trend over the Mn surface fraction (Figure 4.19), in agreement with the observation that Cu loading introduces defects into the perovskite´s structure. [201] These latter results highlight the complexity of the system under near working conditions, showing how an increase of lattice species correlates positively with the Mn surface fraction and consequently with the selectivity trend measured in the plug flow reactor, while the O1s defects species, which are equivalent for all the three catalysts in dry feed in the NAP-XPS cell (Figure 4.17), change to different extent in wet feed, rendering the catalysts too active and thus responsible for the total combustion path. [9] Moreover, the defect concentration might exert an influence on the formal oxidation state of Mn. The Mn oxidation state from L-edges (Figure 4.16) as suggested by fingerprint, presents the following order: $PrM_{0.6}Cu_{0.4}O_3$ > $PrM_{0.75}Cu_{0.25}O_3$ > $PrM_{0.9}Cu_{0.1}O_3$, which is exactly the same order for O defect (Figure 4.17 and 4.19), correlating the increase in selectivity in wet feed with Mn ox state reduction. [275, 357]

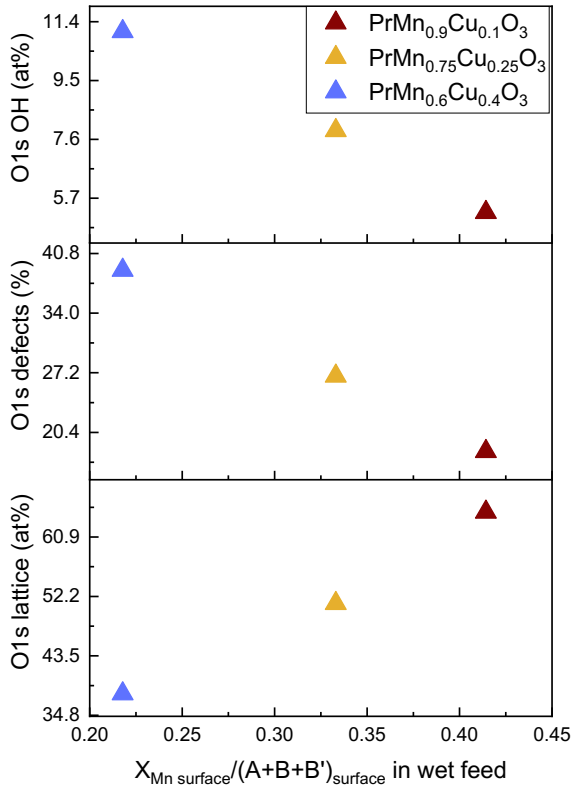

Figure 4.19. *O1s fraction of lattice oxygen, defect oxygen and OH oxygen species over the Mn surface content in wet feed from the NAP-XPS measurements of $PrMn_{0.9}Cu_{0.1}O_3$ (brown), $PrMn_{0.75}Cu_{0.25}O_3$ (yellow) and $PrMn_{0.6}Cu_{0.4}O_3$ (light blue).*

4.2.1.2 Operando Microwave Cavity Perturbation Technique (MCPT) in propane oxidation. From Reference [290]

Since the most of the perovskite crystal structures of the (La,Pr)$Mn_{(1-x)}Cu_xO_3$ series present lattice distortion (Figure 3.2) which affects bulk's and surface's electronic structure by influencing the charge-carrier dynamics of the bulk [358] , Operando Microwave Cavity Perturbation Technique experiments have been performed over the whole (La,Pr)$Mn_{(1-x)}Cu_xO_3$ series in propane oxidation. Operando MCPT measurement protocol has reproduced that of propane oxidation measurements in the plug flow reactor, where the catalysts have been pre-treated at 300°C (heating rate 5 K/min) for 45 min in lean air (O_2/N_2=10/90), where the reference conductivity has been measured (σr), then, in MCPT performed experiments the samples have been cooled down until 260°C and the reaction feed has been switch to dry feed ($C_3H_8/O_2/N_2$=5/10/85) and a temperature programmed reaction has been performed until 300°C in dry feed measuring each 10°C increment. Finally, after the variation of 3 different contact time at 300°C, the feed has been switched from dry feed to lean air (O_2/N_2=10/90) at 300°C in order to measure the change in conductivity ($\Delta\sigma(\phi)/\sigma r$).

For all the measured samples, the conductivity normalized on the reference conductivity rises up with the increasing of temperature, highlighting the semiconducting behavior of the tested catalysts (Figure 4.20). The most of the catalysts behave as n-type semiconductors under testing condition, presenting a higher conductivity at 300°C in reducing atmosphere (such as the propane feed) with respect to the conductivity measured in lean air at 300°C (always 1) and then reporting a decrease in conductivity when switched to lean air after dry feed. While, (La,Pr)$Mn_{0.6}Cu_{0.4}O_3$ and $PrMn_{0.75}Cu_{0.25}O_3$ present p-type behaviour, being their conductivity at 300°C in reducing atmosphere lower with respect to the reference one measured in lean air and reporting an increase in the conductivity (positive $\Delta\Omega$) while switching from dry feed to lean air. The p-type behavior is probably ascribable to a conduction mechanism driven by the hopping of positive holes into the perovskite´s d-band, where the charge carriers are localized on Mn^{4+}.[271] Indeed, the increase of Cu^{2+} content is correlated with the increase of Mn^{4+} fraction in order to maintain the charge neutrality into the perovskite lattice, presenting the two catalysts with highest Cu loading ((La,Pr)$Mn_{0.6}Cu_{0.4}O_3$) the highest amount of Mn^{4+} fraction. While, (La,Pr)MnO_3 present n-type behavior, although $LnMO_3$ perovskites are generally reported to be p-type semiconductors in the literature since the Mn^{4+} fraction, which is the believed to act a charge carrier center for hopping-polaron model, might also be formed as a result of native defects. [271, 272] In the specific case of the studied catalysts, there might be not a sufficient amount of Mn^{4+} fraction to present p-type conduction behavior, except for the cases with the highest Cu loading ($AMn_{0.6}Cu_{0.4}O_3$), where Mn^{4+} fraction amount increases in order to maintain the charge neutrality. Finally, there seems not to be

any direct correlation either between the absolute conductivity measured at 300°C in dry feed (σ) or the activation energy of the conductivity (Ea (σ)) and the Cu content (Table 4.3).

Table 4.3. Table with listed the absolute conductivity measured at 300°C in dry feed C3H8/O2/N2=5/10/85, the conductivity change as a function of the equivalence ration and the activation energies of the conductivity calculated from the temperature programmed reaction performed from 260 until 300°C in dry feed.

x_{Cu}	*A-site*	*σ (S/m) at 300°C in feed ($C_3/O_2/N_2$=5/10/85)*	*Δσ(ϕ) (S/m)*	*Ea (σ) (KJ/mol)*
0	La	30.184	0.038 / n-type	5.79
	Pr	2.306	0.017 / n-type	11.87
0.1	La	4.755	0.066 / n-type	13.60
	Pr	10.937	0.014 / n-type	2.00
0.2	La	2.234	0.010 / n-type	9.71
	Pr	3.018	0.013 / n-type	8.10
0.25	La	2.104	0.043 / n-type	18.30
	Pr	1.514	0.024 / n-type	8.38
0.3	La	2.524	0.057 / n-type	16.30
	Pr	4.158	0.014 / n-type	5.02
0.35	La	1.285	0.023 / n-type	13.70
	Pr	1.156	0.020 / n-type	2.69
0.4	La	6.090	-0150 / p-type	10.02
	Pr	0.891	-0.065 / p-type	6.47

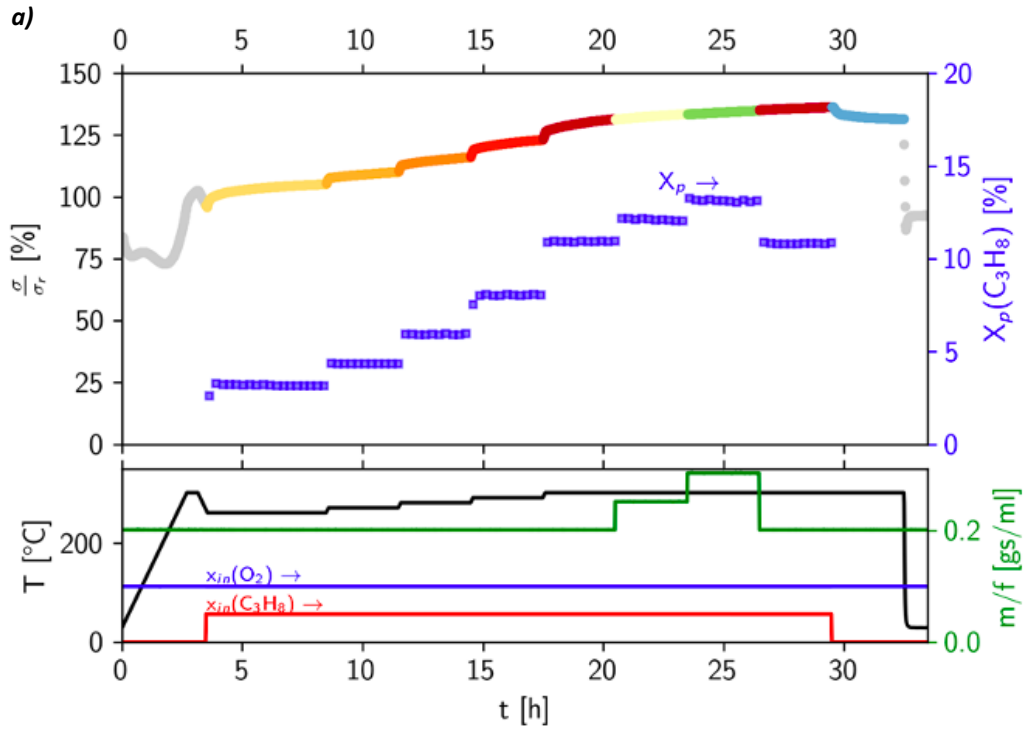

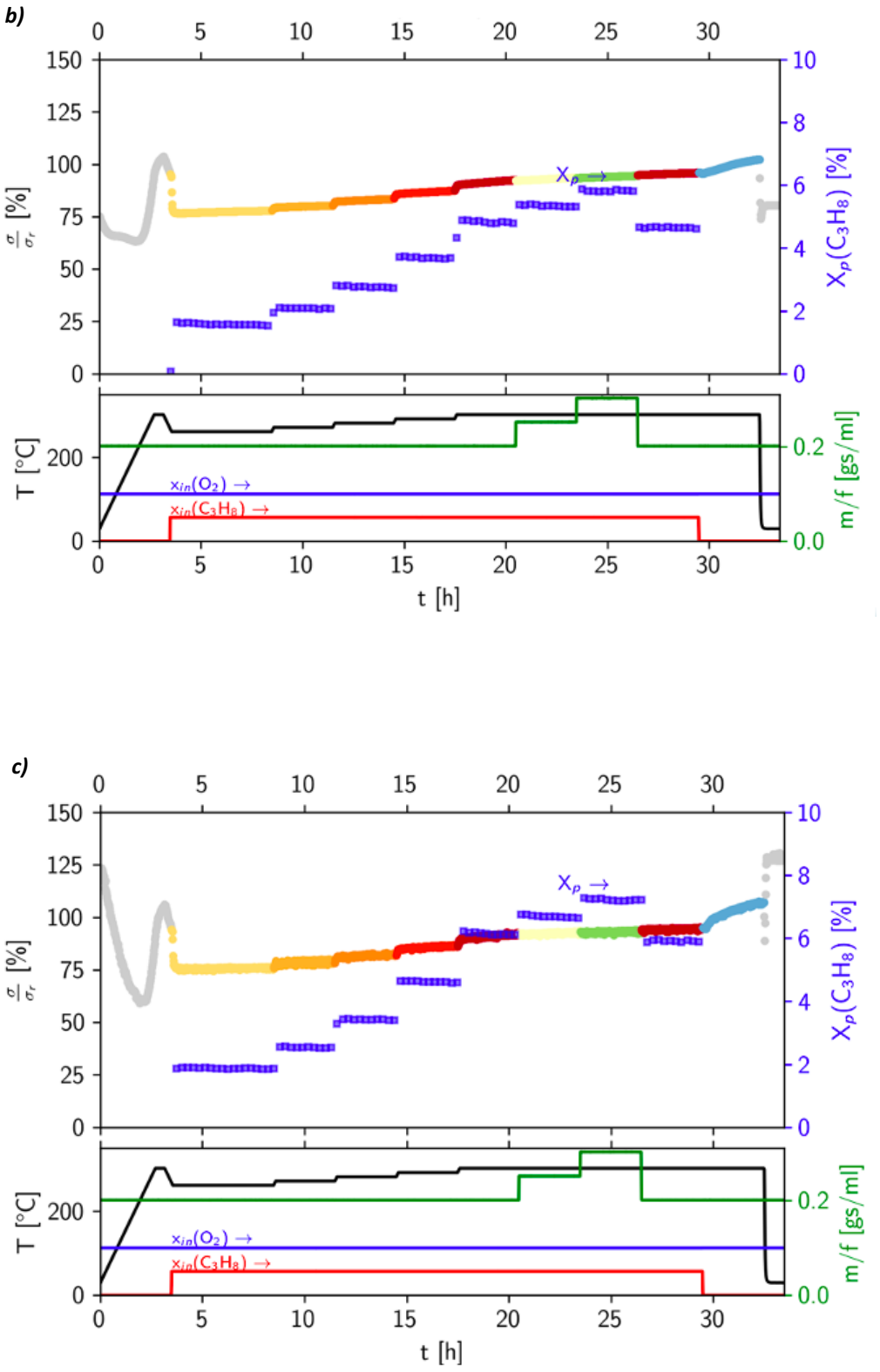

Figure 4.20. *MCPT Operando experiments in propane oxidation for* ***a)*** *$LaMn_{0.9}Cu_{0.1}O_3$ (n-type behaviour);* ***b)*** *$LaMn_{0.6}Cu_{0.4}O_3$ (p-type behaviour) and* ***c)*** *$PrMn_{0.6}Cu_{0.4}O_3$ (p-type behaviour). Catalytic parameters are reported in the lower side of the plot, while the conductivity and catalytic results in the upper side. Lower side plot's color-code : red :propane flow rate; blue: oxygen flow rate; green :contact time variation profile and black : temperature profile. Upper side plot's color-code: blue: propane conversion; grey: conductivity during pre-treatment in lean air; yellow: measurements at 260°C; light orange: measurements at 270°C; orange: measurements at 280°C ; red: measurements at 290°C ;dark red-white-green: measurements at 300°C with contact time variation; light blue: dry feed is switched to lean air at 300°C.*

4.2.2 $AMn_{0.7}B'_{0.3}O_3$ Perovskites

The propane oxidation experiments have been performed from 260 until 300°C measuring in steady-state conditions at each 10 °C increment (Figure 4.21) and then applying four different contact times (W/F=0.18-1.2 $g \cdot s \cdot mL^{-1}$) in dry feed $C_3H_8/O_2/Ne/N_2$ = 5/10/2/83 (Figure 4.22 a) and three different contact times (W/F=0.3-1.2 $g \cdot s \cdot mL^{-1}$) in wet feed $C_3H_8/O_2/Ne/N_2/H_2O$ = 5/10/2/43/40 (Figure 4.22 b).

The activity increases with temperature for all the catalysts, starting from 2% and achieving a maximum of 10%, for most of the catalysts, with the exception of $PrMn_{0.7}Ru_{0.3}O_3$ (+3% of RuO_2), which shows a very pronounced activity with respect to all the other tested catalysts, laying in range which starts from 40% conversion at 260°C and reaches up to 45% conversion at 300°C (Figure 4.21), highlighting the intrinsic property of Ru for propane oxidation [359-363], which in this specific case could to be either hindered or even pronounced by the presence of around 3% of RuO_2, which, is reported to boost the activity for propane oxidation with respect to metallic Ru [362, 363]. While, the other $AMn_{0.7}B'_{0.3}O_3$ tested catalysts, present the following activity order in the temperature programmed reaction: Zn > Ni > Co > Fe > Cr > Pd. The results are in good agreement with those present in the literature, indeed, it is generally reported that Ni and Co substitution in $LaMnO_3$ perovskites leads to an increased catalytic performance in propane oxidation. [364, 365] On the other hand, the effect of Fe in $AB_{(1-x)}B'_{0.3}O_3$ is reported to be limited to preserve the structure by inhibiting B-site segregation or shifting [366] and although, supported Palladium catalysts usually present excellent activity for propane oxidation, [367-369] the Pd influence on the catalytic performance seems to be drastically decreased when incorporated as metal oxide into the perovskite's lattice.

Moreover, from the contact time variation in dry feed (Figure 4.22 a), it is clearly evident that the catalytic scenario is dominated by Mn and the comparison between Pr-based catalysts (B'=Zn, Ni, Co, Ru and Pd) further highlights the crucial role of the B-site on the catalytic performance, [200] presenting the discussed catalysts very different catalytic performance and having all the same A-site. As expected, the addition of steam into the reaction feed (Figure 4.22 b, 4.23 b) leads to selectivity jump up for all catalysts, especially for $PrMn_{0.7}Co_{0.3}O_3$ and $NdMn_{0.7}Fe_{0.3}O_3$, while no beneficial effect is detected for Ru- and Pd-based perovskites, being the Ruthenium-based catalyst very active, while it is not the case for the Pd-based one, especially in wet feed. The selectivity to propene for these last two mentioned catalysts is always almost 0, irrespective of the feed composition.

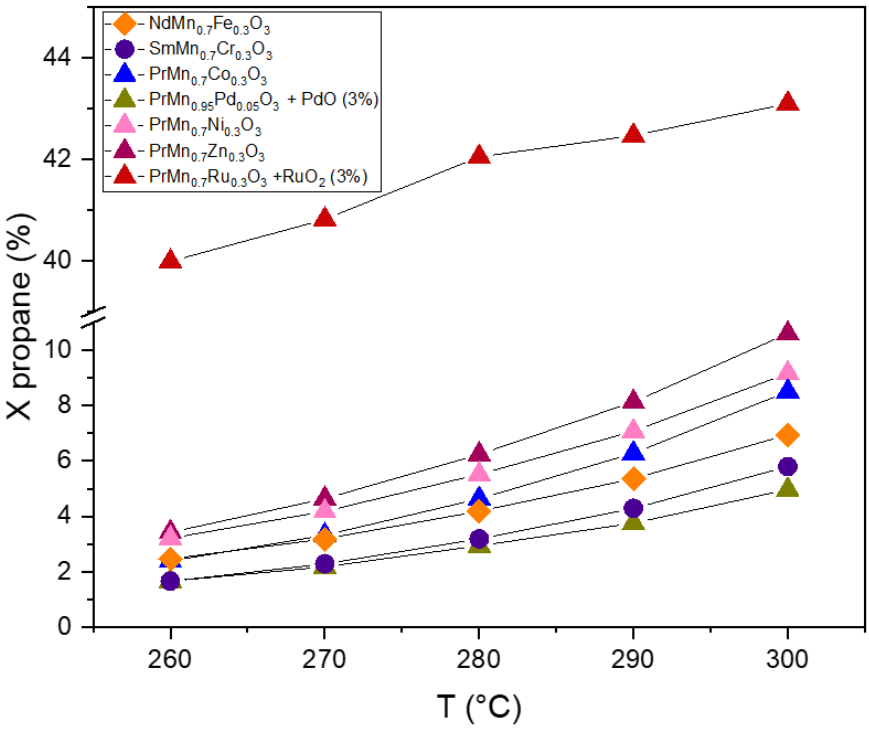

Figure 4.21. *Conversion of propane as a function of the temperature for all $AMn_{0.7}B'_{0.3}O_3$ catalysts in dry feed C_3H_8/O_2/inert: 5/10/85. B' color-code: magenta: Zn; fuchsia: Ni; light blue: Co; green: Cu; orange: Fe; violet: Cr; dull green: Pd and red: Ru.*

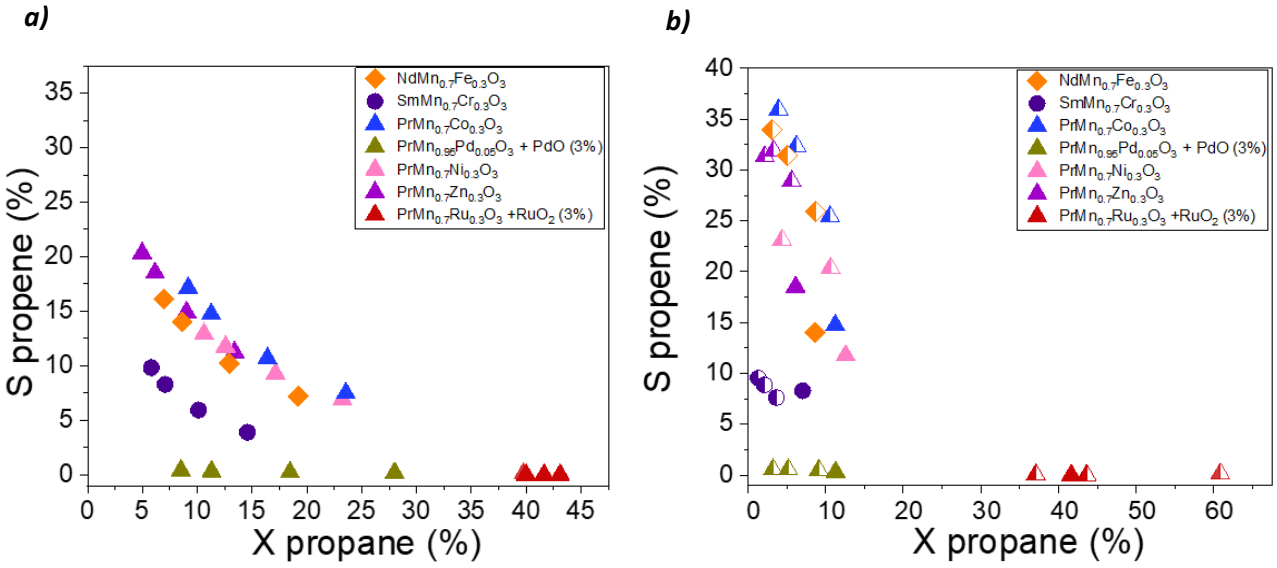

Figure 4.22. *Contact time variation (W/F = 0.18-1.2 g·s·mL^{-1}) for all catalysts at 300°C in* ***a)*** *dry feed and* ***b)*** *wet feed (in which filled data points represent dry feed at W/F=0.3 g·s·mL^{-1} and half-filled data points represent wet feed contact time variation at W/F=0.3-1.2 g·s·mL^{-1}). B' color-code: magenta: Zn; fuchsia: Ni; light blue: Co; green: Cu; orange: Fe; violet: Cr; dull green: Pd and red: Ru.*

The initial rate results confirmed those already presented in temperature programmed reaction and in the X-S plots, being the Ru-based perovskite a total combustion catalyst for propane oxidation, producing only CO_2. According to the literature, propane adsorbs on Ru sites to form isopropyl groups for Ru/Al_2O_3 system, then isopropyl groups are converted to acetone, which is decomposed to acetate or formed species, which are further decomposed to CO_2 and H_2O, as evidenced by DRIFT studies [359]. The initial rates of CO_2 formation trend among the catalysts follows that of propane consumption (Figure 4.23 a and c), indicating that total combustion path might be the driving force for propane oxidation, underlying in this way the highly defective nature of the examined systems. [9] On the other hand, the initial rate of propene formation plot (Figure 4.23 b) resembles very closely the same trend shown in CO oxidation rate plots (Figure 4.4), except for Pd-based sample, suggesting how CO oxidation might work as probe reaction for propene formation in $AMn_{0.7}B'_{0.3}O_3$ perovskites studied system. [354]

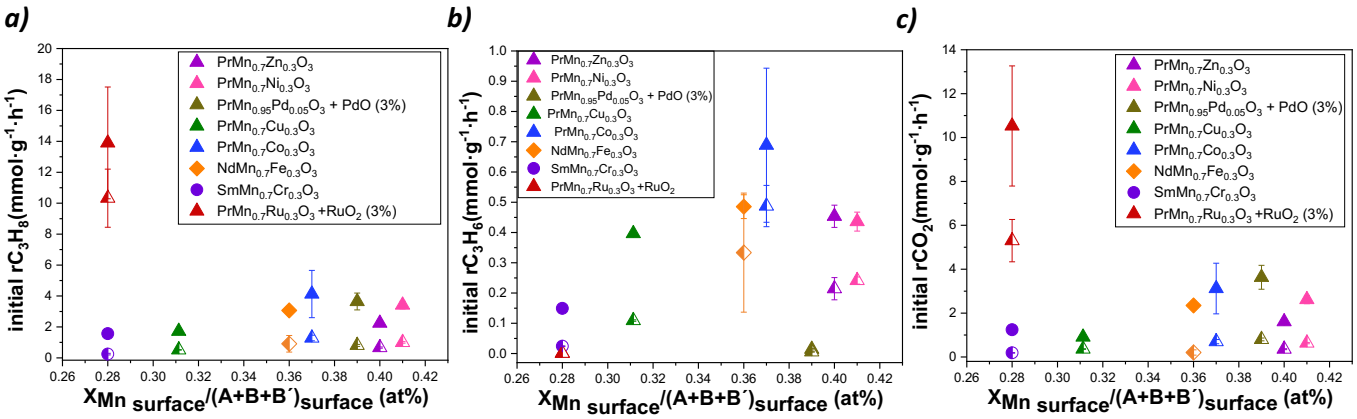

Figure 4.23. a) *Initial rate of propane consumption,* ***b)*** *initial rates of propene formation and* ***c)*** *initial rates of CO_2 formation over the Mn surface fraction in dry feed (filled data points) and wet feed (half-filled data point). B' color-code: magenta: Zn; fuchsia: Ni; light blue: Co; green: Cu; orange: Fe; violet: Cr; dull green: Pd and red: Ru.*

5. Artificial-Intelligence analysis

It is generally believed that the structural aspects, together with surface and electronic structure properties constitute the material's genome able to encode the catalytic performance. In simple words, as the DNA for biological living systems, the physicochemical properties of a material contain all the information, which cause and are linked to the macroscopic behaviour of this latter one and the encoding of their correlation combined with catalysis data can facilitate the understanding and prediction of the catalytic performance, leading in this way towards a significant breakthrough in the knowledge of the reaction process. In this context, the most important "pillars", which have been believed for several years for being the key descriptors of the catalytic performance in selective oxidation, are: (1) Lattice oxygen mobility, (2) Multifunctionality of the active site, (3) Site isolation, (4) Phase cooperation, (5) Strength of metal-oxygen bond, (6) Motif of the host structure and (7) Redox properties of the cation. [9] Although this formula contains all the key parameters which account for the best electronic structure, it remains rather a formal concept for the design of a new catalyst in selective oxidation, because the dynamic intrinsic phenomenological nature of the catalytic process can not be included. Indeed, the identification of descriptive parameters is very challenging since the desired reaction product (selectivity to propene or oxygenates) in gas-solid catalyzed reactions results from the tangled interplay of multiple processes which are not related only to the catalyst itself, but also to reaction condition (temperature, reaction atmosphere, contact time et cetera). In addition, the picture is complicated by the fact that the reaction mechanism varies across the different catalysts' surfaces and active sites, which means that, even when it could be untangled and explained for a given surface, it should be redefined for each different catalyst. Most important, the material itself becomes a "living system" under operation condition, due to simultaneous bond-breaking and forming on the surface, catalyst's structure modification in reaction atmosphere and the gas reactants and products diffusion within the material. [370] In this regard, careful determination of the electronic structure under operando condition constitutes the key-issue towards untangling the reaction mechanism and the rational design of a new catalyst. High-throughput DFT calculations [276-278] and artificial intelligence [279-282] have already been widely used for accelerating materials and catalyst discovery. With respect to artificial intelligence, atomistic DFT calculations are a physical model, however computation prohibitive methods would be required for the atomistic model evaluation of large, consecutive and multistep reaction networks of the catalytic process. [371, 372] Indeed, the lack of reliable methods for identifying the materials´descriptors has always been the key issue which shielded efficient material discovery. [373] Given the elements mentioned above, modeling reaction processes in selective oxidation by starting from ab initio calculation and atomistic modeling would not be a feasible approach for material discovery and therefore in the following project it has been

chosen to employ experimental data combined with AI. In this context, Artificial intelligence (AI) has shown very promising results because even when applied only to a small number of candidate materials, [374, 375] it was able to identify the key physico-chemical properties which are linked to the target of the catalytic performance (product selectivity). Nevertheless, it becomes vital to remark that the mesoscale, charge-transfer processes and heat and mass transport phenomena and their further complex coupling of these latter ones occurring at different time and length scale need to be included into AI analysis, however it is not trivial how to represent these phenomena into defined variables (primary features) and therefore it becomes challenging for AI to fully withstand with kinetic properties and to predict kinetics, which go beyond the classical Sabatier principle of the optimal strength between the catalyst and the substrate molecule. [21] AI helps in finding non-linear expression which correlate different variables (primary features) with the catalytic performance and as a result of finding these expressions, the key primary features are identified by the model expressions. These latter models have two main functions: identifying and understanding which are the main processes governing catalysis by looking at the relevant primary features and estimate the reactivity of new materials. The SISSO-derived final descriptors display physicochemical properties (primary features) which need to be correctly interpreted by chemical knowledge combined with catalysis phenomena understanding which go far beyond the mathematical expressions, it might be compared to DNA encoding process of a new system.

Due to their tolerance factor, [50] perovskite-type like materials present a high degree of structural flexibility and hence it becomes possible to tune the bulk and electronic structure by easily substituting the A or B-site metals, [376] rendering perovskites a very suitable base for the investigation of structure-function relations. [202] Indeed, many attempts of material discovery starting from perovskite-like materials through AI have been widely reported in the literature, [377-380] although in the most of the cases, the origin of the data collected from the computational simulations or performed measurements reported in the literature present incompleteness and inconsistency. [381] In some cases, the predicted optimal perovskite-like structures have been synthesized and tested in order to validate the found final descriptor, however the input data deriving from 18 perovskite materials have been always gathered from literature in the reported study. [382] While, in the following project, 21 phase-pure materials synthesized, characterized and tested in identical conditions, have been employed as input data for AI. In this context, the correlations between the physicochemical properties of the materials and the catalytic performance have been identified employing the SISSO approach. [375, 383] SISSO is the acronym which stands for “Sure Independence Screening and Sparsifying Operator”, which is able to yield a model to describe the target property (i.e. selectivity) from a combination of relevant features of the studied materials, by facing huge and correlated feature spaces. Indeed, SISSO is a compressed sensing based methodology, [384-386] capable of predicting power, yielding models expressed by analytical

formula and build from physicochemical features. In details, SISSO is able to identify descriptors from the so-called "primary features", which are complex and non-linear analytical expressions deriving on the input parameters and, since in ML jargon these descriptors are representations, SISSO might be called a "representation-learning algorithm". [374] The optimal model with respect to the averaged error for a given target property "*P*" (i.e. the kinetic property which is under examination, such as the rate of CO oxidation or the yield of propane oxidation) presents the general formula:

$$P^{(SISSO)} = c_0 + \sum_{i=1}^{D} c_i d_i \qquad \text{(Eq. 5.1)}$$

Where d_i are the components of the descriptor in which the most relevant primary features the selected from billions of generated candidates appear, c_0 is the intercept, c_i the weighting coefficients and D is the descriptor dimension. Indeed, the SISSO approach starts from the collection of the primary features, which are the input data of the algorithm and are constituted by the physicochemical parameters deriving from the characterization of the material, but might also be parameters of different nature which could be possibly relevant for the catalytic target property of interest (for instance, CO oxidation rates might be employed as primary feature to describe propane oxidation, since CO oxidation usually works as probe reaction). Then, by following the symbolic regression approach, [384-386] the primary features are combined by SISSO employing mathematical operator such addition, (absolute) difference, multiplication, division, exponential, power, square and cubic roots, logarithm and absolute value, and this step results in generating billions of descriptor candidates. Finally, the SISSO ++ (c++) code selects a reduced amount of candidate descriptor per dimension (D), being D typically equal to 1,2, or 3, forming in this way the so-called SIS-selected subspaces of the total space of billions of descriptors. Further details about this selection step might be found in reference. [387] In the linear combination also the coefficient, which are identified by compressed sensing as well, [384-386] play a fundamental role.

The evaluation of the optimal complexity for a given model is performed through the leave-one-material-out-cross-validation (CV) approach. In the CV approach one material is removed from the training model and its estimation of the target property is done based on the best models for the remaining materials. This procedure is iterated until all materials are removed once from the dataset. Finally, the performance metric of the model is assessed by the root mean squared errors averaged over all cross validation iterations (averaged CV-RMSEs), being the optimal complexity of a model the one with the lowest CV-RMSE (Figure 5.1). [374]

The two parameters which describe the optimal complexity of the model (lowest CV-RMSE) are the rung (*q)*, which accounts for the number of times the mathematical operators are simultaneously applied to the primary features in order to develop the descriptors and the dimension D, whose linear combination yield the best fit for the desired target property, being the final descriptor the

vector containing the initial candidate descriptor as individual components (eq. 5.1). While, the training error is the root mean square of the average of each data point from the diagonal shown in the model. It is a value which expresses how good the fit is in the linear regression and it posses the same unit of the target property.

The primary features appearing in the optimal model do not have to be considered as the properties which improve the reaction process, but rather as properties linked to this latter one, by either hindering or controlling the reactivity.

Moreover, the methodology of the SISSO approach has been extended to a "multi-task-learning" approach (MT-SISSO), [383] which is even able to identify a single descriptor for multiple target properties of the material or external conditions simultaneously. In this way, it becomes possible to identify descriptors at different reaction conditions, thus enhancing the reliability of the descriptor itself by increasing the number of the datapoints. For instance, the data deriving from the temperature programmed reaction (260-300°C) experiments in propane oxidation might be employed in the input dataset, since each temperature becomes a different task. This approach is very suitable for heterogeneous catalysis database with low data or in which not all properties are reported in the training set for all materials. In the specific project, it has not been applied, since the number of materials and primary feature were sufficient to provide reliable models and the fact that different phenomena might control the reactivity at different reaction conditions has not to be excluded.

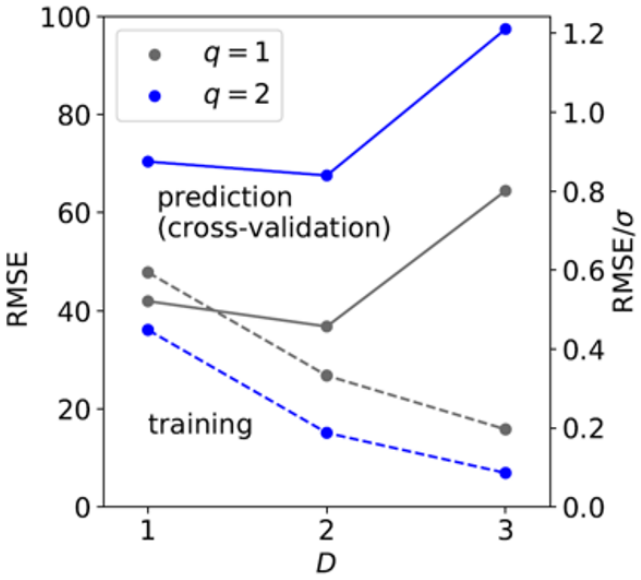

Figure 5.1. *CV analysis of models calculated by SISSO for the CO oxidation rates at 130°C in feed CO/O₂/inert=1/20/79. The CV errors shown on the primary y axis (left one) corresponds to the averaged RMSE across the leave-out-one-material-CV-iterations. The optimal complexity in the specific case is shown by rung q=1 and dimension D=2. The secondary y axis (right one) displays the CV-RMSE as a fraction of the standard deviation of the rates of CO oxidation among the whole training set. Color-code: grey: rung=1 and blue: rung=2. Continuous lines: calculated prediction and dotted lines: training.*

5.1 CO Oxidation

Although its seemingly aspect of a simple catalyzed chemical reaction, CO oxidation hinders a multitude of different and still untangled facets which reflect the complexity and richness of Heterogeneous Catalysis. Indeed, despite it is believed to be one of the best known heterogeneous reaction and it is generally employed as benchmark for other catalyzed oxidation reactions, CO oxidation reveals in some cases the incompleteness of the deep understanding of its own mechanism. [354] The reaction mechanism of CO oxidation is generally reported to follow the LH (Langmuir-Hinshelwood) kinetic and has mainly be studied over noble metal catalyst. [388, 389] While, with metal-oxides the kinetic scenario becomes more intricated. Among the literature both interfacial MvS (Mars van Krevelen) and suprafacial (LH) mechanisms have been reported for CO oxidation over perovskite-type oxides. In most of the cases it is reported to be interfacial, [205, 210, 390, 391] although in some works it has been claimed to be suprafacial. [342, 392] Some other studies report that the type of mechanism depends on either on the reaction temperature [205] or on the adsorption site.[393] The critical issue is the lack of control and the knowledge of how the "aristocracies of atoms", as named by Taylor, [394] (which compose the active sites) influence the gas phase reactants under reaction condition, playing the local structure of the binding sites a major role on chemical properties. Moreover, the hypothesis that the reaction product CO_2 is inert and no further reacts, remains valid until no reducing species, which neutralizes the oxygen on the surface, are not chemisorbed. [166, 347] In this context, the identification of geometric and electronic property for reaction kinetic in CO oxidation for isolated clusters has been identified by the comparison between experiments and theory. But, when it comes to more extended systems, the reaction dynamic is controlled by competing adsorbate phases which limit the free space for the reaction on the surface and the knowledge of the charge state of the adsorbate-substrate formed complex and of the charge-transfer process become crucial key issues to encode the chemical activation and interaction which compose the kinetic mechanism. The idea is thus to extend the strategy pioneered by Ertl et al. of the fundamental investigation on single crystals to more complex system with the support of alternative methods, such as Artifical Intelligence, in order to investigate CO oxidation beyond its prototype role, at defined temperature and pressure, employing a broad number of rather complex catalysts with different physico-chemical properties.

5.1.1 (La,Pr)$Mn_{(1-x)}Cu_xO_3$ series

CO oxidation has been extensively studied over $LaMn_{(1-x)}Cu_xO_3$ series and perovskite material of similar composition and some conclusions has been drawn on the responsible parameters which drive the reaction process. [166, 199, 200, 308, 317, 395, 396] However, a lack of homogeneity is present for the CO oxidation data reported in the literature for the specific La-based series (such as: different reaction temperatures, contact times, pre-treatment et cetera) rendering thus the drawn models not generalizable and even partially incorrect. Indeed, for instance, some studies claim that Cu is the responsible element among the two B-site metal in the $LaMn_{(1-x)}Cu_xO_3$ series for the catalytic performance in CO oxidation, [166] while other studies report that Cu doping might boost the catalytic performance by creating more oxygen vacancies, [201] but Mn has a higher catalytic activity compared to Cu. [308] Additionally, the effect of the substitution of the A-site in the above mentioned series in CO oxidation has never been object of investigation, although the influence on the surface composition and geometry induced by the crystallographic structural strain which is established by changing the A-site metal is well known. [313, 344] In order to solve the intricated labyrinth, La has been systematically substituted at the A-site by Pr in the $AMn_{(1-x)}Cu_xO_3$ series, the materials have been calcined, characterized and tested in identical conditions and SISSO calculation has been performed in order to find the most relevant physicochemical properties of the materials coupled to the kinetic process. The 14 candidate materials and the 30 employed primary features for the training set are listed below in **Table 5.1** and **5.2**, respectively.

Table 5.1. Table with listed the nominal Cu loading, the A-site, the ID number and the CO oxidation rates measured at 130°C, in W/F=0.036 $g \cdot s \cdot mL^{-1}$, in CO/O_2/inert : 1/20/79 (mmol/gh) of the materials employed for the SISSO analysis in CO oxidation over the (La,Pr)$Mn_{(1-x)}Cu_xO_3$ series. Color-code: orange: La-based samples and green: Pr-based ones.

Nominal X_{Cu}	A site	Sample's ID #	Target property: CO oxidation rate (mmol/gh)
0	La	30649	104.045
	Pr	31345	257.075
0.1	La	30867	122.430
	Pr	31070	204.485
0.2	La	31180	177.307
	Pr	31021	152.567
0.25	La	30635	246.023
	Pr	30637	74.223
0.3	La	30659	306.832
	Pr	30934	115.668

Table 5.1 (cont.)

0.35	La	30624	168.872
	Pr	31176	81.004
0.4	La	31285	348.617
	Pr	29908	166.230

Table 5.2. Table with listed the symbols, the unit, the description and the characterization technique of the primary features used for the SISSO analysis in CO oxidation over the (La,Pr)$Mn_{(1-x)}Cu_xO_3$ series.

Symbol	Unit	Description	Technique
V	*Å³*	*Normalized unit cell volume for formula unit (ABO_3)*	*XRD*
*a**	*Å*	*Cubic root of V*	*XRD*
D	*Å*	*Deviation parameter for the unit cell able to capture the deviation of the reduced lattice parameters from a**	*XRD*
$<BO>_\mu$	*Å*	*Mean value of B-O interatomic distance*	*XRD*
$<BO>_\sigma$	*Å*	*Deviation of single B-O values from the mean. It reflects the octahedral and Jahn-Teller distortion*	*XRD*
$<AO>_\mu$	*Å*	*Mean value of A-O interatomic distance*	*XRD*
$<AO>_\sigma$	*Å*	*Deviation of single A-O values from the mean. It reflects the cuboctahedral distortion*	*XRD*
$<OO>_\mu$	*Å*	*Mean value of O-O interatomic distance*	*XRD*
$<OO>_\sigma$	*Å*	*Deviation of single O-O values from the mean*	*XRD*
$<BOB>_\mu$	*2Theta*	*Mean of the BOB angles' values. It is related to the mean tilt of the octahedra*	*XRD*
$<BOB>_\sigma$	*2Theta*	*Absolute deviation of single O-B-O angles' values from the ideal octahedral values* [a]	*XRD*
$BOB_{RMS,dev}$	*2Theta*	*Root mean squared of BOB_σ. It reflects the amount of angular distortion in BO_6 octahedra*	*XRD*
T_obs	*adimensional*	*Observed tolerance factor* [b]	*XRD*
A_{bulk}	*at%*	*Amount of A-site in the bulk*	*ICP-OES*
B_{bulk}	*at%*	*Amount of B-site in the bulk*	*ICP-OES*
B'_{bulk}	*at%*	*Amount of B'-site in the bulk*	*ICP-OES*
$O_{tot\ (bulk+surfacce)}$	*at%*	*Amount of oxygen in the material*	*O_2 determination analysis*

Table 5.2 (cont.)

$A_{surface}$	*at%*	*Amount of A-site on the surface*	*XPS*
$B_{surface}$	*at%*	*Amount of B-site on the surface*	*XPS*
$B'_{surfcae}$	*at%*	*Amount of B'-site on the surface*	*XPS*
$O_{surfacce}$	*at%*	*Amount of oxygen on the surface*	*XPS*
$O_{lattice\ surf}$	*%*	*O1s surface species from fitting*	*XPS*
$O_{defects\ surf}$	*%*	*O1s surface species from fitting*	*XPS*
$O_{surface\ surf}$	*%*	*O1s surface species from fitting*	*XPS*
$O_{carbonates\ surf}$	*%*	*O1s surface species from fitting*	*XPS*
$O_{OH\ surface}$	*%*	*O1s surface species from fitting*	*XPS*
$O_{H2O\ surface}$	*%*	*O1s surface species from fitting*	*XPS*
$O_{oxy\ surface}$	*%*	*O1s surface species from fitting*	*XPS*
Centroid O1s peak	*eV*	*Centroid of the binding energy of the O1s peak* **c**	*XPS*
VB onset	*eV*	*Onset of valance band relative to Fermi level*	*XPS*
S_{BET}	m^2/g	*Surface area*	N_2 *adsorption*

a: The distortion of O-B-O angles will be mostly cancelled out due to geometric reasons and therefore they can not be simply averaged like the interatomic distance. Because of this, the deviations have been calculated as absolute ones from the ideal octahedral values, which are: 90° for cis angle and 180° for trans angles.

b: The tolerance factors have been calculated from the experimental data as follows: $tobs=\frac{<A-O>\mu}{<B-O>\mu*\sqrt{2}}$.

c: The centroid of the O1s peak's function, which indicates the center of the spectrum mass, has been employed as primary feature of the O1s peak, in order to feed SISSO with an O1s parameter which is independent from the O1s fitting.

Only primary features present for all the analyzed dataset might be included in the calculation, because SISSO is not able to work with missing data among the dataset.

SISSO calculations have been performed using rung from 1 to 3 and the best model, where the optimal complexity presents the lower CV error is defined by rung q=1 and dimension D=2 (Figure 5.2). Rung=3 analysis have been performed employing 15 primary features, which have been previously selected by analysis with q=1 and 2, by following the same approach reported in a previous work. [374]

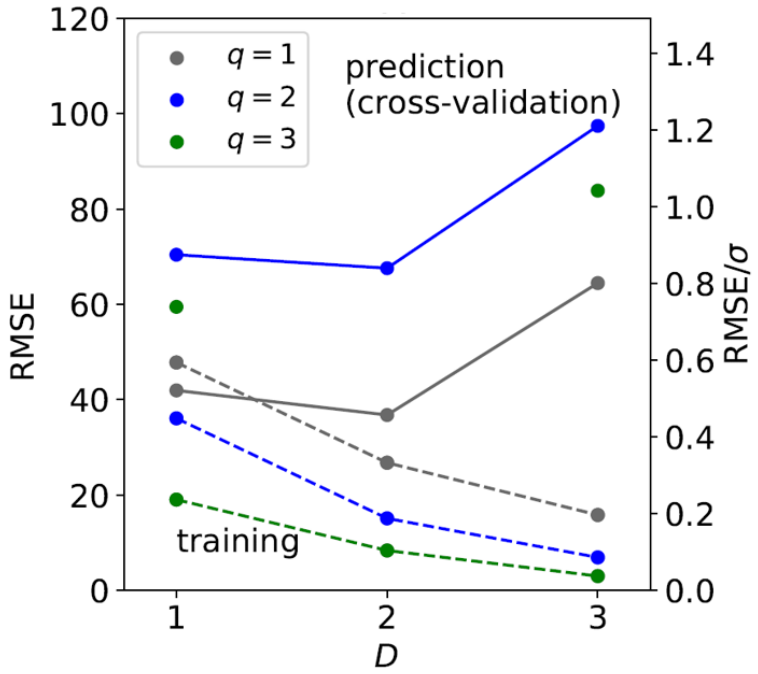

Figure 5.2. *CV analysis of models calculated by SISSO for the CO oxidation rates at 130°C in feed CO/O₂/inert=1/20/79 over the (La,Pr)-series. The CV errors shown on the primary y axis (left one) corresponds to the averaged RMSE across the leave-out-one-material-CV-iterations. The optimal complexity in the specific case is shown by rung q=1 and dimension D=2. The secondary y axis (right one) displays the CV-RMSE as a fraction of the standard deviation of the rates of CO oxidation among the whole training set. Color-code: grey: rung=1, blue: rung=2 and green rung=3. Continuous lines: calculated prediction and dotted lines: training.*

The fitted model, where finally the La- and Pr-based series follows the same trend in contrast to what shown in Figure 4.3, where the rates are plotted over the B-site surface fraction, is displayed in Figure 5.3, presenting the general equation:

$$r_{CO\ oxidation}^{SISSO}\ (mmol \cdot g^{-1} \cdot h^{-1}) = 1230 + 21.43 * [(B'_{surface}) / (D)] - 2655 * (A\_{surface} + A\_{bulk}) \quad \text{(Eq. 5.2)}$$

The found descriptor fits linearly almost all the materials, with $LaMn_{0.7}Cu_{0.3}O_3$ presenting the most scattered datapoint. The primary features involved in the model with the optimal complexity (lowest CV error) for CO oxidation steady-state experiments over the $(La,Pr)Mn_{(1-x)}Cu_xO_3$ series performed at 130°C in feed CO/O_2/inert: 1/20/79 are : the concentration of Cu on the surface (at%) derived from laboratory XPS analysis, the parameter D (Å) derived from Rietveld Refinement, which is an expression for the deviation of the reduced lattice parameters ($a/\sqrt{2}$, $b/\sqrt{2}$ and $c/\sqrt{2}$) from the cubic root of the normalized unit cell volume (a*), and the concentration of the A-site (La or Pr) on the surface and on the bulk (at%).

The found model with the optimal complexity (Equation 5.2) confirms that a single primary feature based on chemical intuition is not sufficient to fully describe the properties linked to the catalytic

performance, highlighting the still untangled facets of CO oxidation mentioned above in Section 5.1. In this specific context, it seems that AI (artificial Intelligence) has functioned as a suitable support to encode the experimental data, by fulfilling the hypothesis and expectations discussed in Section 5.1.1. Indeed, the indirect influence of the A-site´s size on the catalytic performance discussed in Section 4.1.1, by tuning the structure and consequently the electronic and defective properties of the materials, [313, 344] seems to be a passepartout in order to solve the opposite trends always shown between the La- and Pr-series when plotted over a descriptor composed by a single physico-chemical property (Figure 4.3). Beside of the amount of the A-site both on the bulk and on the surface (at%), the presence of D in the SISSO equation, which might be related to the structural strain established by the A-site size, is a further confirmation of the previously discussed indirect influence exerted by the structural modifications. Finally, matching the most counted and accepted conclusions drawn in oxidation catalysis over the element responsible for the catalytic activity in perovskite-like structures, [166, 200, 201, 308] the B´ amount (which is strictly correlated also to the B amount) plays a fundamental role as well in defining the best descriptor for the catalytic performance of CO oxidation over the (La,Pr)$Mn_{(1-x)}Cu_xO_3$ series.

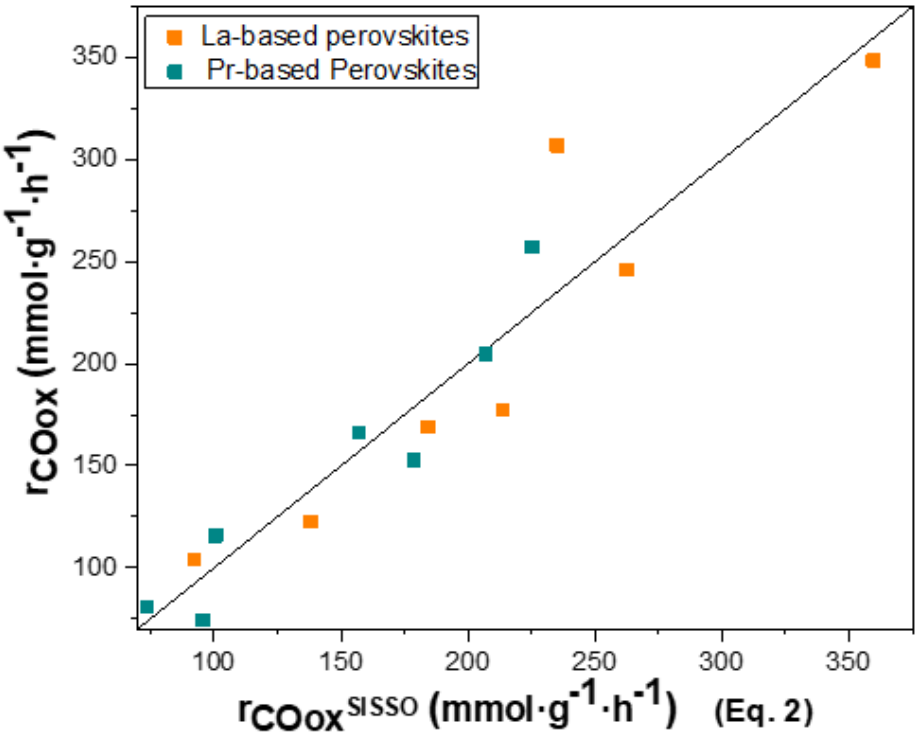

Figure 5.3. *Graphs showing the rates in CO oxidation measured at 130°C in feed CO/O₂/inert: 1/20/79 over the descriptor calculated by SISSO employing the data reported in Table 13 and 14 as dataset. Orange: La-based samples, green: Pr-based samples.*

In addition, as mentioned above, the avoidance of overinterpretation of the displayed physico-chemical parameters becomes a crucial point. In this regard, it might be useful to check if the

primary features which are considered physically meaningful are present in the equations with similar training RMSE errors (Table SI 1). In this specific case, it seems that the hypothesis formulated to encode the catalytic performance by using the Eq. 5.2 are validated. Indeed, a primary feature accounting for the amount of the A-site and a crystallographic parameter related to structural strain/distortion is always present in each train model (from 0 to 9) of dimension D=2 and rung r=1. Finally, also the primary feature which accounts for the amount of either B or B´ is displayed in all the descriptors for each training, except of that of training 9, the one with the highest training error.

5.1.2. (La,Pr)$Mn_{(1-x)}Cu_xO_3$ series plus (Pr,Nd)$Mn_{0.7}B'_{0.3}O_3$ catalysts

In order to expand the elemental folding fan of the input matrix from the (La,Pr)$Mn_{(1-x)}Cu_xO_3$ series, double B-site perovskites containing different B'-site (B'=Ni, Zn, Co and Fe) and presenting the general formula $AMn_{0.7}B'_{0.3}O_3$ have been inserted into the input dataset for SISSO calculation. $PrMn_{0.95}Pd_{0.05}O_3$ and $PrMn_{0.7}Ru_{0.3}O_3$ have been excluded from the dataset since they present around the 3% of by-phases according to XRD detection limit (Figure SI 7), while $(La,Pr)_2CuO_4$ structures have been left out as well due to the fact that the data of the O1s surfaces species for these two catalysts are not available and SISSO can not calculate descriptor from incomplete input dataset. Different metals have been substituted at the medium loading content of the series (x=0.3), in order to investigate how different metals in synergy with Mn may affect the catalytic performance and to which extent. [199, 200] All the employed B´metals have been chosen according to the possible easy generation of oxidation state 2+ (Cu is 2+ in (La,Pr)-series) and due to their know catalytic properties. Co and Ni are very well know active element in oxidation catalysis, [352, 364, 365, 397-399] Zn is less studied in oxidation catalysis with respect to the last mentioned one, but it still reported to be an active element both for CO [400, 401] and propane oxidation, [402, 403]while Fe is generally reported to be less active than the other employed metals. [353] However, the studied system reveals that the synergistic effect of Fe combined by Mn is able to boost the catalytic activity to a higher degree than Mn-Zn or Mn-Ni in CO oxidation (Figure 4.4). The intrinsic reason of this phenomenon might be elucidated through the support of AI, by identifying which physicochemical properties might change by combining Mn with very different 3d metals.

The 18 candidate materials are listed below in Table 5.3, while the 30 employed primary features for the training set are the same of the SISSO calculation over the (La,Pr)-based series reported in Table 5.2.

Table 5.3. Table with listed the nominal composition, the ID number and the CO oxidation rates measured at 130°C, in W/F=0.036 g·s·mL^{-1}, in CO/O_2/inert: 1/20/79 (mmol/gh) of the materials employed for the SISSO analysis in CO oxidation over the whole perovskite matrix.

Nominal Formula	Sample's ID #	Target property: CO oxidation rate (mmol/gh)
$LaMnO_3$	30649	104.045
$LaMn_{0.9}Cu_{0.1}O_3$	30867	122.430
$LaMn_{0.8}Cu_{0.2}O_3$	31180	177.307
$LaMn_{0.75}Cu_{0.25}O_3$	30635	246.023
$LaMn_{0.7}Cu_{0.3}O_3$	30659	306.832
$LaMn_{0.65}Cu_{0.35}O_3$	30624	168.872
$LaMn_{0.6}Cu_{0.4}O_3$	31285	348.617
$PrMnO_3$	31345	257.075
$PrMn_{0.9}Cu_{0.1}O_3$	31070	204.485
$PrMn_{0.8}Cu_{0.2}O_3$	31021	152.567
$PrMn_{0.75}Cu_{0.25}O_3$	30637	74.223
$PrMn_{0.7}Cu_{0.3}O_3$	30934	115.668
$PrMn_{0.65}Cu_{0.35}O_3$	31176	81.004
$PrMn_{0.6}Cu_{0.4}O_3$	29908	166.230
$PrMn_{0.7}Zn_{0.3}O_3$	33380	106.126
$PrMn_{0.7}Ni_{0.3}O_3$	33366	128.899
$PrMn_{0.7}Co_{0.3}O_3$	33454	346.542
$NdMn_{0.7}Fe_{0.3}O_3$	33621	248.289

Also with this input dataset, SISSO calculations have been performed using rung from 1 to 3, but, differently from the (La,Pr)-series, in this latter case the best model is defined by q=3 and D=1 (Figure 5.4).

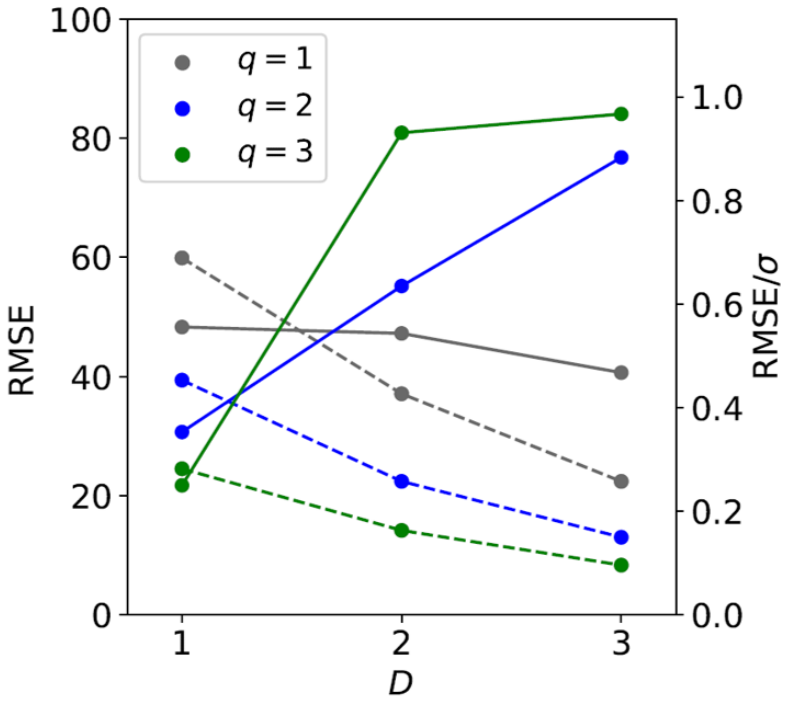

Figure 5.4. *CV analysis of models calculated by SISSO for the CO oxidation rates at 130°C in feed CO/O₂/inert=1/20/79 over the whole perovskite matrix. The CV errors shown on the primary y axis (left one) corresponds to the averaged RMSE across the leave-out-one-material-CV-iterations. The optimal complexity in the specific case is shown by rung q=3 and dimension D=1. The secondary y axis (right one) displays the CV-RMSE as a fraction of the standard deviation of the rates of CO oxidation among the whole training set. Color-code: grey: rung=1, blue: rung=2 and green rung=3. Continuous lines: calculated prediction and dotted lines: training.*

The fitted model, where all the perovskite of the matrix present a linear correlation is displayed in Figure 5.5, presenting the general equation:

$$r_{CO\ oxidation}^{SISSO}\ (mmol \cdot g^{-1} \cdot h^{-1}) = 42.30 + 0.509 * [(VB\_onset * O_{OH\ surface}) / |B'_{surface} - A_{surface}|] / [(D / O_{tot\ (bulk+surface)}) * A_{surface}^{2}] \quad \text{(Eq. 5.3)}$$

This model for CO oxidation steady-state experiments over the whole perovskite matrix (Table 5.3) performed at 130°C in feed CO/O₂/inert: 1/20/79 might be generally seen as an expansion of the one calculated only over the (La,Pr)-series (Eq. 5.2). Indeed, it contains all the primary features already identified with Eq. 5.2, such as: the surface concentration of the A-site, that of the B´-site and the deviation parameter D. Additionally, it identifies as master key physicochemical properties the total amount of oxygen (at%), the surface OH groups from O1s fitting (%) and the valence band onset (eV). The correlation between surface OH groups and Mn-site is the most intuitive, since many studies report the formation of Mn-OH groups in wet feed condition. [275, 404] On the other side, the amount of total oxygen (bulk+surface) might be directly interpreted as the major role that the bulk oxygen has on reaction mechanism in case it belongs to interfacial class and also on its correlation with oxygen vacancies formation, which are known to be fundamental to control the

catalytic activity. [9, 201, 405-407] In some cases, it was even reported that CO oxidation mechanism over a perovskite like catalysts proceeds through LH mechanism, where the molecular O_2 from the gas phase favorably adsorbed and dissociated on the oxygen vacancies sites. [213] Finally, the valance band onset is a parameter which basically explains the elemental diversity in the matrix, since it accounts for the electronic density which is different from atom to atom, by affecting the physical electronic structure and the binding site. [408]

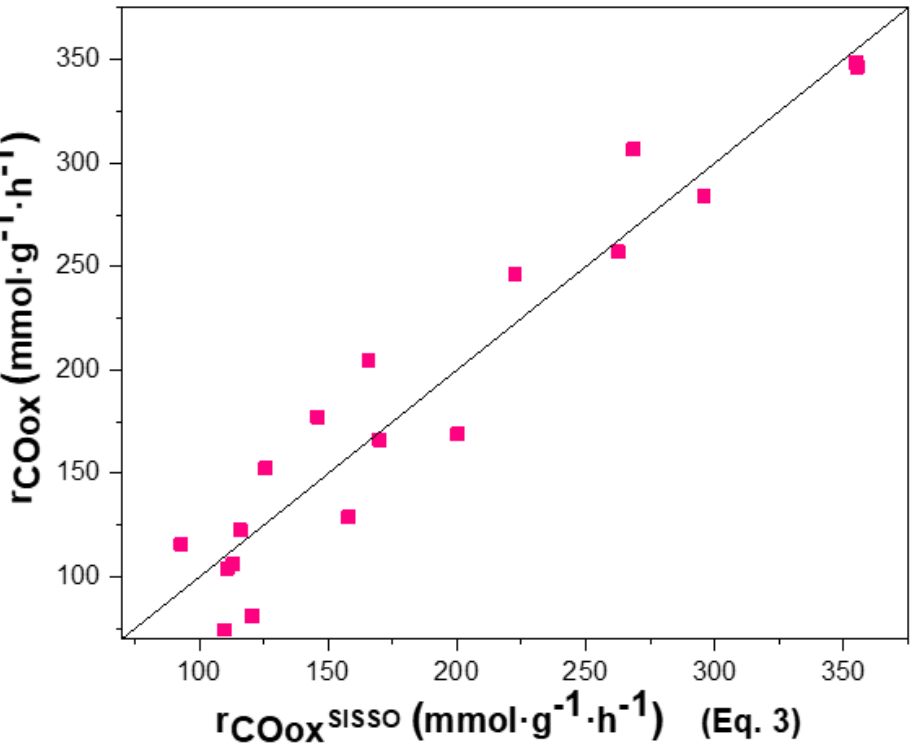

Figure 5.5. *Graphs showing the rates in CO oxidation measured at 130°C in feed CO/O₂/inert: 1/20/79 over the descriptor calculated by SISSO employing the data reported in Table 16 and 14 as dataset.*

It can be concluded that the major outcome from the both calculated SISSO models for CO oxidation over perovskite-like catalysts (Eq. 5.2 and 5.3) is the confirmation of the discussed hypothesis in the following Thesis (Section 4.1), which states that not only the B-site plays a major role for the catalytic performance, but also the A-one, due to the structural and electronic modifications indirectly induced by its different size. [313, 344]

5.2 Propane Oxidation

The selective oxidation of propane belongs to a very important class of catalytic reactions for the changeover from oil-based feedstock in (petro)chemical industry, where the challenge still remains in finding an environmental benign integrated route to produce oxygenates from alkanes. Its three most relevant target products are propene, which constitutes one of the main building-block of petrochemical industry, followed by acetaldehyde and finally by acrylic acid (AA), which is one of the most important intermediate in the production of acrylates. The reaction starts with the activation of propane by the nucleophilic oxygen of the catalysts, [409] which breaks a C-H bond of propane (this step is also called alpha-abstraction), while it is believed that electrophilic oxygen for oxygen insertion is then required in order to proceed with the reaction process to oxygenate products (acetaldehyde) and finally to acrylic acid. [11] In order to perform all the reaction step to AA, an aristocracy of atoms (or active sites) as named by Taylor [394] should be composed by multimeric units capable of regeneration upon reduction. The nature of these ensembles of atoms together with the deep understanding of their functioning under dynamic conditions is still largely unknown for many catalysts, although some empirical findings, such as site-isolation and surface termination, have been elucidated for some materials. [410] Multiple parallel and consecutive reaction steps compose the entire complex and intricated network of the reaction mechanism of propane oxidation rendering in this way the deep understanding of the active sites' nature and their role in each step very difficult. On this subject, isotope labelled studies over V-based catalysts (M1 phase and 6V/SBA-15) have revealed a multitude of parallel and consecutive reaction steps with dozens of intermediates as detected by GC, where the rate limiting step has been identified to be the alpha abstraction of the methylene group of propane molecule and that of methyl and methylene group simultaneously for 6V/SBA-15 and M1, respectively. [371] The identification of the physicochemical properties which are responsible for the selectivity, limiting the production of environmentally harmful undesired by-products, such as CO and CO_2, becomes the crucial issue of the whole designing process of a new catalyst. In this regard, alternative approaches to the classical ones, which are described previously in the following Thesis, for modelling and designing are urgently needed and AI might decipher the feature which encode the catalytic performance.

5.2.1 (La,Pr)$Mn_{(1-x)}Cu_xO_3$ series

Propane oxidation has been largely studied over perovskite-like structures, [192-194] but not in particular over the $AMn_{(1-x)}Cu_xO_3$ series, where propene and CO_2 are the only detected products. In the literature, it is generally emphasized the central role of the B-site element for the catalytic

performance in the selective oxidation [199, 200] and the benefical synergistic effect which is established when Mn is partially substituted by Cu. [309] These findings have been confirmed also in the following Thesis (Figure 4.6), although they seem to be incomplete to explain the whole catalytic scenario, especially when La is substituted by Pr. Indeed, the substitution of the A-site seem to change the catalytic trend for the (La,Pr)$Mn_{(1-x)}Cu_xO_3$ series, as it was the case for CO oxidation (Figure 4.9 and 4.11). In detail, the Pr-based presents a linear correlation in propane oxidation, where CO oxidation seems to work as probe reaction (Figure 4.3 and 4.9 c), [354] while the La-based series does not display any particular trend in each reaction conditions (Figure 4.19 and 4.11). Although the concentration of the two B-site for La- and Pr-based series is slightly different on the surface, this latter reason can not fully explain such a different catalytic performance. The A-site size has probably some more extended influence on the material than just increasing the surface concentration of one element with respect to a second one. Indeed, as discussed above, the structural distortion is able to induce electronic and charge transfer modifications into the catalysts, affecting thus the active ensembles and their cooperation under working conditions. [344] This aspect has never been discussed in the literature for $LaMn_{(1-x)}Cu_xO_3$ so far and from the findings presented in the following Thesis project (Chapter 4.2), it results evident that the interplay of the underlying processes is rather intricated and for this reason AI has been chosen as supporting tool to identify the most relevant primary features and to elucidate better the connection among these latter one for the catalytic performance. In order to do so, the initial rate of propane consumption, the initial rate propene and CO_2 formation and the $\frac{\text{initial rate of propene formation}}{\text{initial rate of } CO_2 \text{ formation}}$ ratio have been chosen as target properties in dry ($C_3H_8/O_2/Ne/N_2$=5/10/2/83) and in wet feed ($C_3H_8/O_2/Ne/N_2/H_2O$=5/10/2/43/40). The initial rates (see initial rate calculation in Section 2), instead of the rates at each contact time, have been employed as target properties in order to use a catalytic value which is independent from the contact time variation applied in propane oxidation at 300°C (see Section 2 for propane oxidation details), avoiding so to perform the SISSO calculation for a single catalytic condition. The 12 candidate materials and the 33 employed primary features for the training set are listed below in Table 5.4 and 5.5, respectively.

Table 5.4. Table with listed the nominal Cu loading, the A-site and the ID number of the materials employed for the SISSO analysis in propane oxidation over the (La,Pr)$Mn_{(1-x)}Cu_xO_3$ series. Color-code: orange: La-based samples and green: Pr-based ones.

Nominal X_{Cu}	A site	Sample's ID #
0	La	30649
0.1	La	30867
	Pr	31070

Table 5.4 (cont.)

0.2	La	31180
	Pr	31021
0.25	La	30635
	Pr	30637
0.3	La	30659
	Pr	30934
0.35	La	30624
	Pr	31176
0.4	La	31285

Table 5.5. Table with listed the symbols, the unit, the description and the characterization technique of the primary features used for the SISSO analysis in propane oxidation over the (La,Pr)$Mn_{(1-x)}Cu_xO_3$ series.

Symbol	Unit	Description	Technique
V	*Å³*	*Normalized unit cell volume for formula unit (ABO_3)*	*XRD*
*a**	*Å*	*Cubic root of V*	*XRD*
D	*Å*	*Deviation parameter for the unit cell able to capture the deviation of the reduced lattice parameters from a**	*XRD*
$<BO>_\mu$	*Å*	*Mean value of B-O interatomic distance*	*XRD*
$<BO>_\sigma$	*Å*	*Deviation of single B-O values from the mean. It reflects the octahedral and Jahn-Teller distortion*	*XRD*
$<AO>_\mu$	*Å*	*Mean value of A-O interatomic distance*	*XRD*
$<AO>_\sigma$	*Å*	*Deviation of single A-O values from the mean. It reflects the cuboctahedral distortion*	*XRD*
$<OO>_\mu$	*Å*	*Mean value of O-O interatomic distance*	*XRD*
$<OO>_\sigma$	*Å*	*Deviation of single O-O values from the mean*	*XRD*
$<BOB>_\mu$	*2Theta*	*Mean of the BOB angles' values. It is related to the mean tilt of the octahedra*	*XRD*
$<BOB>_\sigma$	*2Theta*	*Absolute deviation of single O-B-O angles' values from the ideal octahedral values* [a]	*XRD*
$BOB_{RMS,dev}$	*2Theta*	*Root mean squared of BOB_σ. It reflects the amount of angular distortion in BO_6 octahedra*	*XRD*
T_obs	*adimensional*	*Observed tolerance factor* [b]	*XRD*
A_{bulk}	*at%*	*Amount of A-site in the bulk*	*ICP-OES*

B_{bulk}	*at%*	*Amount of B-site in the bulk*	*ICP-OES*
B'_{bulk}	*at%*	*Amount of B'-site in the bulk*	*ICP-OES*
$O_{tot\ (bulk+surfacce)}$	*at%*	*Amount of oxygen in the material*	*O_2 determination analysis*
$A_{surface}$	*at%*	*Amount of A-site on the surface*	*XPS*
$B_{surface}$	*at%*	*Amount of B-site on the surface*	*XPS*
$B'_{surfcae}$	*at%*	*Amount of B'-site on the surface*	*XPS*
$O_{surfacce}$	*at%*	*Amount of oxygen on the surface*	*XPS*
$O_{lattice\ surf}$	*%*	*O1s surface species from fitting*	*XPS*
$O_{defects\ surf}$	*%*	*O1s surface species from fitting*	*XPS*
$O_{surface\ surf}$	*%*	*O1s surface species from fitting*	*XPS*
$O_{carbonates\ surf}$	*%*	*O1s surface species from fitting*	*XPS*
$O_{OH\ surface}$	*%*	*O1s surface species from fitting*	*XPS*
$O_{H2O\ surface}$	*%*	*O1s surface species from fitting*	*XPS*
$O_{oxy\ surface}$	*%*	*O1s surface species from fitting*	*XPS*
Centroid O1s peak	*eV*	*Centroid of the binding energy of the O1s peak* [c]	*XPS*
VB onset	*eV*	*Onset of valance band relative to Fermi level*	*XPS*
S_{BET}	*m^2/g*	*Surface area*	*N_2 adsorption*
Averaged Δx	*adimensional*	*n of O_2 atoms transferred during the TPO/TPR cycle/ n of ABO_3*	*TPO/TPR cycling*
CO_2 amount	*wt%*	*Amount of CO_2 released by heating the sample up to 1000°C (dwell of 1h)*	*TG-MS*
Rate of CO consumption	*$mmol \cdot g^{-1} \cdot h^{-1}$*	*Rate of CO consumption measured in steady-state experiments at 130°C in feed CO/O_2/inert: 1/20/79*	*CO oxidation catalytic measurements*

a: The distortion of O-B-O angles will be mostly cancelled out due to geometric reasons and therefore they can not be simply averaged like the interatomic distance. Because of this, the deviations have been calculated as absolute ones from the ideal octahedral values, which are: 90° for cis angle and 180° for trans angles. **b**: The tolerance factors have been calculated from the experimental data as follows: $tobs=\frac{<A-O>\mu}{<B-O>\mu * \sqrt{2}}$. **c**: The centroid of the O1s peak's function, which indicates the center of the spectrum mass, has been employed as primary feature of the O1s peak, in order to feed SISSO with an O1s parameter which is independent from the O1s fitting.

In the following calculation, two catalysts are missing with respect to the dataset employed for CO oxidation SISSO analysis (Table 5.1), such as $PrMnO_3$ and $PrMn_{0.6}Cu_{0.4}O_3$. This is a consequence of the choice to use the rate of CO oxidation as primary feature. Indeed, the steady-state experiments in CO oxidation where performed over the batches #31345 and 29908, while propane oxidation

was measured over #30650 and #31163, for $PrMnO_3$ and $PrMn_{0.6}Cu_{0.4}O_3$, respectively. Additionally, a second primary feature has been added with respect to those employed in the SISSO calculation for CO oxidation (Table 5.2), the amount of CO_2 as detected by TG-MS experiments (see Section 3.2.2 and Figure SI 6).

5.2.1.1 $(La,Pr)Mn_{(1-x)}Cu_xO_3$ series in dry feed experiments ($C_3H_8/O_2/Ne/N_2$=5/10/2/83)

The fitted models calculated with q=1,2 are reported below in Table 5.6 and Figure 5.7, respectively. Both the SISSO calculated models for initial rates of both propane consumption and propene formation present optimal complexity having q=2 and D=1 (Figure 5.6 a and b). While, for the initial rates of CO_2 formation and the products ratio, the optimal complexity is defined by q=1 and D=1 (Figure 5.6 c and d).

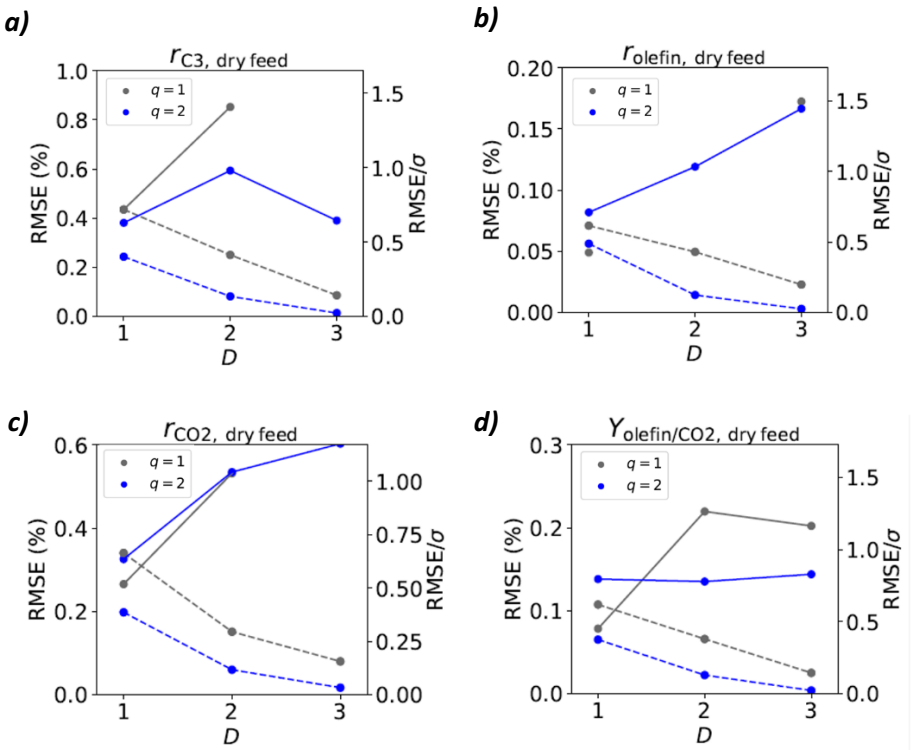

Figure 5.6. *CV analysis of models calculated by SISSO for initial rates in propane at 300°C in dry feed $C_3H_8/O_2/Ne/N_2$=5/10/2/83 over the $(La,Pr)Mn_{(1-x)}Cu_xO_3$ series. The CV errors shown on the primary y axis (left one) corresponds to the averaged RMSE across the leave-out-one-material-CV-iterations. The secondary y axis (right one) displays the CV-RMSE as a fraction of the standard deviation of the rates in propane oxidation among the whole training set. Color-code: grey: rung=1 and blue: rung=2. Continuous lines: calculated prediction and dotted lines: training.*

Table 5.6. Table with listed optimal models for each target property and the equation number for the SISSO calculation performed in propane oxidation in dry feed (C_3H_8/O2/Ne/N_2=5/10/2/83) at 300°C over the (La,Pr)Mn(1-x)CuxO3 series.

Target property **(mmol·g^{-1}·h^{-1})**	**Equation #**	**Calculated SISSO descriptor**
Initial rate of propane consumption	5.4	3.020 + 3.399 *[(B′$_{bulk}$ / surface area) / (O $_{H2O\ surface}$ − O $_{surface\ surface}$)]
Initial rate of propene formation	5.5	1.350 -6.149 * |(averaged Δx * O $_{surface\ surface}$) − (O $_{OH\ surface}$ − O $_{defect\ surface}$)|
Initial rate of CO_2 formation	5.6	1.071 + 1.689 * O $_{surface\ surface}$ / averaged Δx
Initial rate of propene/initial rate of CO_2	5.7	0.203 + 3.998 * (O $_{H2O\ surface}$ * $<BOB>_{\sigma}$)

Among the found descriptors listed in Table 5.6, the one which presents the highest train RMSE (0.340) is Eq. 5.6, plotted in Figure 5.7 c. While, the initial rates seem to present a rather good linear correlation with the optimal SISSO calculated descriptors (Figure 5.6 a-c). From the SISSO analysis in propane oxidation in dry feed it emerges that the oxygen species from O1s fitting, are present in each model, emphasizing the primary role of surface oxygen in propane oxidation (Eq. 5.4-7). Indeed, the oxygen mobility on the surface has widely been reported to be strictly connected to the catalytic performance of perovskite-like catalysts in propane oxidation, [207, 275, 364, 411] since also the oxygen vacancies are involved into its functioning under dynamic conditions. In particular, a close parallel has been found between the catalytic activity in propane oxidation and the oxygen species adsorbed on the vacancies sites, suggesting that propane oxidation proceeds through a suprafacial mechanism over the $La_{(1-x)}Ca_xCoO_3$ material. [411] Interestingly, the presence of oxygen surface fraction is frequent among the found descriptors, appearing in the optimal models for the initial rates of propane consumption, propene formation and CO_2 formation (Eq. 5.4-6). This O1s species is believed to be related to electrophilic oxygen on the surface, which has generally been attributed to be responsible for oxygen insertion step in propane oxidation (from propene to acetaldehyde), [11] but more recent studies over perovskite catalysts have evidenced how this species seems to synergistically cooperate with OH species for the selectivity to propene, in contrast to oxygen defect concentration which shows a depletion in parallel to the selectivity's increase (which is always displayed in Eq. 5.5 for the selectivity to propene together with oxygen surface species). [275] In moderate contradiction with the general beliefs in catalysis, [207, 412-414] the surface area is seemingly not particularly relevant for the catalytic performance according to SISSO analysis, since it appears only in one optimal model (Eq. 5.4). In agreement with the expectations, O1 species related to Mn as adsorption site (O1s OH and H_2O) [275, 404] and Cu are displayed between the relevant primary features for the catalytic activity (Eq. 5.4 and 5.5), confirming the key-role of the B-site metals for

the catalytic performance. [199, 200] Instead of the Cu amount, in the models for the selectivity to propene and to CO_2 it is presented the averaged delta x (see delta x calculation in Section 2) deriving from the TPO/TPR cycling experiments performed at 300°C (same temperature of propane oxidation experiment). The averaged delta x accounts for the oxygen capacity of the material since it basically represents the amount of oxygen which is exchanged either during TPO or during TPR cycles and in the studied systems it is linearly correlated with Cu bulk amount as shown in Figure 3.17 in Section 3.2.4. The bulk oxygen capacity is a property which is also strictly related to the lattice oxygen mobility and the motif of the host structure, [9] being always slightly higher for Pr-samples in comparison with the corresponding La-based ones (as shown in Figure 3.16 and 3.17 in Section 3.2.4), probably ascribable to the fact that the enhanced crystallographic strain induced by Pr's size is partially influencing also the bulk vacancies by tuning the oxygen lattice structure. Finally, the only structural parameters which appears among the relevant primary feature is $<BOB>_{\sigma,}$ which is related to the octahedral tilting and thus indirectly also to the crystallographic strain and the A-site size. [313]

In conclusion, the SISSO calculations performed in propane oxidation in dry feed over the $(La,Pr)Mn_{(1-x)}Cu_xO_3$ show results that also in this case (like it was for CO oxidation) are in line with the formulated hypothesis in Section 4.2.1. The explained role of some primary features might present a lower degree of reliability, since it is largely based on the interpretation and comparison with literature, like for instance the association of OH and H2O species to Mn and the electrophilic nature of oxygen surface species, [275, 404] while other interpretation, like the cited relation between the averaged delta x with the Cu bulk amount, are supported by experimental evidence (Figure 3.17). Finally, in spite of the SISSO results presented in Eq. 5.2 and 5.3, the A-site is not present in any of the discussed Equations (Eq. 5.4-7). Some other primary features indirectly related to it rather appear, such as the $<BOB>_{\sigma}$ and maybe the averaged delta x, since it always shows a difference between Pr and La samples, as shown in Figure 3.16 and 3.17. The lack of the direct correlation of a primary feature representing the A-site in propane oxidation can be perfectly contextualized in the catalytic results presented in Section 4. Indeed, differently from CO oxidation, where it is clearly evident that the La-based samples present an inverse correlation of reaction rate with respect to the Pr-based ones (Figure 4.3), in propane oxidation two opposite trends between the two series are never generated (Figure 4.9). The calculated models indicate that the influence of A-site size has less importance in propane oxidation with respect to CO oxidation, as it was already suggested by analyzing the catalytic trends (Figure 4.3 and 4.9).

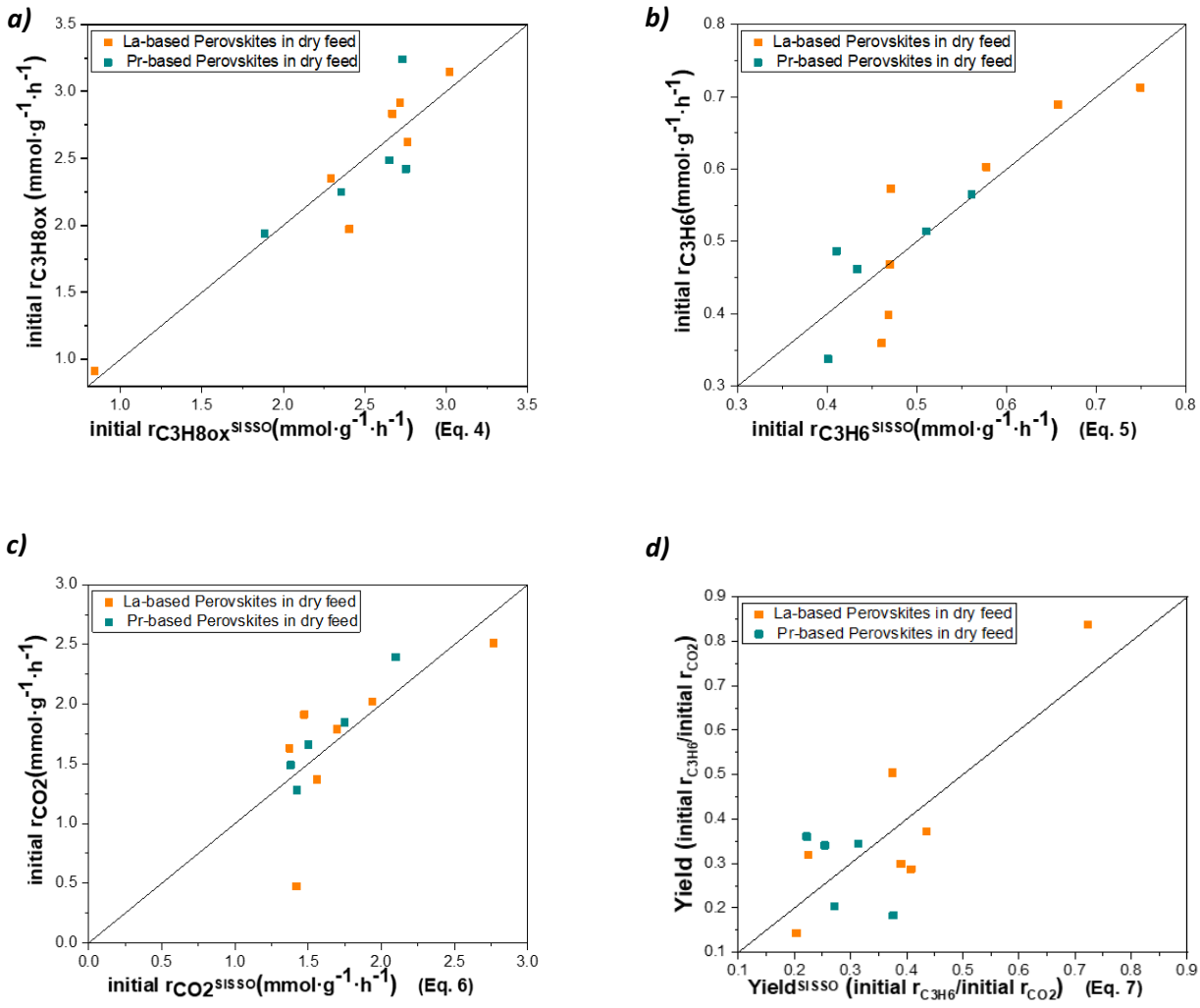

Figure 5.7. *Graphs showing the initial rates of* ***a)*** *propane consumption,* ***b)*** *propene formation,* ***c)*** *CO_2 formation and* ***d)*** *the product ratio measured at 300°C in dry feed $C_3H_8/O_2/Ne/N_2$: 5/10/2/83 over the descriptor calculated by SISSO employing the data reported in Table 16 and 17 as dataset. Orange: La-based samples, green: Pr-based samples*

5.2.1.2 (La,Pr)$Mn_{(1-x)}Cu_xO_3$ series in wet feed experiments ($C_3H_8/O_2/Ne/N_2/H_2O$=5/10/2/43/40)

The fitted models calculated with q=1,2 are reported below in Table 5.7 and Figure 5.9, respectively. All the SISSO calculated optimal models are defined by rung=1, being D=2 in each case, except for the model of the initial rate of propene formation (Figure 5.8 b, 5.9 b).

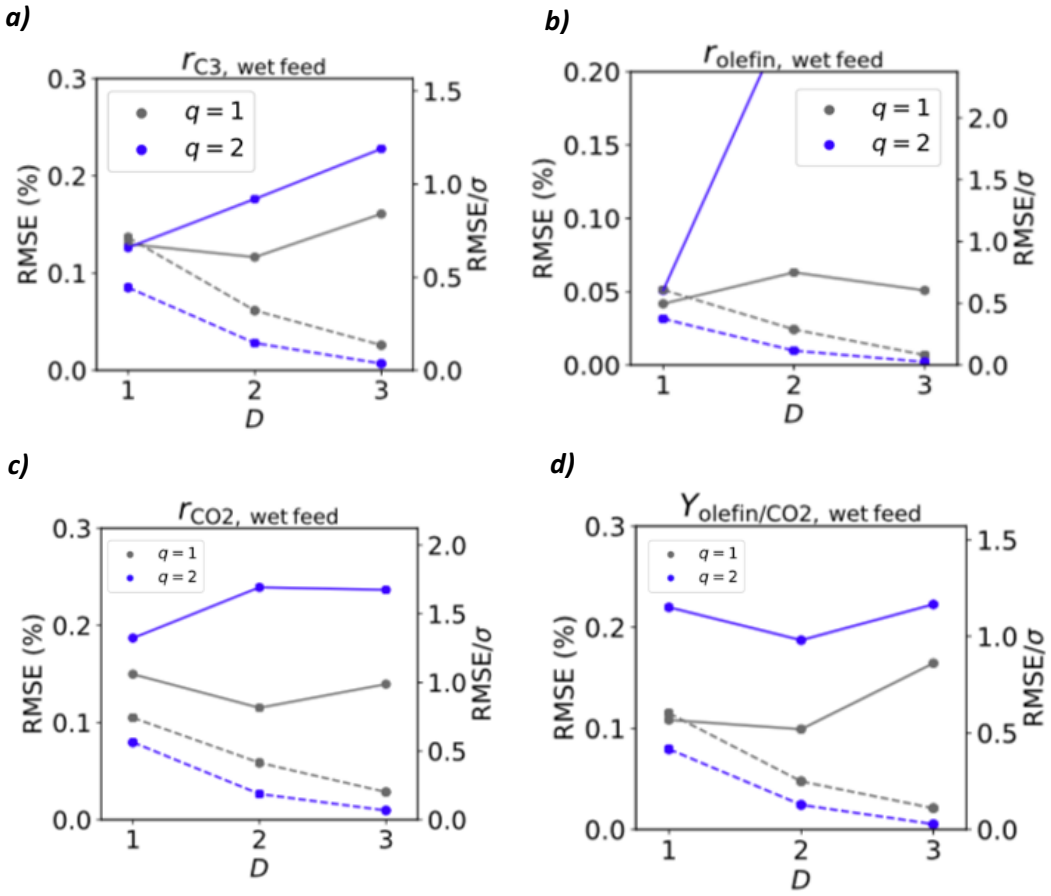

Figure 5.8. *CV analysis of models calculated by SISSO for initial rates in propane at 300°C in dry feed $C_3H_8/O_2/Ne/N_2/H2O=5/10/2/43/40$ over the (La,Pr)$Mn_{(1-x)}Cu_xO_3$ series. The CV errors shown on the primary y axis (left one) corresponds to the averaged RMSE across the leave-out-one-material-CV-iterations. The secondary y axis (right one) displays the CV-RMSE as a fraction of the standard deviation of the rates in propane oxidation among the whole training set. Color-code: grey: rung=1 and blue: rung=2. Continuous lines: calculated prediction and dotted lines: training.*

Table 5.7. Table with listed optimal models for each target property and the equation number for the SISSO calculation performed in propane oxidation in wet feed ($C_3H_8/O_2/Ne/N_2/H_2O=5/10/2/43/40$) at 300°C over the (La,Pr)$Mn_{(1-x)}Cu_xO_3$ series.

Target property (mmol·g^{-1}·h^{-1})	**Equation #**	**Calculated SISSO descriptor**
Initial rate of propane consumption	5.8	1.054 -6.529* |O $_{carbonates\ surface}$ – O $_{surface\ surface}$| - 50.01 * (averaged Δx)^6
Initial rate of propene formation	5.9	0.960 – 19.010 * (A $_{surface}$ / Mn 3s splitting)
Initial rate of CO_2 formation	5.10	-722.6 + 0.001 *(surface area / O $_{H2O\ surface}$)+ 1.362 *(centroid O1s + VB onset)
Initial rate of propene/initial rate of CO_2	5.11	0.718 + 5.851 * |O $_{carbonates\ surface}$ -O $_{surface\ surface}$| -730.5 *(O $_{carbonates\ surface}$ /r CO consumption)

The SISSO results for wet feed experiments over the (La,Pr)$Mn_{(1-x)}Cu_xO_3$ series reflects how the steam addition change the catalytic scenario in propane oxidation (Figure 4.7, 4.10 and 4.11 in Chapter 4.2.1). Carbonates species on the surface appear in the optimal models for the rate of propane consumption and the products ratio (Eq. 5.8 and 5.11), while it was never present in the models calculated for dry feed (Eq. 5.4-7). It is difficult to believe that O1 carbonates are directly involved in the catalytic activity, since also their amount seems to be very close to 0 in wet feed at 300°C, as detected in NAP-XPS measurements for three Pr-based catalysts (Figure 4.17). It is more intuitive to address the relevance of O1s carbonates species to surface sites on which they might likely adsorb and block their function, such as electrophilic sites and Lewis-acid sites. [406] If, on the one hand it seems easy to determine the nature of these sites by the following approach, on the other hand its exact determination becomes very challenging. Indeed, it could be either the A-site surface termination, or the B-metal one, or the oxygen vacancies on the surface or a combination of them. However, the involvement of surface adsorbed carbonates species into the catalytic performance should not be neglected, since in some cases it has been reported to exert an influence on catalysis or even to boost the activity. [415, 416] The averaged delta x, i.e. the oxygen capacity and the O1s surface species (probably electrophilic oxygen) are displayed as relevant primary features for the rates of propane consumption (Eq. 5.8) in wet feed, as it is in dry one (Eq. 5.4). This latter result highlight how the redox property of the material are important for propane conversion, indicating that probably the engine of the reaction mechanism of propane oxidation is not highly depended on the feed composition. The Equation 5.9 for the selectivity in wet feed can be interpreted as a confirmation of the results presented in Chapter 4.2.1. Indeed, only Pr-based samples present a positive trend between the Mn surface content and the selectivity (Figure 4.11 b) and the Mn oxidation state as evaluated by Mn3s splitting, increases in wet feed, following the same order of the selectivity among the catalysts (Figure 4.11 b, 4.14, 4.15 and Table 4.2). Therefore, the primary features display in Eq. 5.9 posses physical and cross-checked experimental sense. Once again, the surface area is seemingly not a decisive parameter to describe all the target properties, appearing only in CO_2 formation rates (Eq. 5.10), where also the centroid of O1s peak (the only primary feature for O1s which is independent from the fitting model) and the valance band onset, which account for the electronic density, appear. It seems that the properties which count most for the total combustion path can be summarized into the surface electronic function of the material combined with Mn amount or other electrophilic adsorption sites for water and the surface area. Finally, the rates of CO consumption are displayed as relevant primary feature in the found descriptor of the products' ratio (Eq. 5.11), highlighting how CO oxidation might partially works as probe reaction for propane oxidation. However, other primary features needs to be involved in the model in order to fit the catalytic data, such as the carbonates and surface species, whose nature and identification still remains not fully elucidated.

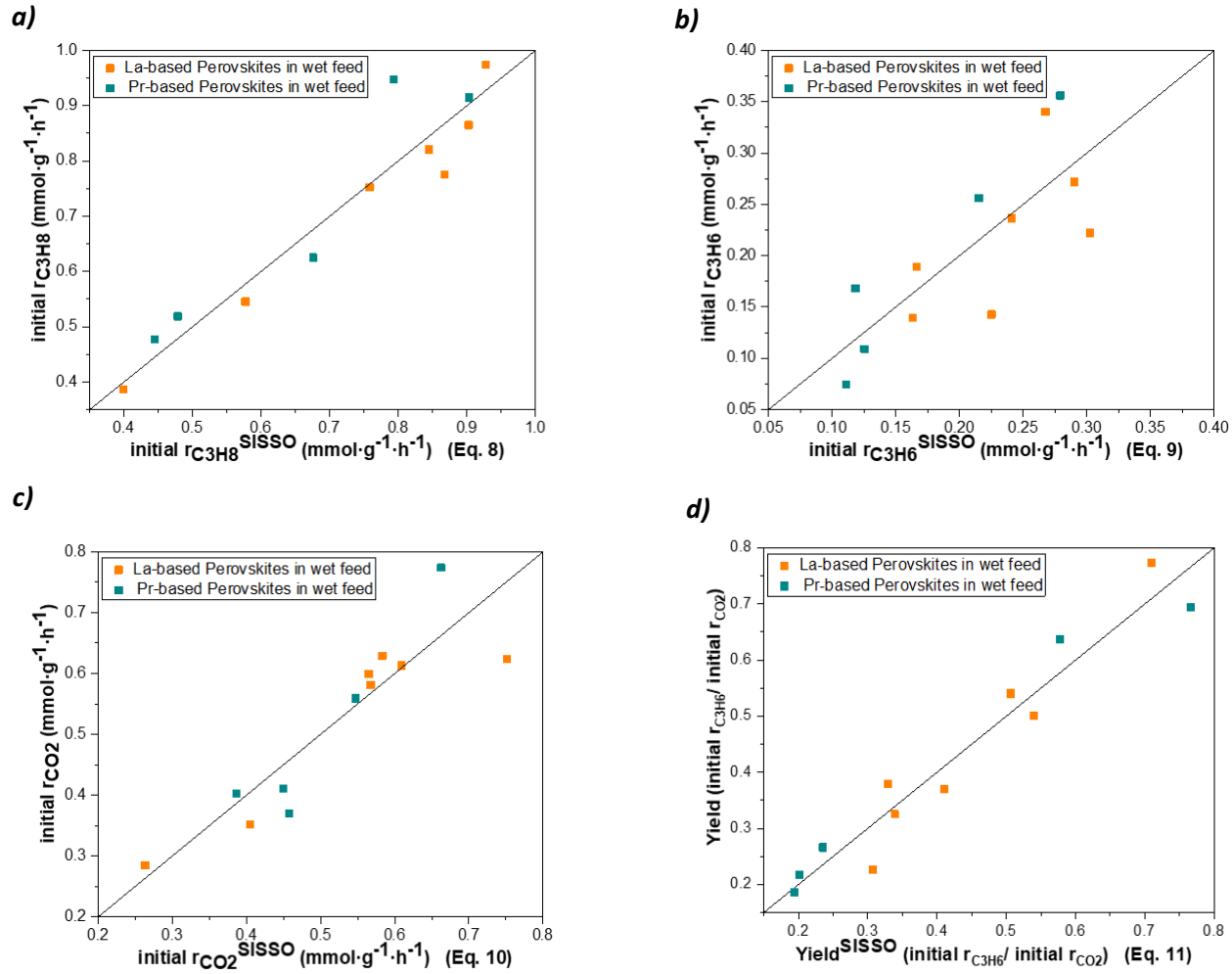

Figure 5.9. *Graphs showing the initial rates of* ***a)*** *propane consumption,* ***b)*** *propene formation,* ***c)*** *CO_2 formation and* ***d)*** *the products' ratio measured at 300°C in wet feed $C_3H_8/O_2/Ne/N_2/H_2O$: 5/10/2/43/40 over the descriptor calculated by SISSO employing the data reported in Table 16 and 17 as dataset. Orange: La-based samples, green: Pr-based samples*

5.2.2 (La,Pr)$Mn_{(1-x)}Cu_xO_3$ series plus (Pr,Nd)$Mn_{0.7}B'_{0.3}O_3$ catalysts

As it was done for CO oxidation SISSO analysis (Section 5.1.2), it has been chosen to implement the elemental variability also for the SISSO calculation in propane oxidation and in order to do so, the catalysts series including different B´-site has been added to the dataset (Table 5.8). By analyzing the measured data in propane oxidation, it seems that the activity seems to be dominated principally by Mn (Figure 4.21 and 4.22), although from the Temperature programmed reaction it emerges some differences can be detected among the Mn-based catalysts following the order : Zn > Ni > Co > Fe (Figure 4.21 b) . The found results in propane oxidation are coherent with what is generally reported in the literature, where it is claimed that Co and Ni boost Mn-based perovskites activity [364, 365] and that the influence of Fe is limited to preserve the structure by inhibiting B-site segregation or shifting. [366] However, the selectivity plot, clearly shows how the synergistic effect of a double B-site [309] might change the rules into the catalytic game. Indeed, $NdMn_{0.7}Fe_{0.3}O_3$

presents higher initial rate of selectivity formation in comparison with Ni and Zn-based catalysts (Figure 4.23 b). Additionally, it seems that the selectivity order among the catalysts strongly resemble the one created for CO oxidation rate (Figure 4.4 and 4.23 b), highlighting how the processes which control CO oxidation might influence also the selectivity to propene and not only for the conversion, as it was speculated just by looking at the (La,Pr)$Mn_{(1-x)}Cu_xO_3$ catalytic data (Figure 4.3 and 4.9 a, c). AI analysis can help to better individuate the relevant primary feature able to encode the differences presented in the catalytic performance of the (Pr,Nd)$Mn_{0.7}B'_{0,3}O_3$ samples (Section 4.2.2), but most important, they can elucidate whether the results found for the (La,Pr)$Mn_{(1-x)}Cu_xO_3$ series are still valid and therefore generalizable for similar compounds. Also for this calculation the initial rate of propane consumption, the initial rate of propene and CO_2 formation and the $\frac{\text{initial rate of propene formation}}{\text{initial rate of } CO_2 \text{ formation}}$ ratio have been chosen as target properties in dry ($C_3H_8/O_2/Ne/N_2$=5/10/2/83) and in wet feed ($C_3H_8/O_2/Ne/N_2/H_2O$=5/10/2/43/40). The 16 candidate materials and the 31 employed primary features for the training set are listed above in Table 5.5 and below in Table 5.8 (minus CO_2 amount, Mn3s splitting and averaged delta x), respectively.

Table 5.8. Table with listed the nominal composition, the ID number, the A-site metals and the B´-site one of the materials employed for the SISSO analysis in propane oxidation over the whole perovskite matrix.

Nominal Formula	Sample's ID #	A-site	B´-site	B´ loading amount
$LaMnO_3$	30649	La	Cu	0
$LaMn_{0.9}Cu_{0.1}O_3$	30867	La	Cu	0.1
$LaMn_{0.8}Cu_{0.2}O_3$	31180	La	Cu	0.2
$LaMn_{0.75}Cu_{0.25}O_3$	30635	La	Cu	0.25
$LaMn_{0.7}Cu_{0.3}O_3$	30659	La	Cu	0.3
$LaMn_{0.65}Cu_{0.35}O_3$	30624	La	Cu	0.35
$LaMn_{0.6}Cu_{0.4}O_3$	31285	La	Cu	0.4
$PrMn_{0.9}Cu_{0.1}O_3$	31070	Pr	Cu	0.1
$PrMn_{0.8}Cu_{0.2}O_3$	31021	Pr	Cu	0.2
$PrMn_{0.75}Cu_{0.25}O_3$	30637	Pr	Cu	0.25
$PrMn_{0.7}Cu_{0.3}O_3$	30934	Pr	Cu	0.3
$PrMn_{0.65}Cu_{0.35}O_3$	31176	Pr	Cu	0.35
$PrMn_{0.7}Zn_{0.3}O_3$	33380	Pr	Zn	0.3
$PrMn_{0.7}Ni_{0.3}O_3$	33366	Pr	Ni	0.3

Table 5.8 (cont.)

$PrMn_{0.7}Co_{0.3}O_3$	33454	Pr	Co	0.3
$NdMn_{0.7}Fe_{0.3}O_3$	33621	Nd	Fe	0.3

5.2.2.1 $(La,Pr)Mn_{(1-x)}Cu_xO_3$ series + $(Pr,Nd)Mn_{0.7}B'_{0.3}O_3$ catalysts in dry feed experiments ($C_3H_8/O_2/Ne/N_2$=5/10/2/83)

The fitted models calculated with q=1,2 are reported below in Table 5.9 and Figure 5.11, respectively. All the calculated models present optimal complexity with q=1 and D=1, except the rate of propane consumption, which has q=2 (Figure 5.10 a).

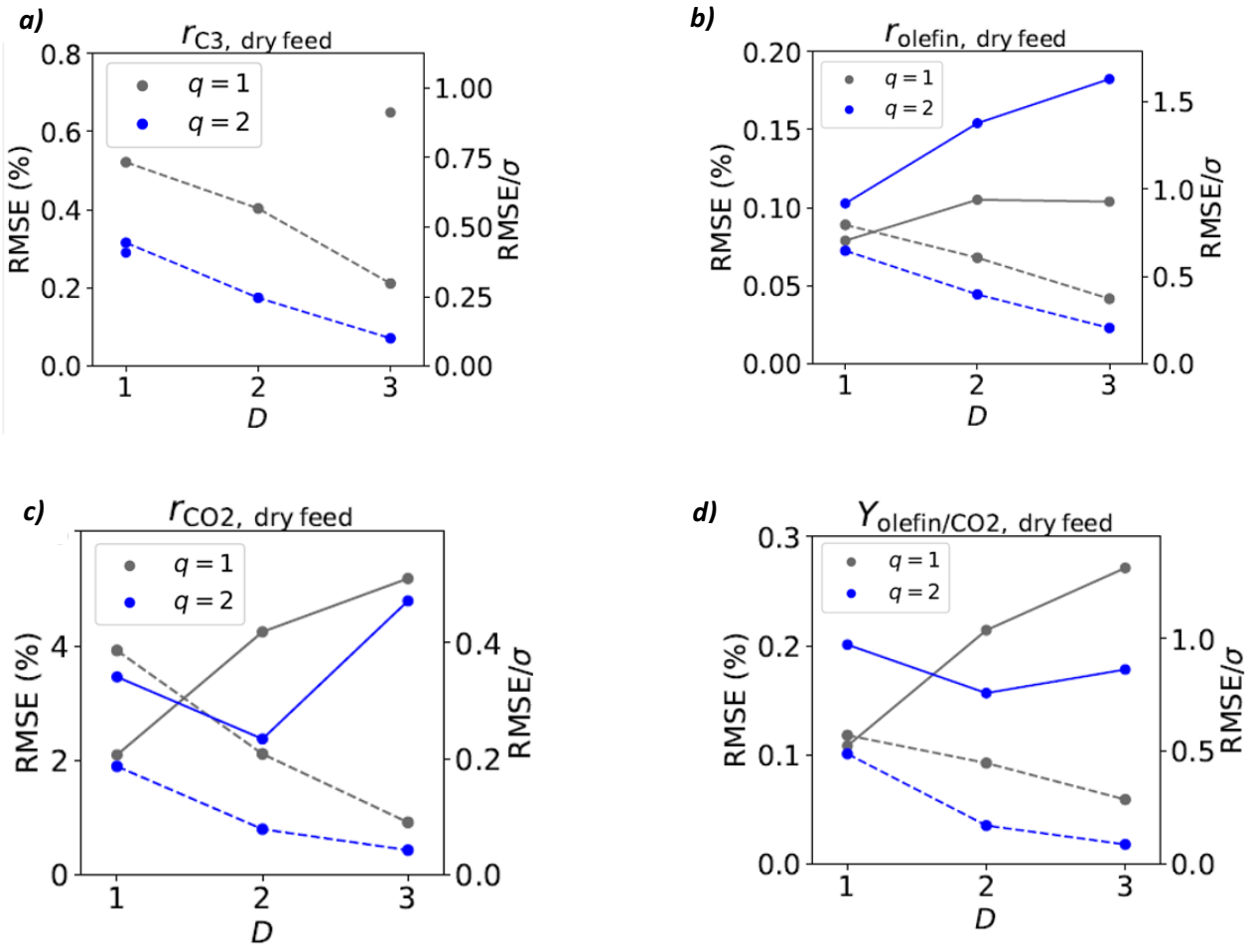

Figure 5.10. *CV analysis of models calculated by SISSO for initial rates in propane at 300°C in dry feed $C_3H_8/O_2/Ne/N_2$ =5/10/2/83 over the whole Perovskite matrix. The CV errors shown on the primary y axis (left one) corresponds to the averaged RMSE across the leave-out-one-material-CV-iterations. The secondary y axis (right one) displays the CV-RMSE as a fraction of the standard deviation of the rates in propane oxidation among the whole training set. Color-code: grey: rung=1 and blue: rung=2. Continuous lines: calculated prediction and dotted lines: training.*

Table 5.9. Table with listed optimal models for each target property and the equation number for the SISSO calculation performed in propane oxidation at 300°C in dry feed ($C_3H_8/O_2/Ne/N_2$=5/10/2/83) over the whole Perovskite matrix.

Target property (mmol·g^{-1}·h^{-1})	**Equation #**	**Calculated SISSO descriptor**
Initial rate of propane consumption	5.12	3.247 + 1.044 * [(VB onset * B´$_{surface}$)/ (O $_{H2O\ surface}$ − O $_{surface\ surface}$)]
Initial rate of propene formation	5.13	0.139 + 2.016 * (O $_{OH\ surface}$ + O $_{carbonates\ surface}$)
Initial rate of CO_2 formation	5.14	-34.770 + 869.2 * (O $_{defect\ surface}$ * A $_{surface}$)
Initial rate of propene/initial rate of CO_2	5.15	0.125 + 5.110 * (O $_{H2O\ surface}$ * $<BOB>_{\sigma}$)

There seems to be a lot of similarity between the calculated optimal models for the whole matrix (Eq. 5.12-15) and their corresponding calculated models for the (La,Pr)$Mn_{(1-x)}Cu_xO_3$ series (Eq.5. 4-7), suggesting that the results of the analyses discussed in Section 5.2.1.1 might be considered rather generalizable beyond the specific analyzed dataset. For instance, Eq. 5.15 shows exactly the same relevant primary features of Eq. 5.7, enforcing the result that an adsorption site for water (probably Mn or some structural pores)[275, 356] and the octahedral tilting due to the A-site size cation [313] play an influence to the product yield in propane oxidation performed in absence of steam. Also in the case of the descriptor for the rate of propane consumption (Eq. 5.12) there are a lot of analogies with that calculated for the (La,Pr)-series (Eq. 5.4). The B´amount together with oxygen surface and H_2O species appear again as relevant primary features, highlighting how H_2O adsorption sites or maybe even H_2O itself which block some active sites, surface electrophilic oxygen [275] and B´content play a central role for propane consumption. While, the best models for the initial rate of propene and CO_2 formation (Eq. 5.13 and 5.14) are rather dissimilar to those calculated for the (La,Pr)-series (Eq. 5.5 and 5.6), indicating that expanding the elemental folding fan on the input dataset makes a difference on the best model. By using the whole perovskite matrix as dataset, in the selectivity models carbonates and OH species are displayed as primary features. It seems that the selectivity is mainly governed by electrophilic and Lewis-acidity adsorption sites on the surface, such as A-site cation surface termination or oxygen vacancies. [406] Also Mn could be involved into the model since OH preferably adsorb on Mn. [404] Finally, CO_2 formation rate seems to depend on the defect concentration, which renders the catalyst too active, leading in this way to the total combustion path, and depends also on the A-site concentration of the surface, which might be indirectly responsible for the formation of active sites. [344]

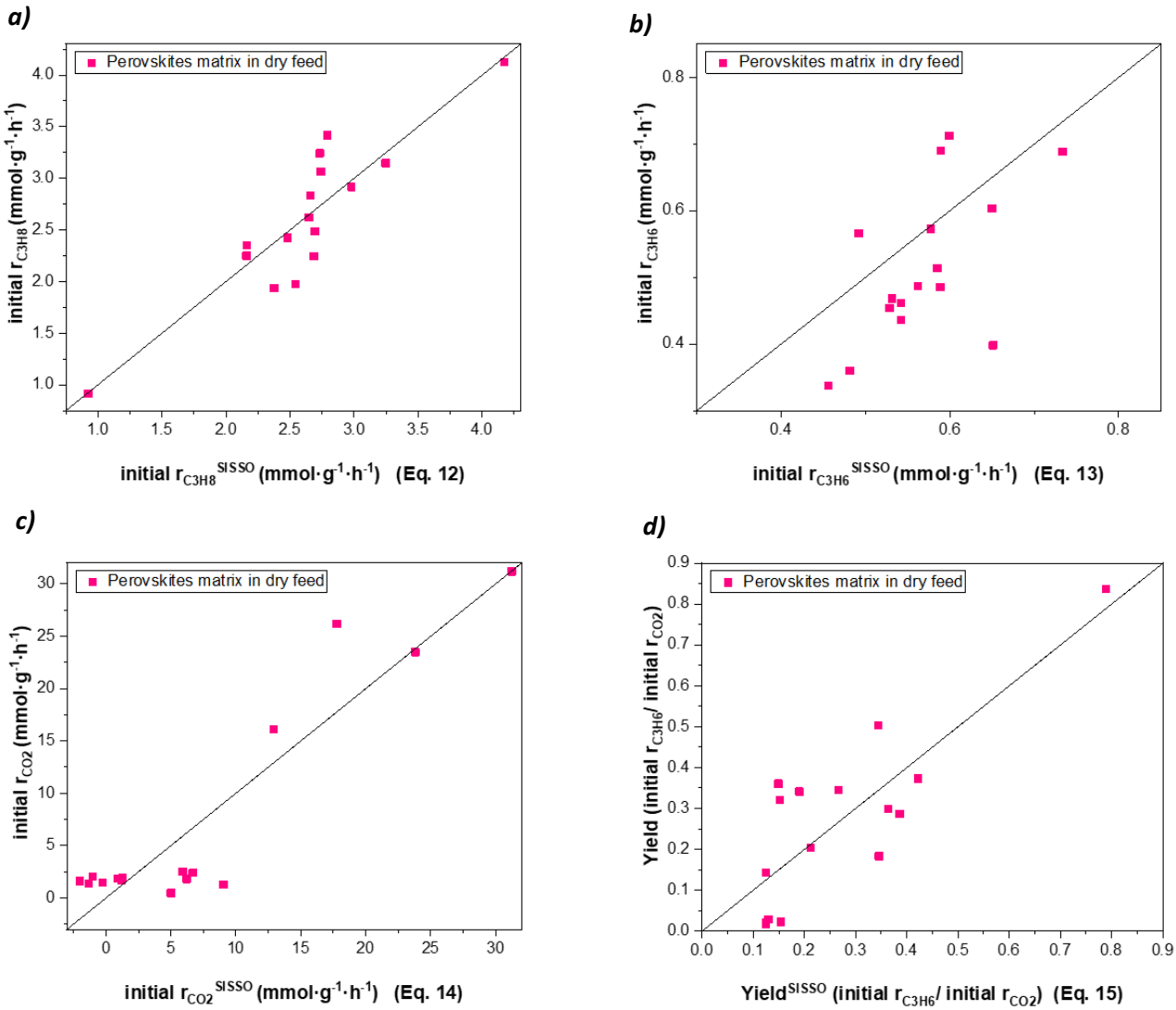

Figure 5.11. *Graphs showing the initial rates of* ***a)*** *propane consumption,* ***b)*** *propene formation,* ***c)*** *CO_2 formation and* ***d)*** *the products' ratio measured at 300°C in dry feed $C_3H_8/O_2/Ne/N_2$: 5/10/2/83 over the descriptor calculated by SISSO employing the data reported in Table 20 and 17 (-CO2 amount and averaged delta x) as dataset.*

5.2.2.2 (La,Pr)$Mn_{(1-x)}Cu_xO_3$ series + (Pr,Nd)$Mn_{0.7}B'_{0.3}O_3$ catalysts in wet feed experiments ($C_3H_8/O_2/Ne/N_2/H_2O$=5/10/2/43/40)

The fitted models calculated with q=1,2 are reported below in Table 5.10 and Figure 5.13, respectively. All the calculated models present optimal complexity with q=2 and D=1, except the rate of propane consumption, which has q=1 (Figure 5.12 a).

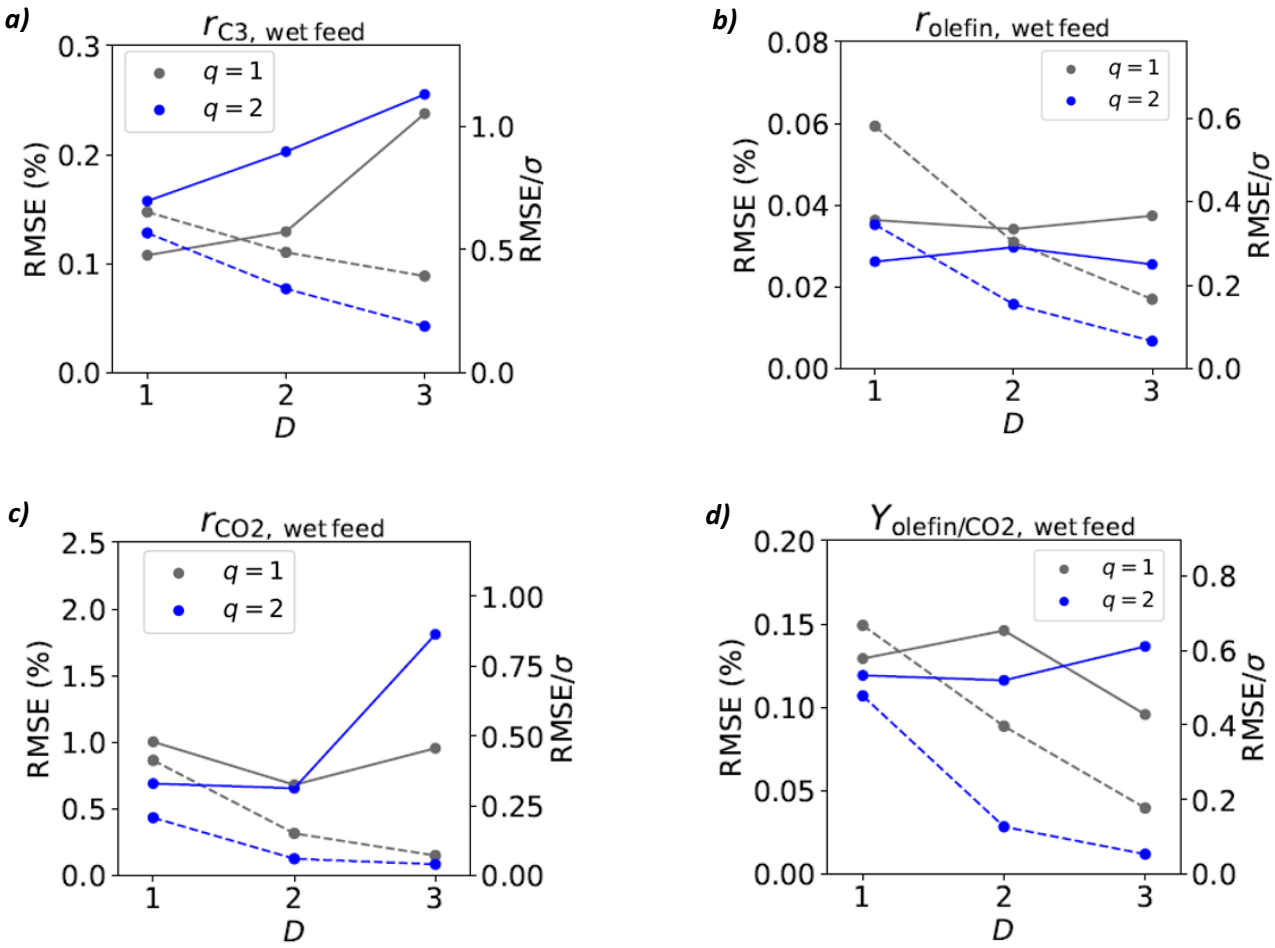

Figure 5.12. *CV analysis of models calculated by SISSO for initial rates in propane at 300°C in wet feed $C_3H_8/O_2/Ne/N_2/H2O$=5/10/2/43/40 over the whole Perovskite matrix. The CV errors shown on the primary y axis (left one) corresponds to the averaged RMSE across the leave-out-one-material-CV-iterations. The secondary y axis (right one) displays the CV-RMSE as a fraction of the standard deviation of the rates in propane oxidation among the whole training set. Color-code: grey: rung=1 and blue: rung=2. Continuous lines: calculated prediction and dotted lines: training.*

Table 5.10. Table with listed optimal models for each target property and the equation number for the SISSO calculation performed in propane oxidation in dry feed ($C_3H_8/O_2/Ne/N_2/H_2O$=5/10/2/43/40) at 300°C over the whole Perovskite matrix.

Target property (mmol·g^{-1}·h^{-1})	**Equation #**	**Calculated SISSO descriptor**
Initial rate of propane consumption	5.16	1.577 - 1.151 * (O $_{lattice\ surface}$ / VB onset)
Initial rate of propene formation	5.17	0.0935 - 0.029 * [(B´$_{surface}$ – Mn $_{bulk}$) * (r CO consumption * $<AO>_{\sigma}$)]
Initial rate of CO_2 formation	5.18	0.580 + 79.160 * ||B´$_{surface}$ – B´$_{bulk}$| - (B´$_{surface}$ – B´$_{bulk}$)|
Initial rate of propene/initial rate of CO_2	5.19	0.155 – 0.393 *[(O $_{H2O\ surface}$ * $<BOB>_{\sigma}$) / (O $_{H2O\ surface}$ – O $_{carbonates\ surface}$)]

In spite of dry feed results for SISSO analysis, where many analogies between the optimal models for the whole perovskites matrix and those for the (La,Pr)-series have been found, the results of SISSO analyses over the whole matrix in wet feed (Eq. 5.16-19) are very different from those obtained by using the (La,Pr)-series as input dataset (Eq. 5.8-11). This might indicate that the steam addition into the reaction feed could affect the catalytic scenario to different extent depending on the involved sample. In the rate of propane consumption, the lattice oxygen species and the VB onset are displayed as relevant chemicophysical properties (Eq. 5.16). The lattice oxygen might account also for Mn surface amount, since the amount of lattice oxygen species on the surface increases linearly with that of Mn on the surface in wet feed, as evidenced by NAP-XPS measurements performed over three Pr-based catalysts (Figure 4.19). However, it could also be that the lattice oxygen on the surface itself is involved into the catalytic activity in wet feed. As expected from the analysis of CO and propane oxidation data (Figure 4.4 and 4.23 b), CO oxidation works as probe reaction for the selectivity to propene (Eq. 5.17). [354] Apart from CO consumption rates, it seems that also bulk Mn amount and surface B´ one play a central role for the selectivity, but it is not only about the B-site, since also the cuboctahedral distortion induced by the A-site size appears in the equation. [344] Interestingly, the B´-site distribution between surface and bulk seems to be the most important parameter for the selectivity to CO_2 (Eq. 5.18). This latter result suggests that B´ concentration exerts a huge role on the structure of the material, by tuning the defects amount [201] and consequently affecting the total combustion path. The reason why this phenomenon becomes clear only using wet feed data as input dataset and B´concentration does not appear in the model for CO_2 selectivity in dry feed (Eq. 5.14), needs further elucidation. Finally, the model for the product yield in wet feed for the whole matrix (Eq. 5.19) strongly resemble that for dry feed for (La,Pr)-series and for the whole matrix (Eq. 5.7 and 5.15, respectively). This latter result indicates that water addition does not affect the product yield of the reaction for the whole matrix samples, rendering the drawn conclusion about the relevant primary features for the examined target property rather generalizable for Mn-based perovskite sample in propane oxidation. Indeed, it could be concluded that by regulating the amount of adsorption sites for water (probably Mn or some structural pores) [275, 356] and by tuning the the A-site size [313] , the control over the product yield in propane oxidation employing Mn-based perovskites catalysts might become feasible.

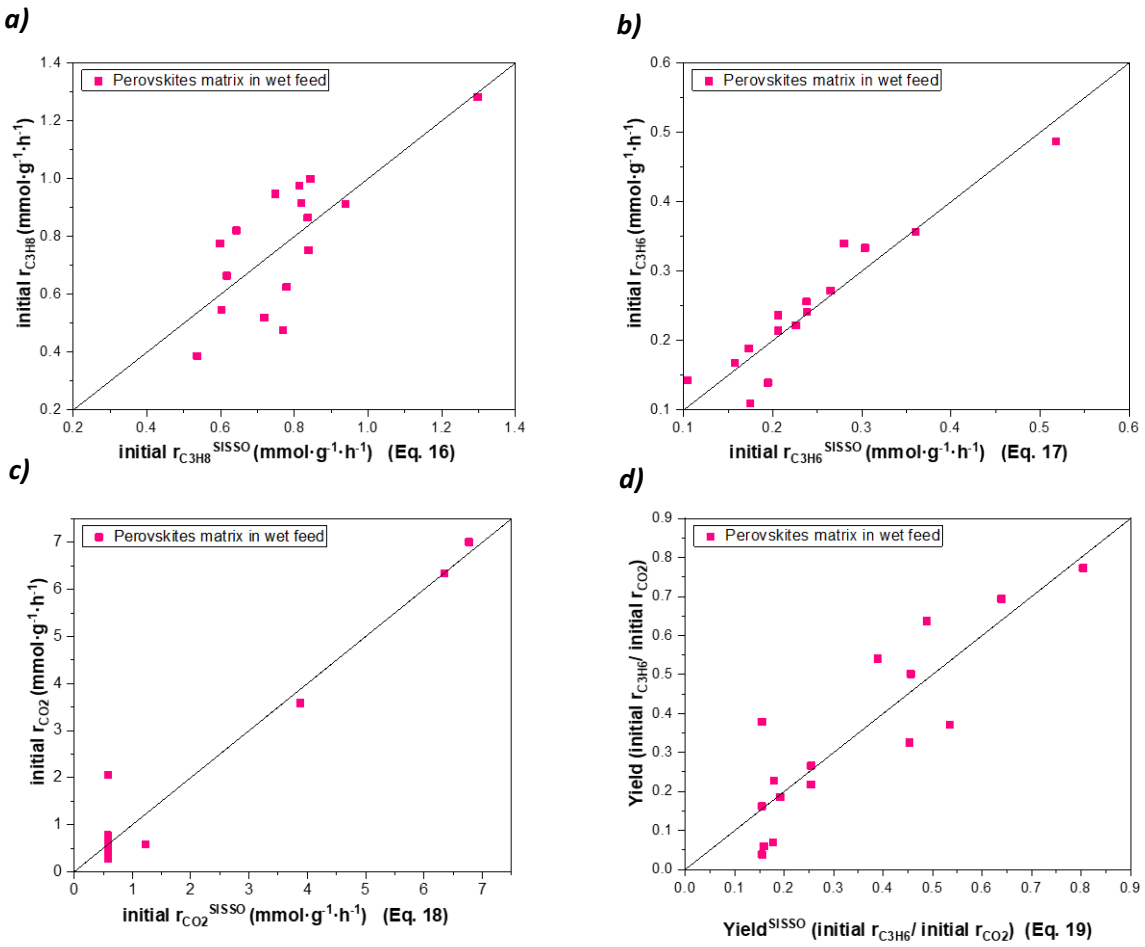

Figure 5.13. *Graphs showing the initial rates of* ***a)*** *propane consumption,* ***b)*** *propene formation,* ***c)*** *CO_2 formation and* ***d)*** *the products' ratio measured at 300°C in wet feed $C_3H_8/O_2/Ne/N_2/H_2O$: 5/10/2/43/40 over the descriptor calculated by SISSO employing the data reported in Table 20 and 17 (-CO2 amount and averaged delta x) as dataset.*

6. Conclusions

The selective oxidation of light alkanes plays an important role in heterogeneous catalysis, since olefins constitute the key building blocks for the (petro)chemical industry and their manufacture process has a fundamental economical and environmental role. [6, 7] Due to impending oil shortage in the near future, it is vital to find an economical and environmental-friendly route to produce alternative building blocks for chemical industry, such as propene and acrylic acid. Many attempts have been done in the past decades in order to implement an efficient and suitable catalyst for alkane oxidation. However, no real breakthrough has been achieved in the catalytic community from the discovery of MoVTeNb M1 phase-pure catalyst patented by Mitsubishi Corp. in the early 1990s. The lack of homogeneity of data presented in the literature, regarding the many proposed catalytic systems, addresses the new oxidation catalysis research back to fundamental roots, since only a deep understanding and a systematic study of the intrinsic nature of the catalyst may constitute the key for the future. In the past, there have been made many attempts to determine key-factors, which aim to gain control over the activity and selectivity of catalytic systems. [9, 14-24] The investigated features could be divided into three main groups: structural aspects, surface properties and the electronic structure/properties. It is generally accepted that the characterization of some of the properties mentioned above for a given catalyst and their further correlation with catalysis could lead to significant breakthrough in the knowledge of the reaction process. Nevertheless, in gathering data reported in the literature, a lack of homogeneity in these latter ones is evident and hence they cannot really serve as basis for a comparison to extrapolate general rules. The “seven pillars” of heterogeneous selective oxidation provide a useful framework for the development of complex selective oxidation catalysts and link the catalytic properties with the material science part of them. [31] However, the dynamic nature of the catalyst is not included. Therefore, the seven “pillars” still remains a rather formal concept to design a new catalyst, because they are not universally applicable. Designing a new catalyst is a challenging task, particularly when it is addressed to the selective oxidation of alkanes. This is because of the numerous consecutive/parallel reaction steps which compose the complex reaction network. [25, 265] Anyway, some design parameters, such as: (a) phase purity of the bulk which confer structural stability, (b) multifunctionality of the active sites in order to satisfy the required various reaction steps, (c) semiconducting properties of the bulk beneficial to the transfer of a high number of electrons and (d) balanced oxygen activation to avoid the total combustion to carbon dioxide, are considered to be important. [20, 266] Looking into this direction, perovskite-like oxide phase-pure catalyst seems to be the most suitable candidate as “starting” catalyst to be improved because it fulfills most of criteria cited above. These bulk oxide catalysts present a high level of flexibility without destroying their structure, due to the tolerance factor [50] and their crystal structure can present lattice distortion, due to the tilting of the octahedra,

which depends on the temperature and affects bulk and surface electronic properties by influencing the charge-carrier dynamics of the bulk. Indeed, perovskites act as a chemiresistor where it becomes possible to modulate the electronic structure of the surface tuning the conductivity of the bulk. [267-272] They can be either n-type or p-type semiconductors, behaving mostly as p-type semiconductors under oxidative feed. [270, 271] Furthermore, the defect chemistry of perovskites, beside of providing a high number of oxygen vacancies, which is beneficial to control the oxygen activation during reaction process, [273] can equilibrate with changes in the electric conductivity under various temperatures and oxygen activities. The present Thesis aims to implement the fundamental knowledge in oxidation catalysis through the so-called descriptor-based approach. For this purpose twenty-three phase-pure perovskite-like catalysts (two of them are 97% phase-pure perovskite-like catalysts) have been synthesized, characterized and tested in CO and in propane oxidation in order to serve as basis for artificial intelligence analysis. The main idea of this project is to synthesize many perovskites, perovskite-like structures and other structures composed by Mn as B-site cation combined with an other metal belonging to the 3d or 4d row of the periodic table (the synergistic effect is claimed to be beneficial to the catalytic performance). The selected element at the B-site have similar ionic radius between each other (ionic radii in six coordination: Co^{2+} = 0.65 Å, Zn^{2+}= 0.74 Å, Ni^{2+}=0.69 Å, Fe^{2+}=0.61 Å, Cr^{2+}=0.73 Å, Pd^{2+}=0.86 Å, Cu^{2+}= 0.73 Å and $Mn^{3+/4+}$=0.53-0.64 Å,). The most utilized metals as B-site have been Cu and Mn, where Cu is reported to be a promoter in oxidation reaction [10, 284-286] and finally Mn is a well-known element in oxidation catalysis [287] and it was also found to be selective in alkane oxidation. [288, 289] The A-site cation has been changed between La^{3+}, Pr^{3+}, Nd^{3+} and Sm^{3+} to tune the structural and electronic properties. Therefore, twenty-one purely phase-pure perovskites, among which fourteen present the general formula $(La,Pr)Mn_{(1-x)}Cu_xO_3$ (with x=0-0.4) and other five with general formula $AMn_{0.7}B'_{0.3}O_3$ (with A=Pr, Nd and Sm and B'=Co, Zn, Ni, Fe, Cr) and $(La,Pr)_2CuO_4$ perovskite-related structures have been synthesized, tested in CO and propane oxidation and subjected to standard structural characterizations in order to obtain numerical values of some properties (also known as basic descriptors) for artificial intelligence analysis. As first step, the $(La,Pr)Mn_{(1-x)}Cu_xO_3$ series has been investigated in detail. From the combined analysis of the characterizations data with those of catalysis, it emerges the high complexity generated by the synergistic effect of a double B-site into the catalytic dynamic. Despite of what is generally reported in the literature where it is claimed that the B-site is the responsible element for the catalytic performance, [200, 201, 310] the catalytic results highlight that also the A-site indirectly influences the catalytic performance, in particular in CO oxidation, where the oxidation rates present two opposite correlations over the Mn surface content (Figure 4.3). This is probably due to the fact the structural modifications conferred by the different A-site [313] induce the generation of diverse active sites and different active oxygen species on the catalysts´ surface. [344-346] Also in propane oxidation the difference between the La- and the Pr-based series is present, in particular in the selectivity to propene in wet feed, where Pr-based samples generate a positive

trend with the selectivity and La-based samples do not (Figure 4.11 b). As next step, NAP-XPS studies over three Pr-based catalysts with different Cu loading have been performed in order to investigate the catalysts' surface and subsurface regions under reaction conditions in propane oxidation. From the near-working-conditions measurements it emerges that the lattice oxygen species correlates positively with Mn surface content in wet feed, which in turn correlates positively also with the selectivity to propene, as measured in the plug flow reactor. The Artificial Intelligence analysis performed over the (La,Pr)$Mn_{(1-x)}Cu_xO_3$ series, where the optimal model is defined by q=1 and D=2 (Figure 5.3), have highlighted how a single primary feature based on chemical intuition is not sufficient to fully describe the properties linked to the catalytic performance in CO oxidation. Additionally, the found optimal model has confirmed the hypothesis and expectations formulated for the (La,Pr)-based series, where also the A-site is indirectly involved in the catalytic performance in CO oxidation. Indeed, in the reported model in Eq. 5.2 appear the following primary features: the Cu surface content, the distorsion parameter D (which is an expression for the deviation of the reduced lattice parameters from the cubic root of the normalized unit cell volume) and the concentration of the A-site both on the surface and on the bulk. Indeed, beside of the fundamental role of the B-site for the catalytic performance, [166, 200, 201, 308] the indirect influence of the A-site´s size on the catalytic scenario discussed in Section 4.1.1, which acts by tuning the structure and consequently the electronic and defective properties of the materials, [313, 344] seems to be a passepartout in order to solve the opposite trends always shown between the La- and Pr-series when plotted over a descriptor composed by a single physico-chemical property (Figure 4.3). Beside of the amount of the A-site both on the bulk and on the surface (at%), the presence of D in the SISSO equation (Eq. 5.2), which might be related to the structural strain established by the A-site size, is a further confirmation of the previously discussed indirect influence exerted by the structural modifications. Also the SISSO analysis performed over the whole perovskite matrix ((La,Pr)$Mn_{(1-x)}Cu_xO_3$ series + $AMn_{0.7}B'_{0.3}O_3$ series) presented in Eq. 5.3 confirms the results discussed for the (La,Pr)-series in CO oxidation. Indeed, among the primary features appear the content of B and A on the surface, the distorsion parameter D and in addition the valence band onset, the total oxygen content and the amount of OH species on the surface. The optimal model for the whole matrix in CO oxidation could basically been interpreted as an expansion of the model for the (La,Pr)-series, where the valence band onset is a parameter which basically explains the elemental diversity in the matrix, since it accounts for the electronic density which is different from atom to atom, by affecting the physical electronic structure and the binding site. [408] Additionally, it identifies also the OH surface species as master key physicochemical property which is generally correlated to the presence of Mn-OH surface groups in presence of steam. [275, 404] On the other side, the amount of total oxygen (bulk+surface) might be directly interpreted as the major role that the bulk oxygen has on the reaction mechanism, in case this latter one belongs to interfacial class, and also on its correlation with oxygen vacancies formation, which are known to be fundamental to control the

catalytic activity. [9, 201, 405-407] Finally, it can be concluded that the major outcome from the calculated SISSO models in CO oxidation is the confirmation of the formulated hypothesis that also the A-site plays a role on the catalytic performance, due to the structural and electronic modifications indirectly induced by its different size. [313, 344] Different conclusions can be drawn from the SISSO analysis performed over the data deriving from propane oxidation. First of all, as expected, they highlight how the steam addition changes the catalytic performance in propane oxidation and more important, it emerges how the addition of steam into the reaction feed could affect the catalytic scenario to different extents depending on the involved samples. Indeed, in spite of dry feed results for SISSO analysis, where many analogies between the optimal models for the whole perovskites matrix and those for the (La,Pr)-series have been found, the results of SISSO analyses over the whole matrix in wet feed (Eq. 5.16-19) are very different from those obtained by using the (La,Pr)-series as input dataset (Eq. 5.8-11). As mentioned above, the SISSO results for the (La,Pr)$Mn_{(1-x)}Cu_xO_3$ series might be considered rather generalizable beyond the specific analyzed dataset. For instance, Eq. 5.15 shows exactly the same relevant primary features of Eq. 5.7, enforcing the result that an adsorption site for water (probably Mn or some structural pores)[275, 356] and the octahedral tilting due to the A-site size cation [313] play an influence to the product yield in propane oxidation performed in absence of steam. Also in the case of the descriptor for the rate of propane consumption (Eq. 5.12) there are a lot of analogies with that calculated for the (La,Pr)-series (Eq. 5.4). The B´amount together with O1s surface and H_2O species appear again as relevant primary features, highlighting how H_2O adsorption sites or maybe even H_2O itself which block some active sites, surface electrophilic oxygen [275] and B´content play a central role for propane consumption. While, the best models for the initial rate of propene and CO_2 formation (Eq. 5.13 and 5.14) are rather dissimilar to those calculated for the (La,Pr)-series (Eq. 5.5 and 5.6), indicating that expanding the elemental folding fan on the input dataset makes a difference on the best model. The relevant primary features linked to the selectivity seem to depend strongly on the feed composition and on the catalysts used for the employed input dataset. Indeed, the selectivity for the (La,Pr)-series in dry feed is linked to the averaged delta x, the oxygen surface, defects and OH species (Eq. 5.5). The oxygen surface species is believed to be related to electrophilic oxygen on the surface, which has generally been attributed to be responsible for oxygen insertion step in propane oxidation (from propene to acetaldehyde), [11] but more recent studies over perovskite catalysts have evidenced how this species seems to synergistically cooperate with OH species for the selectivity to propene, in contrast to defect oxygen concentration which shows a depletion in parallel to the selectivity's increase .[275] While, employing the whole perovskite matrix as input dataset, the results are slightly changed and the selectivity is linked to OH and carbonates surface species (Eq. 5.13), suggesting that the selectivity is mainly governed by electrophilic and Lewis-acidity adsorption sites on the surface, such as A-site cation surface termination or oxygen vacancies. [406] Also Mn could be involved into the model since OH preferably adsorb on Mn. [404]

Finally, it seems that the rates of CO oxidation is a relevant primary feature for the selectivity in wet feed for the whole perovskite matrix (Eq. 5.17), highlighting how CO oxidation might work as probe reaction for propane oxidation.

In conclusions, in the herein doctorate project, different perovskite-like catalysts have been synthesized, characterized and tested in CO and propane oxidation in order to better elucidate the structure-function relations with the support of artificial intelligence. This latter one has proven to be a suitable tool in many analyses able to identify the relevant properties linked to the catalytic performance, since, in many cases, the optimal models have fulfilled the expectations hypothesized by chemical intuition (especially in the case of Eq. 5.2 and 5.3). However, the relevant primary features appearing in the optimal models need to be correctly interpreted by chemical knowledge combined with catalysis phenomena understanding which go far beyond the mathematical expressions, it might be compared to DNA encoding process of a new system (as it is the case in Eq. 5.5, 5.7 and 5.13 for instance).

Appendices

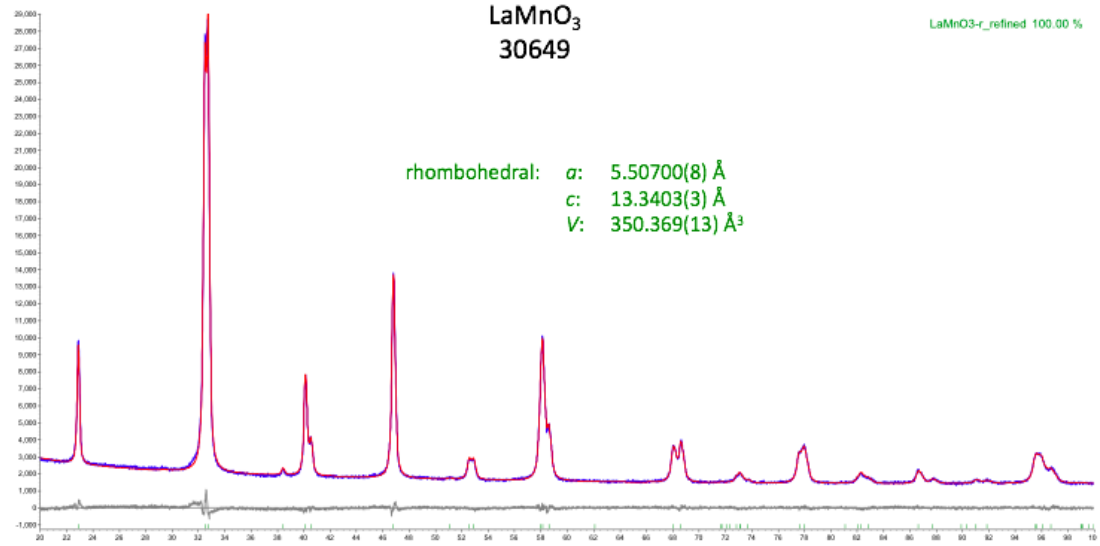
LaMnO3
30649
LaMnO3-r_refined 100.00 %
rhombohedral: a: 5.50700(8) Å
c: 13.3403(3) Å
V: 350.369(13) Å3

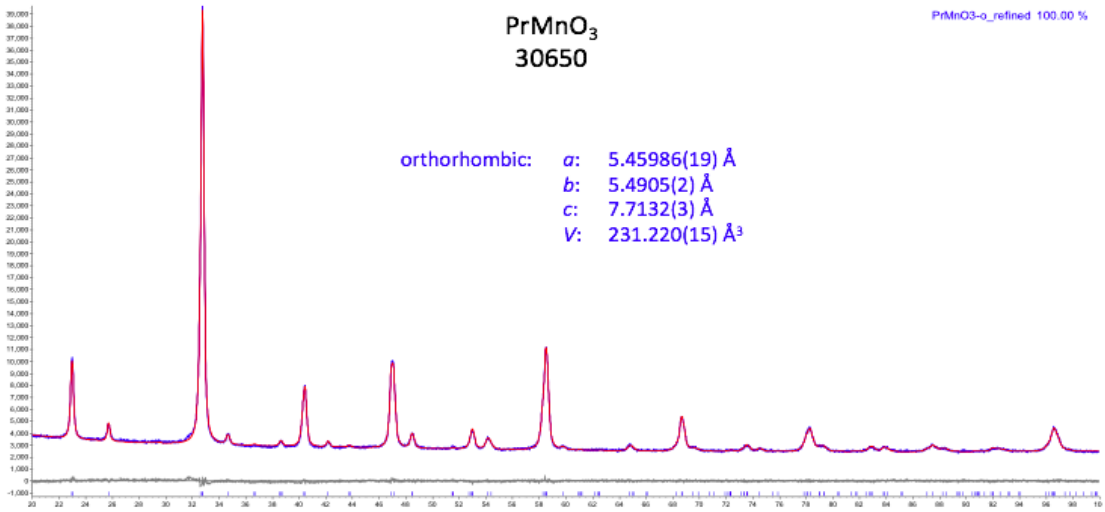
PrMnO3
30650
PrMnO3-o_refined 100.00 %
orthorhombic: a: 5.45986(19) Å
b: 5.4905(2) Å
c: 7.7132(3) Å
V: 231.220(15) Å3

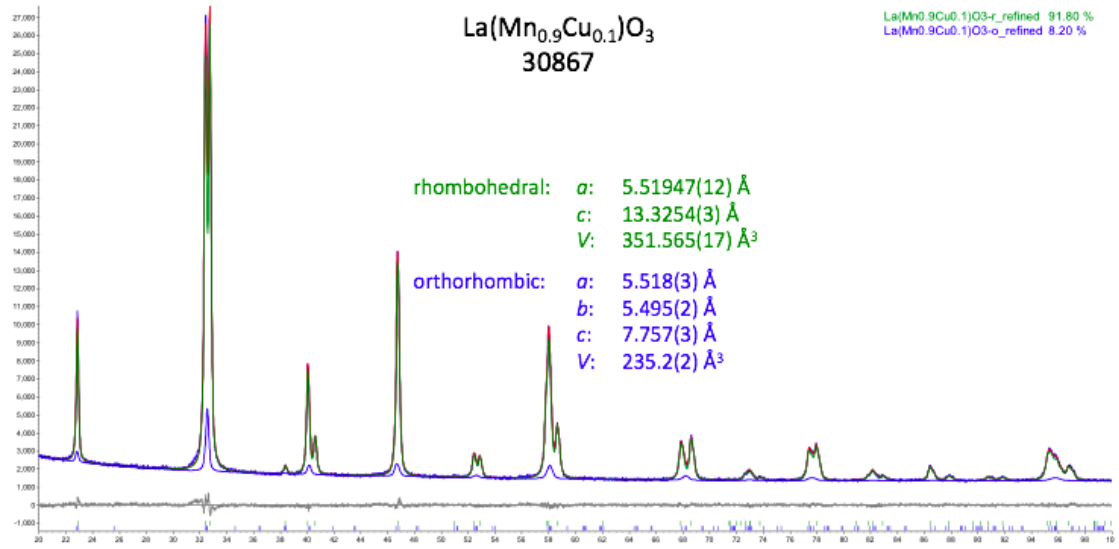
La(Mn0.9Cu0.1)O3-r_refined 91.80 %
La(Mn0.9Cu0.1)O3-o_refined 8.20 %
La(Mn0.9Cu0.1)O3
30867
rhombohedral: a: 5.51947(12) Å
c: 13.3254(3) Å
V: 351.565(17) Å3
orthorhombic: a: 5.518(3) Å
b: 5.495(2) Å
c: 7.757(3) Å
V: 235.2(2) Å3

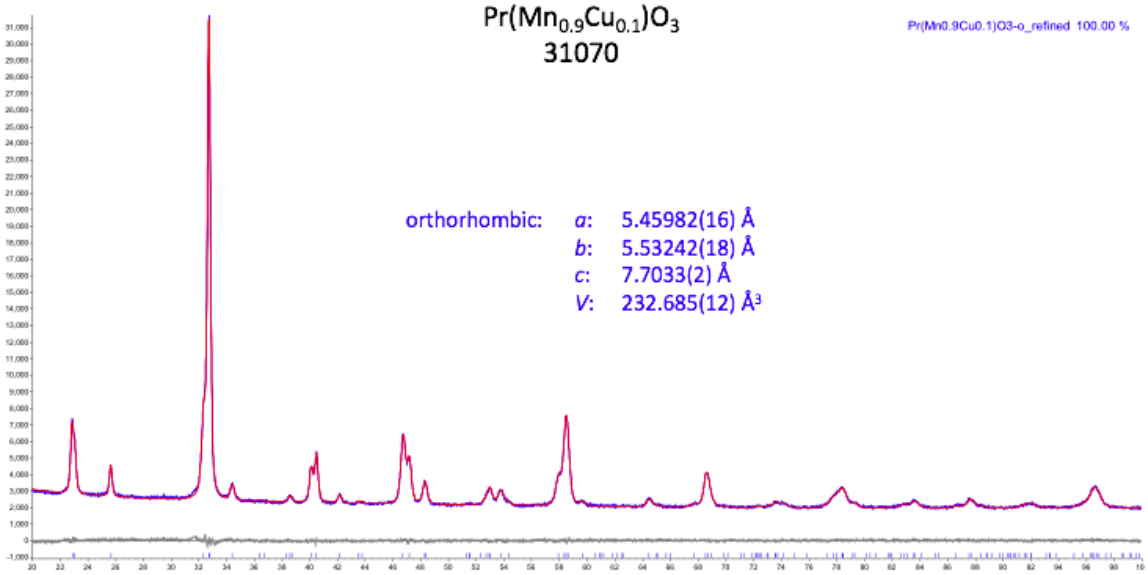
Pr(Mn0.9Cu0.1)O3-o_refined 100.00 %
Pr(Mn0.9Cu0.1)O3
31070
orthorhombic: a: 5.45982(16) Å
b: 5.53242(18) Å
c: 7.7033(2) Å
V: 232.685(12) Å3

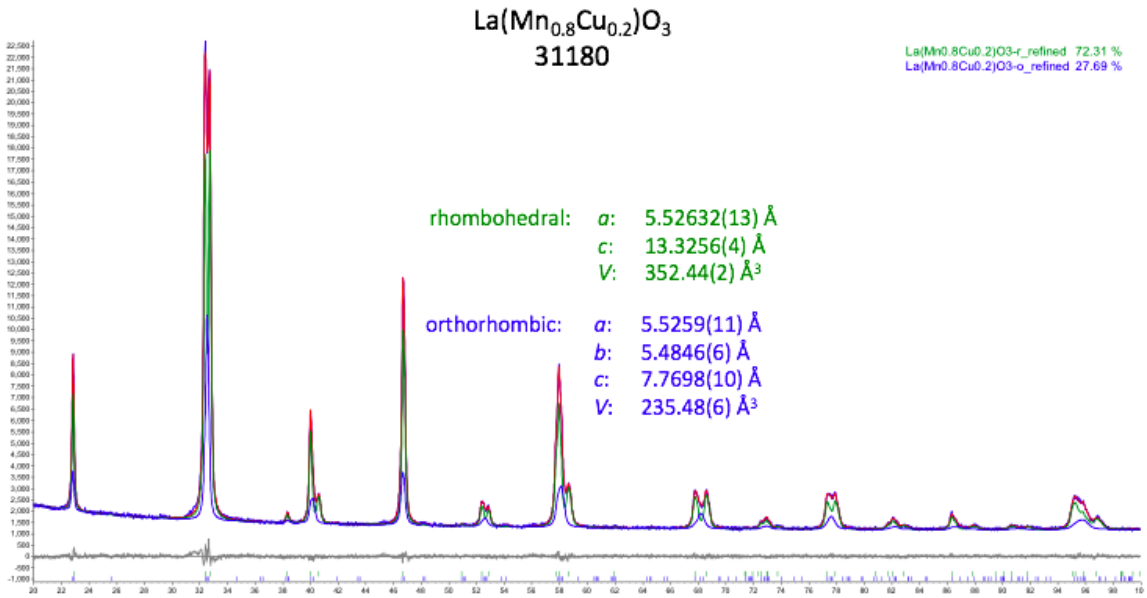

$La(Mn_{0.8}Cu_{0.2})O_3$
31180

rhombohedral: *a*: 5.52632(13) Å
c: 13.3256(4) Å
V: 352.44(2) Å³

orthorhombic: *a*: 5.5259(11) Å
b: 5.4846(6) Å
c: 7.7698(10) Å
V: 235.48(6) Å³

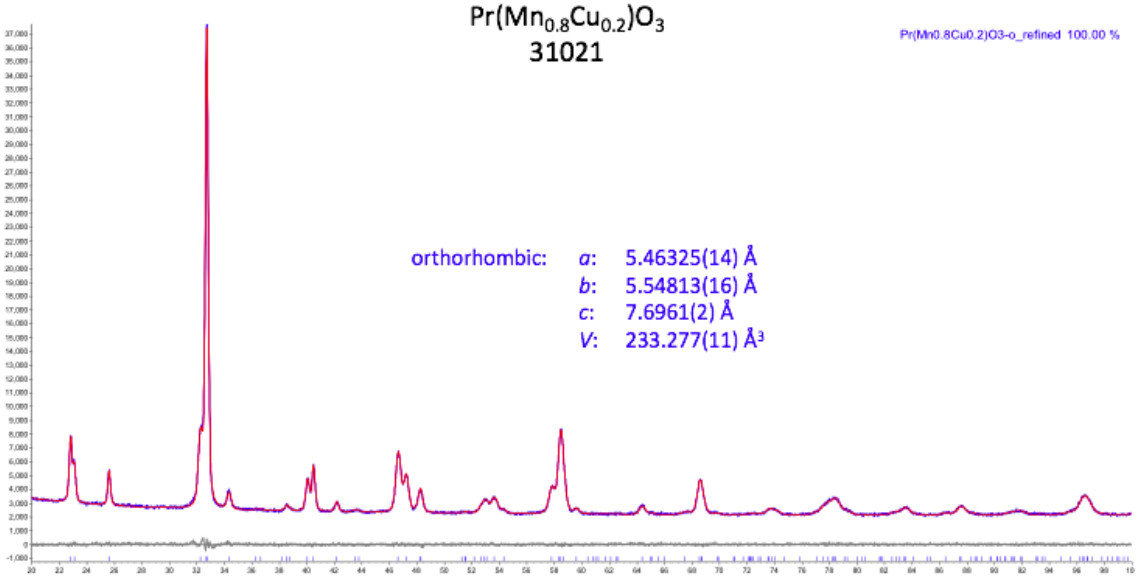

$Pr(Mn_{0.8}Cu_{0.2})O_3$
31021

orthorhombic: *a*: 5.46325(14) Å
b: 5.54813(16) Å
c: 7.6961(2) Å
V: 233.277(11) Å³

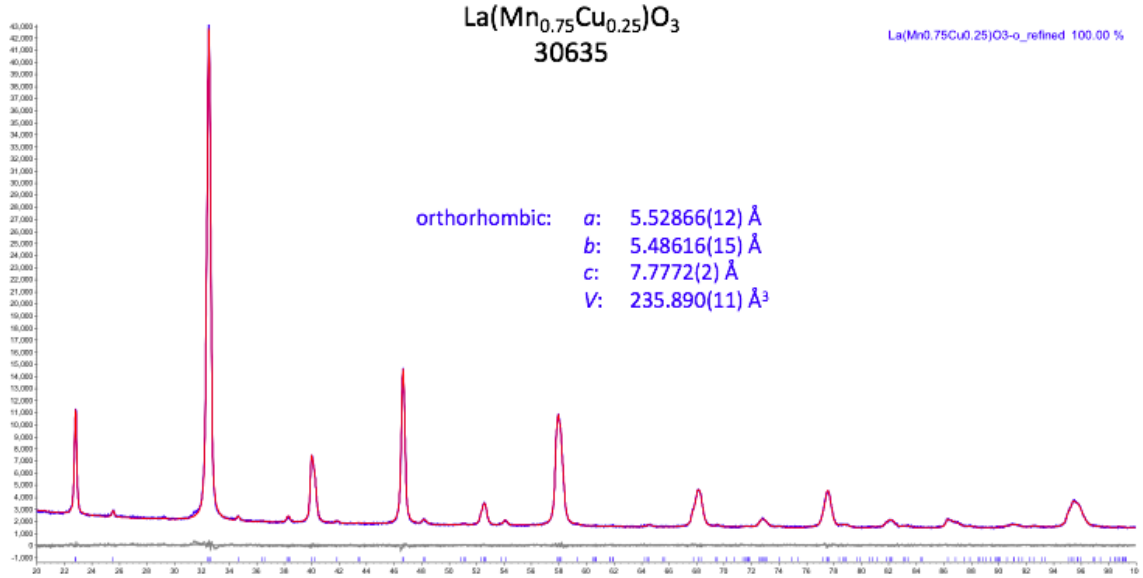
La(Mn0.75Cu0.25)O3
30635
La(Mn0.75Cu0.25)O3-o_refined 100.00 %
orthorhombic: a: 5.52866(12) Å
b: 5.48616(15) Å
c: 7.7772(2) Å
V: 235.890(11) Å3

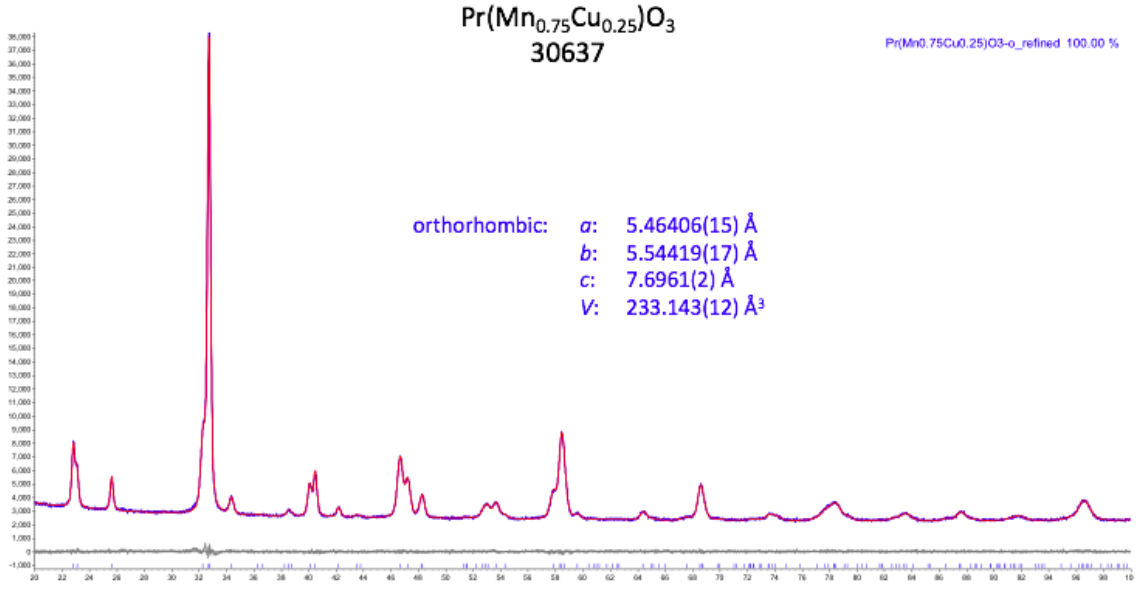
Pr(Mn0.75Cu0.25)O3
30637
Pr(Mn0.75Cu0.25)O3-o_refined 100.00 %
orthorhombic: a: 5.46406(15) Å
b: 5.54419(17) Å
c: 7.6961(2) Å
V: 233.143(12) Å3

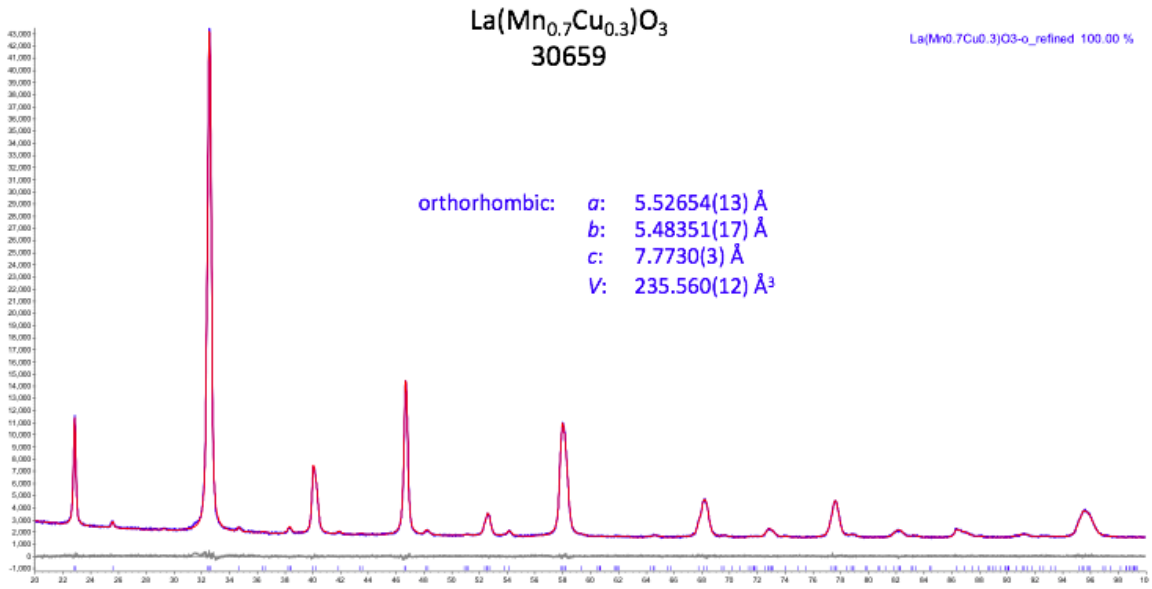
La(Mn0.7Cu0.3)O3
30659
La(Mn0.7Cu0.3)O3-o_refined 100.00 %
orthorhombic: a: 5.52654(13) Å
b: 5.48351(17) Å
c: 7.7730(3) Å
V: 235.560(12) Å3

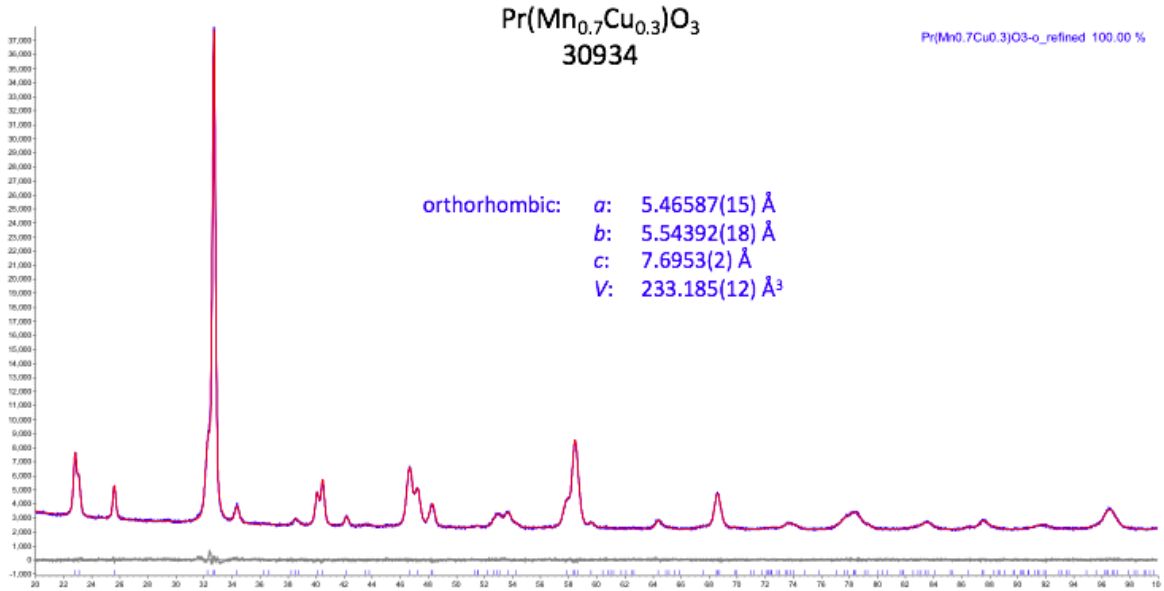
Pr(Mn0.7Cu0.3)O3
30934
Pr(Mn0.7Cu0.3)O3-o_refined 100.00 %
orthorhombic: a: 5.46587(15) Å
b: 5.54392(18) Å
c: 7.6953(2) Å
V: 233.185(12) Å3

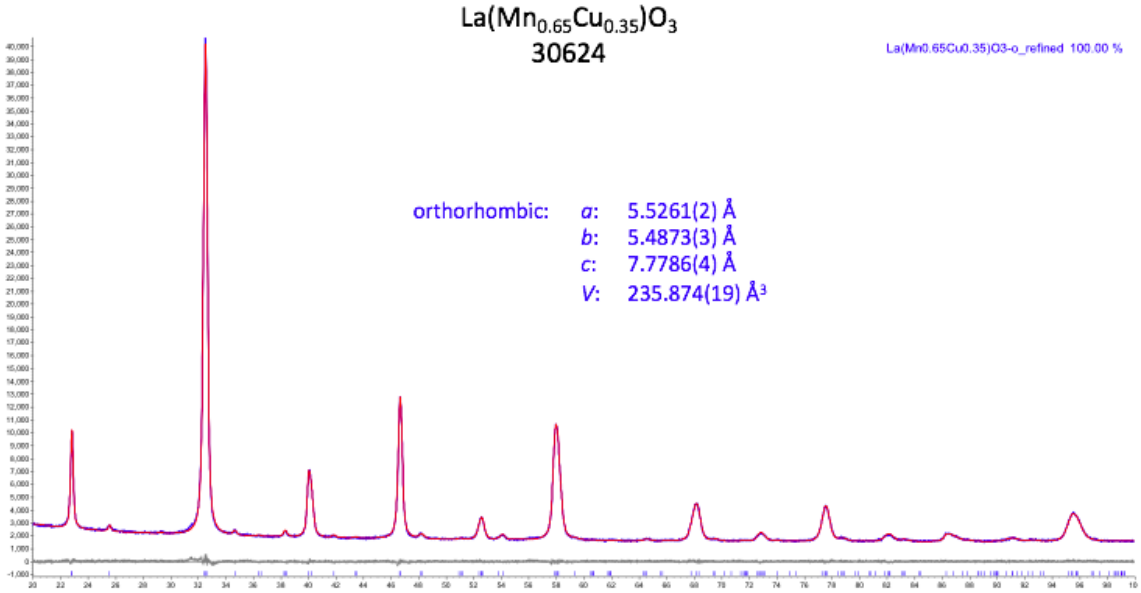
La(Mn0.65Cu0.35)O3
30624
La(Mn0.65Cu0.35)O3-o_refined 100.00 %
orthorhombic:
a: 5.5261(2) Å
b: 5.4873(3) Å
c: 7.7786(4) Å
V: 235.874(19) Å3

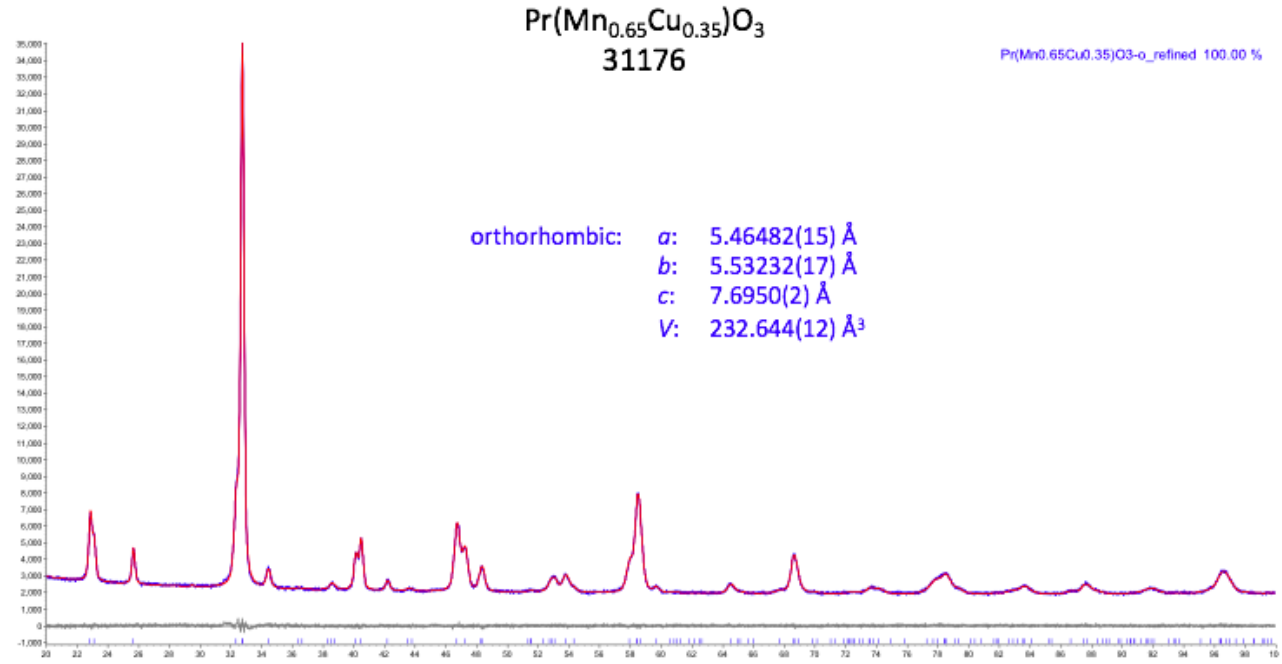
Pr(Mn0.65Cu0.35)O3
31176
Pr(Mn0.65Cu0.35)O3-o_refined 100.00 %
orthorhombic:
a: 5.46482(15) Å
b: 5.53232(17) Å
c: 7.6950(2) Å
V: 232.644(12) Å3

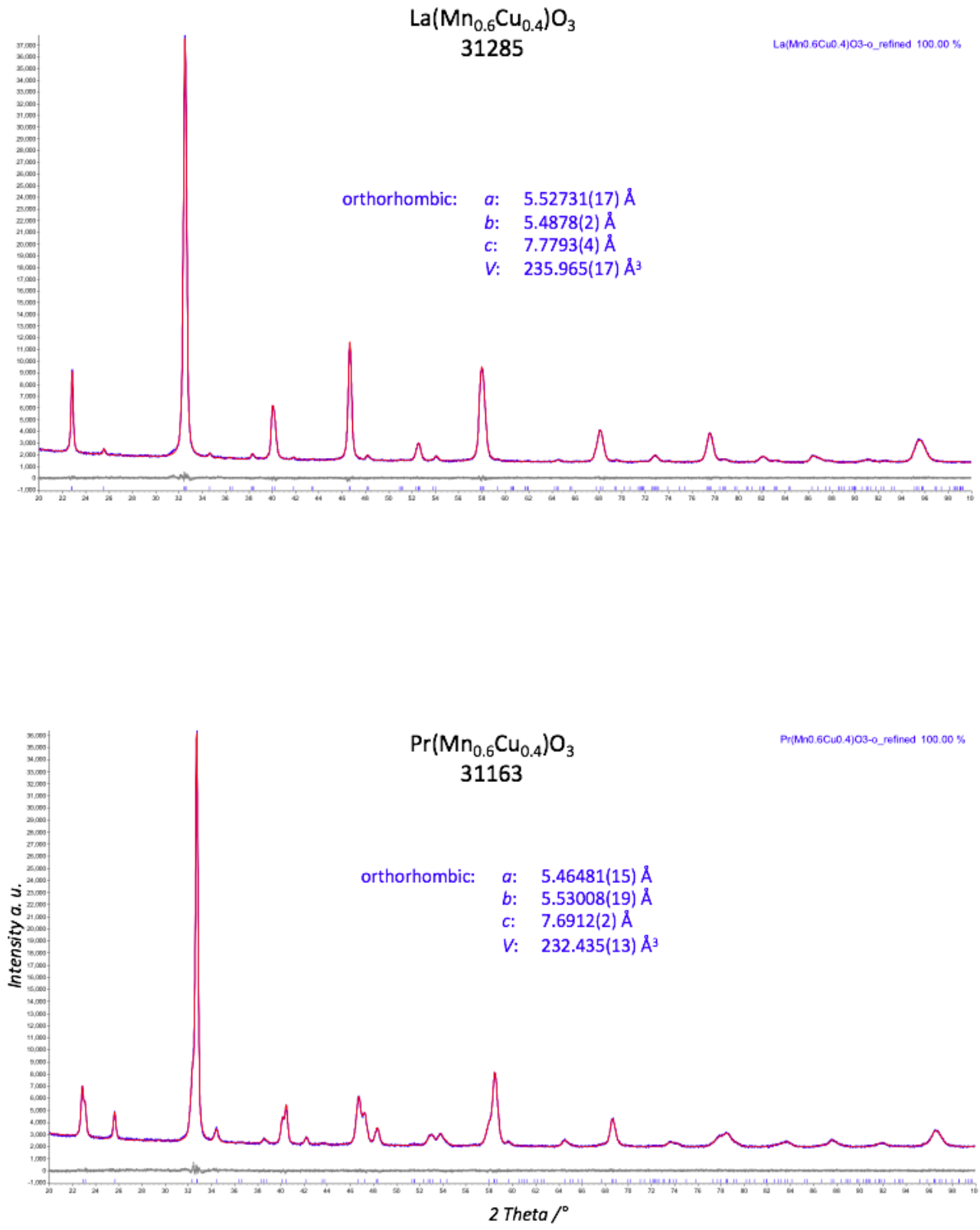

Figure S1. *Rietveld Refinement for (La,Pr)$Mn_{(1-x)}Cu_xO_3$ series. Color-code: Red: measured pattern, Blue: fitted pattern orthorhombic, green: fitted pattern rhombohedral and grey difference between measured and fitted pattern.*

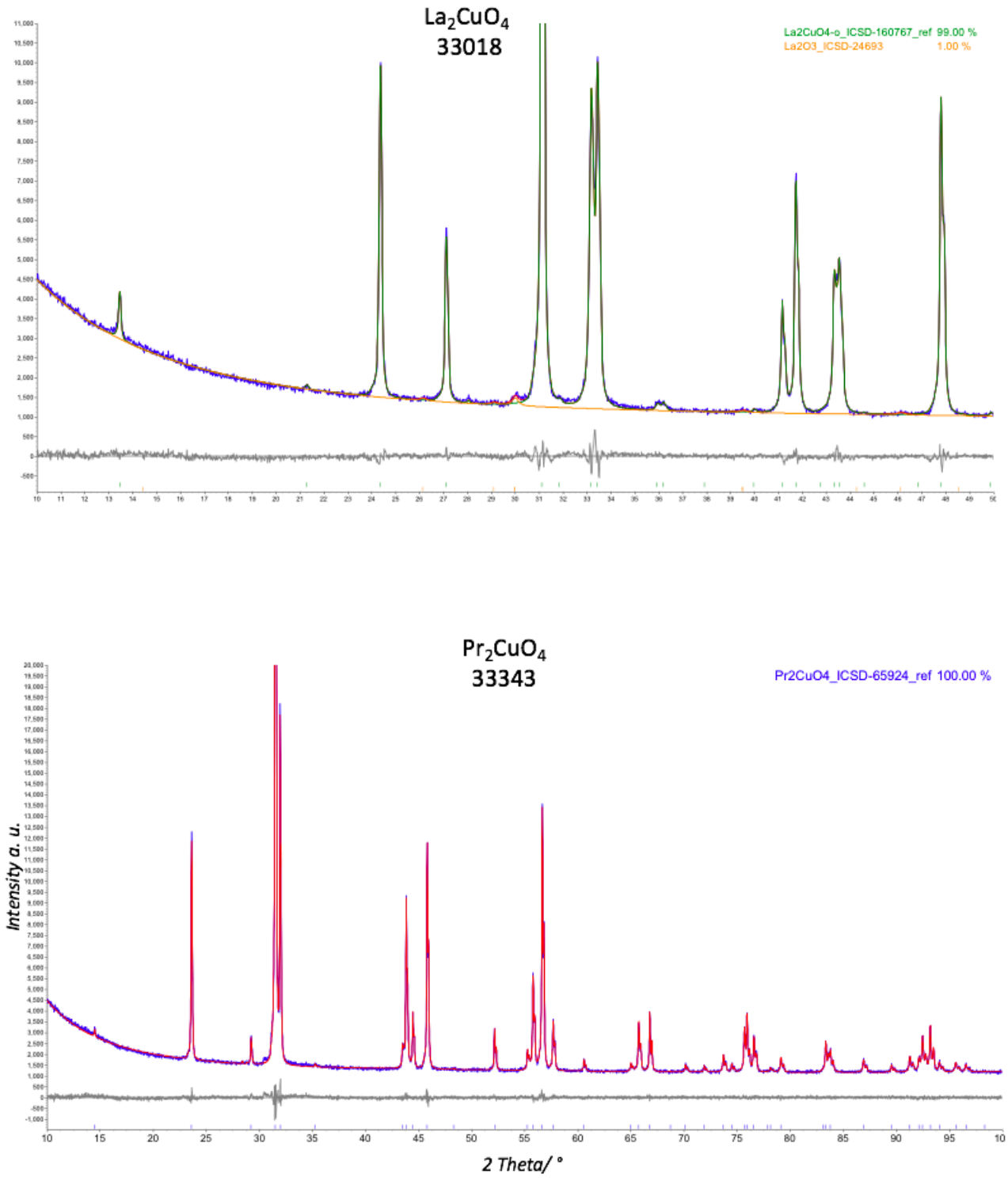

Figure S2. *Rietveld Refinement for $(La,Pr)_2CuO_4$ samples. Color-code: Red: measured pattern, Blue or green or yellow: fitted pattern and grey difference between measured and fitted pattern.*

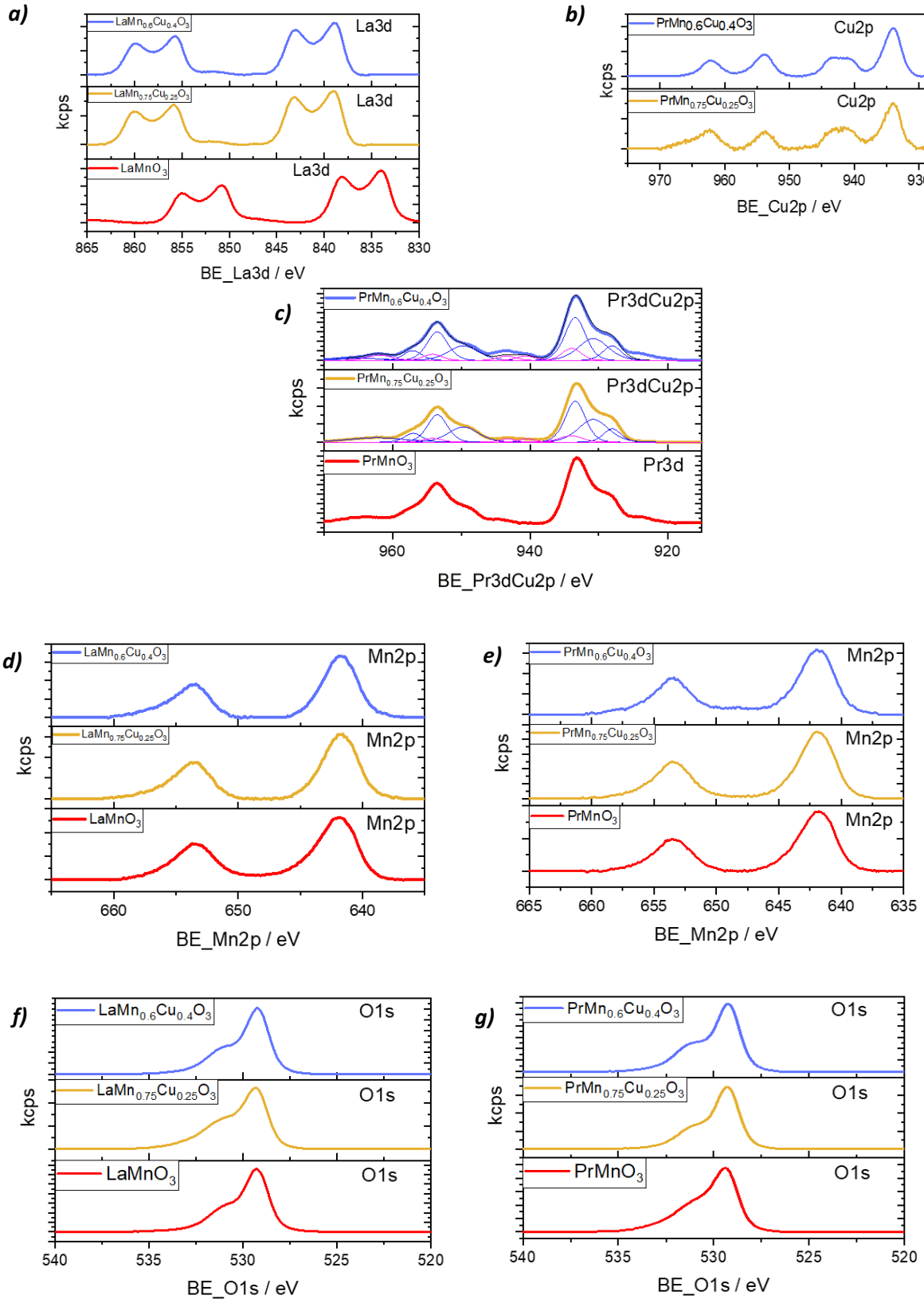

Figure S3. *Core levels spectra for (La,Pr)$Mn_{(1-x)}Cu_xO_3$ series with x=0, 0.25 and 0.4.* ***a)*** *La3d spectra for La-based series;* ***b)*** *Cu2p spectra for La-based series;* ***c)*** *Pr3dCu2p spectra for Pr-based series; Mn2p spectra for* ***d)*** *La-based series and* ***e)*** *Pr-based series. O1s spectra for* ***f)*** *La-based series and g) Pr-based series. Color-code: red : (La,Pr)MnO_3; yellow: (La,Pr)$Mn_{0.75}Cu_{0.25}O_3$; light blue: (La,Pr)$Mn_{0.6}Cu_{0.4}O_3$; dark blue: Pr3d fit and pink: Cu2p fit.*

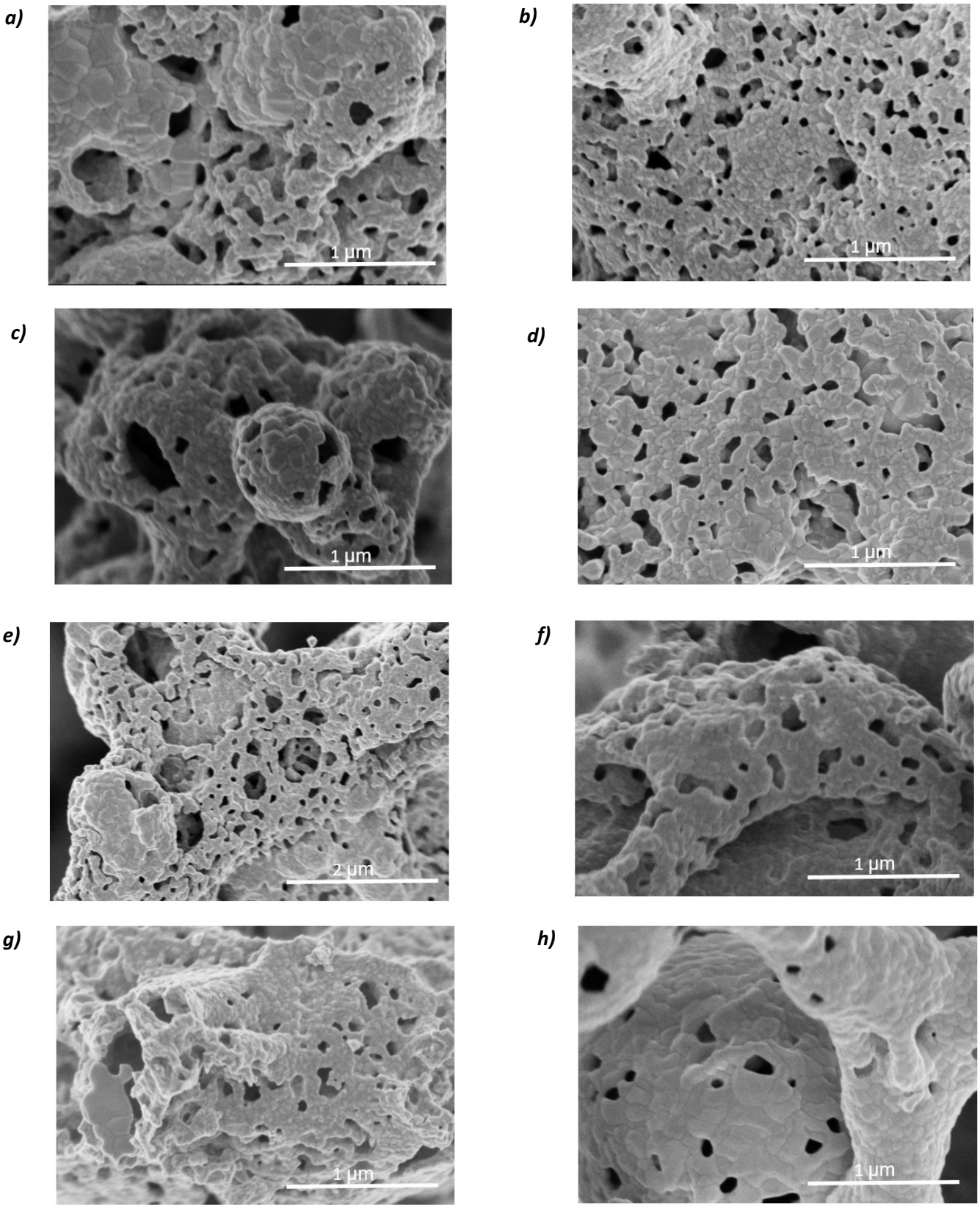

Figure S4. *SEM images at 1 µm of* ***a)*** *$LaMn_{0.9}Cu_{0.1}O_3$;* ***b)*** *$PrMn_{0.9}Cu_{0.1}O_{3,}$;* ***c)*** *$LaMn_{0.8}Cu_{0.2}O_3$;* ***d)*** *$PrMn_{0.8}Cu_{0.2}O_3$;* ***e)*** *$LaMn_{0.7}Cu_{0.3}O_3$;* ***f)*** *$PrMn_{0.7}Cu_{0.3}O_3$;* ***g)*** *$LaMn_{0.65}Cu_{0.35}O_3$ and* ***h)*** *$PrMn_{0.65}Cu_{0.35}O_3$.*

a)

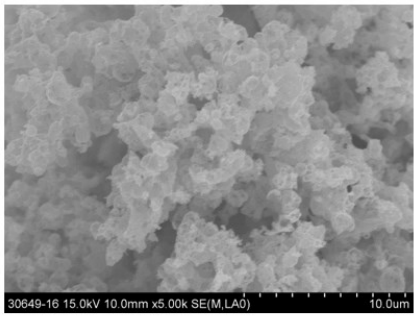
30649-16 15.0kV 10.0mm x5.00k SE(M,LA0)
10.0um

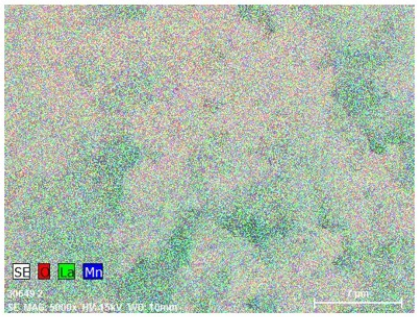
SE
O
La
Mn

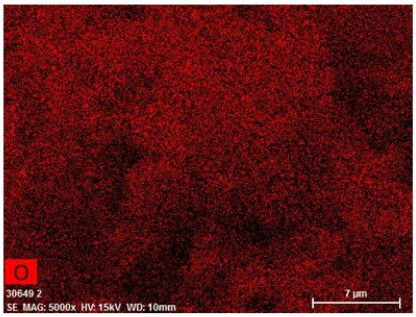
O
30649 2
SE MAG: 5000x HV: 15kV WD: 10mm
7 µm

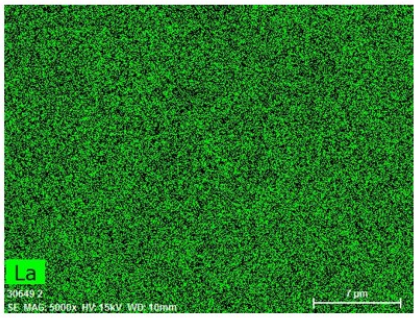
La
30649 2
SE MAG: 5000x HV: 15kV WD: 10mm
7 µm

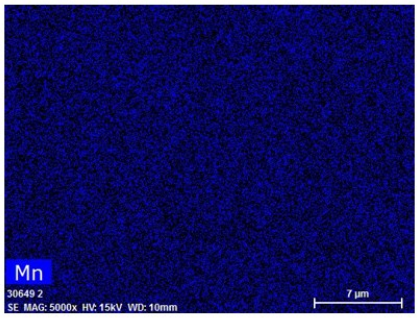
Mn
30649 2
SE MAG: 5000x HV: 15kV WD: 10mm
7 µm

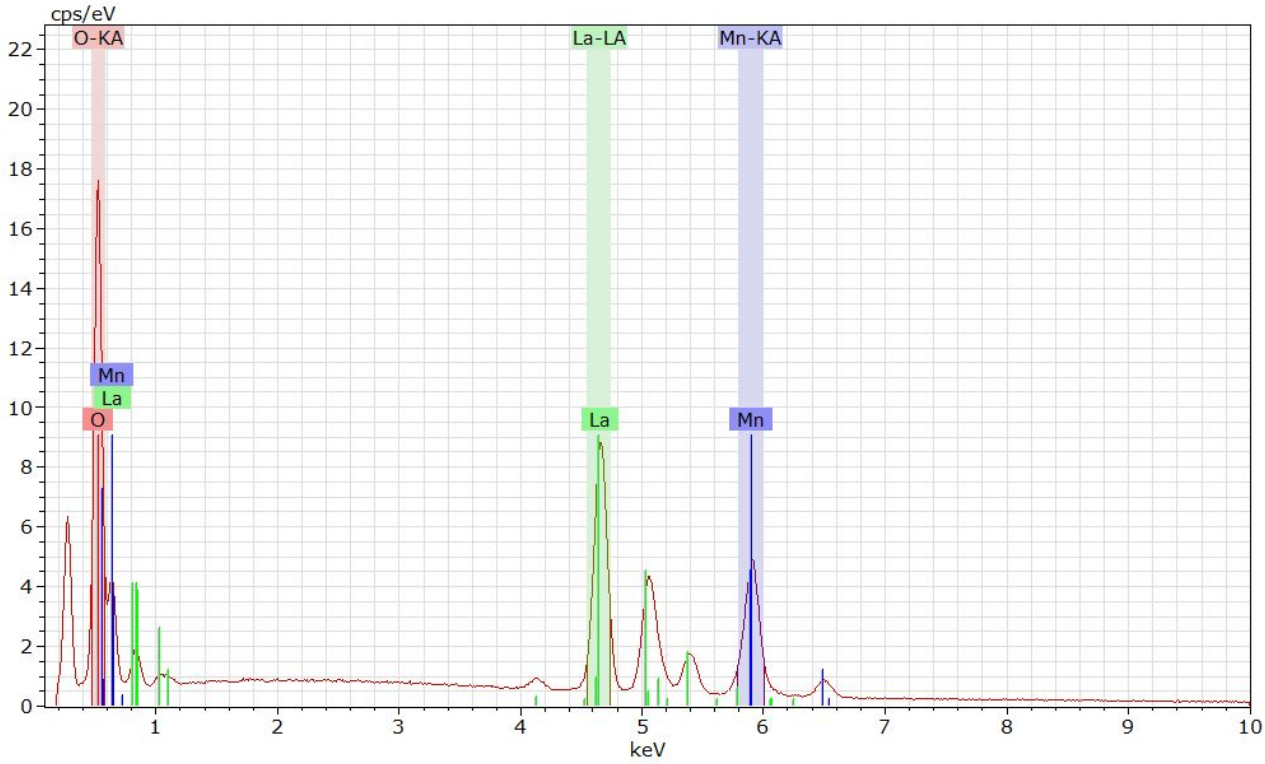
cps/eV
O-KA
La-LA
Mn-KA
Mn
La
O
La
Mn
keV

b)

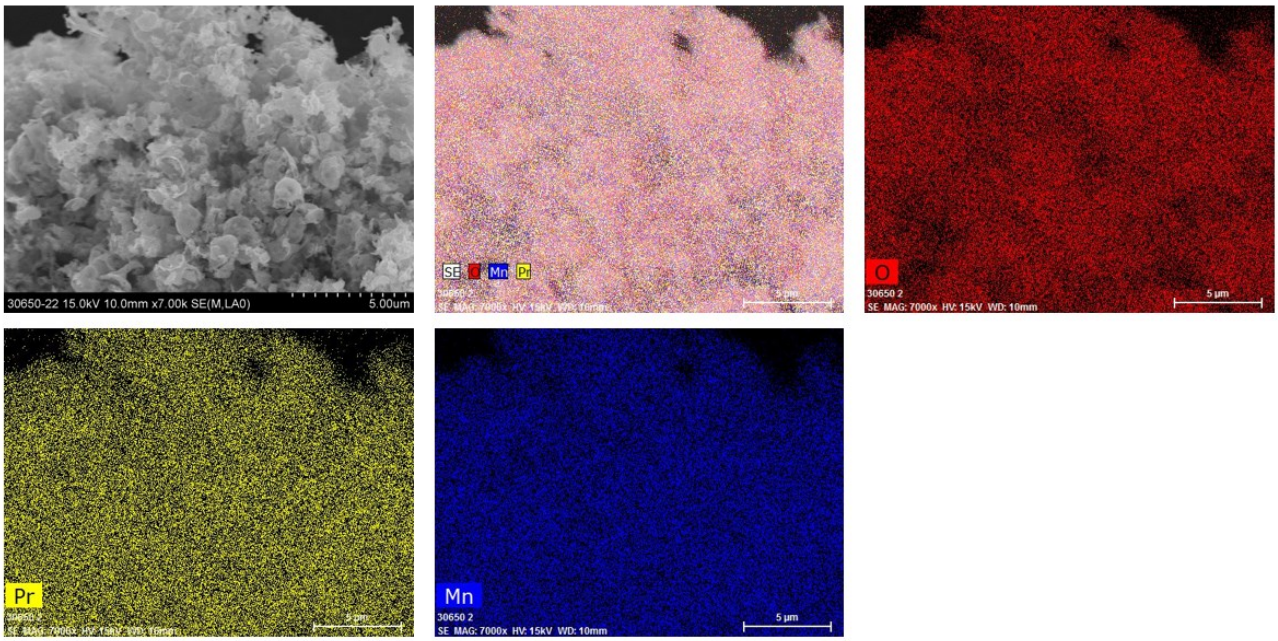
30650-22 15.0kV 10.0mm x7.00k SE(M,LA0)
5.00um
SE
O
Mn
Pr
O
30650 2
SE MAG: 7000x HV: 15kV WD: 10mm
5 µm
Pr
Mn
30650 2
SE MAG: 7000x HV: 15kV WD: 10mm
5 µm

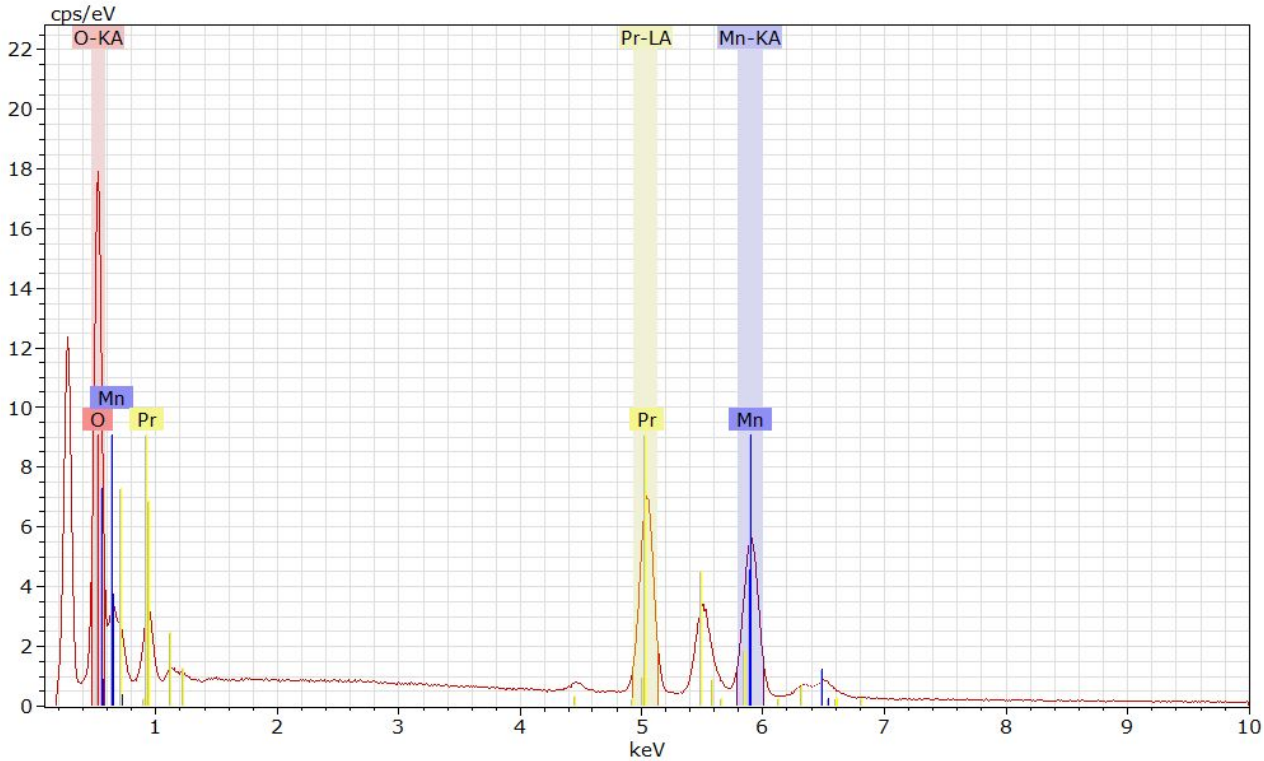
cps/eV
O-KA
Pr-LA
Mn-KA
Mn
O
Pr
Pr
Mn
keV
0
2
4
6
8
10
12
14
16
18
20
22
1
2
3
4
5
6
7
8
9
10

c)

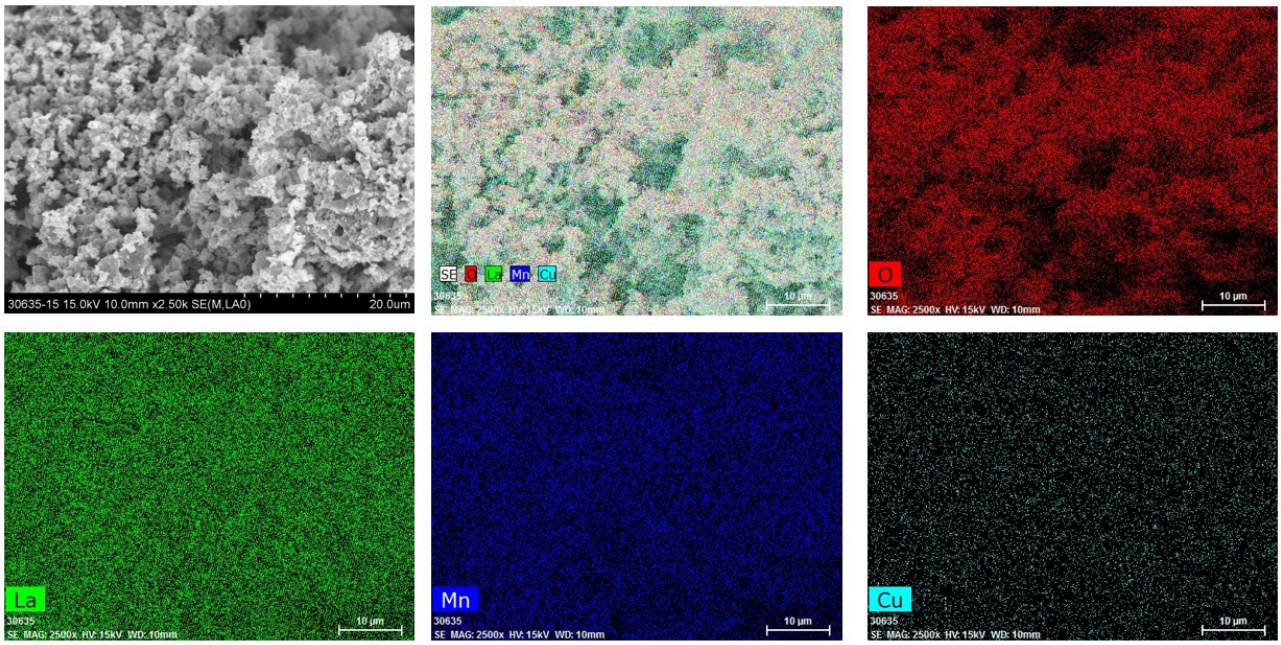
30635-15 15.0kV 10.0mm x2.50k SE(M,LA0)
20.0um
SE O La Mn Cu
O
La
Mn
Cu
10 µm
SE MAG: 2500x HV: 15kV WD: 10mm

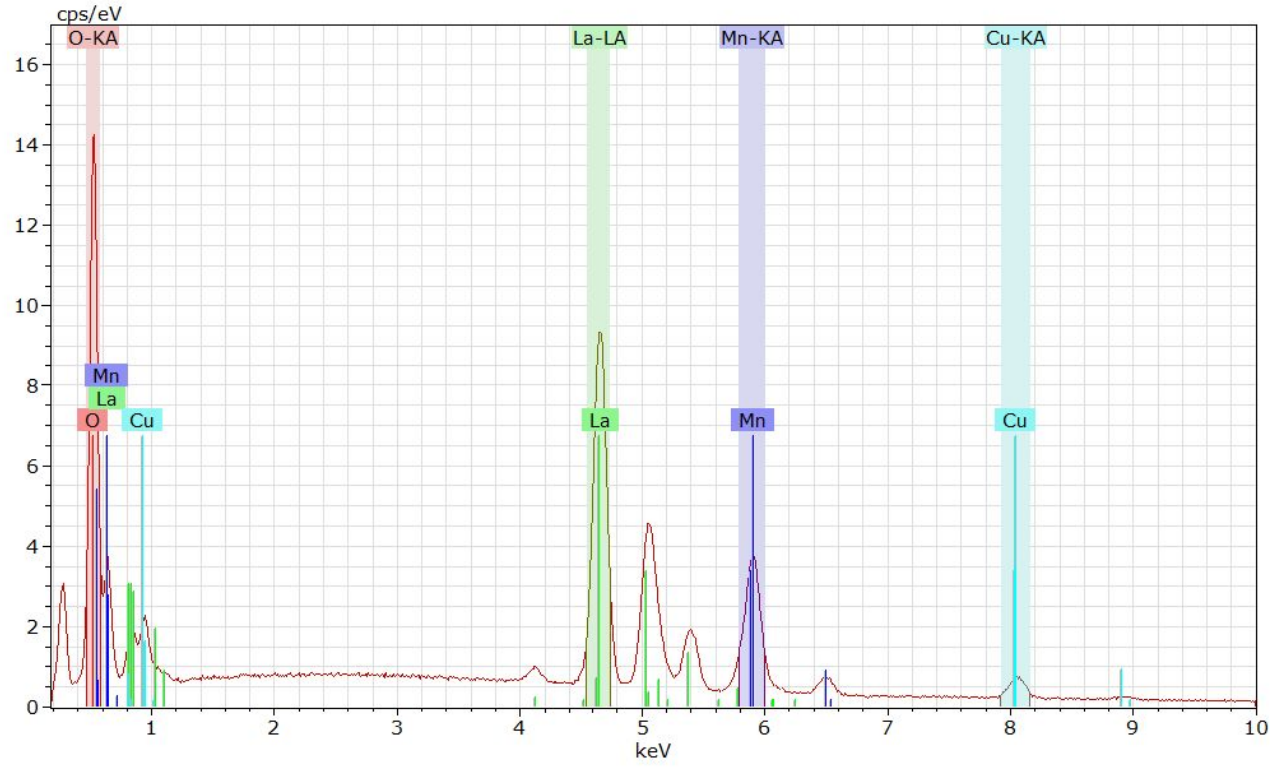
cps/eV
O-KA
La-LA
Mn-KA
Cu-KA
Mn
La
O
Cu
La
Mn
Cu
keV
0
2
4
6
8
10
12
14
16
1
2
3
4
5
6
7
8
9
10

d)

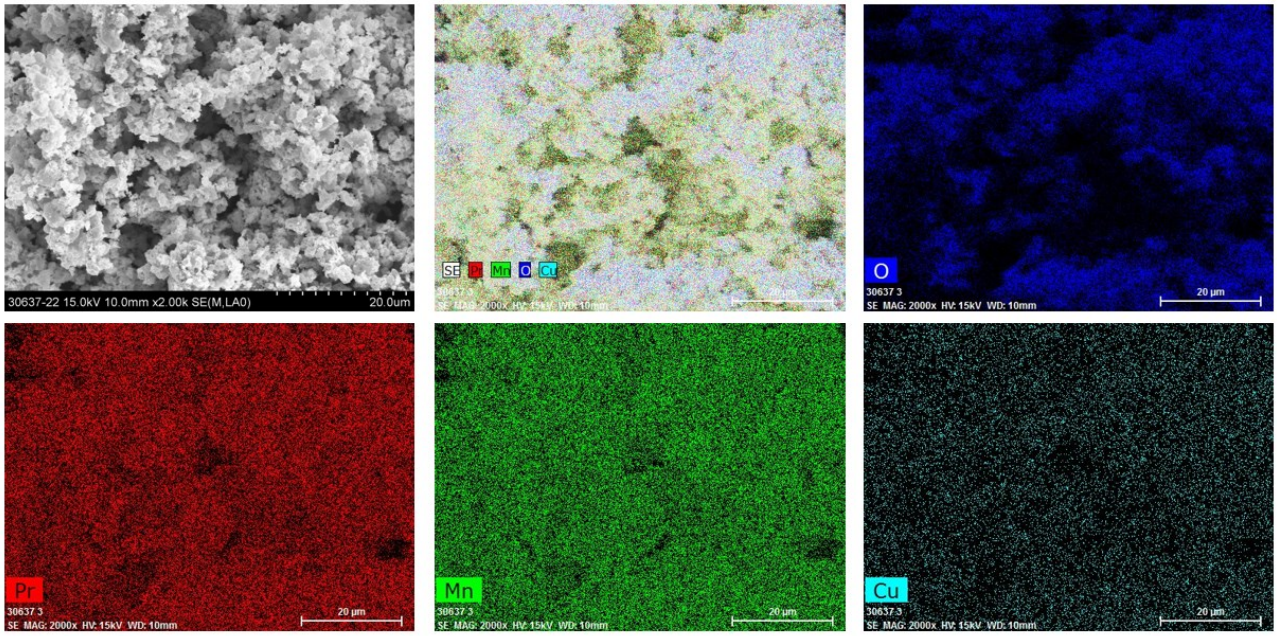
30637-22 15.0kV 10.0mm x2.00k SE(M,LA0)
20.0um
SE Pr Mn O Cu
O
30637 3
SE MAG: 2000x HV: 15kV WD: 10mm
20 µm
Pr
Mn
Cu

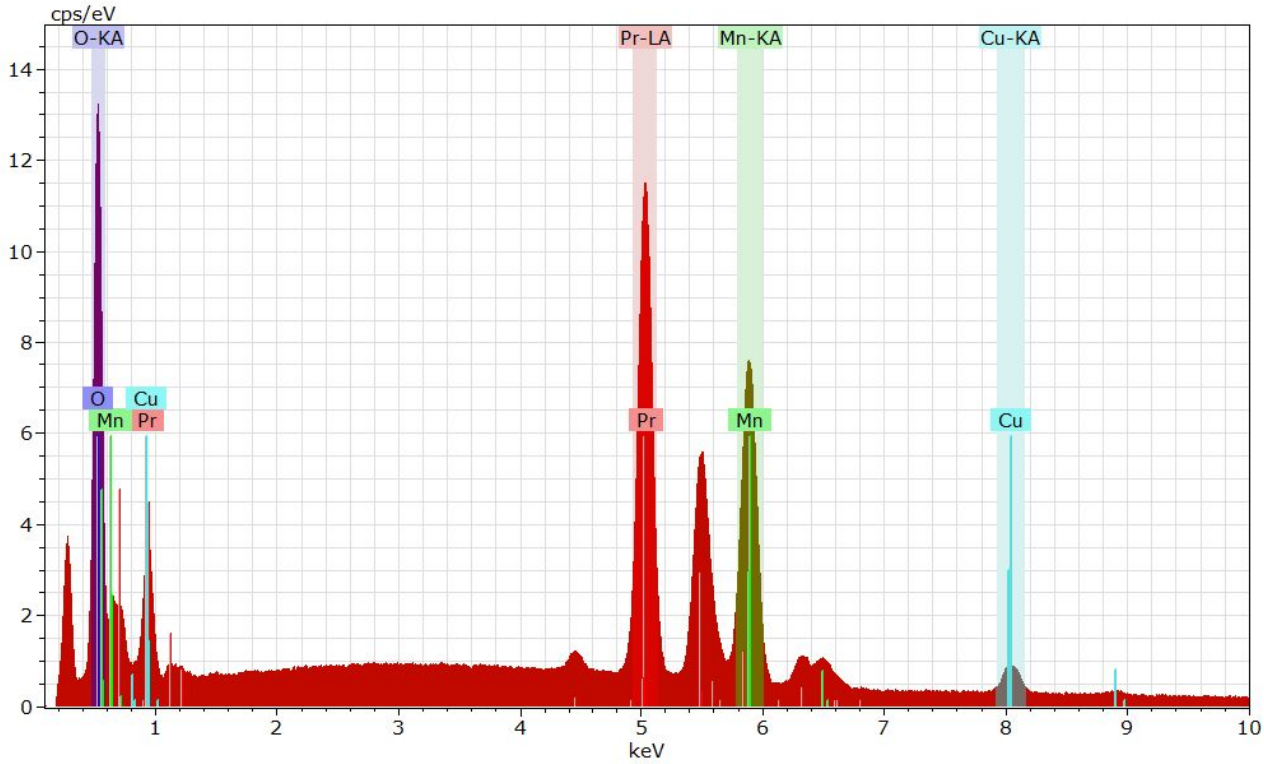
cps/eV
O-KA
Pr-LA
Mn-KA
Cu-KA
O
Cu
Mn
Pr
Pr
Mn
Cu
0
2
4
6
8
10
12
14
1
2
3
4
5
6
7
8
9
10
keV

e)

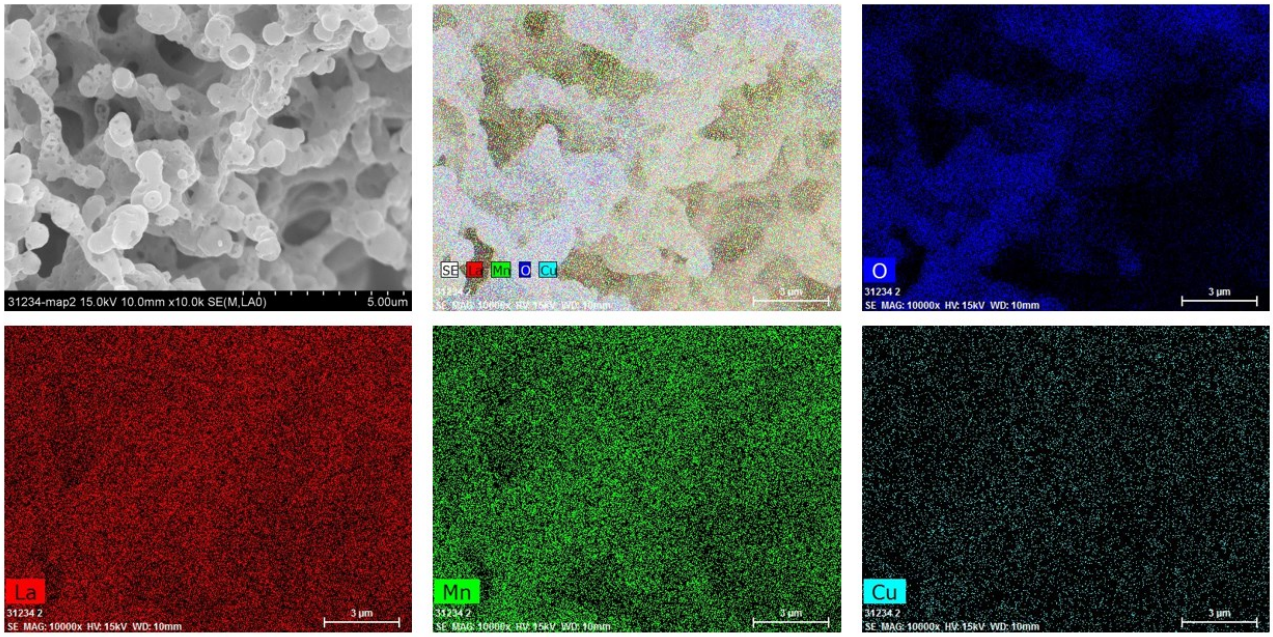
31234-map2 15.0kV 10.0mm x10.0k SE(M,LA0) 5.00um
SE La Mn O Cu
O
La
Mn
Cu
31234 2
SE MAG: 10000x HV: 15kV WD: 10mm
3 µm

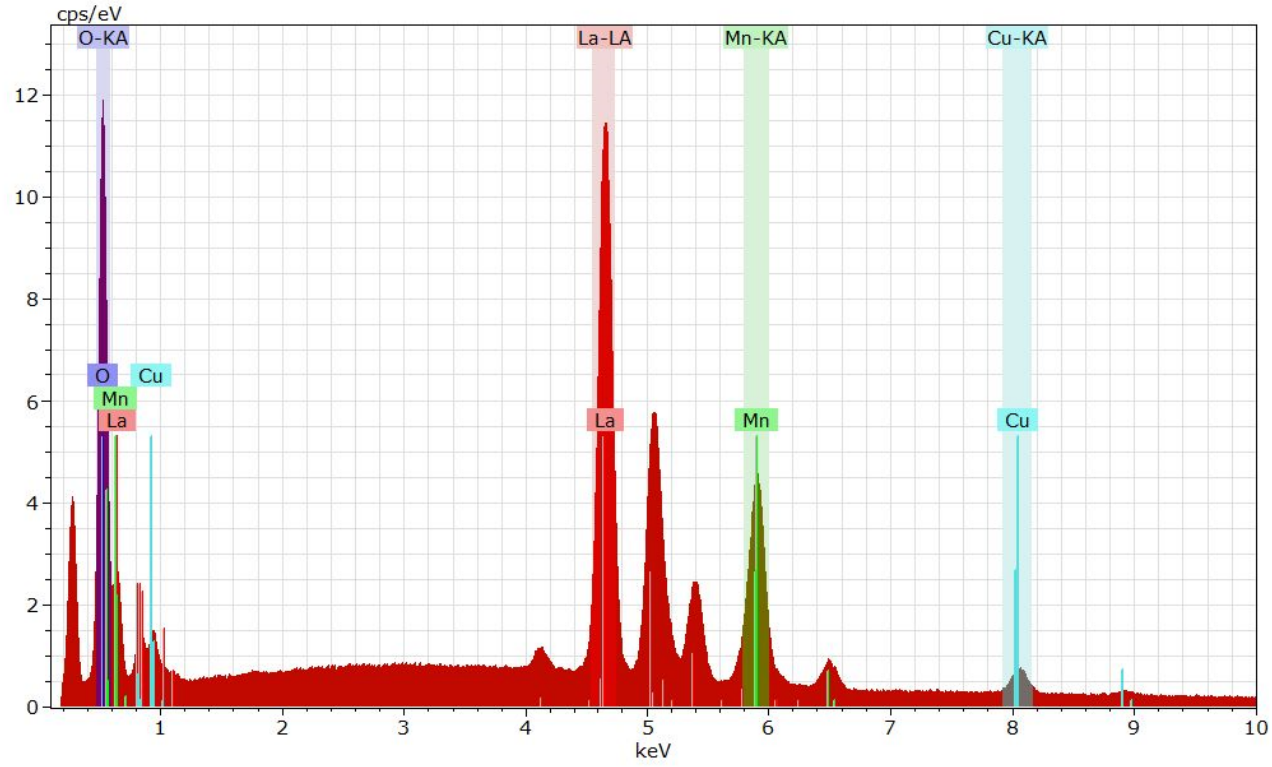
cps/eV
O-KA
La-LA
Mn-KA
Cu-KA
O
Cu
Mn
La
La
Mn
Cu
0
2
4
6
8
10
12
1
2
3
4
5
6
7
8
9
10
keV

f)

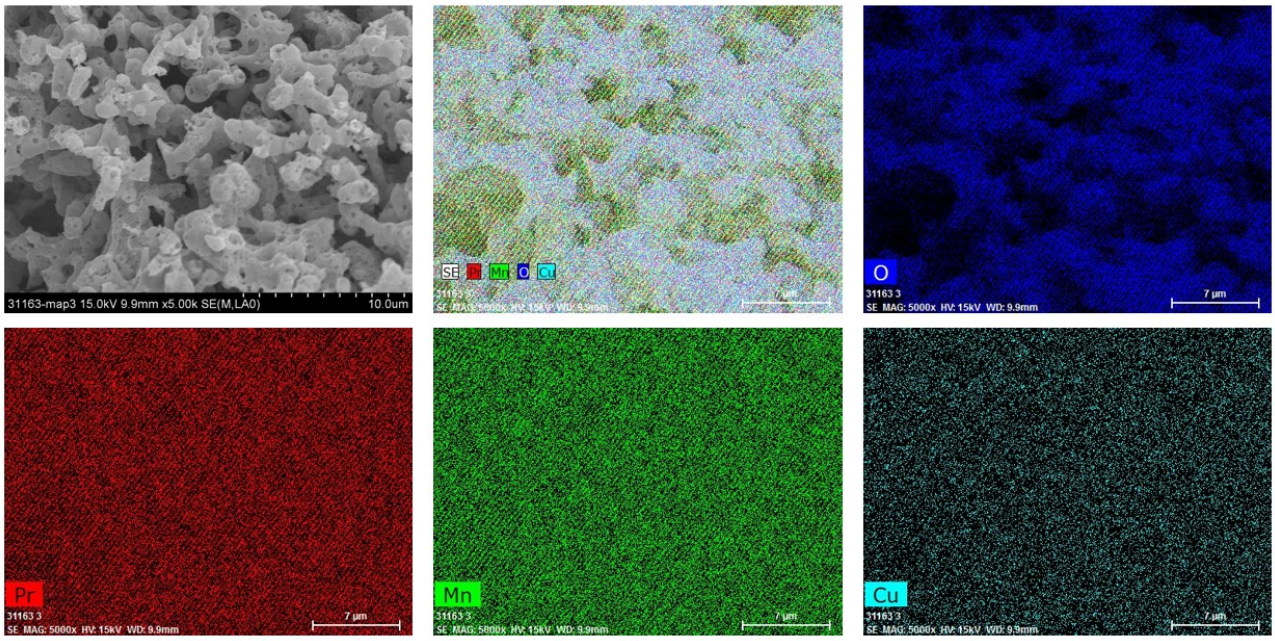

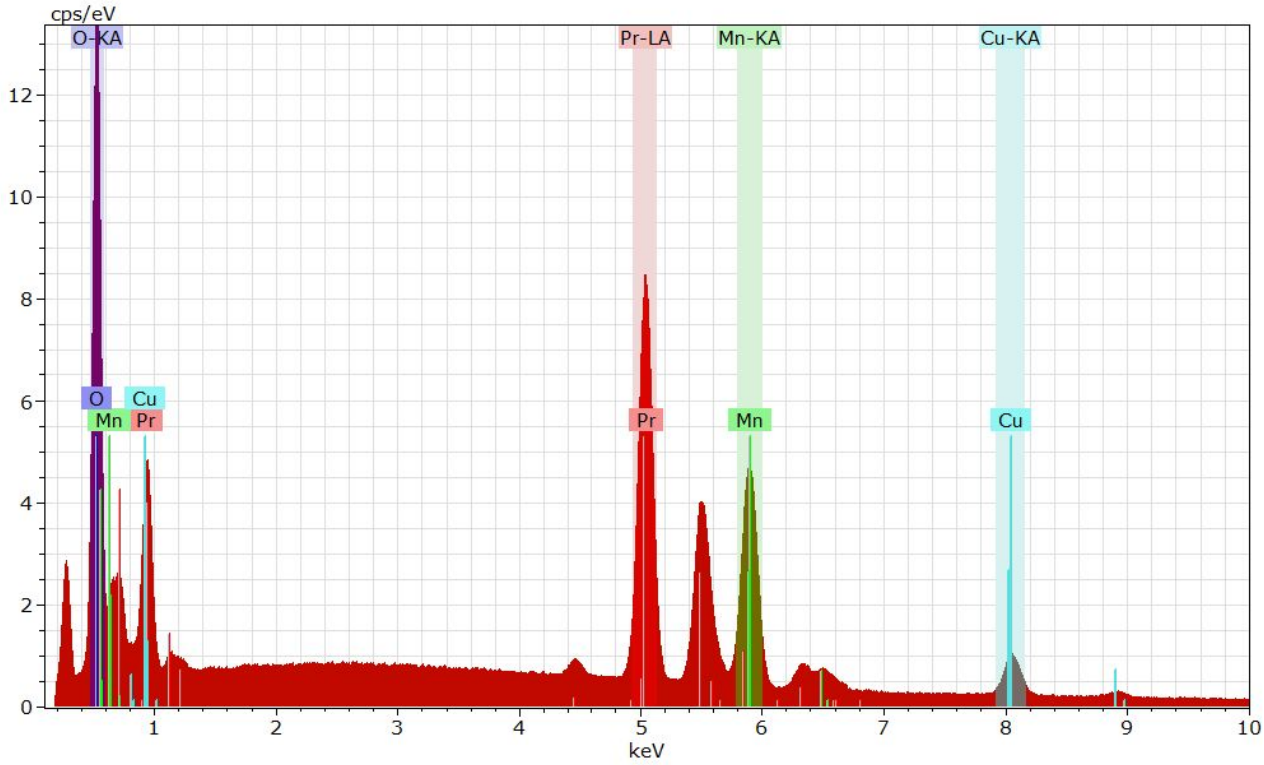

Figure S5. *EDX maps and corresponding spectra of* ***a)*** $LaMn_{0.9}Cu_{0.1}O_3$; ***b)*** $PrMn_{0.9}Cu_{0.1}O_3$,; ***c)*** $LaMn_{0.75}Cu_{0.25}O_3$;***d)*** $PrMn_{0.75}Cu_{0.25}O_3$; ***e)*** $LaMn_{0.6}Cu_{0.4}O_3$ *and* ***f)*** $PrMn_{0.6}Cu_{0.4}O_3$.

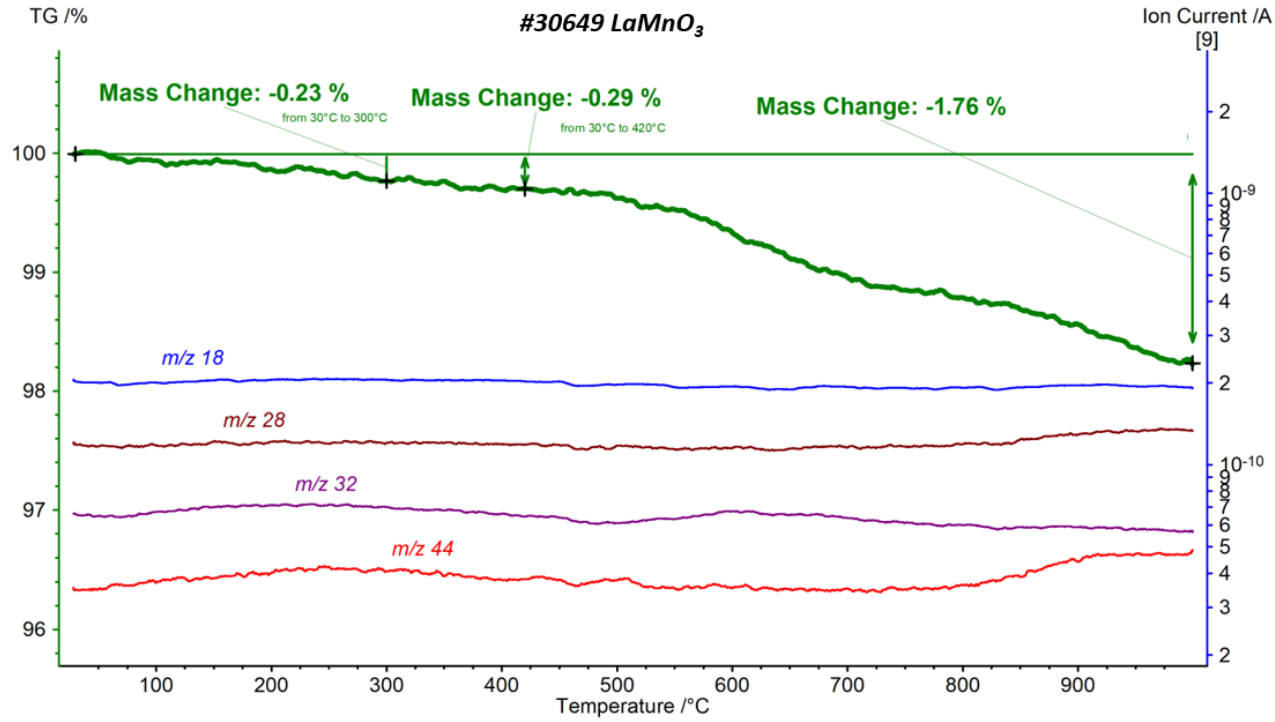
TG /%
#30649 LaMnO3
Ion Current /A
[9]
Mass Change: -0.23 %
from 30°C to 300°C
Mass Change: -0.29 %
from 30°C to 420°C
Mass Change: -1.76 %
m/z 18
m/z 28
m/z 32
m/z 44
Temperature /°C

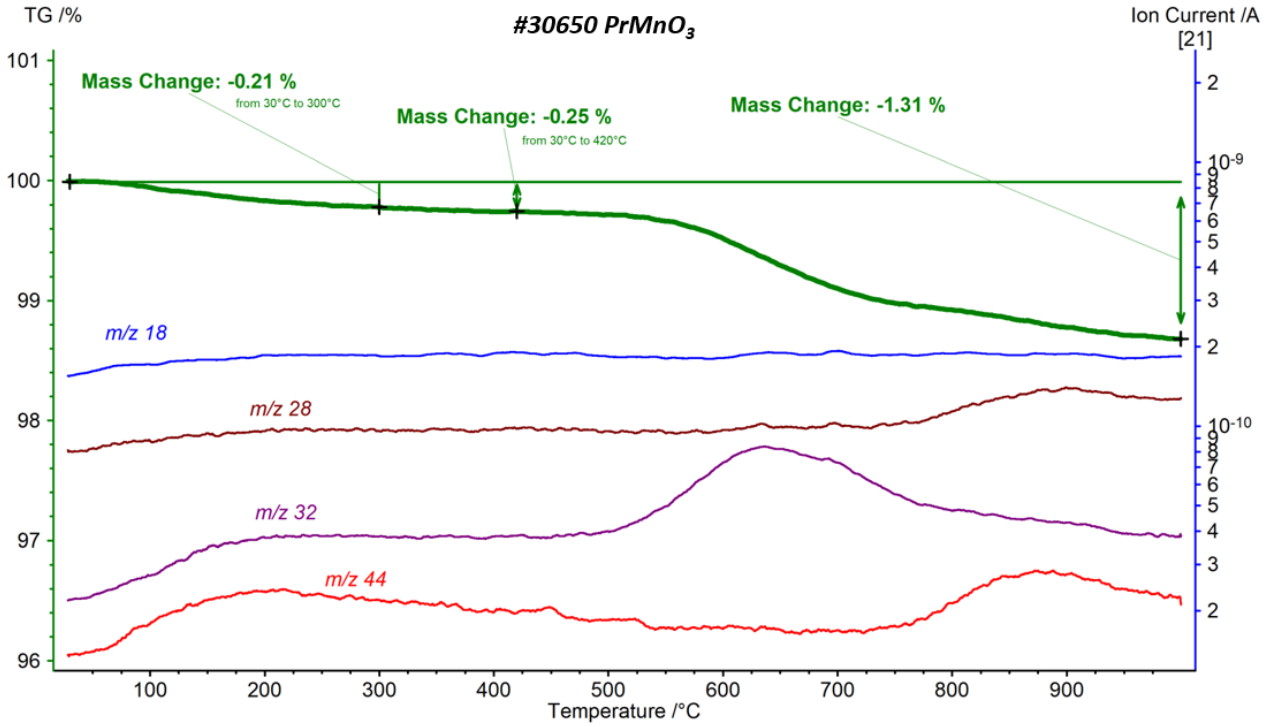
TG /%
#30650 PrMnO3
Ion Current /A
[21]
Mass Change: -0.21 %
from 30°C to 300°C
Mass Change: -0.25 %
from 30°C to 420°C
Mass Change: -1.31 %
m/z 18
m/z 28
m/z 32
m/z 44
Temperature /°C

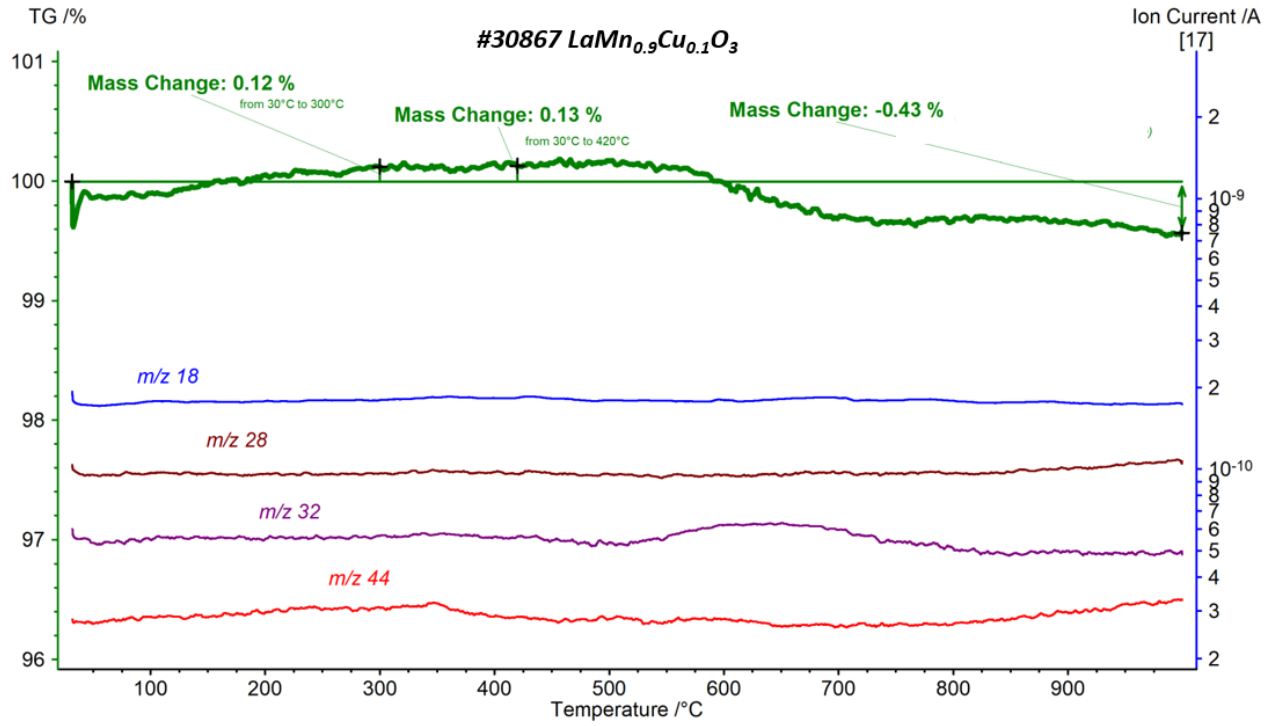
TG /%
#30867 LaMn0.9Cu0.1O3
Ion Current /A
[17]
Mass Change: 0.12 %
from 30°C to 300°C
Mass Change: 0.13 %
from 30°C to 420°C
Mass Change: -0.43 %
m/z 18
m/z 28
m/z 32
m/z 44
Temperature /°C

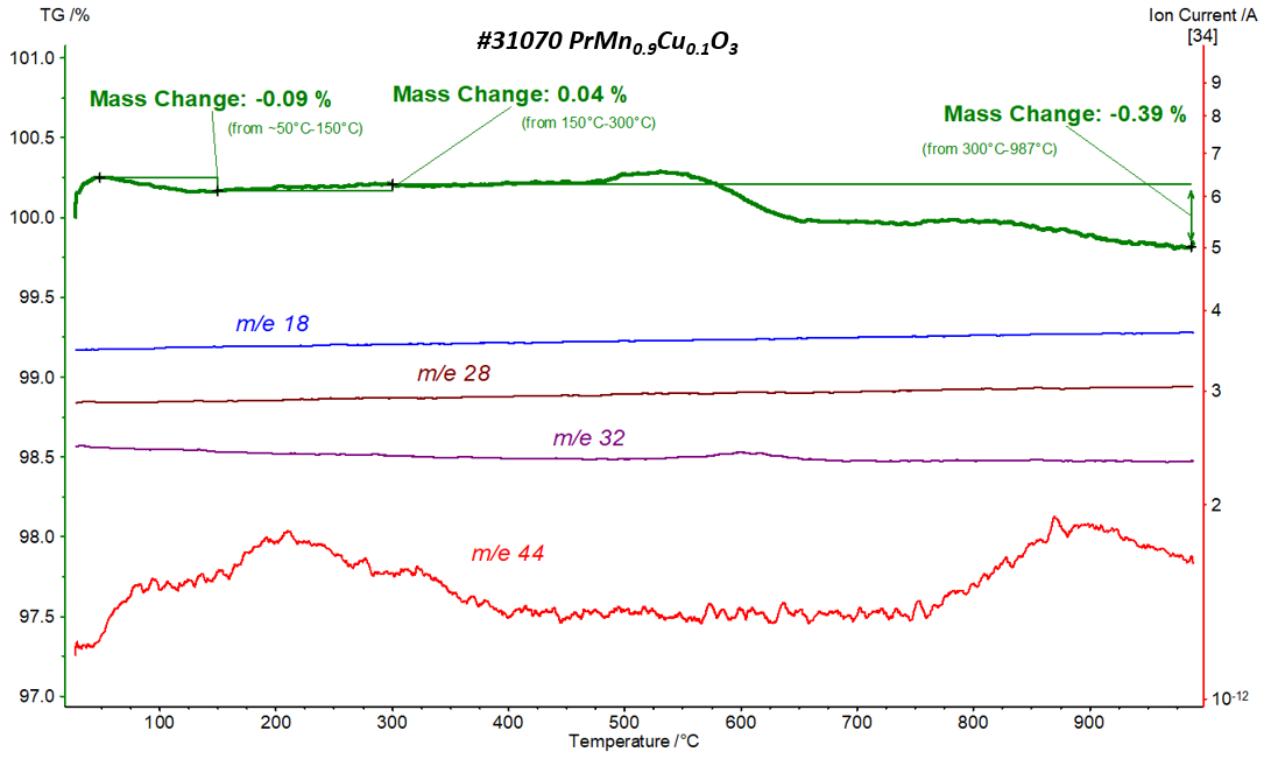
TG /%
#31070 PrMn0.9Cu0.1O3
Ion Current /A
[34]
Mass Change: -0.09 %
(from ~50°C-150°C)
Mass Change: 0.04 %
(from 150°C-300°C)
Mass Change: -0.39 %
(from 300°C-987°C)
m/e 18
m/e 28
m/e 32
m/e 44
Temperature /°C

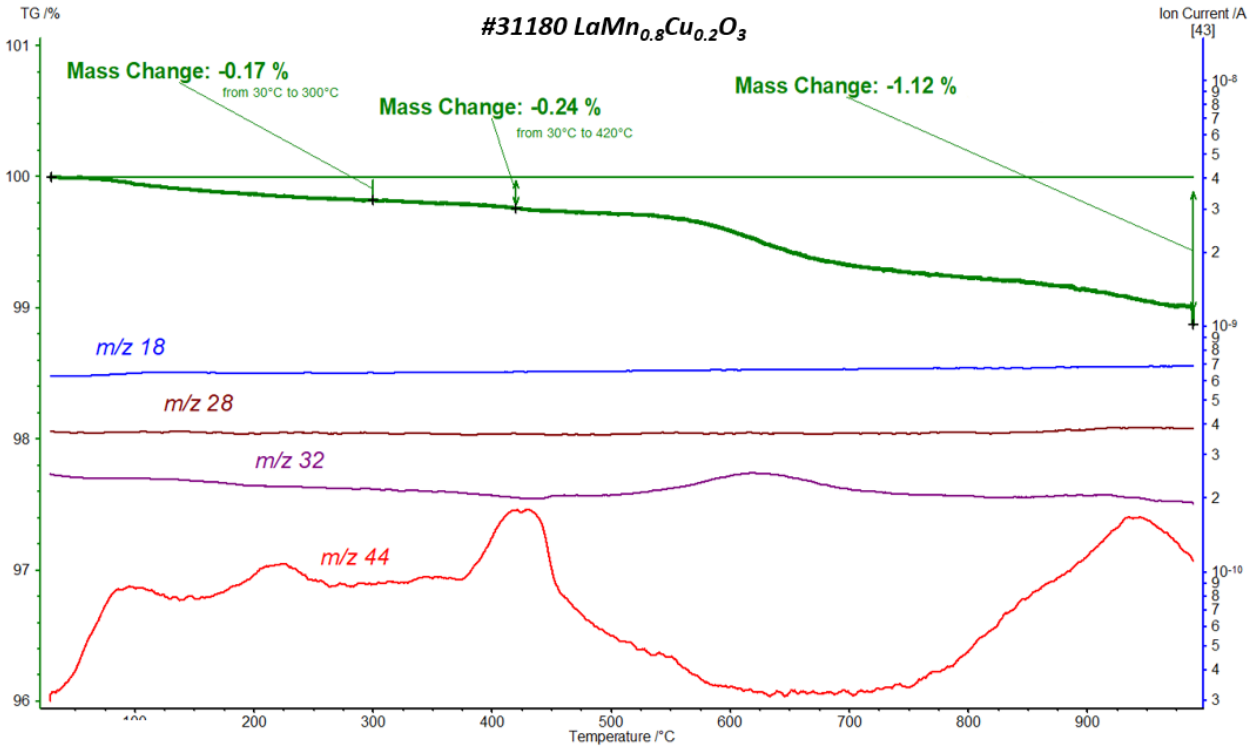
TG /%
#31180 LaMn0.8Cu0.2O3
Ion Current /A
[43]
Mass Change: -0.17 %
from 30°C to 300°C
Mass Change: -0.24 %
from 30°C to 420°C
Mass Change: -1.12 %
m/z 18
m/z 28
m/z 32
m/z 44
Temperature /°C

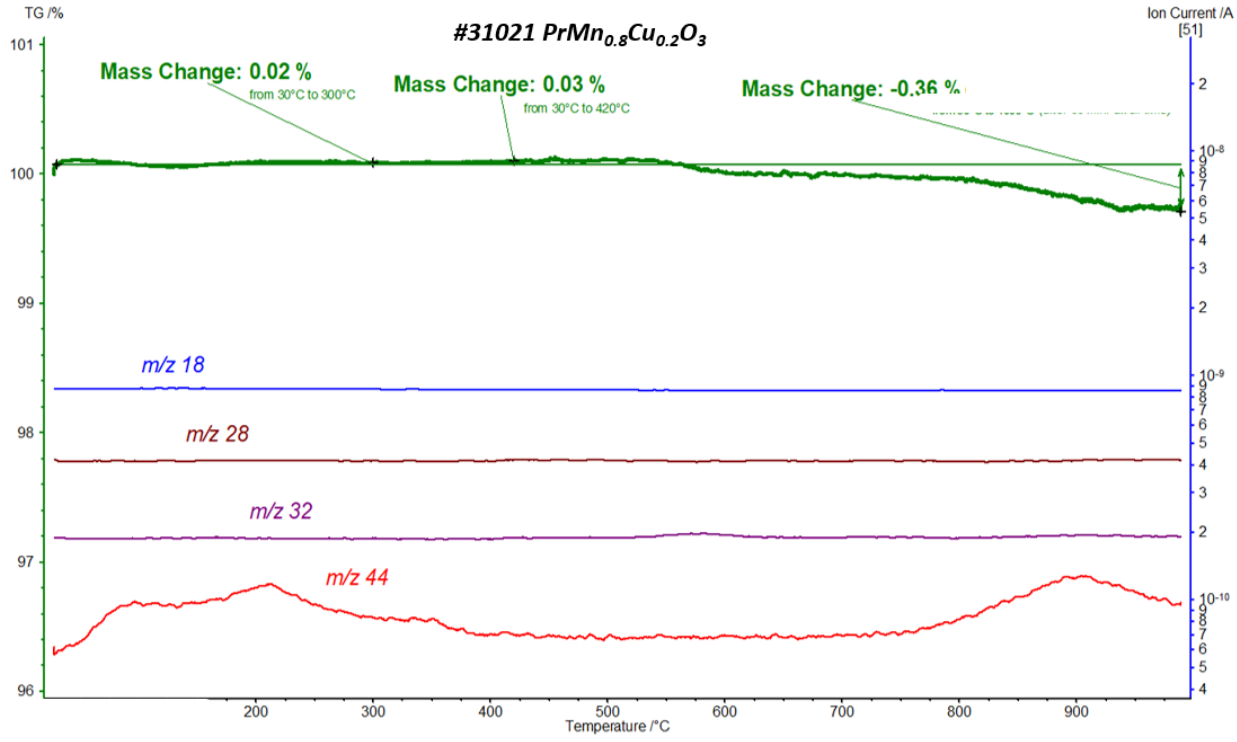
TG /%
#31021 PrMn0.8Cu0.2O3
Ion Current /A
[51]
Mass Change: 0.02 %
from 30°C to 300°C
Mass Change: 0.03 %
from 30°C to 420°C
m/z 18
m/z 28
m/z 32
m/z 44
Temperature /°C

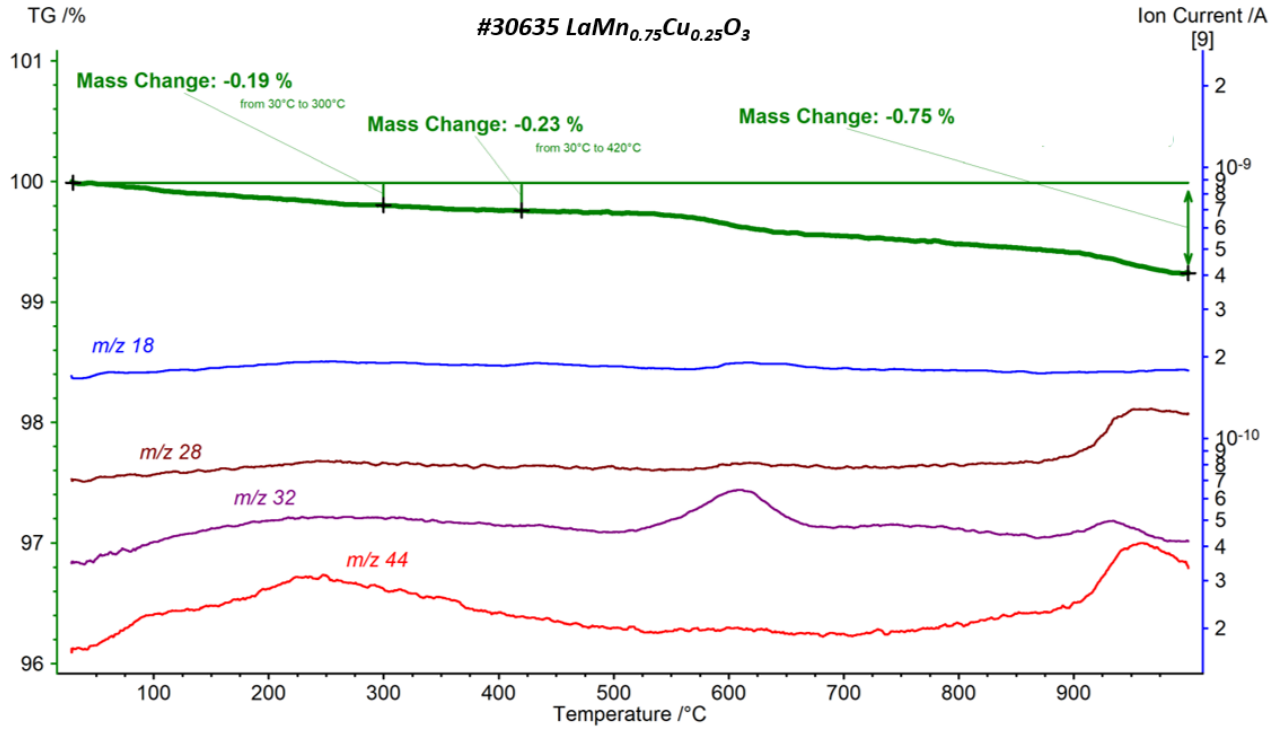
TG /%
#30635 LaMn0.75Cu0.25O3
Ion Current /A
[9]
Mass Change: -0.19 %
from 30°C to 300°C
Mass Change: -0.23 %
from 30°C to 420°C
Mass Change: -0.75 %
m/z 18
m/z 28
m/z 32
m/z 44
Temperature /°C

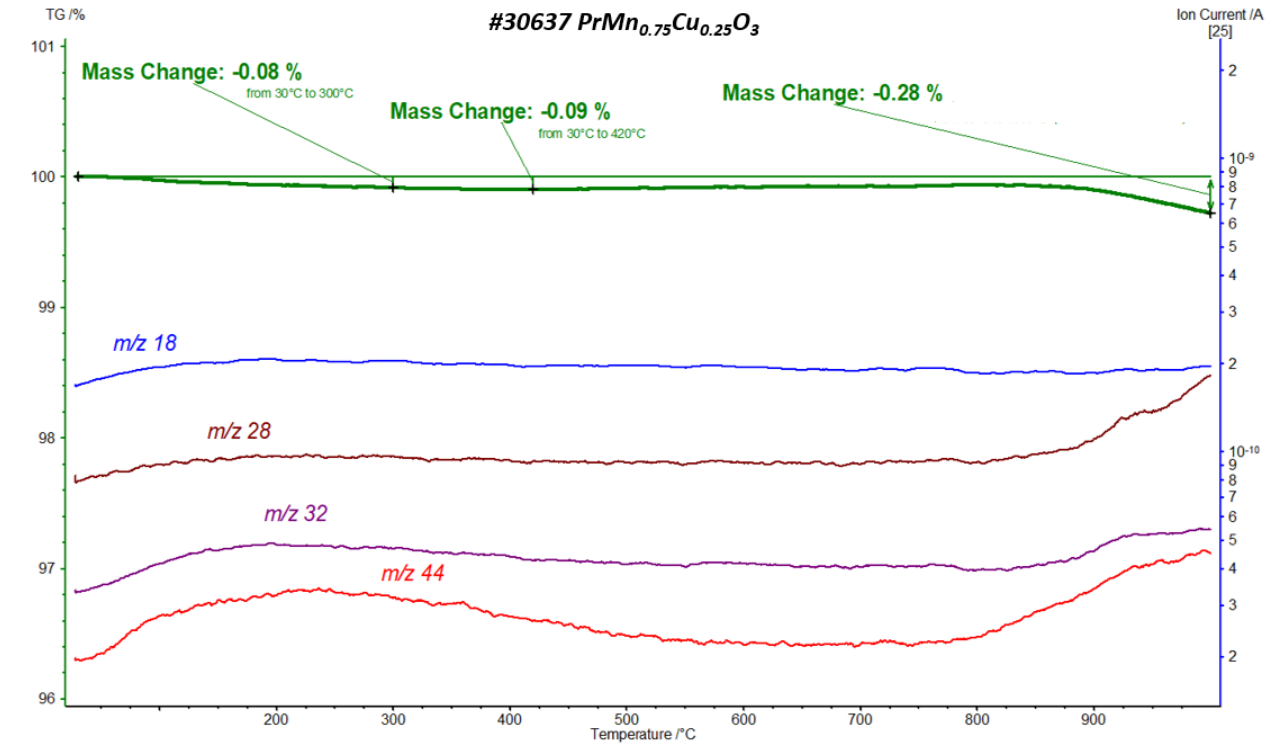
TG /%
#30637 PrMn0.75Cu0.25O3
Ion Current /A
[25]
Mass Change: -0.08 %
from 30°C to 300°C
Mass Change: -0.09 %
from 30°C to 420°C
Mass Change: -0.28 %
m/z 18
m/z 28
m/z 32
m/z 44
Temperature /°C

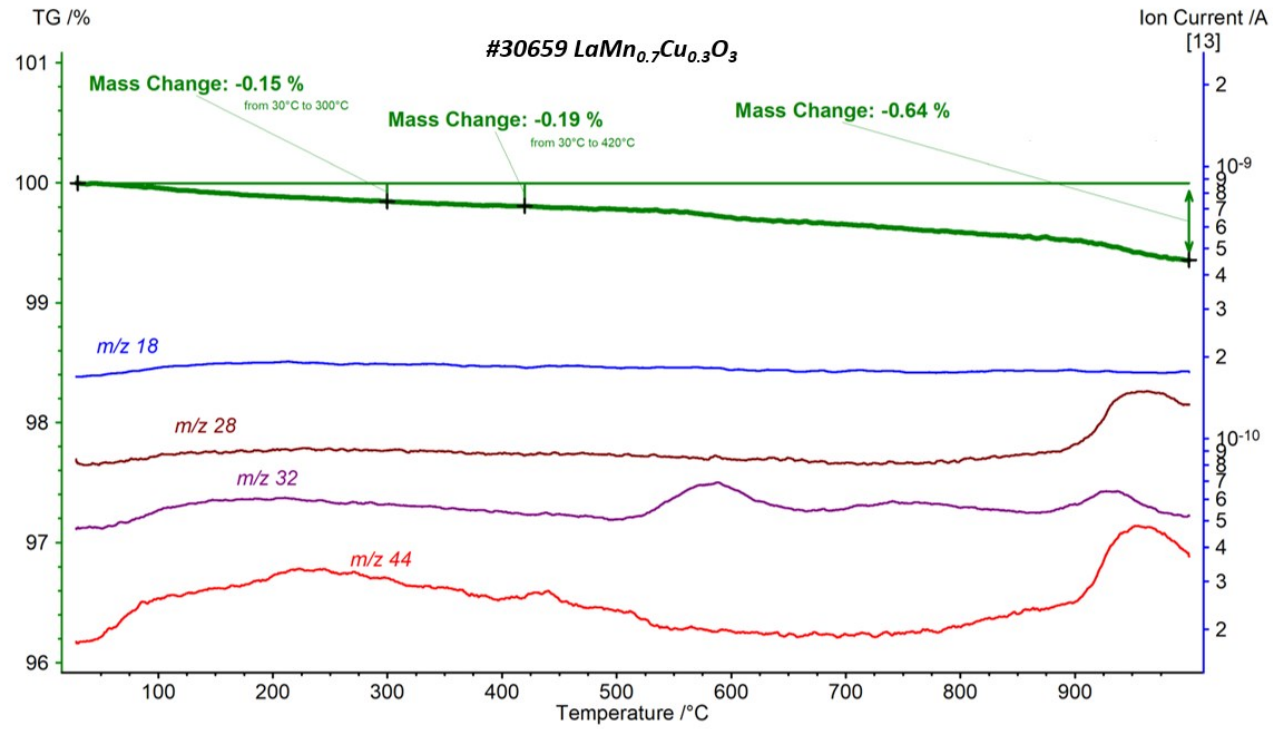
TG /%
Ion Current /A
[13]
#30659 LaMn0.7Cu0.3O3
Mass Change: -0.15 %
from 30°C to 300°C
Mass Change: -0.19 %
from 30°C to 420°C
Mass Change: -0.64 %
m/z 18
m/z 28
m/z 32
m/z 44
Temperature /°C

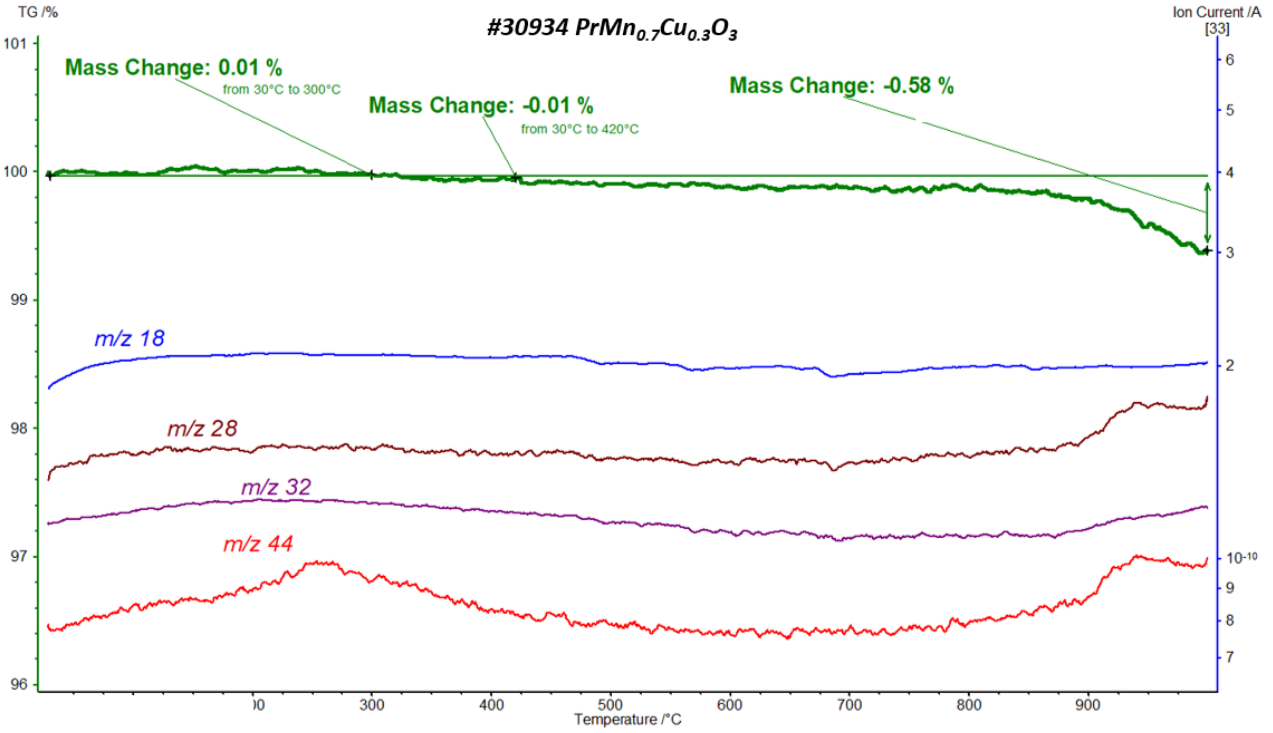
TG /%
Ion Current /A
[33]
#30934 PrMn0.7Cu0.3O3
Mass Change: 0.01 %
from 30°C to 300°C
Mass Change: -0.01 %
from 30°C to 420°C
Mass Change: -0.58 %
m/z 18
m/z 28
m/z 32
m/z 44
Temperature /°C

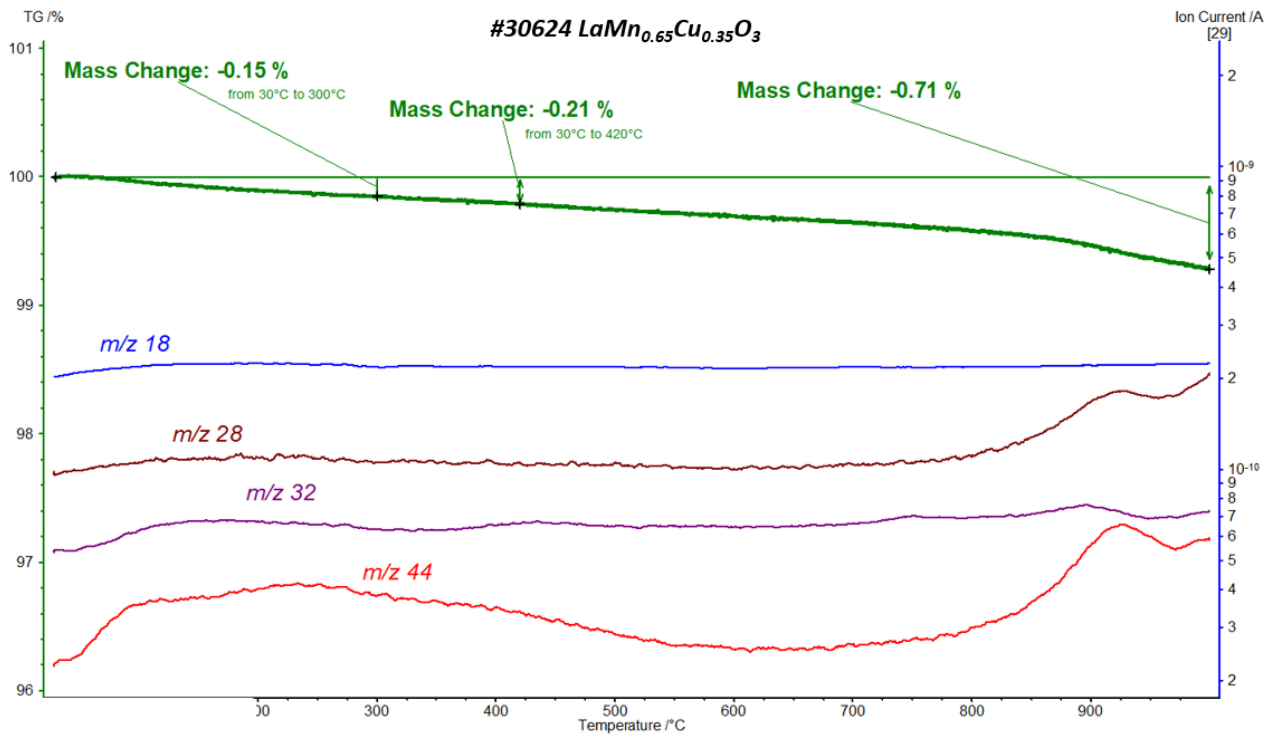
#30624 LaMn0.65Cu0.35O3
TG /%
Ion Current /A
[29]
Mass Change: -0.15 %
from 30°C to 300°C
Mass Change: -0.21 %
from 30°C to 420°C
Mass Change: -0.71 %
m/z 18
m/z 28
m/z 32
m/z 44
Temperature /°C

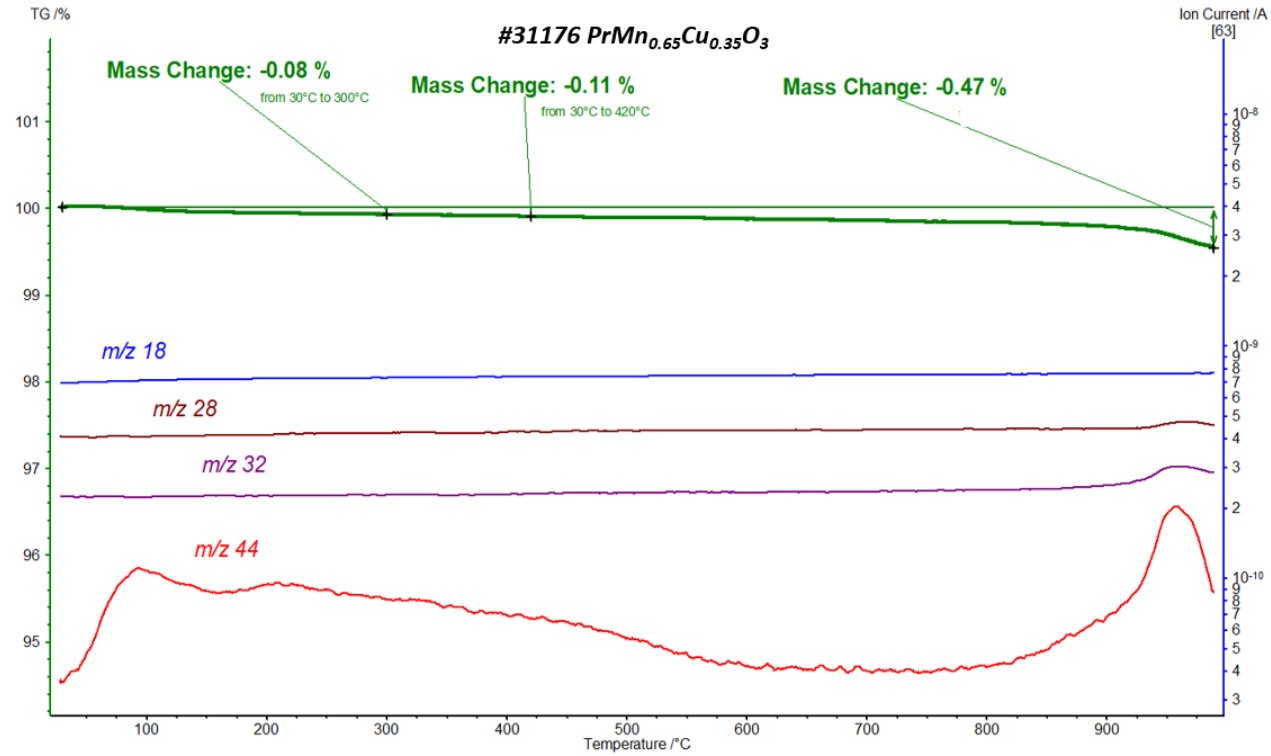
#31176 PrMn0.65Cu0.35O3
TG /%
Ion Current /A
[63]
Mass Change: -0.08 %
from 30°C to 300°C
Mass Change: -0.11 %
from 30°C to 420°C
Mass Change: -0.47 %
m/z 18
m/z 28
m/z 32
m/z 44
Temperature /°C

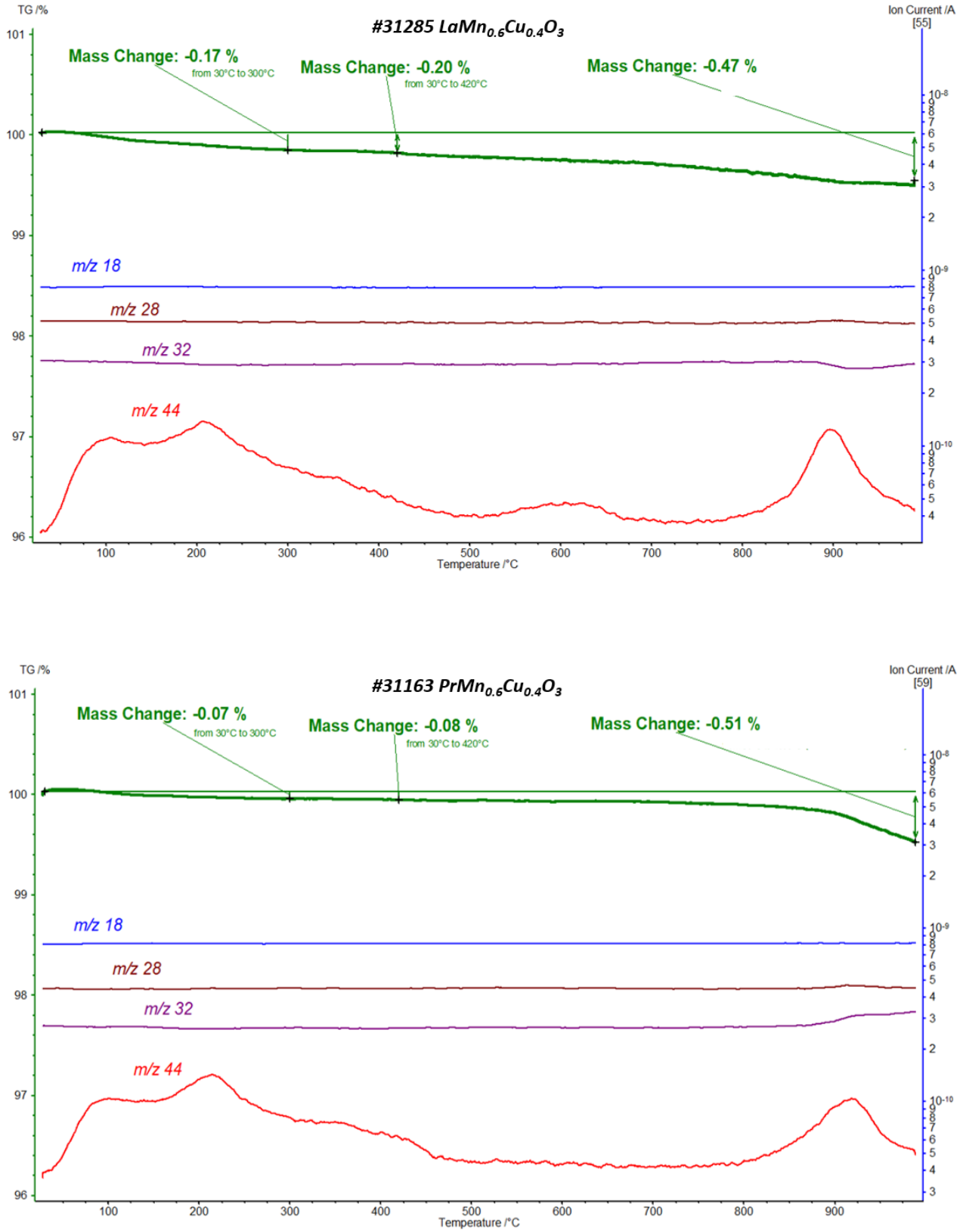

Figure S6. *Plot representing TG-MS results for all the samples of (La,Pr)-series. Color-code : green : TG mass loss; blue: water signal in the MS; brawn: CO or N_2 signal in the MS; purple: O_2 signal in the MS and red: CO_2 signal in the MS. The total mass loss after 1 h of dwelling at 1000°C is reported in Table 3.6 and Table 3.7.*

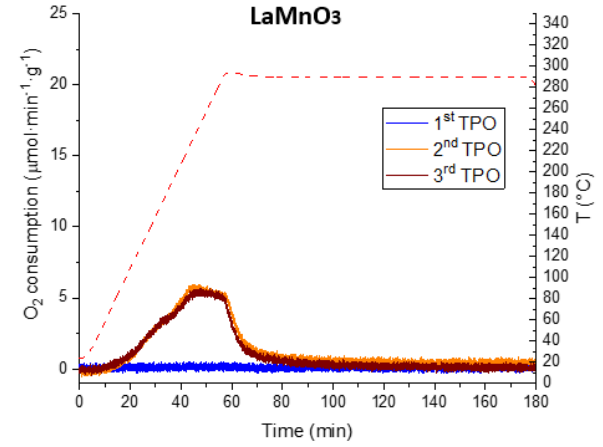
LaMnO3
1st TPO
2nd TPO
3rd TPO
O2 consumption (µmol·min-1·g-1)
T (°C)
Time (min)

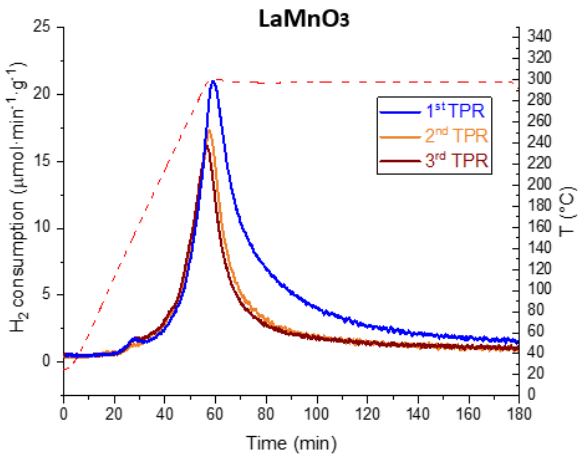
LaMnO3
1st TPR
2nd TPR
3rd TPR
H2 consumption (µmol·min-1·g-1)
T (°C)
Time (min)

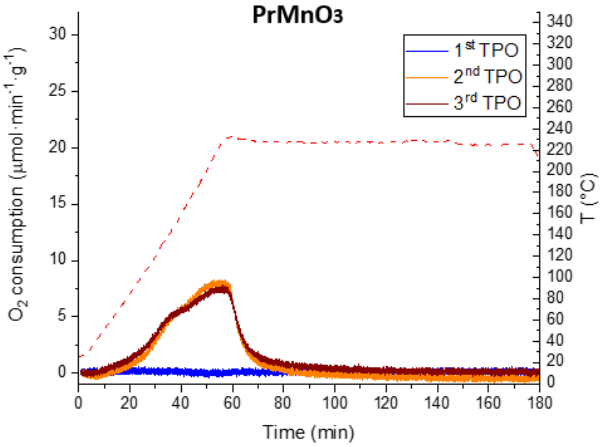
PrMnO3
1st TPO
2nd TPO
3rd TPO
O2 consumption (µmol·min-1·g-1)
T (°C)
Time (min)

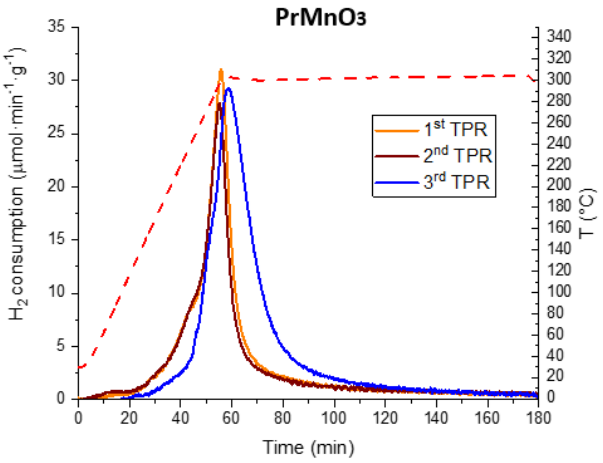
PrMnO3
1st TPR
2nd TPR
3rd TPR
H2 consumption (µmol·min-1·g-1)
T (°C)
Time (min)

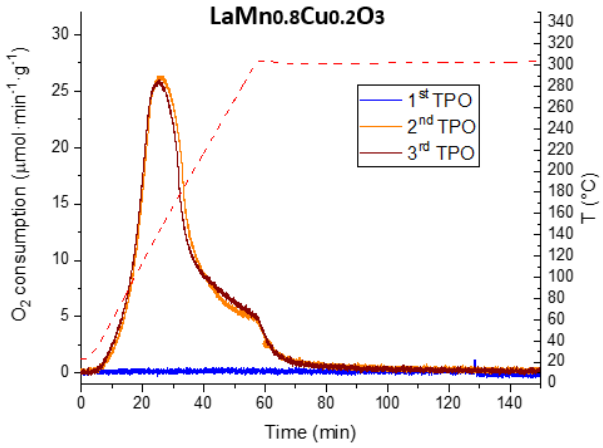
LaMn0.8Cu0.2O3
1st TPO
2nd TPO
3rd TPO
O2 consumption (µmol·min-1·g-1)
T (°C)
Time (min)

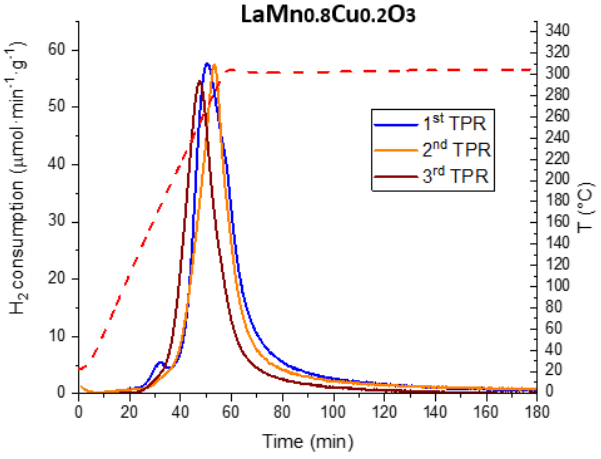
LaMn0.8Cu0.2O3
1st TPR
2nd TPR
3rd TPR
H2 consumption (µmol·min-1·g-1)
T (°C)
Time (min)

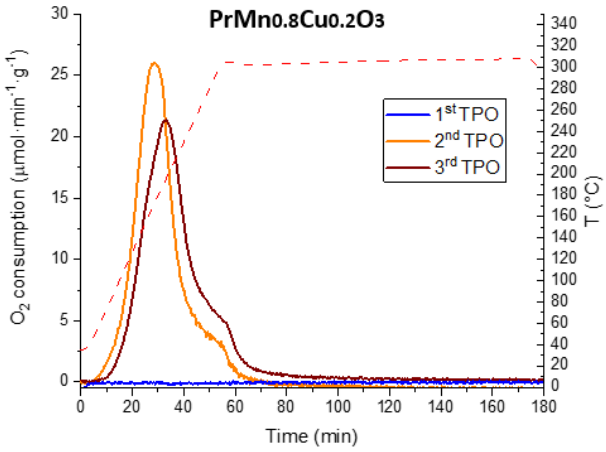
PrMn0.8Cu0.2O3
1st TPO
2nd TPO
3rd TPO
O2 consumption (μmol·min-1·g-1)
T (°C)
Time (min)

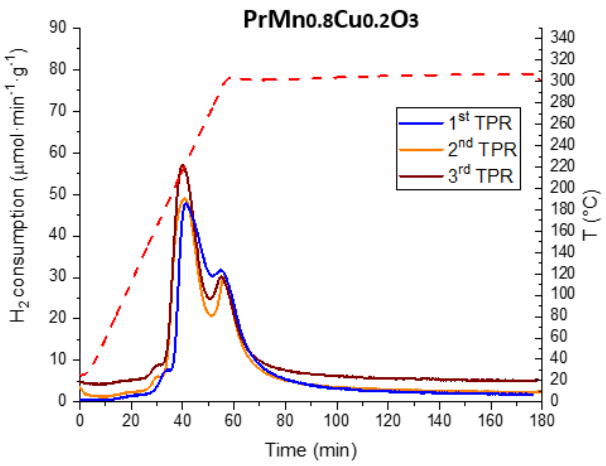
PrMn0.8Cu0.2O3
1st TPR
2nd TPR
3rd TPR
H2 consumption (μmol·min-1·g-1)
T (°C)
Time (min)

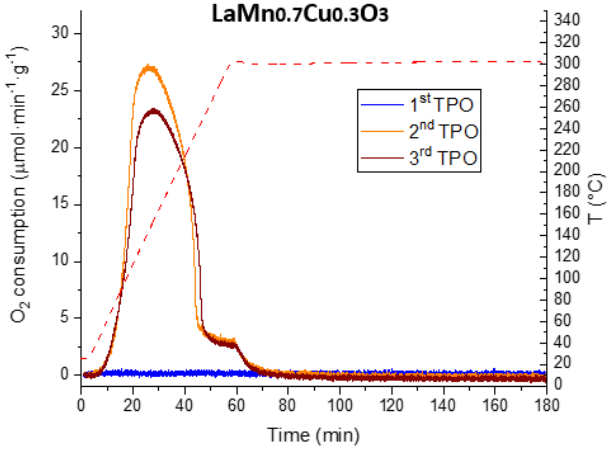
LaMn0.7Cu0.3O3
1st TPO
2nd TPO
3rd TPO
O2 consumption (μmol·min-1·g-1)
T (°C)
Time (min)

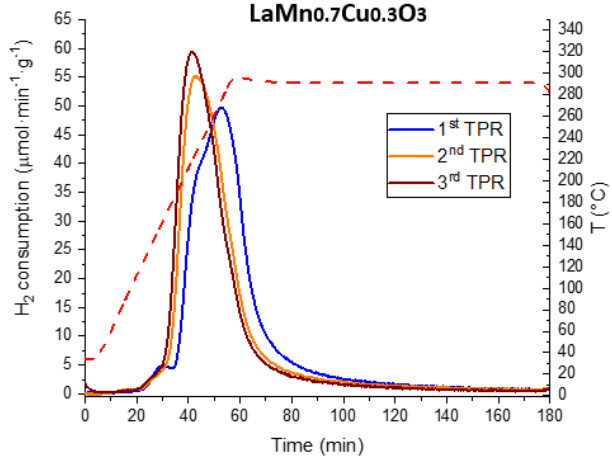
LaMn0.7Cu0.3O3
1st TPR
2nd TPR
3rd TPR
H2 consumption (μmol·min-1·g-1)
T (°C)
Time (min)

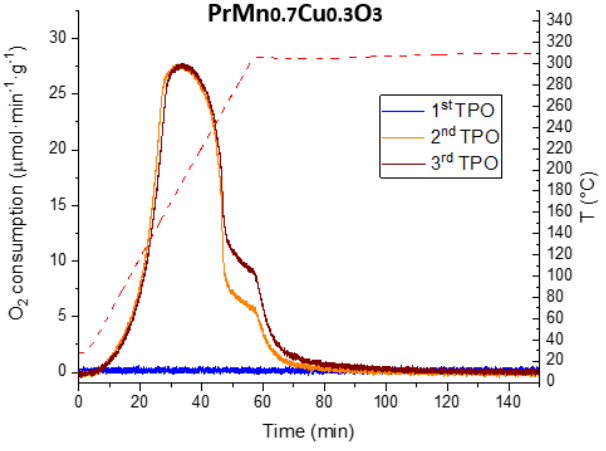
PrMn0.7Cu0.3O3
1st TPO
2nd TPO
3rd TPO
O2 consumption (μmol·min-1·g-1)
T (°C)
Time (min)

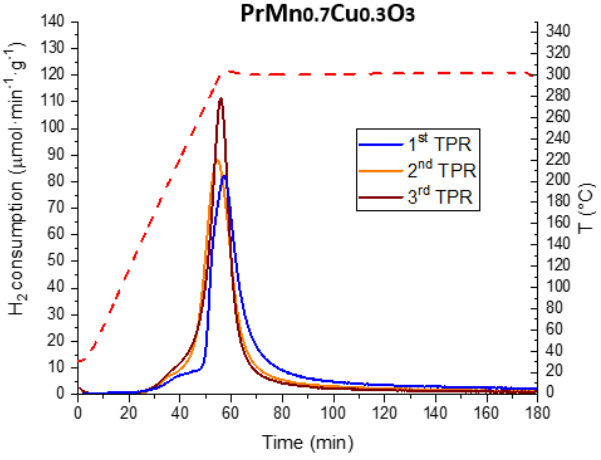
PrMn0.7Cu0.3O3
1st TPR
2nd TPR
3rd TPR
H2 consumption (μmol·min-1·g-1)
T (°C)
Time (min)

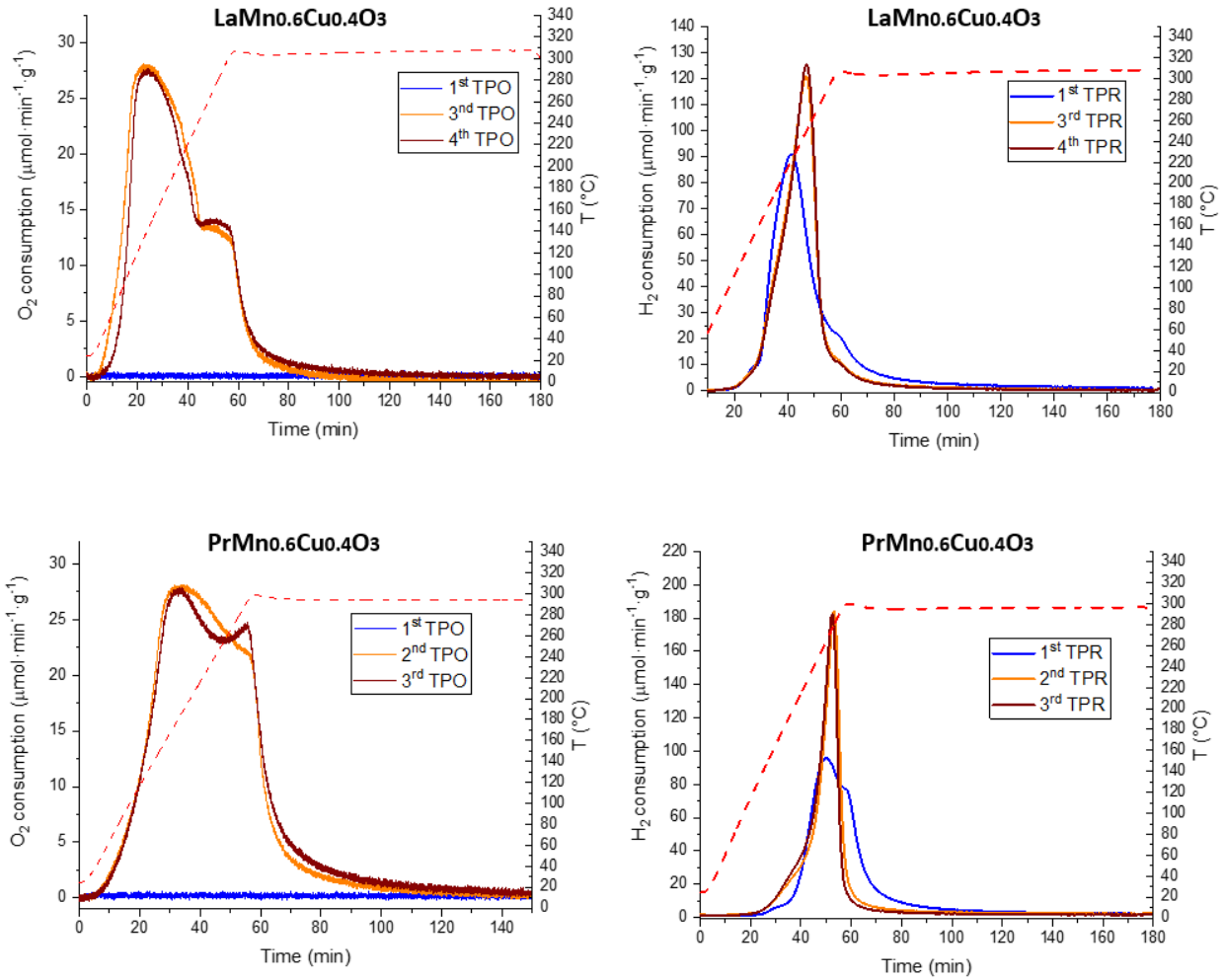

Figure S7. *TPO and TPR cycle performed at 300°C. Color-code : blue: 1st cycle; orange: 2nd cycle; brown: 3rd cycle and red dotted line : Temperature profile.*

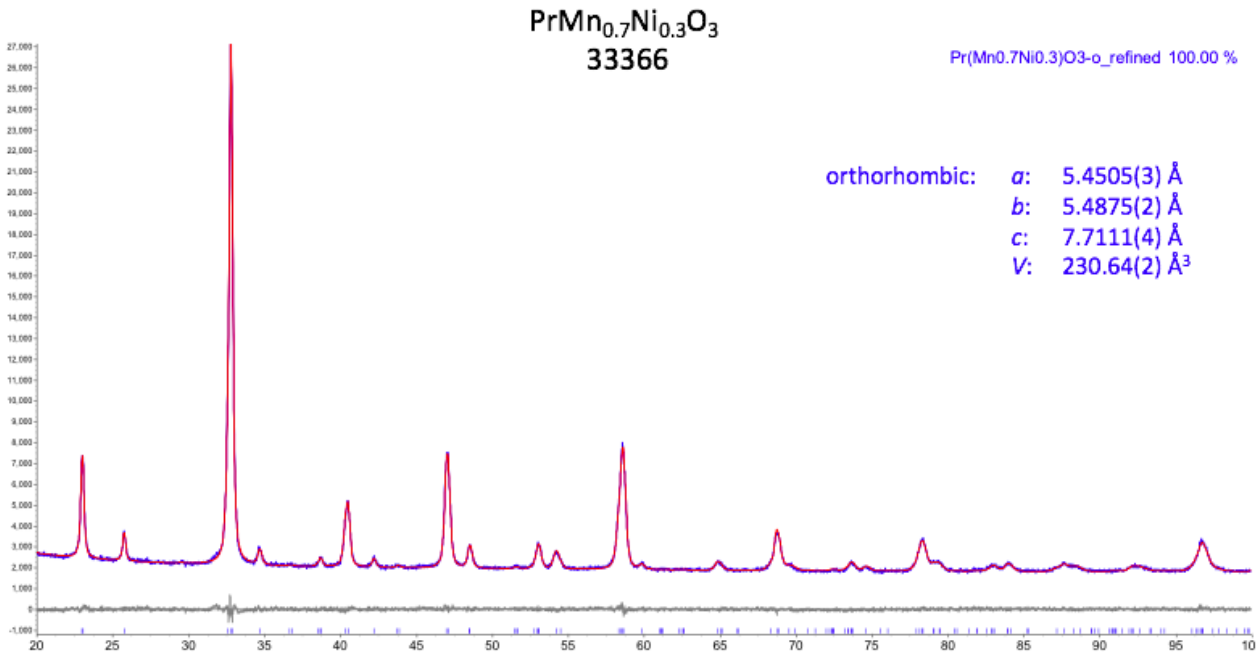
PrMn0.7Ni0.3O3
33366
Pr(Mn0.7Ni0.3)O3-o_refined 100.00 %
orthorhombic: a: 5.4505(3) Å
b: 5.4875(2) Å
c: 7.7111(4) Å
V: 230.64(2) Å3

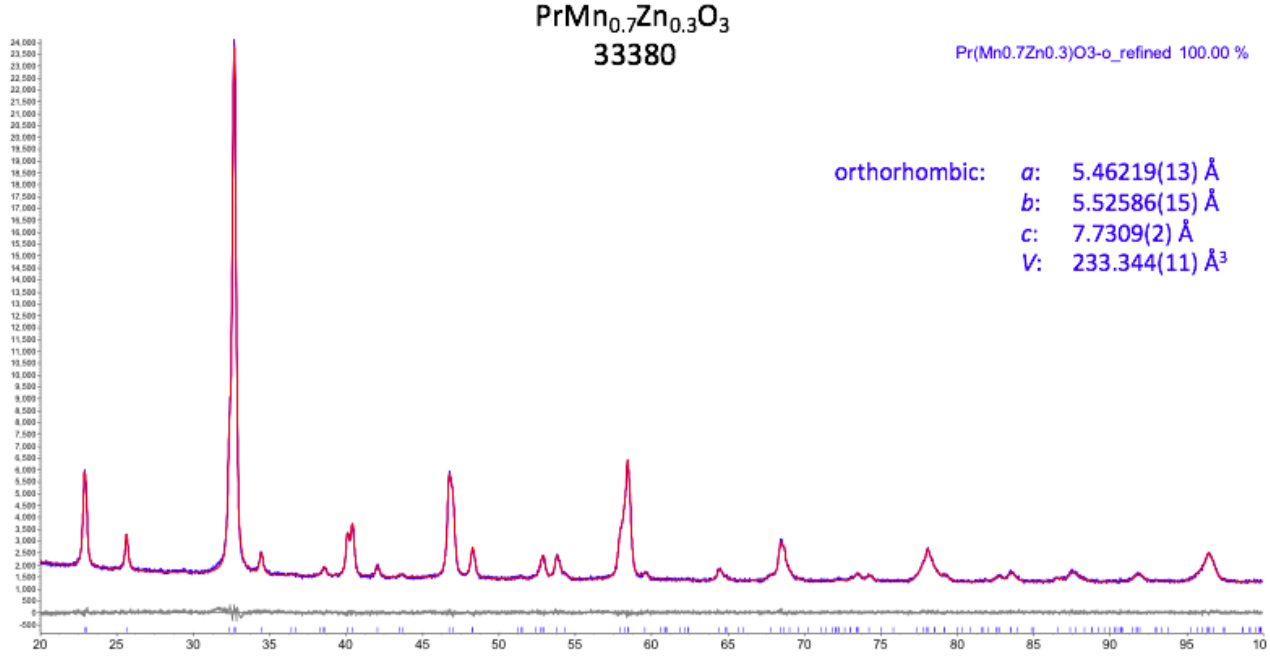
PrMn0.7Zn0.3O3
33380
Pr(Mn0.7Zn0.3)O3-o_refined 100.00 %
orthorhombic: a: 5.46219(13) Å
b: 5.52586(15) Å
c: 7.7309(2) Å
V: 233.344(11) Å3

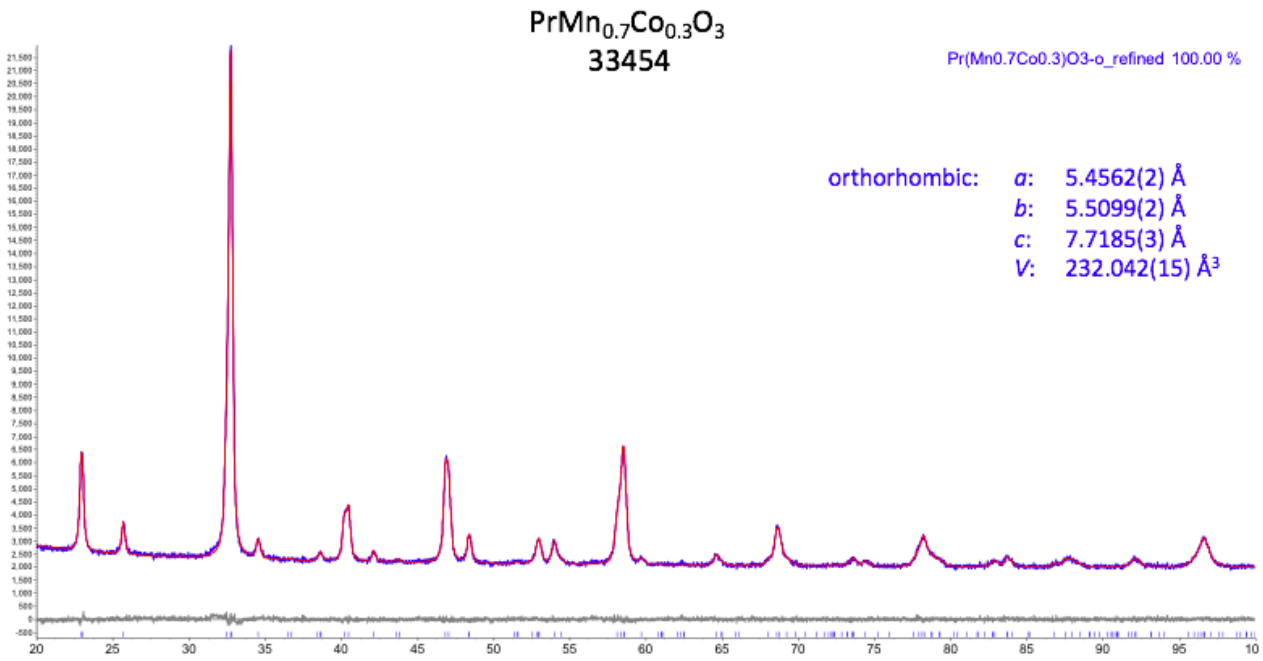
PrMn0.7Co0.3O3
33454
Pr(Mn0.7Co0.3)O3-o_refined 100.00 %
orthorhombic: a: 5.4562(2) Å
b: 5.5099(2) Å
c: 7.7185(3) Å
V: 232.042(15) Å3

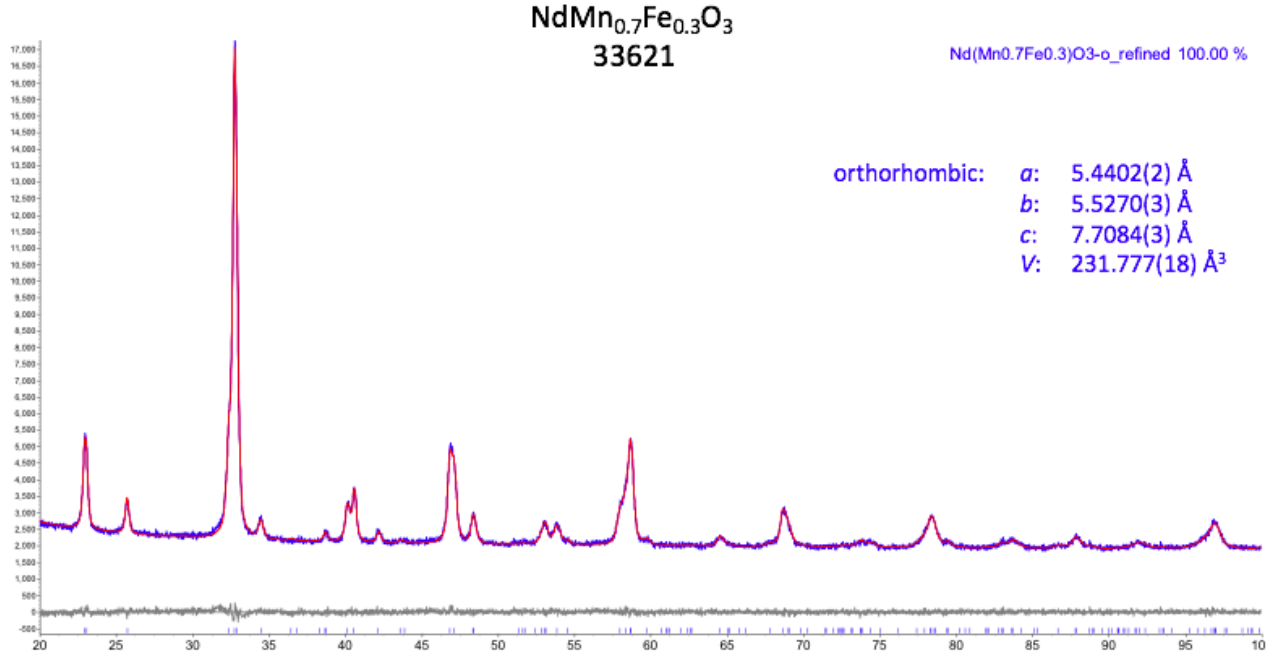
NdMn0.7Fe0.3O3
33621
Nd(Mn0.7Fe0.3)O3-o_refined 100.00 %
orthorhombic: a: 5.4402(2) Å
b: 5.5270(3) Å
c: 7.7084(3) Å
V: 231.777(18) Å3

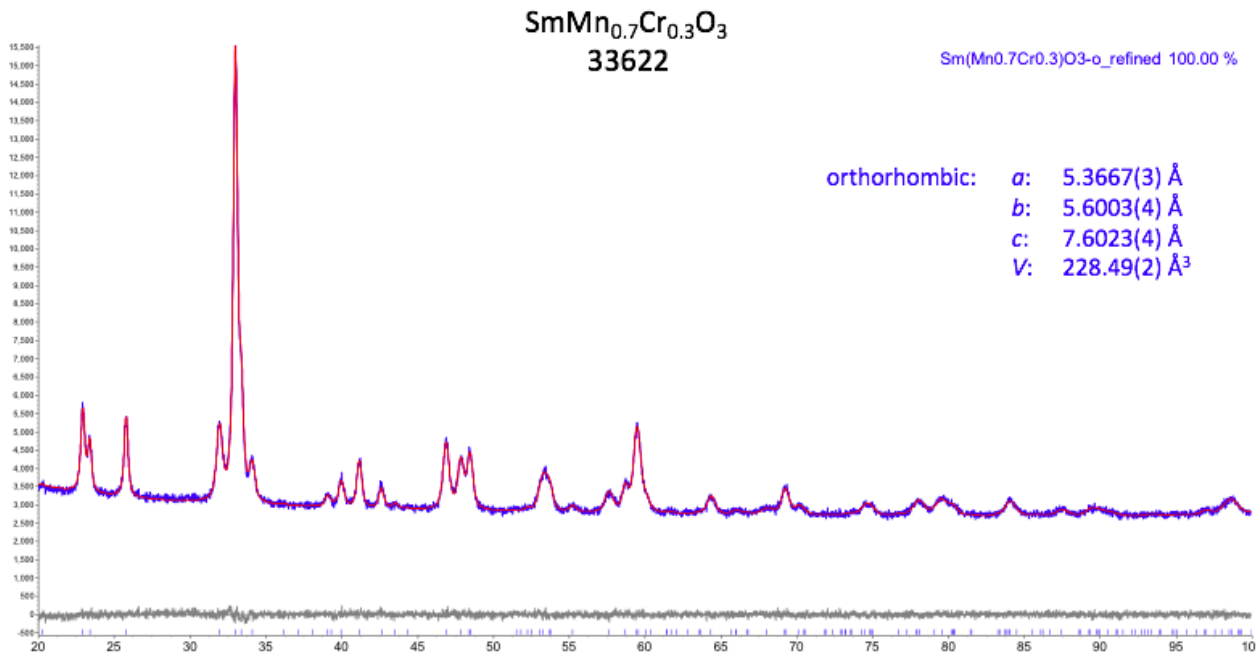
SmMn0.7Cr0.3O3
33622
Sm(Mn0.7Cr0.3)O3-o_refined 100.00 %
orthorhombic: a: 5.3667(3) Å
b: 5.6003(4) Å
c: 7.6023(4) Å
V: 228.49(2) Å3

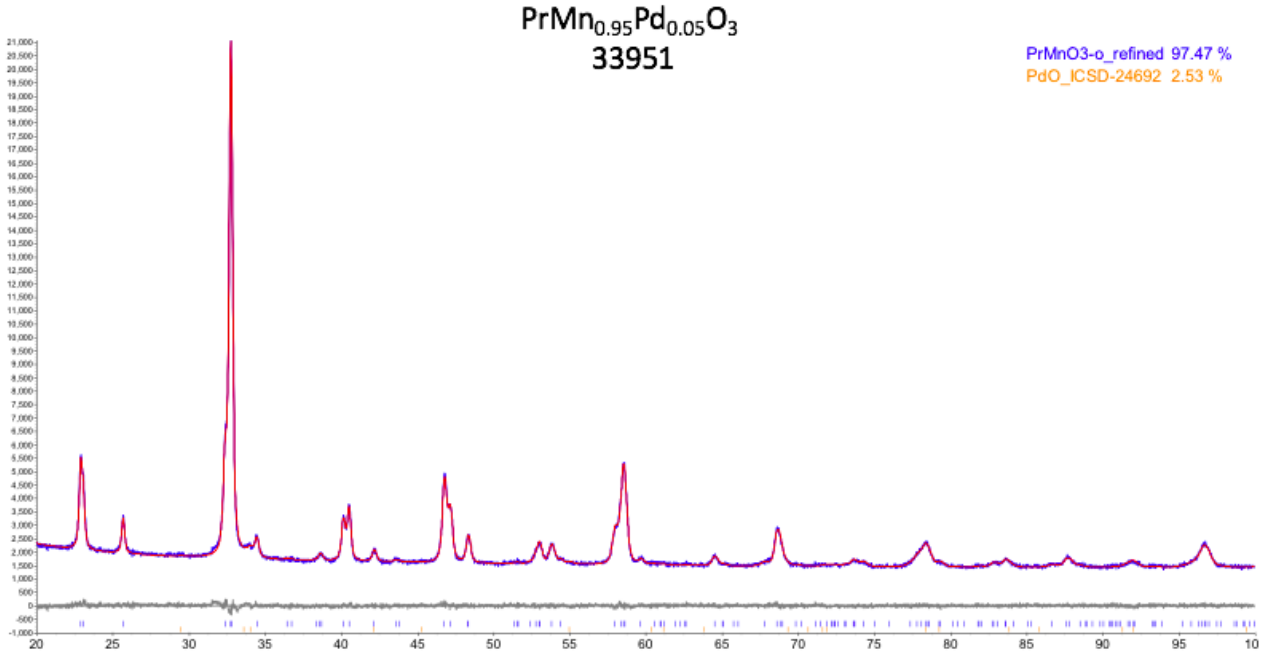
PrMn0.95Pd0.05O3
33951
PrMnO3-o_refined 97.47 %
PdO_ICSD-24692 2.53 %

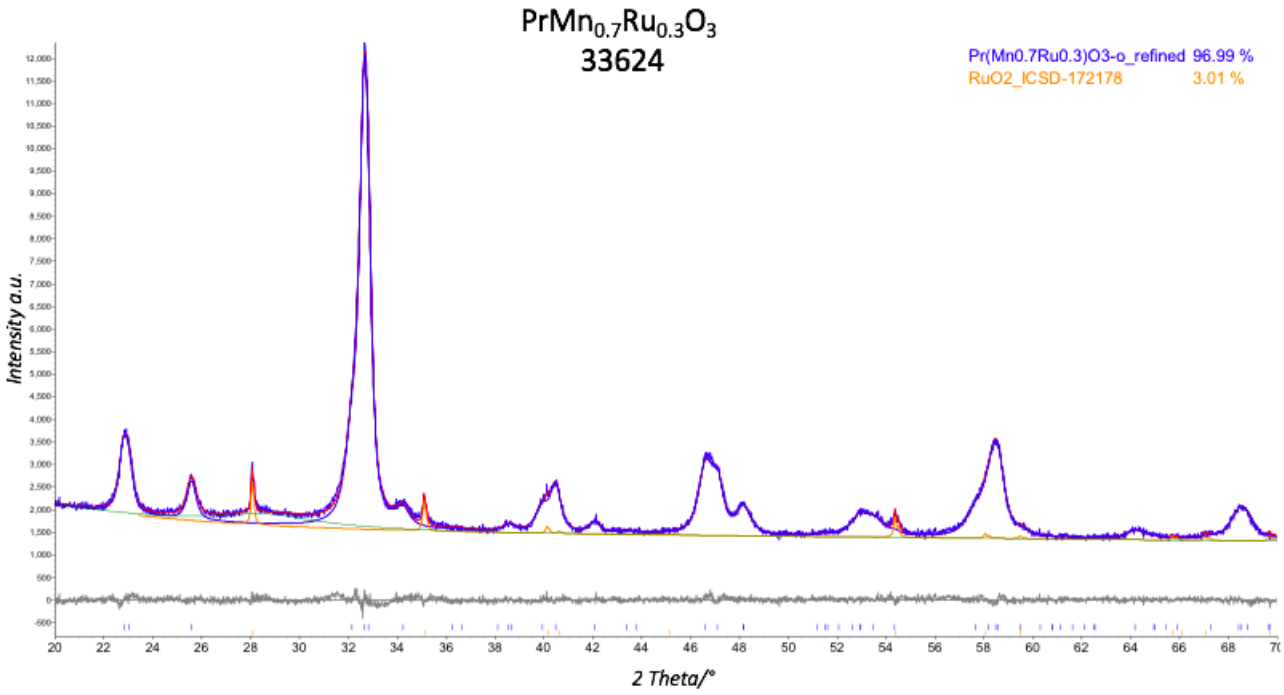

Figure S8. *Rietveld Refinement for (Pr,Nd,Sm)$Mn_{0.7}B'_{0.3}O_3$ samples. Color-code: Red: measured pattern, Blue: fitted pattern, grey difference between measured and fitted pattern and yellow: PdO and RuO_2 by-phases for $PrMn_{0.95}Pd_{0.05}O_3$ and $PrMn_{0.7}Ru_{0.3}O_3$, respectively.*

a)

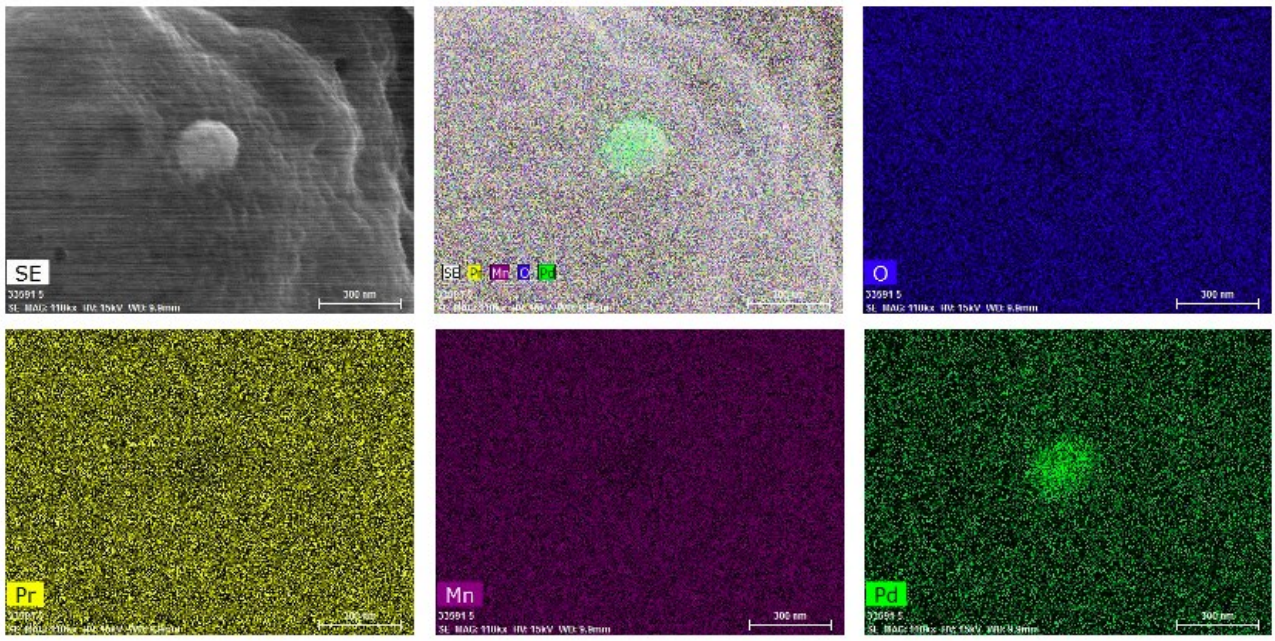

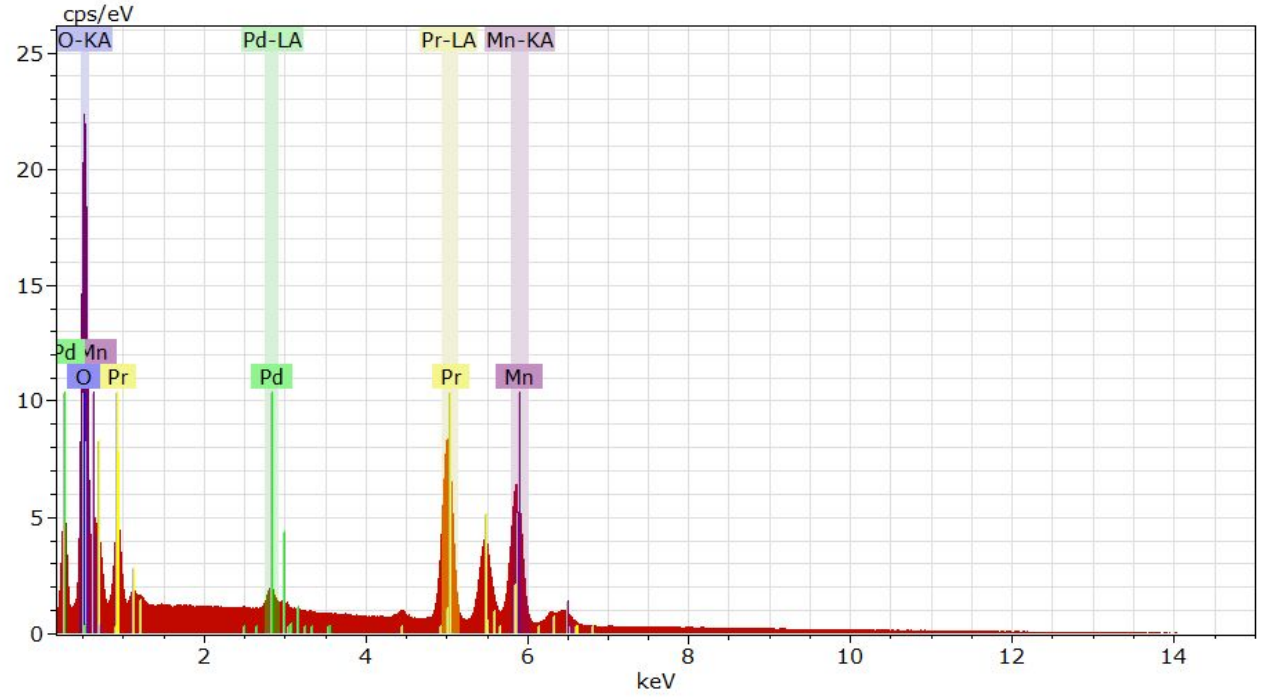
cps/eV
O-KA
Pd-LA
Pr-LA
Mn-KA
25
20
15
10
5
0
O
Pr
Pd
Pr
Mn
2
4
6
8
10
12
14
keV

b)

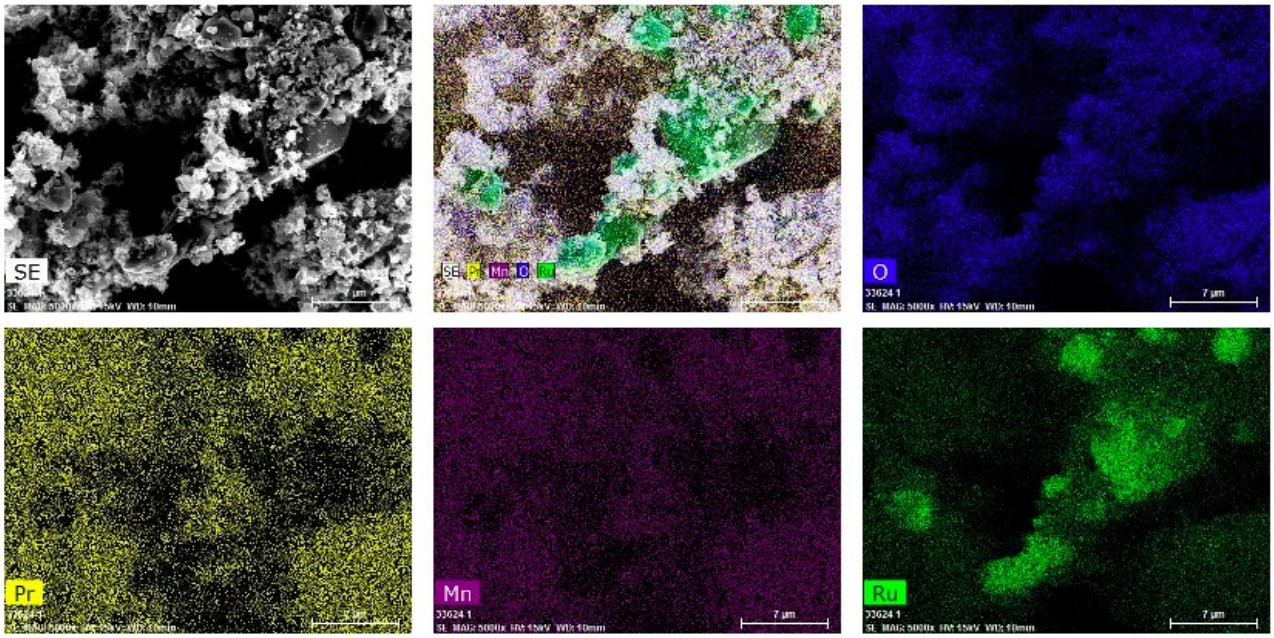
SE
O
Pr
Mn
Ru

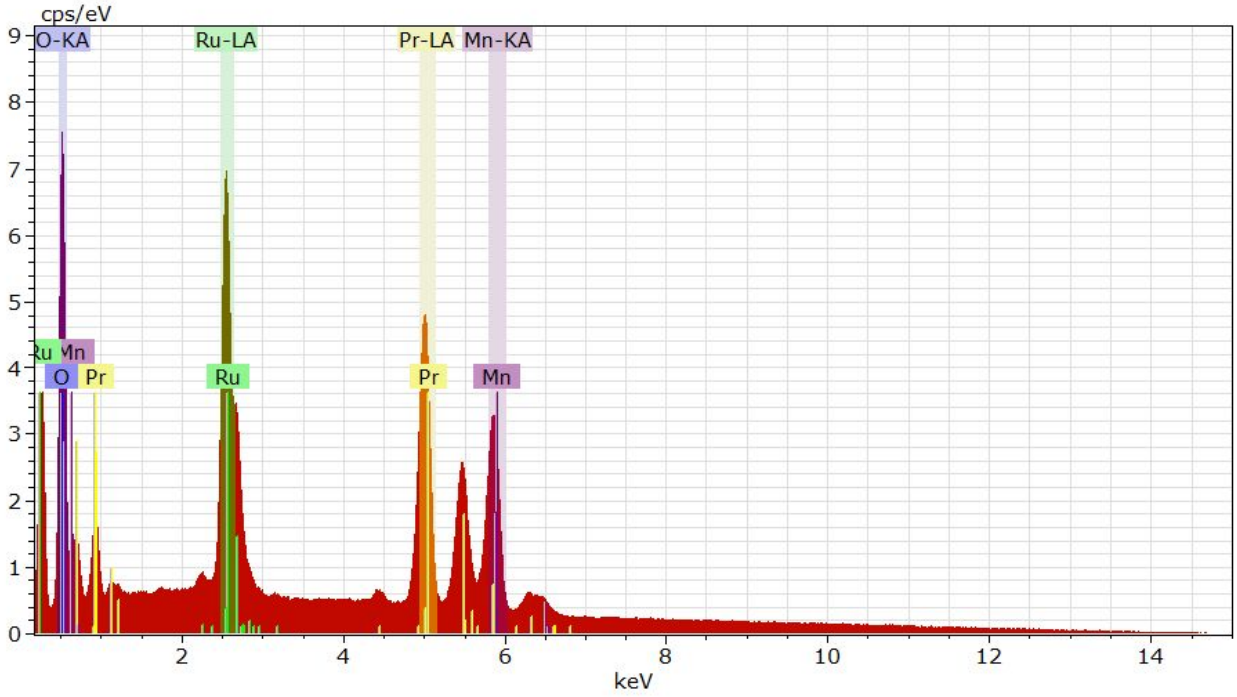

Figure S9. *EDX mapping of* ***a)*** $PrMn_{0.95}Pd_{0.05}O_3$ *and* ***b)*** $PrMn_{0.7}Ru_{0.3}O_3$.

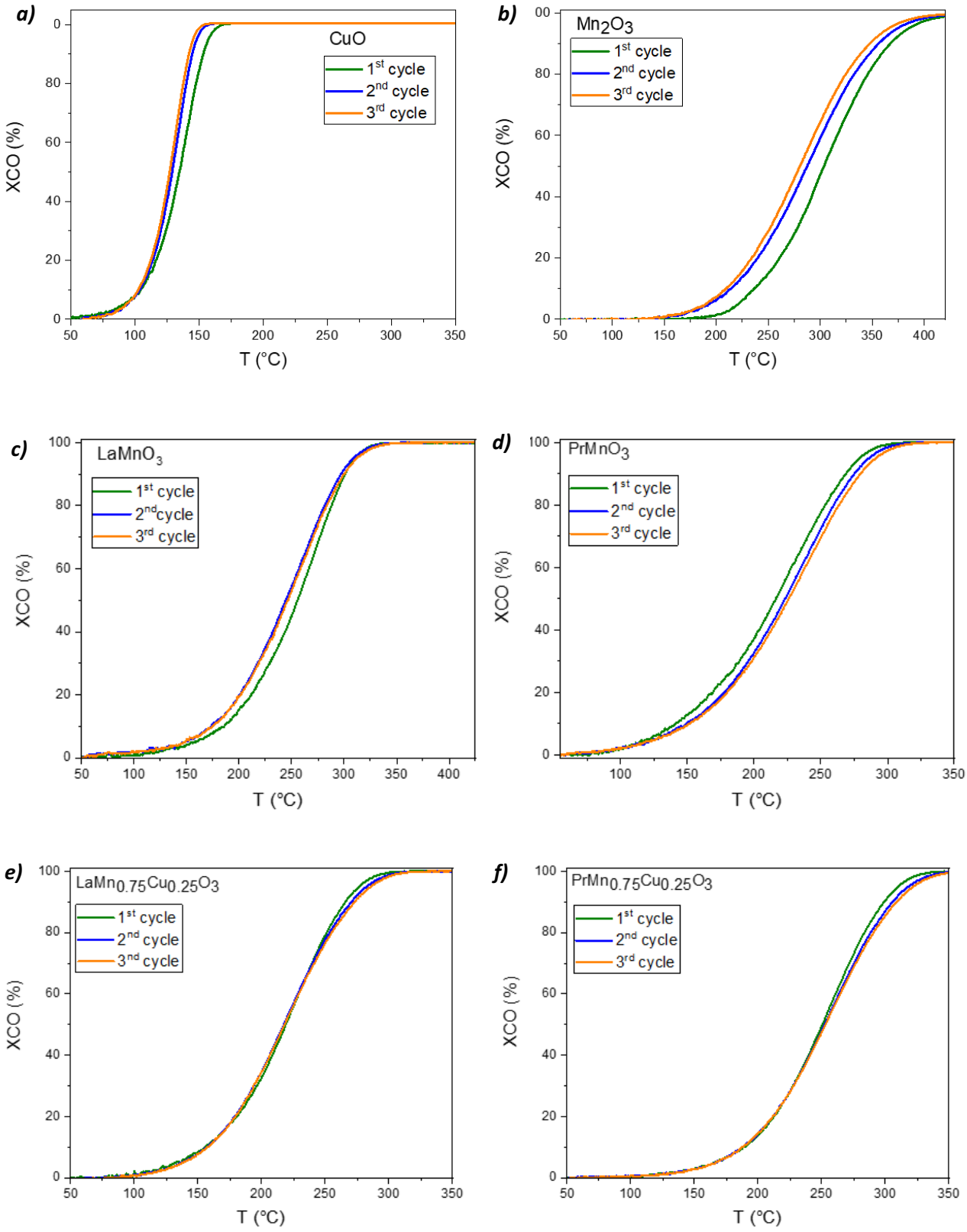
a)
CuO
1st cycle
2nd cycle
3rd cycle
XCO (%)
T (°C)
b)
Mn2O3
1st cycle
2nd cycle
3rd cycle
XCO (%)
T (°C)
c)
LaMnO3
1st cycle
2ndcycle
3rd cycle
XCO (%)
T (°C)
d)
PrMnO3
1st cycle
2nd cycle
3rd cycle
XCO (%)
T (°C)
e)
LaMn0.75Cu0.25O3
1st cycle
2nd cycle
3nd cycle
XCO (%)
T (°C)
f)
PrMn0.75Cu0.25O3
1st cycle
2nd cycle
3rd cycle
XCO (%)
T (°C)

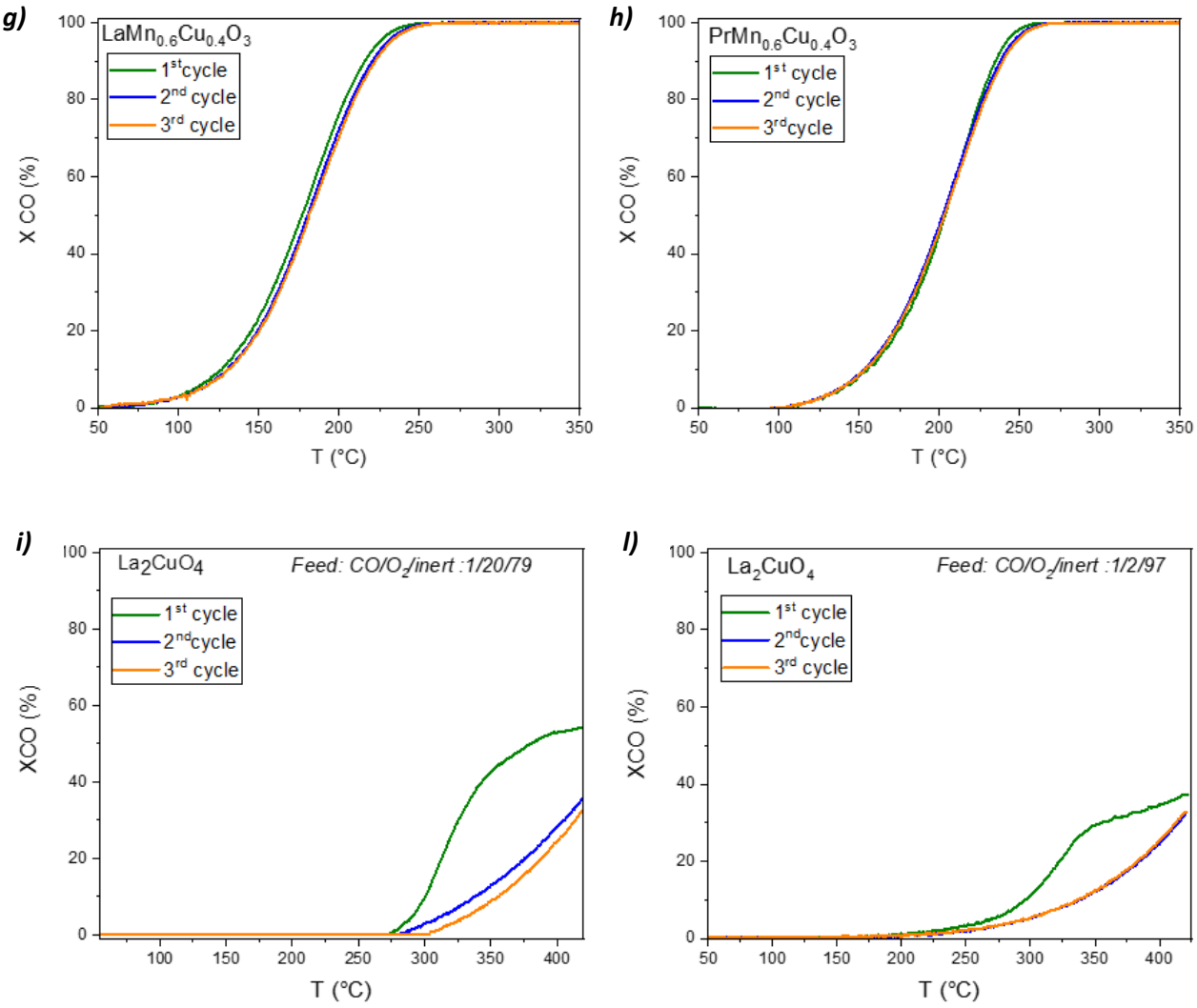

Figure S10. *X_T curve measured in feed CO/O₂/inert: 1/20/79 for* ***a)*** *CuO;* ***b)*** *Mn_2O_3;* ***c)*** *$LaMnO_3$;* ***d)*** *$PrMnO_3$;* ***e)*** *$LaMn_{0.75}Cu_{0.25}O_3$;* ***f)*** *$PrMn_{0.75}Cu_{0.25}O_3$;* ***g)*** *$LaMn_{0.6}Cu_{0.4}O_3$;* ***h)*** *$PrMn_{0.6}Cu_{0.4}O_3$;* ***i)*** *La_2CuO_4 and* ***l)*** *La_2CuO_4 measured in feed CO/O₂/inert: 1/2/97.*

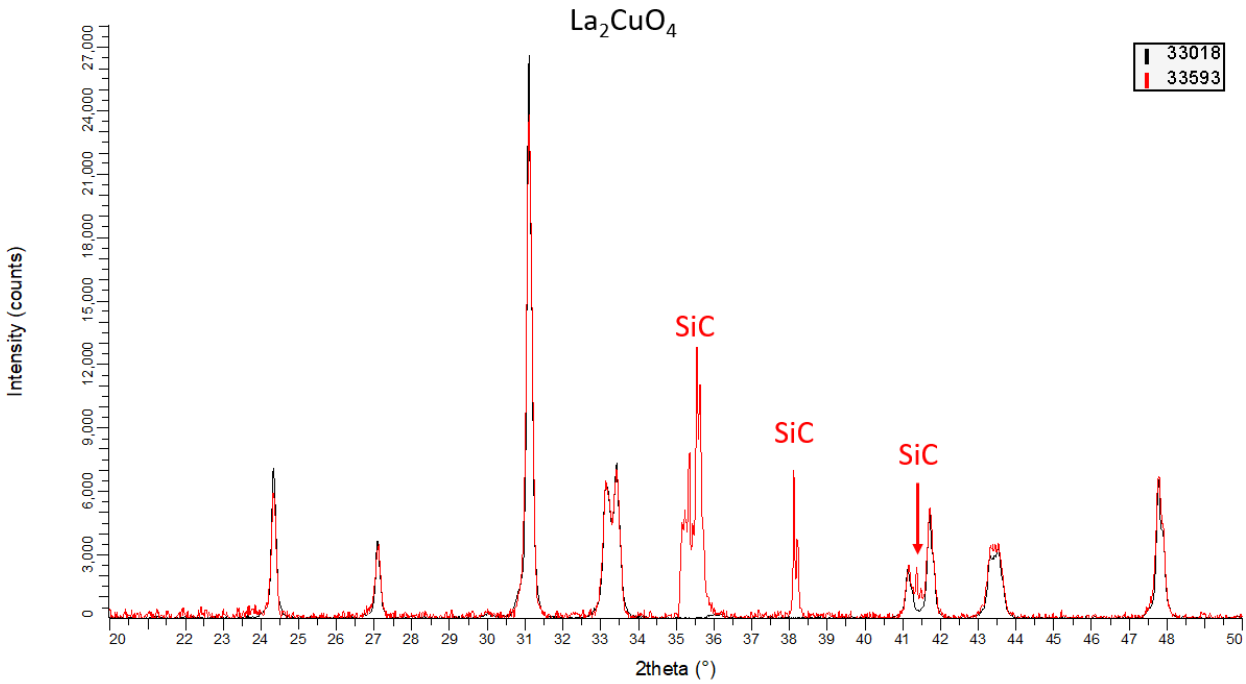

Figure S11. *Overlapped XRD diffractograms of the fresh La_2CuO_4 catalyst (#33018) and the CO oxidation post-mortem one (#33593). SiC fragments are present in the CO ox post-mortem sample because SiC is employed in the catalytic bed. Color-code: black: XRD pattern of the fresh catalyst (#30018) and red: XRD pattern of the post-mortem one (#33593).*

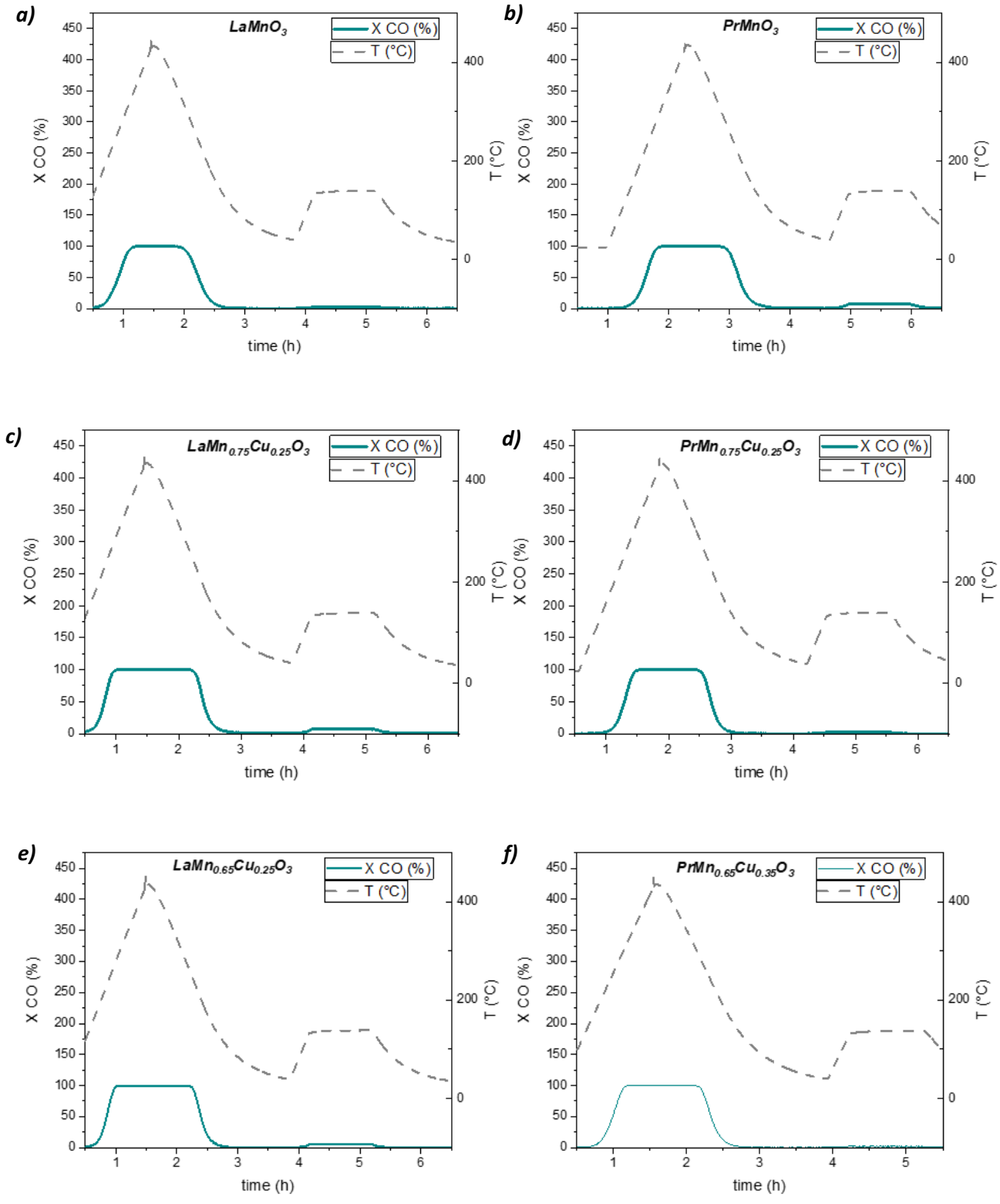

Figure S12. *Staedy-state experiments for rate determination in CO oxidation measured in feed CO/O₂/inert: 1/20/79 for* ***a)*** *$LaMnO_3$;* ***b)*** *$PrMnO_3$;* ***c)*** *$LaMn_{0.75}Cu_{0.25}O_3$;* ***d)*** *$PrMn_{0.75}Cu_{0.25}O_3$;* ***e)*** *$LaMn_{0.65}Cu_{0.35}O_3$;* ***f)*** *$PrMn_{0.65}Cu_{0.35}O_3$.*

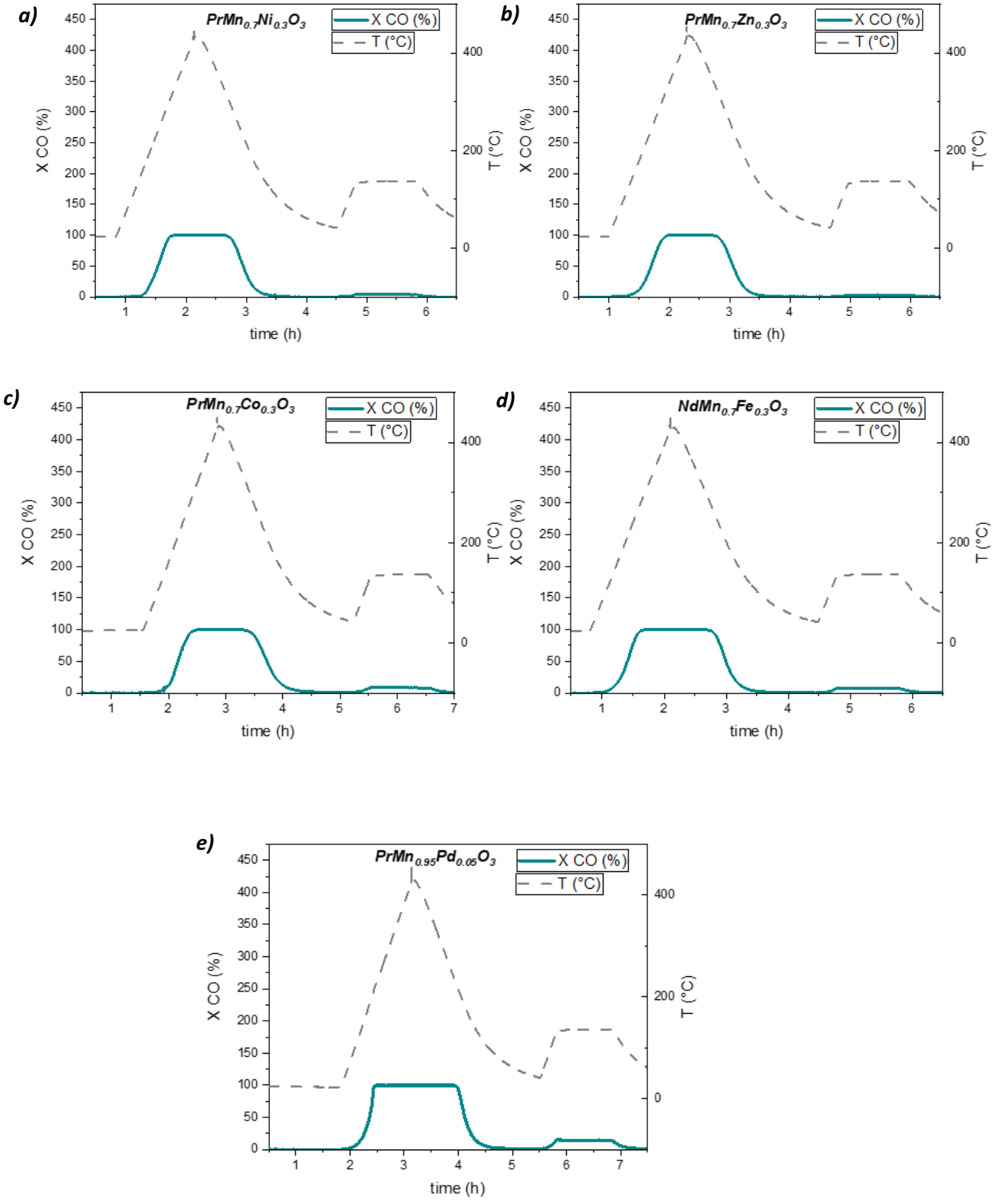

Figure S13. *Staedy-state experiments for rate determination in CO oxidation measured in feed CO/O_2/inert: 1/20/79 for* ***a)*** *$PrMn_{0.7}Ni_{0.3}O_3$;* ***b))*** *$PrMn_{0.7}Zn_{0.3}O_3$;* ***c)*** *$PrMn_{0.7}Co_{0.3}O_3$;* ***d)*** *$NdMn_{0.7}Fe_{0.3}O_3$;* ***e)*** *$PrMn_{0.95}Pd_{0.05}O_3$.*

Table S1. *Table with listed the training RMSEes and the corresponding descriptors found for the trainings from 0-9 in the SISSO calculation performed for CO oxidation over the (La,Pr)$Mn_{(1-x)}Cu_xO_3$ series.*

Training	RMSE	Descriptor
0	26.778	c0 + a0 * [(B´$_{surface}$) / (D)] + a1 * (A$_{_surface}$ + A$_{_bulk}$)
1	26.921	c0 + a0 * [(B´$_{surface}$) / (D)] + a1 * [(A$_{_surface}$) * (A$_{_bulk}$)]
2	26.940	c0 + a0 * [(O $_{surface}$) * (A$_{_surface}$)] + a1 * [(O $_{defect\ surf}$ * (D)]
3	27.626	c0 + a0 * [(B´ $_{bulk}$) / (D)] + a1 * (A$_{_surface}$ + A$_{_bulk}$)
4	28.250	c0 + a0 * [(B´ $_{bulk}$) / (D)] + a1 * [(A $_{surface}$) * (A$_{_bulk}$)]
5	29.447	c0 + a0 * (A$_{_surface}$)^3 + a1 * [(B $_{bulk}$) * (D)]
6	30.210	c0 + a0 * (A$_{_surface}$)^2 + a1 * [(B $_{bulk}$) * (D)]
7	30.420	c0 + a0 * [(A$_{_surface}$) * (<BOB>$_{\mu}$)] + a1 * [(B $_{bulk}$) * (D)]
8	30.464	c0 + a0 * [(A$_{_surface}$) / (O $_{tot\ (bulk+surface)}$)] + a1 * [(B´$_{bulk}$) / (D)]
9	30.493	c0 + a0 * [(A$_{_surface}$) * (A$_{_bulk}$)] + a1 * |<AO>$_{\mu}$ - (D)|

References

1. Balachandran, P.V., et al., *Predictions of new ABO3 perovskite compounds by combining machine learning and density functional theory.* Physical Review Materials, 2018. **2**(4): p. 043802.
2. Li, W., R. Jacobs, and D. Morgan, *Predicting the thermodynamic stability of perovskite oxides using machine learning models.* Computational Materials Science, 2018. **150**: p. 454-463.
3. Odabaşı, Ç. and R. Yıldırım, *Performance analysis of perovskite solar cells in 2013–2018 using machine-learning tools.* Nano Energy, 2019. **56**: p. 770-791.
4. Pilania, G., et al., *Classification of ABO3 perovskite solids: a machine learning study.* Acta Crystallographica Section B: Structural Science, Crystal Engineering and Materials, 2015. **71**(5): p. 507-513.
5. Pilania, G., et al., *Finding new perovskite halides via machine learning.* Frontiers in Materials, 2016. **3**: p. 19.
6. Blay, V., et al., *Converting olefins to propene: Ethene to propene and olefin cracking.* Catalysis Reviews, 2018. **60**(2): p. 278-335.
7. Schlögl, R., *Active Sites for Propane Oxidation: Some Generic Considerations.* Topics in Catalysis, 2011. **54**(10): p. 627.
8. Cavani, F., N. Ballarini, and A. Cericola, *Oxidative dehydrogenation of ethane and propane: How far from commercial implementation?* Catalysis Today, 2007. **127**(1): p. 113-131.
9. Grasselli, R.K., *Fundamental Principles of Selective Heterogeneous Oxidation Catalysis.* Topics in Catalysis, 2002. **21**(1): p. 79-88.
10. R. K. Grasselli, J.D.B., *Oxidation of low-molecular-weight hydrocarbons, in Handbook of Heterogeneous Catalysis (2nd Edition)*. Vol. 7. 2008, Weinheim: Wiley-VCH.
11. Schlogl, R., *Active Sites for Propane Oxidation: Some Generic Considerations.* Topics in Catalysis, 2011. **54**(10-12): p. 627-638.
12. J. M. Thomas, W.J.T., *Principles and Practice of Heterogeneous Catalysis*, ed. Wiley-VCH. 2015, Weinheim, Germany.
13. Ertl, G., *Elementary Steps in Heterogeneous Catalysis.* Angewandte Chemie International Edition in English, 1990. **29**(11): p. 1219-1227.
14. Grasselli, R.K., *Site isolation and phase cooperation: Two important concepts in selective oxidation catalysis: A retrospective.* Catalysis Today, 2014. **238**: p. 10-27.
15. Grasselli, R.K., *Genesis of site isolation and phase cooperation in selective oxidation catalysis.* Topics in Catalysis, 2001. **15**(2): p. 93-101.
16. Batiot, C. and B.K. Hodnett, *The role of reactant and product bond energies in determining limitations to selective catalytic oxidations.* Applied Catalysis A: General, 1996. **137**(1): p. 179-191.
17. Getsoian, A.B., Z. Zhai, and A.T. Bell, *Band-Gap Energy as a Descriptor of Catalytic Activity for Propene Oxidation over Mixed Metal Oxide Catalysts.* Journal of the American Chemical Society, 2014. **136**(39): p. 13684-13697.
18. Norskov, J.K., et al., *Density functional theory in surface chemistry and catalysis.* Proceedings of the National Academy of Sciences of the United States of America, 2011. **108**(3): p. 937-943.
19. Eichelbaum, M., et al., *Towards Physical Descriptors of Active and Selective Catalysts for the Oxidation of n-Butane to Maleic Anhydride.* ChemCatChem, 2013. **5**(8): p. 2318-2329.
20. Albonetti, S., F. Cavani, and F. TrifirÒ, *Key Aspects of Catalyst Design for the Selective Oxidation of Paraffins.* Catalysis Reviews, 1996. **38**(4): p. 413-438.
21. Medford, A.J., et al., *From the Sabatier principle to a predictive theory of transition-metal heterogeneous catalysis.* Journal of Catalysis, 2015. **328**: p. 36-42.

22. Abild-Pedersen, F., et al., *Scaling properties of adsorption energies for hydrogen-containing molecules on transition-metal surfaces.* Physical Review Letters, 2007. **99**(1): p. 4.
23. Grasselli, R.K. and J.D. Burrington, *Selective Oxidation and Ammoxidation of Propylene by Heterogeneous Catalysis*, in *Advances in Catalysis*, D.D. Eley, H. Pines, and P.B. Weisz, Editors. 1981, Academic Press. p. 133-163.
24. Oyama, S.T., *Adsorbate bonding and the selection of partial and total oxidation pathways.* Journal of Catalysis, 1991. **128**(1): p. 210-217.
25. Naumann d'Alnoncourt, R., et al., *The reaction network in propane oxidation over phase-pure MoVTeNb M1 oxide catalysts.* Journal of Catalysis, 2014. **311**: p. 369-385.
26. Sanfiz, A.C., et al., *Dynamics of the MoVTeNb Oxide M1 Phase in Propane Oxidation.* The Journal of Physical Chemistry C, 2010. **114**(4): p. 1912-1921.
27. Wagner, J.B., et al., *Surface texturing of Mo–V–Te–Nb–O x selective oxidation catalysts.* Topics in Catalysis, 2006. **38**(1): p. 51-58.
28. Hävecker, M., et al., *Surface chemistry of phase-pure M1 MoVTeNb oxide during operation in selective oxidation of propane to acrylic acid.* Journal of Catalysis, 2012. **285**(1): p. 48-60.
29. Kubas, A., et al., *A combined experimental and theoretical spectroscopic protocol for determination of the structure of heterogeneous catalysts: developing the information content of the resonance Raman spectra of M1 MoVOx.* Chemical Science, 2017. **8**(9): p. 6338-6353.
30. Trunschke, A., et al., *The Impact of the Bulk Structure on Surface Dynamics of Complex Mo–V-based Oxide Catalysts.* ACS Catalysis, 2017. **7**(4): p. 3061-3071.
31. Schlögl, R., *Selective Oxidation: From a Still Immature Technology to the Roots of Catalysis Science.* Topics in Catalysis, 2016. **59**(17): p. 1461-1476.
32. Barber, S., et al., *The influence of crystallographic shear planes on the behavior of molybdenum-tungsten oxide catalysts for the selective oxidation of propene.* Journal of Catalysis, 1982. **77**(1): p. 180-191.
33. Glaum, R., et al., *Resource-Efficient Alkane Selective Oxidation on New Crystalline Solids: Searching for Novel Catalyst Materials.* Chemie Ingenieur Technik, 2012. **84**(10): p. 1766-1779.
34. Batiot, C., et al., *Selectivity of active sites on oxide catalysts*, in *Studies in Surface Science and Catalysis*, R.K. Grasselli, et al., Editors. 1997, Elsevier. p. 1097-1106.
35. Grasselli, R.K., C.G. Lugmair, and A.F. Volpe, *Doping of MoVNbTeO (M1) and MoVTeO (M2) Phases for Selective Oxidation of Propane and Propylene to Acrylic Acid.* Topics in Catalysis, 2008. **50**(1): p. 66-73.
36. Häggblad, R., et al., *Substituted Mo–V(Ti)–Te(Ce)-oxide M2 Catalysts for Propene Ammoxidation.* Topics in Catalysis, 2008. **50**(1): p. 52-65.
37. McFarland, E.W. and H. Metiu, *Catalysis by Doped Oxides.* Chemical Reviews, 2013. **113**(6): p. 4391-4427.
38. Mestl, G., et al., *Combinatorial design and preparation of transition metal doped MoVTe catalysts for oxidation of propane to acrylic acid.* Applied Catalysis A: General, 2014. **474**: p. 3-9.
39. Hammer, B. and J.K. Norskov, *Why gold is the noblest of all the metals.* Nature, 1995. **376**: p. 238.
40. Hummelshoj, J.S., et al., *CatApp: A Web Application for Surface Chemistry and Heterogeneous Catalysis.* Angewandte Chemie-International Edition, 2012. **51**(1): p. 272-274.
41. Latimer, A.A., et al., *Understanding trends in C-H bond activation in heterogeneous catalysis.* Nature Materials, 2017. **16**(2): p. 225-229.

42. Medford, A.J., et al., *CatMAP: A Software Package for Descriptor-Based Microkinetic Mapping of Catalytic Trends.* Catalysis Letters, 2015. **145**(3): p. 794-807.
43. Nørskov, J.K., et al., *Towards the computational design of solid catalysts.* Nature Chemistry, 2009. **1**: p. 37.
44. Ulissi, Z.W., et al., *To address surface reaction network complexity using scaling relations machine learning and DFT calculations.* Nature Communications, 2017. **8**: p. 14621.
45. Yu, J., et al., *A combined HAADF STEM and density functional theory study of tantalum and niobium locations in the Mo–V–Te–Ta(Nb)–O M1 phases.* Catalysis Communications, 2012. **29**: p. 68-72.
46. Yu, J., Y. Xu, and V.V. Guliants, *Propane ammoxidation over Mo–V–Te–Nb–O M1 phase: Density functional theory study of propane oxidative dehydrogenation steps.* Catalysis Today, 2014. **238**: p. 28-34.
47. Tilley, R.J.D., *Perovskites: Structure-Property Relationships*. 2016, New York: John Wiley and Sons.
48. Hazen, R.M., Sci. Am., 1988. **6**: p. 52.
49. Royer, S., et al., *Perovskites as Substitutes of Noble Metals for Heterogeneous Catalysis: Dream or Reality.* Chemical Reviews, 2014. **114**(20): p. 10292-10368.
50. Goldschmidt, V.M., *The laws of crystal chemistry.* Naturwissenschaften, 1926. **14**: p. 477-485.
51. O. Muller, R.R., *The Major Ternary Structural Families.* Springer-Verlag, 1974: p. 175-196.
52. Glazer, M., *The classification of tilted octahedra in perovskites.* Acta Crystall. B, 1972. **28**: p. 3384-3392.
53. Goodenough, J.B., *Perspective on Engineering Transition-Metal Oxides.* Chemistry of Materials, 2014. **26**(1): p. 820-829.
54. Alonso, J.A., et al., *Enhanced magnetoresistance in the complex perovskite LaCu3Mn4O12.* Applied Physics Letters, 2003. **83**(13): p. 2623-2625.
55. Zhang, S., et al., *Site-Selective Doping Effect in AMn3V4O12 (A = Na+, Ca2+, and La3+).* Journal of the American Chemical Society, 2013. **135**(16): p. 6056-6060.
56. Voorhoeve, R.J.H., J.P. Remeika, and L.E. Trimble, *DEFECT CHEMISTRY AND CATALYSIS IN OXIDATION AND REDUCTION OVER PEROVSKITE-TYPE OXIDES.* Annals of the New York Academy of Sciences, 1976. **272**(1): p. 3-21.
57. Royer, S., F. Bérubé, and S. Kaliaguine, *Effect of the synthesis conditions on the redox and catalytic properties in oxidation reactions of LaCo1−xFexO3.* Applied Catalysis A: General, 2005. **282**(1): p. 273-284.
58. Li, F., et al., *Solid-State Synthesis of LaCoO3 Perovskite Nanocrystals.* Journal of the American Ceramic Society, 2002. **85**(9): p. 2177-2180.
59. Alonso, J.A., et al., *High Oxygen Pressure Preparation, Structural Refinement, and Thermal Behavior ofRMn2O5(R==La, Pr, Nd, Sm, Eu).* Journal of Solid State Chemistry, 1997. **129**(1): p. 105-112.
60. Ristić, M.M., S.D. Milošević, and P. Miljanić, *Mechanical activation of inorganic materials*. Vol. 639. 1998: Serbian Academy of Sciences and Arts.
61. Stojanovic, B.D., *Mechanochemical synthesis of ceramic powders with perovskite structure.* Journal of Materials Processing Technology, 2003. **143-144**: p. 78-81.
62. Manik, S.K. and S.K. Pradhan, *Microstructure characterization of ball milled prepared nanocrystalline perovskite CaTiO3 by Rietveld method.* Materials Chemistry and Physics, 2004. **86**(2): p. 284-292.
63. Ghasdi, M. and H. Alamdari, *CO sensitive nanocrystalline LaCoO3 perovskite sensor prepared by high energy ball milling.* Sensors and Actuators B: Chemical, 2010. **148**(2): p. 478-485.
64. Wang, H., et al., *Preparation and characterization of perovskite ceramic powders by gelcasting.* Journal of Materials Science, 1999. **34**(6): p. 1163-1167.

65. Nakayama, S., et al., *Carbon oxidation activity of complex oxides (Part 1)-RE2CuO4 (RE = La-Gd) and RE2Cu2O5 (RE = Dy-Yb, Y).* Journal of the Ceramic Society of Japan, 2011. **119**(1396): p. 961-964.
66. García-Espejo, G., et al., *Mechanochemical synthesis of three double perovskites: Cs2AgBiBr6, (CH3NH3)2TlBiBr6 and Cs2AgSbBr6.* Nanoscale, 2019. **11**(35): p. 16650-16657.
67. Mahesh, M.L.V., V.V. Bhanuprasad, and A.R. James, *Enhanced Piezoelectric Properties and Tunability of Lead-Free Ceramics Prepared by High-Energy Ball Milling.* Journal of Electronic Materials, 2013. **42**(12): p. 3547-3551.
68. Kadyrova, N.I., et al., *High-pressure defect phase NdxCu3V4O12.* Russian Journal of Inorganic Chemistry, 2009. **54**(12): p. 1872.
69. Kadyrova, N.I., et al., *High-pressure defect phase LaxCu3V4O12.* Russian Journal of Inorganic Chemistry, 2007. **52**(6): p. 825-828.
70. Sánchez-Benítez, J., et al., *Preparation under high pressures and neutron diffraction study of new ferromagnetic RCu3Mn4O12(R = Pr, Sm, Eu, Gd, Dy, Ho, Tm, Yb) perovskites.* Journal of Physics: Condensed Matter, 2005. **17**(40): p. S3063-S3068.
71. Au, C.-T. and W.-D. Zhang, *Oxidative dehydrogenation of propane over rare-earth orthovanadates.* Journal of the Chemical Society, Faraday Transactions, 1997. **93**(6): p. 1195-1204.
72. Ciambelli, P., et al., *AMnO3 (A=La, Nd, Sm) and Sm1−xSrxMnO3 perovskites as combustion catalysts: structural, redox and catalytic properties.* Applied Catalysis B: Environmental, 2000. **24**(3): p. 243-253.
73. Cortés-Gil, R., et al., *Magnetoresistance and Ferromagnetism in Disordered LaCu0.5Mn0.5O3 Perovskite.* Chemistry of Materials, 2013. **25**(10): p. 2100-2108.
74. Zhu, J., et al., *Recycle—new possible mechanism of NO decomposition over perovskite(-like) oxides.* Journal of Molecular Catalysis A: Chemical, 2005. **233**(1): p. 29-34.
75. Zhu, J., et al., *Active Site Structure of NO Decomposition on Perovskite(-like) Oxides: An Investigation from Experiment and Density Functional Theory.* The Journal of Physical Chemistry C, 2007. **111**(3): p. 1487-1490.
76. Zhu, J., et al., *Study of La2−xSrxCuO4 (x=0.0, 0.5, 1.0) catalysts for NO+CO reaction from the measurements of O2-TPD, H2-TPR and cyclic voltammetry.* Journal of Molecular Catalysis A: Chemical, 2005. **238**(1): p. 35-40.
77. Souza, A.M.G.P., et al., *Synthesis and characterization of LaNixCo1-xO3 perovskites via complex precursor methods.* 2010.
78. Gallagher, P.K., D.W. Johnson, and F. Schrey, *Studies of some supported perovskite oxidation catalysts.* Materials Research Bulletin, 1974. **9**(10): p. 1345-1352.
79. Wachowski, L., *Influence of the method of preparation on the porous structure of perovskite oxides.* Surface and Coatings Technology, 1986. **29**(4): p. 303-311.
80. Baythoun, M.S.G. and F.R. Sale, *Production of strontium-substituted lanthanum manganite perovskite powder by the amorphous citrate process.* Journal of Materials Science, 1982. **17**(9): p. 2757-2769.
81. Taguchi, H., et al., *Surface characterization of LaCoO3 synthesized using citric acid.* Materials Research Bulletin, 2002. **37**(1): p. 69-76.
82. Cousin, P. and R.A. Ross, *Preparation of mixed oxides: a review.* Materials Science and Engineering: A, 1990. **130**(1): p. 119-125.
83. Tejuca, L.G., J.L.G. Fierro, and J.M.D. Tascón, *Structure and Reactivity of Perovskite-Type Oxides*, in *Advances in Catalysis*, D.D. Eley, H. Pines, and P.B. Weisz, Editors. 1989, Academic Press. p. 237-328.
84. Arai, H., et al., *Catalytic combustion of methane over various perovskite-type oxides.* Applied Catalysis, 1986. **26**: p. 265-276.

85. Zhang, H.M., et al., *Oxygen sorption and catalytic properties of La1−xSrxCo1−yFeyO3 Perovskite-type oxides.* Journal of Catalysis, 1990. **121**(2): p. 432-440.
86. Galkin, A.A. and V.V. Lunin, *Subcritical and supercritical water: a universal medium for chemical reactions.* Russian Chemical Reviews, 2005. **74**(1): p. 21.
87. Dawson, W.J., *Hydrothermal synthesis of advanced ceramic powders.* American Ceramic Society Bulletin, 1988. **67**(10): p. 1673-1678.
88. Barrer, R.M., *Hydrothermal chemistry of zeolites*. 1982: Academic press.
89. Demazeau, G., *Solvothermal processes: a route to the stabilization of new materials.* Journal of Materials Chemistry, 1999. **9**(1): p. 15-18.
90. Cabanas, A., et al., *A continuous and clean one-step synthesis of nano-particulate CeZrO solid solutions in near-critical water.* Chemical Communications, 2000(11): p. 901-902.
91. Ma, Y.J., et al., *Hydrothermal synthesis of (Bi1/2Na1/2)TiO3 piezoelectric ceramics.* Materials Chemistry and Physics, 2006. **98**(1): p. 5-8.
92. Wendelbo, R., et al., *Combinatorial hydrothermal synthesis and characterisation of perovskites.* Journal of the European Ceramic Society, 2006. **26**(6): p. 849-859.
93. Mao, Y., S. Banerjee, and S.S. Wong, *Hydrothermal synthesis of perovskite nanotubes.* Chemical Communications, 2003(3): p. 408-409.
94. Zhang, L., et al., *Hydrothermal synthesis and catalytic performance of single-crystalline La2−xSrxCuO4 for methane oxidation.* Catalysis Today, 2010. **153**(3): p. 143-149.
95. Ifrah, S., et al., *Conventional hydrothermal process versus microwave-assisted hydrothermal synthesis of La1−xAgxMnO3+δ (x=0, 0.2) perovskites used in methane combustion.* Comptes Rendus Chimie, 2007. **10**(12): p. 1216-1226.
96. Rubel, M.H.K., et al., *Hydrothermal Synthesis, Crystal Structure, and Superconductivity of a Double-Perovskite Bi Oxide.* Chemistry of Materials, 2016. **28**(2): p. 459-465.
97. Zhang, Y., et al., *Hydrothermal Fabrication and Catalytic Properties of YBa2Cu3O7 Single Crystallites for Methane Combustion.* Catalysis Letters, 2010. **135**(1): p. 126-134.
98. Dumas, A., et al., *Fast-Geomimicking using Chemistry in Supercritical Water.* Angewandte Chemie, 2016. **128**(34): p. 10022-10025.
99. Darr, J.A., et al., *Continuous Hydrothermal Synthesis of Inorganic Nanoparticles: Applications and Future Directions.* Chemical Reviews, 2017. **117**(17): p. 11125-11238.
100. Aymonier, C., et al., *Review of supercritical fluids in inorganic materials science.* The Journal of Supercritical Fluids, 2006. **38**(2): p. 242-251.
101. Darr, J.A. and M. Poliakoff, *New Directions in Inorganic and Metal-Organic Coordination Chemistry in Supercritical Fluids.* Chemical Reviews, 1999. **99**(2): p. 495-542.
102. Kalinichev, A.G. and S.V. Churakov, *Size and topology of molecular clusters in supercritical water: a molecular dynamics simulation.* Chemical Physics Letters, 1999. **302**(5): p. 411-417.
103. Biswas, R. and B. Bagchi, *Ion solvation dynamics in supercritical water.* Chemical Physics Letters, 1998. **290**(1): p. 223-228.
104. Adschiri, T., K. Kanazawa, and K. Arai, *Rapid and continuous hydrothermal crystallization of metal oxide particles in supercritical water.* Journal of the American Ceramic Society, 1992. **75**(4): p. 1019-1022.
105. Tighe, C.J., et al., *Investigation of counter-current mixing in a continuous hydrothermal flow reactor.* The Journal of Supercritical Fluids, 2012. **62**: p. 165-172.
106. Lester, E., et al., *Reaction engineering: The supercritical water hydrothermal synthesis of nano-particles.* The Journal of Supercritical Fluids, 2006. **37**(2): p. 209-214.
107. Zielke, P., et al., *Simulation, design and proof-of-concept of a two-stage continuous hydrothermal flow synthesis reactor for synthesis of functionalized nano-sized inorganic composite materials.* The Journal of Supercritical Fluids, 2016. **117**: p. 1-12.

108. Gruar, R.I., C.J. Tighe, and J.A. Darr, *Scaling-up a confined jet reactor for the continuous hydrothermal manufacture of nanomaterials.* Industrial & Engineering Chemistry Research, 2013. **52**(15): p. 5270-5281.
109. Abe, Y., et al., *Formation of La-based perovskite compounds in supercritical water.* Ceramics International, 2018. **44**(11): p. 12996-13003.
110. Lu, J., et al., *Preparation of Ca0. 8Sr0. 2Ti1− xFexO3− δ (x= 0.1–0.3) nanoparticles using a flow supercritical reaction system.* The Journal of Supercritical Fluids, 2008. **46**(1): p. 77-82.
111. Weng, X., et al., *Continuous hydrothermal flow syntheses of nanosized energy materials used in solid oxide fuel cells.* Clean Technol. 2008: Bio Energy, Renew., Green Build., Smart Grid, Stor Water, 2008: p. 261-264.
112. Dunne, P.W., et al., *The rapid size-and shape-controlled continuous hydrothermal synthesis of metal sulphide nanomaterials.* Nanoscale, 2014. **6**(4): p. 2406-2418.
113. Galkin, A.A., et al., *Continuous reactions in supercritical water: A new route to La2CuO4 with a high surface area and enhanced oxygen mobility.* Angewandte Chemie International Edition, 2000. **39**(15): p. 2738-2740.
114. Wang, W., et al., *Rapid syntheses of ultrafine LaMnO3 nano-crystallites with superior activity for catalytic oxidation of toluene.* Catalysis Communications, 2016. **84**: p. 167-170.
115. Sue, K., et al., *Continuous hydrothermal synthesis of Pr-doped CaTiO3 nanoparticles from a TiO2 Sol.* Industrial & Engineering Chemistry Research, 2016. **55**(28): p. 7628-7634.
116. Xu, Y., et al., *Continuous Hydrothermal Flow Synthesis of LaCrO3 in Supercritical Water and Its Application in Dual-Phase Oxygen Transport Membranes.* Industrial & Engineering Chemistry Research, 2018. **57**(6): p. 2123-2130.
117. Clark, I., et al., *Continuous hydrothermal synthesis of Ca2Al-NO3 layered double hydroxides: The impact of reactor temperature, pressure and NaOH concentration on crystal characteristics.* Journal of colloid and interface science, 2017. **504**: p. 492-499.
118. Teoh, W.Y., R. Amal, and L. Mädler, *Flame spray pyrolysis: An enabling technology for nanoparticles design and fabrication.* Nanoscale, 2010. **2**(8): p. 1324-1347.
119. Angel, S., et al., *Spray-flame synthesis of La (Fe, Co) O3 nano-perovskites from metal nitrates.* AIChE Journal, 2020. **66**(1): p. e16748.
120. Campagnoli, E., et al., *Effect of preparation method on activity and stability of LaMnO3 and LaCoO3 catalysts for the flameless combustion of methane.* Applied Catalysis B: Environmental, 2005. **55**(2): p. 133-139.
121. Chiarello, G.L., et al., *Solvent nature effect in preparation of perovskites by flame-pyrolysis: 1. Carboxylic acids.* Applied Catalysis B: Environmental, 2007. **72**(3-4): p. 218-226.
122. Chiarello, G.L., et al., *Solvent nature effect in preparation of perovskites by flame pyrolysis: 2. Alcohols and alcohols+ propionic acid mixtures.* Applied Catalysis B: Environmental, 2007. **72**(3-4): p. 227-232.
123. Giacomuzzi, R.A.M., et al., *A new method for preparing nanometer-size perovskitic catalysts for CH4 flameless combustion*, in *Studies in Surface Science and Catalysis*. 2000, Elsevier. p. 197-202.
124. Heine, C., et al., *Ambient-Pressure Soft X-ray Absorption Spectroscopy of a Catalyst Surface in Action: Closing the Pressure Gap in the Selective n-Butane Oxidation over Vanadyl Pyrophosphate.* The Journal of Physical Chemistry C, 2014. **118**(35): p. 20405-20412.
125. Jung, D.S., S.K. Hong, and Y.C. Kang, *Nano-sized LaMnO3 powders prepared by spray pyrolysis from spray solution containing citric acid.* Journal of the Ceramic Society of Japan, 2008. **116**(1349): p. 141-145.
126. Liu, G., et al., *Effects of cerium incorporation on the catalytic oxidation of benzene over flame-made perovskite La1− xCexMnO3 catalysts.* Particuology, 2015. **19**: p. 60-68.

127. Maik, E., et al., *The Intimate Relationship between Bulk Electronic Conductivity and Selectivity in the Catalytic Oxidation of n-Butane.* Angewandte Chemie International Edition, 2012. **51**(25): p. 6246-6250.
128. Maik, E., et al., *Towards Physical Descriptors of Active and Selective Catalysts for the Oxidation of n-Butane to Maleic Anhydride.* ChemCatChem, 2013. **5**(8): p. 2318-2329.
129. Nguyen, P.T., R.D. Hoffman, and A.W. Sleight, *Structure of (VO)2P2O7.* Materials Research Bulletin, 1995. **30**(9): p. 1055-1063.
130. Rossetti, I. and L. Forni, *Catalytic flameless combustion of methane over perovskites prepared by flame–hydrolysis.* Applied Catalysis B: Environmental, 2001. **33**(4): p. 345-352.
131. Shimada, H., et al., *Extremely fine structured cathode for solid oxide fuel cells using Sr-doped LaMnO3 and Y2O3-stabilized ZrO2 nano-composite powder synthesized by spray pyrolysis.* Journal of Power Sources, 2017. **341**: p. 280-284.
132. Bhalla, A.S., R. Guo, and R. Roy, *The perovskite structure—a review of its role in ceramic science and technology.* Materials Research Innovations, 2000. **4**(1): p. 3-26.
133. Iwahara, H., *Proton Conduction in Sintered Oxides Based on BaCeO[sub 3].* Journal of The Electrochemical Society, 1988. **135**(2): p. 529.
134. Misono, M., *Chapter 3 - Catalysis of Perovskite and Related Mixed Oxides*, in *Studies in Surface Science and Catalysis*, M. Misono, Editor. 2013, Elsevier. p. 67-95.
135. Cross, L.E., *Relaxor ferroelectrics.* Ferroelectrics, 1987. **76**(1): p. 241-267.
136. Ka, M., *iller, H. Burkard.* Phys. Rev. B, 1979. **19**: p. 3593.
137. Luiz, A.M., *Room Temperature Superconductivity.* Superconductivity: Theory and Applications, 2011. **3**: p. 1.
138. Wu, M.-K., et al., *Superconductivity at 93 K in a new mixed-phase Y-Ba-Cu-O compound system at ambient pressure.* Physical review letters, 1987. **58**(9): p. 908.
139. Klissurski, D. and V. Rives, *High-temperature superconductors in catalysis.* Applied Catalysis A: General, 1994. **109**(1): p. 1-44.
140. von Helmolt, R., et al., *Giant negative magnetoresistance in perovskitelike La 2/3 Ba 1/3 MnO x ferromagnetic films.* Physical Review Letters, 1993. **71**(14): p. 2331.
141. Ohtomo, A. and H.Y. Hwang, *A high-mobility electron gas at the LaAlO3/SrTiO3 heterointerface.* Nature, 2004. **427**(6973): p. 423-426.
142. Reyren, N., et al., *Superconducting Interfaces Between Insulating Oxides.* Science, 2007. **317**(5842): p. 1196.
143. Suntivich, J., et al., *Design principles for oxygen-reduction activity on perovskite oxide catalysts for fuel cells and metal–air batteries.* Nature Chemistry, 2011. **3**(7): p. 546-550.
144. Hwang, J., et al., *Perovskites in catalysis and electrocatalysis.* Science, 2017. **358**(6364): p. 751.
145. Fei, D.Q., T. Hudaya, and A.A. Adesina, *Visible-light activated titania perovskite photocatalysts: Characterisation and initial activity studies.* Catalysis Communications, 2005. **6**(4): p. 253-258.
146. Suntivich, J., et al., *A Perovskite Oxide Optimized for Oxygen Evolution Catalysis from Molecular Orbital Principles.* Science, 2011. **334**(6061): p. 1383.
147. Li, J., et al., *Direct Evidence of Ion Diffusion for the Silver-Electrode-Induced Thermal Degradation of Inverted Perovskite Solar Cells.* Advanced Energy Materials, 2017. **7**(14): p. 1602922.
148. Shi, Z. and A.H. Jayatissa, *Perovskites-based solar cells: A review of recent progress, materials and processing methods.* Materials, 2018. **11**(5): p. 729.
149. Ansari, M.I.H., A. Qurashi, and M.K. Nazeeruddin, *Frontiers, opportunities, and challenges in perovskite solar cells: A critical review.* Journal of Photochemistry and Photobiology C: Photochemistry Reviews, 2018. **35**: p. 1-24.

150. Asghar, M.I., et al., *Device stability of perovskite solar cells–A review.* Renewable and Sustainable Energy Reviews, 2017. **77**: p. 131-146.
151. Song, Z., et al., *Pathways toward high-performance perovskite solar cells: review of recent advances in organo-metal halide perovskites for photovoltaic applications.* Journal of Photonics for Energy, 2016. **6**(2): p. 022001.
152. Chen, J., et al., *Recent progress in stabilizing hybrid perovskites for solar cell applications.* Journal of Power Sources, 2017. **355**: p. 98-133.
153. Huang, Y.-H., et al., *Double Perovskites as Anode Materials for Solid-Oxide Fuel Cells.* Science, 2006. **312**(5771): p. 254.
154. Ishihara, T., *Perovskite oxide for solid oxide fuel cells*. 2009: Springer Science & Business Media.
155. Bonanos, N., K.S. Knight, and B. Ellis, *Perovskite solid electrolytes: Structure, transport properties and fuel cell applications.* Solid State Ionics, 1995. **79**: p. 161-170.
156. Tarancón, A., et al., *Layered perovskites as promising cathodes for intermediate temperature solid oxide fuel cells.* Journal of Materials Chemistry, 2007. **17**(30): p. 3175-3181.
157. Huang, K., R.S. Tichy, and J.B. Goodenough, *Superior Perovskite Oxide-Ion Conductor; Strontium- and Magnesium-Doped LaGaO3: I, Phase Relationships and Electrical Properties.* Journal of the American Ceramic Society, 1998. **81**(10): p. 2565-2575.
158. Takeguchi, T., et al., *Layered Perovskite Oxide: A Reversible Air Electrode for Oxygen Evolution/Reduction in Rechargeable Metal-Air Batteries.* Journal of the American Chemical Society, 2013. **135**(30): p. 11125-11130.
159. Jung, K.-N., et al., *Doped Lanthanum Nickelates with a Layered Perovskite Structure as Bifunctional Cathode Catalysts for Rechargeable Metal–Air Batteries.* ACS Applied Materials & Interfaces, 2013. **5**(20): p. 9902-9907.
160. Hardin, W.G., et al., *Highly Active, Nonprecious Metal Perovskite Electrocatalysts for Bifunctional Metal–Air Battery Electrodes.* The Journal of Physical Chemistry Letters, 2013. **4**(8): p. 1254-1259.
161. G. Kim, H., et al., *Highly donor-doped (110) layered perovskite materials as novel photocatalysts for overall water splitting.* Chemical Communications, 1999(12): p. 1077-1078.
162. Kudo, A., H. Kato, and S. Nakagawa, *Water Splitting into H2 and O2 on New Sr2M2O7 (M = Nb and Ta) Photocatalysts with Layered Perovskite Structures: Factors Affecting the Photocatalytic Activity.* The Journal of Physical Chemistry B, 2000. **104**(3): p. 571-575.
163. Carrillo, R.J., et al., *Oxygen Nonstoichiometry and Defect Equilibria of Yttrium Manganite Perovskites with Strontium A-Site and Aluminum B-Site Doping.* The Journal of Physical Chemistry C, 2020. **124**(8): p. 4448-4458.
164. Tascón, J.M.D., J.L.G. Fierro, and L.G. Tejuca, *Kinetics and Mechanism of CO Oxidation on LaCoO3*, in *Zeitschrift für Physikalische Chemie*. 1981. p. 249.
165. Chan, K.S., et al., *Catalytic carbon monoxide oxidation over strontium, cerium and copper-substituted lanthanum manganates and cobaltates.* Applied Catalysis A: General, 1994. **107**(2): p. 201-227.
166. Yasuda, H., et al., *Oxidation of carbon monoxide on LaMn1 -CuO3 perovskite-type mixed oxides.* Journal of the Chemical Society, Faraday Transactions, 1994. **90**(8): p. 1183-1189.
167. Zhao, P., et al., *A mullite oxide catalyst of SmMn2O5 for three-way catalysis: synthesis, characterization, and catalytic activity evaluation.* RSC Advances, 2016. **6**(70): p. 65950-65959.
168. Kim, C.H., et al., *Strontium-Doped Perovskites Rival Platinum Catalysts for Treating NO_x in Simulated Diesel Exhaust.* Science, 2010. **327**(5973): p. 1624.

169. Amar, I.A., et al., *Solid-state electrochemical synthesis of ammonia: a review.* Journal of Solid State Electrochemistry, 2011. **15**(9): p. 1845.
170. Mignard, D., et al., *Revisiting strontium-doped lanthanum cuprate perovskite for the electrochemical reduction of CO2.* Journal of CO2 Utilization, 2014. **5**: p. 53-59.
171. Trikalitis, P.N., et al., *A Rietveld analysis of the transformation of (La–Sr–V–O)reduced to (La–Sr–V–O)oxidized solids and the effect on their surface catalytic properties.* Applied Catalysis A: General, 1998. **167**(2): p. 295-308.
172. Doroftei, C. and L. Leontie, *Synthesis and characterization of some nanostructured composite oxides for low temperature catalytic combustion of dilute propane.* Rsc Advances, 2017. **7**(45): p. 27863-27871.
173. Miniajluk, N., J. Trawczyński, and M. Zawadzki, *Properties and catalytic performance for propane combustion of LaMnO3 prepared under microwave-assisted glycothermal conditions: Effect of solvent diols.* Applied Catalysis A: General, 2017. **531**: p. 119-128.
174. AS. Subramanian, C.S.S., *Studies on catalytic decomposition of nitrous oxide (N2O) on Bi-Sr-(Ca)-Cu-O oxide superconductors.* Journal of Materials Svience Letters, 1996. **15**: p. 107-111.
175. Wentao, X., et al., *Highly Effective Direct Decomposition of Nitric Oxide by Microwave Catalysis over BaMeO3 (Me=Mn, Co, Fe) Mixed Oxides at Low Temperature under Excess Oxygen.* ChemCatChem, 2016. **8**(2): p. 417-425.
176. Gao, L.Z. and C.T. Au, *Studies on the decomposition of N2O over Nd2CuO4, Nd1.6Ba0.4CuO4 and Nd1.8Ce0.2CuO4.* Journal of Molecular Catalysis A: Chemical, 2001. **168**(1): p. 173-186.
177. Xu, Y., et al., *Carbon-Coated Perovskite BaMnO3 Porous Nanorods with Enhanced Electrocatalytic Perporites for Oxygen Reduction and Oxygen Evolution.* Electrochimica Acta, 2015. **174**: p. 551-556.
178. Gao, L.Z. and C.T. Au, *CO2 Hydrogenation to Methanol on a YBa2Cu3O7 Catalyst.* Journal of Catalysis, 2000. **189**(1): p. 1-15.
179. Kersen, Ü. and R.L. Keiski, *Preliminary study on the selective oxidation of H2S over LaVO4 and Fe2(MoO4)3 oxides, produced by a solvothermal method.* Catalysis Communications, 2009. **10**(7): p. 1039-1042.
180. Chen, J., et al., *Visible-light-enhanced photothermocatalytic activity of ABO3-type perovskites for the decontamination of gaseous styrene.* Applied Catalysis B: Environmental, 2017. **209**: p. 146-154.
181. Xue, L., et al., *Investigation of the hydrothermal aging of an Mn-based mullite SmMn2O5 catalyst of NO oxidation.* RSC Advances, 2017. **7**(77): p. 49091-49096.
182. Zhaorigetu, B., R. Kieffer, and W. Li, *Investigations on the promoting effect of metal oxides on La–V–O catalyst in propane oxidative dehydrogenation.* Catalysis Letters, 2001. **73**(2): p. 133-136.
183. Zhang, W., C. Au, and H. Wan, *Active site of praseodymium orthovanadate catalyst in oxidative dehydrogenation of propane.* Chinese Science Bulletin, 1998. **43**(3): p. 217-220.
184. Barbero, B.P. and L.E. Cadus, *Vanadium species: Sm-V-O catalytic system for oxidative dehydrogenation of propane.* Applied Catalysis A: General, 2003. **244**(2): p. 235-249.
185. Sun, Y.K. and W.Y. Lee, *Catalytic behavior of YBa2Cu3O7-x in the partial oxidation of ethanol to acetaldehyde.* Catalysis Letters, 1993. **17**(3): p. 263-272.
186. Palas, B., G. Ersöz, and S. Atalay, *Photo Fenton-like oxidation of Tartrazine under visible and UV light irradiation in the presence of LaCuO3 perovskite catalyst.* Process Safety and Environmental Protection, 2017. **111**: p. 270-282.
187. Rahmani, A. and J. Saffari, *Preparation, Structure and Selected Catalytic Properties of La2CuO4 Nano Mixed Metal Oxides.* Journal of Nanostructures, 2016. **6**(4): p. 301-306.

188. Megarajan, S.K., et al., *Effects of Surface and Bulk Silver on PrMnO3+δ Perovskite for CO and Soot Oxidation: Experimental Evidence for the Chemical State of Silver.* ACS Catalysis, 2015. **5**(1): p. 301-309.
189. Nakayama, S., et al., *Carbon oxidation activity of complex oxides (Part 1)-RECuO4 (RE = La-Gd) and RECu2O5 (RE = Dy-Yb, Y).* Journal of the Ceramic Society of Japan, 2011. **119**(1396): p. 961-964.
190. Dhachapally, N., et al., *Metal vanadate catalysts for the ammoxidation of 2-methylpyrazine to 2-cyanopyrazine.* Applied Catalysis A: General, 2012. **443-444**: p. 111-118.
191. Yu Yao, Y.-F., *The oxidation of hydrocarbons and CO over metal oxides: IV. Perovskite-type oxides.* Journal of Catalysis, 1975. **36**(3): p. 266-275.
192. Zhaorigetu, B., R. Kieffer, and W.Z. Li, *Investigations on the promoting effect of metal oxides on La-V-O catalyst in propane oxidative dehydrogenation.* Catalysis Letters, 2001. **73**(2-4): p. 133-136.
193. Zhang, W.D., C.T. Au, and H.L. Wan, *Active site of praseodymium orthovanadate catalyst in oxidative dehydrogenation of propane.* Chinese Science Bulletin, 1998. **43**(3): p. 217-220.
194. Fang, Z.M., et al., *Oxidative dehydrogenation of propane over a series of low-temperature rare earth orthovanadate catalysts prepared by the nitrate method.* Catalysis Letters, 1999. **61**(1-2): p. 39-44.
195. Wang, J., F. Chen, and X.P. Zhou, *Photocatalytic degradation of acetone over a V2O5/LaF3 catalyst under visible light.* Journal of Physical Chemistry C, 2008. **112**(26): p. 9723-9729.
196. Fang, Z.M., et al., *Propane oxidative dehydrogenation over low temperature rare earth orthovanadate catalysts prepared by peroxyl method*, in *Natural Gas Conversion V*, A. Parmaliana, et al., Editors. 1998. p. 629-634.
197. Au, C.T., W.D. Zhang, and H.L. Wan, *Preparation and characterization of rare earth orthovanadates for propane oxidative dehydrogenation.* Catalysis Letters, 1996. **37**(3): p. 241-246.
198. Zhu, J., et al., *Perovskite Oxides: Preparation, Characterizations, and Applications in Heterogeneous Catalysis.* ACS Catalysis, 2014. **4**(9): p. 2917-2940.
199. Tanaka, H. and M. Misono, *Advances in designing perovskite catalysts.* Current Opinion in Solid State and Materials Science, 2001. **5**(5): p. 381-387.
200. Taihei, N., I. Tatsumi, and M. Makoto, *Catalytic Properties of Perovskite-Type Mixed Oxides (ABO3) Consisting of Rare Earth and 3d Transition Metals. The Roles of the A- and B-Site Ions.* Bulletin of the Chemical Society of Japan, 1988. **61**(3): p. 621-626.
201. Tarjomannejad, A., et al., *Catalytic Oxidation of CO Over LaMn1−xBxO3 (B = Cu, Fe) Perovskite-type Oxides.* Catalysis Letters, 2016. **146**(8): p. 1544-1551.
202. Oskoui, S.A., et al., *Modeling Preparation Condition and Composition–Activity Relationship of Perovskite-Type LaxSr1–xFeyCo1–yO3 Nano Catalyst.* ACS Combinatorial Science, 2013. **15**(12): p. 609-621.
203. Sup Song, K., D. Klvana, and J. Kirchnerova, *Kinetics of propane combustion over La0.66Sr0.34Ni0.3Co0.7O3 perovskite.* Applied Catalysis A: General, 2001. **213**(1): p. 113-121.
204. Petrolekas, P.D. and I.S. Metcalfe, *Redox Kinetics of Co Oxidation over a Perovskite Oxide Catalyst.* Chemical Engineering Research & Design, 1995. **73**(2): p. 122-129.
205. Yang, W., et al., *Activity of perovskite-type mixed oxides for the low-temperature CO oxidation: Evidence of oxygen species participation from the solid.* Journal of Catalysis, 2012. **295**: p. 45-58.
206. Alifanti, M., et al., *Oxidation of ethane on high specific surface SmCoO3 and PrCoO3 perovskites.* Catalysis Today, 2009. **143**(3): p. 309-314.

207. Alifanti, M., et al., *Methane and propane combustion over lanthanum transition-metal perovskites: role of oxygen mobility.* Applied Catalysis A: General, 2004. **262**(2): p. 167-176.
208. Klvana, D., K.S. Song, and J. Kirchnerova, *Catalytic performance of La0.66Sr0.34Co0.2Fe0.8O3 perovskite in propane combustion: Effect of preparation and specific surface area.* Korean Journal of Chemical Engineering, 2002. **19**(6): p. 932-939.
209. Czuprat, O., et al., *Oxidative dehydrogenation of propane in a perovskite membrane reactor with multi-step oxygen insertion.* AIChE Journal, 2010. **56**(9): p. 2390-2396.
210. Carlotto, S., et al., *Energetics of CO oxidation on lanthanide-free perovskite systems: the case of Co-doped SrTiO3.* Physical Chemistry Chemical Physics, 2016. **18**(48): p. 33282-33286.
211. Tascon, J.M.D., J.L.G. Fierro, and L.G. Tejuca, *Kinetics and mechanism of CO oxidation on LaCoO3.* Zeitschrift für physikalische Chemie, 1981. **124**(2): p. 249-257.
212. Markova-Velichkova, M., et al., *Complete oxidation of hydrocarbons on YFeO3 and LaFeO3 catalysts.* Chemical Engineering Journal, 2013. **231**: p. 236-244.
213. Yang, J., et al., *Oxygen Vacancy Promoted O2 Activation over Perovskite Oxide for Low-Temperature CO Oxidation.* ACS Catalysis, 2019. **9**(11): p. 9751-9763.
214. Ai, M., *Vapor-Phase Oxidation of Alpha-Methylstyrene to Phenylacrolein*, in *Studies in Surface Science and Catalysis*, G. Centi and F. Trifiro, Editors. 1990, Elsevier. p. 257-266.
215. Andrushkevich, T.V., et al., *Thermolysis of Heteropolyacid H3PMO12O40 and Catalytic Properties of the Thermal Decomposition Products in Oxidation of Acrolein to Acrylic Acid*, in *Studies in Surface Science and Catalysis*, V.C. Corberán and S.V. Bellón, Editors. 1994, Elsevier. p. 837-844.
216. Kim, Y.-C., W. Ueda, and Y. Moro-Oka, *Selective Oxidation of Propane To Acrolein and Ammoxidation To Acrylonitrile Over Ag-Doped Bismuth Vanadomolybdate Catalysts*, in *Studies in Surface Science and Catalysis*, G. Centi and F. Trifiro, Editors. 1990, Elsevier. p. 491-504.
217. Barrault, J., et al., *Selective oxidation of propane in the presence of bismuth-based catalysts*, in *Studies in Surface Science and Catalysis*, V.C. Corberán and S.V. Bellón, Editors. 1994, Elsevier. p. 305-314.
218. Ai, M., *Selective oxidation of acrolein to acrylic acid by V2O5-P2O5 catalysts.* Applied Catalysis, 1986. **27**(1): p. 167-179.
219. Quaranta, N.E., et al., *Selective Dehydrogenation of Ethanol Over Vanadium Oxide Catalyst*, in *Studies in Surface Science and Catalysis*, V.C. Corberán and S.V. Bellón, Editors. 1994, Elsevier. p. 811-818.
220. Hargreaves, J.S.J., et al., *Relationship between morphology and catalytic performance of lithium and gold doped magnesium oxide catalysts for the oxidative coupling of methane.* Catalysis Today, 1992. **13**(2): p. 401-407.
221. Mendelovici, L. and J.H. Lunsford, *Partial oxidation of ethane to ethylene and acetaldehyde over a supported molybdenum catalyst.* Journal of Catalysis, 1985. **94**(1): p. 37-50.
222. Burch*, R. and R. Swarnakar, *Oxidative dehydrogenation of ethane on vanadium-molybdenum oxide and vanadium-niobium-molybdenum oxide catalysts.* Applied Catalysis, 1991. **70**(1): p. 129-148.
223. Vitry, D., et al., *Mo-V-Te-(Nb)-O mixed metal oxides prepared by hydrothermal synthesis for catalytic selective oxidations of propane and propene to acrylic acid.* Applied Catalysis A: General, 2003. **251**(2): p. 411-424.
224. Burch, R. and E.M. Crabb, *Homogeneous and heterogeneous contributions to the oxidative dehydrogenation of propane on oxide catalysts.* Applied Catalysis A: General, 1993. **100**(1): p. 111-130.

225. Colorio, G.C., et al., *Characteristics of alumina boria catalysts used in ethane partial oxidation*, in *Studies in Surface Science and Catalysis*, V.C. Corberán and S.V. Bellón, Editors. 1994, Elsevier. p. 143-149.
226. Stern, D.L. and R.K. Grasselli, *Propane Oxydehydrogenation over Molybdate-Based Catalysts.* Journal of Catalysis, 1997. **167**(2): p. 550-559.
227. Ushikubo, T., et al., *Ammoxidation of propane over Mo-V-Nb-Te mixed oxide catalysts*, in *Studies in Surface Science and Catalysis*, C. Li and Q. Xin, Editors. 1997, Elsevier. p. 473-480.
228. Solsona, B., et al., *Selective oxidation of n-butane over MoV-containing oxidic bronze catalysts.* Journal of Catalysis, 2007. **250**(1): p. 128-138.
229. Botella, P., et al., *Selective oxidative dehydrogenation of ethane on MoVTeNbO mixed metal oxide catalysts.* Journal of Catalysis, 2004. **225**(2): p. 428-438.
230. Chu, B., et al., *Performance of phase-pure M1 MoVNbTeOx catalysts by hydrothermal synthesis with different post-treatments for the oxidative dehydrogenation of ethane.* Applied Catalysis A: General, 2015. **498**: p. 99-106.
231. Trunschke, A., *Propane-selective oxidation in Nanostructured Catalysts: Selective Oxidation* ed. R.S.E. In C. Hess. 2011, Cambridge: Royal Society of Chemistry.
232. Thorsteinson, E.M., et al., *The oxidative dehydrogenation of ethane over catalysts containing mixed oxides of molybdenum and vanadium.* Journal of Catalysis, 1978. **52**(1): p. 116-132.
233. R. K. Grasselli, G.C.a.F.T. *Selenium and Tellurium development*. in *4th International Symposium on Uses of Selenium and Tellurium*. 1989.
234. Cheng, M.-J. and W.A. Goddard, *In Silico Design of Highly Selective Mo-V-Te-Nb-O Mixed Metal Oxide Catalysts for Ammoxidation and Oxidative Dehydrogenation of Propane and Ethane.* Journal of the American Chemical Society, 2015. **137**(41): p. 13224-13227.
235. Ueda, W., D. Vitry, and T. Katou, *Structural organization of catalytic functions in Mo-based oxides for propane selective oxidation.* Catalysis Today, 2004. **96**(4): p. 235-240.
236. Mizuno, N., et al., *Catalytic performance of Cs2.5Fe0.08H1.26PVMo11O40 for direct oxidation of lower alkanes.* Journal of Molecular Catalysis A: Chemical, 1996. **114**(1): p. 309-317.
237. Min, J.-S. and N. Mizuno, *Iron as an effective additive for enhancement of catalytic performance of cesium hydrogen salt of molybdophosphoric acid for selective oxidation of isobutane, propane, and ethane under oxygen-rich and -poor conditions and the catalyst design.* Catalysis Today, 2001. **66**(1): p. 47-52.
238. Min, J.-S. and N. Mizuno, *Effects of additives on catalytic performance of heteropoly compounds for selective oxidation of light alkanes.* Catalysis Today, 2001. **71**(1): p. 89-96.
239. Dimitratos, N. and J.C. Védrine, *Study of Ga modified Cs2.5H1.5PV1Mo11O40 heteropolyoxometallates for propane selective oxidation.* Journal of Molecular Catalysis A: Chemical, 2006. **255**(1): p. 184-192.
240. Bordes, E., *Crystallochemistry of V・P・O phases and application to catalysis.* Catalysis Today, 1987. **1**(5): p. 499-526.
241. Bordes, E., *Nature of the active and selective sites in vanadyl pyrophosphate, catalyst of oxidation of n-butane, butene and pentane to maleic anhydride.* Catalysis Today, 1993. **16**(1): p. 27-38.
242. Cavani, F. and F. Trifirò, *Vanadium/phosphorus mixed oxide from the precursor to the active phase:Catalyst for the oxidation of n-butane to maleic anhydride*, in *Studies in Surface Science and Catalysis*, G. Poncelet, et al., Editors. 1995, Elsevier. p. 1-25.
243. Védrine, J.C., G.J. Hutchings, and C.J. Kiely, *Molybdenum oxide model catalysts and vanadium phosphates as actual catalysts for understanding heterogeneous catalytic partial oxidation reactions: A contribution by Jean-Claude Volta.* Catalysis Today, 2013. **217**: p. 57-64.

244. Ueda, W. and Y. Suzuki, *Partial Oxidation of Propane to Acrylic Acid over Reduced Heteropolymolybdate Catalysts.* Chemistry Letters, 1995. **24**(7): p. 541-542.
245. Pope, M.T. and A. Müller, *Polyoxometalate Chemistry: An Old Field with New Dimensions in Several Disciplines.* Angewandte Chemie International Edition in English, 1991. **30**(1): p. 34-48.
246. Long, D.L., E. Burkholder, and L. Cronin, *Polyoxometalate clusters, nanostructures and materials: From self assembly to designer materials and devices.* Chemical Society Reviews, 2007. **36**(1): p. 105-121.
247. Long, D.-L., R. Tsunashima, and L. Cronin, *Polyoxometalates: Building Blocks for Functional Nanoscale Systems.* Angewandte Chemie International Edition, 2010. **49**(10): p. 1736-1758.
248. Celaya Sanfiz, A., et al., *Preparation of Phase-Pure M1 MoVTeNb Oxide Catalysts by Hydrothermal Synthesis—Influence of Reaction Parameters on Structure and Morphology.* Topics in Catalysis, 2008. **50**(1): p. 19.
249. Aouine, M., J.L. Dubois, and J.M.M. Millet, *Crystal chemistry and phase composition of the MoVTeNbO catalysts for the ammoxidation of propane.* Chemical Communications, 2001(13): p. 1180-1181.
250. Murayama, H., et al., *Structure characterization of orthorhombic phase in MoVTeNbO catalyst by powder X-ray diffraction and XANES.* Applied Catalysis A: General, 2007. **318**: p. 137-142.
251. Grasselli, R.K., et al., *Active centers in Mo–V–Nb–Te–Ox (amm)oxidation catalysts.* Catalysis Today, 2004. **91-92**: p. 251-258.
252. DeSanto, P., et al., *Structural Characterization of the Orthorhombic Phase M1 in MoVNbTeO Propane Ammoxidation Catalyst.* Topics in Catalysis, 2003. **23**(1): p. 23-38.
253. Li, X., et al., *Improvement of the Structural Model for the M1 Phase Mo–V–Nb–Te–O Propane (Amm)oxidation Catalyst.* Topics in Catalysis, 2011. **54**(10): p. 614.
254. Grasselli, R.K., et al., *Multifunctionality of Active Centers in (Amm)oxidation Catalysts: From Bi–Mo–O x to Mo–V–Nb–(Te, Sb)–O x.* Topics in Catalysis, 2003. **23**(1): p. 5-22.
255. DeSanto, P., et al., *Comparison of MoVTaTeO and MoVNbTeO M1 crystal chemistry.* Topics in Catalysis, 2006. **38**(1): p. 31-40.
256. DeSanto, P., et al., *Structural aspects of the M1 and M2 phases in MoVNbTeO propane ammoxidation catalysts*, in *Zeitschrift für Kristallographie - Crystalline Materials*. 2004. p. 152.
257. Grasselli, R.K., et al., *Active centers, catalytic behavior, symbiosis and redox properties of MoV(Nb,Ta)TeO ammoxidation catalysts.* Topics in Catalysis, 2006. **38**(1): p. 7-16.
258. Kubo, J., N. Watanabe, and W. Ueda, *Propane ammoxidation with lattice oxygen of Mo–V–O-based complex metal oxide catalysts.* Chemical Engineering Science, 2008. **63**(6): p. 1648-1653.
259. Shiju, N.R., et al., *XANES Study of Hydrothermal Mo−V-Based Mixed Oxide M1-Phase Catalysts for the (Amm)oxidation of Propane.* Chemistry of Materials, 2008. **20**(21): p. 6611-6616.
260. Heine, C., *The Electronic Structure of Vanadium Oxides as Catalysts in the Selective Oxidation of Small Alkanes*. 2014, Technische Universität Berlin.
261. Y. V. Kolen´ko, W.Z., T. Wolfram, A. Celaya Sanfiz, F. Girgsdies, D. Su, A. Trunschke and R. Schlögl, *Nanostructured Phase-Pure MoV-based Oxides in Selective Oxidation of Propane to Acrylic Acid*. Department of Inorganic Chemistry, Fritz-Haber Institute of the Max Planck Society: Faradayweg 4-6, D-14195 Berlin (Germany).
262. Grasselli, R.K., *Selectivity issues in (amm)oxidation catalysis.* Catalysis Today, 2005. **99**(1): p. 23-31.
263. Ueda, W., D. Vitry, and T. Katou, *Crystalline MoVO based complex oxides as selective oxidation catalysts of propane.* Catalysis Today, 2005. **99**(1): p. 43-49.

264. Heine, C., et al., *Work Function, Band Bending, and Microwave Conductivity Studies on the Selective Alkane Oxidation Catalyst MoVTeNb Oxide (Orthorhombic M1 Phase) under Operation Conditions.* The Journal of Physical Chemistry C, 2013. **117**(51): p. 26988-26997.
265. Kube, P., et al., *Isotope Studies in Oxidation of Propane over Vanadium Oxide.* Chemcatchem, 2017. **9**(18): p. 3446-3455.
266. Selvam, P., et al., *Designing new catalysts: synthesis of new active structures: general discussion.* Faraday Discussions, 2016. **188**(0): p. 131-159.
267. Dai, Z., et al., *Honeycomb-like Periodic Porous LaFeO3 Thin Film Chemiresistors with Enhanced Gas-Sensing Performances.* ACS Applied Materials & Interfaces, 2014. **6**(18): p. 16217-16226.
268. Kang, J.-Y., et al., *Perovskite La0.75Sr0.25Cr0.5Mn0.5O3-delta Sensitized SnO2 Fiber-in-Tube Scaffold: Highly Selective and Sensitive Formaldehyde Sensing.* Journal of Materials Chemistry A, 2018.
269. Alcock, C.B., R.C. Doshi, and Y. Shen, *Perovskite electrodes for sensors.* Solid State Ionics, 1992. **51**(3): p. 281-289.
270. Anderson, H.U., J.H. Kuo, and D.M. Sparlin, *Review of defect chemistry of LaMnO3 and LaCrO3.* ECS Proceedings Volumes, 1989. **1989**: p. 111-128.
271. Arakawa, T., H. Kurachi, and J. Shiokawa, *Physicochemical properties of rare earth perovskite oxides used as gas sensor material.* Journal of Materials Science, 1985. **20**(4): p. 1207-1210.
272. Kuo, J.H., H.U. Anderson, and D.M. Sparlin, *Oxidation-reduction behavior of undoped and Sr-doped LaMnO3: Defect structure, electrical conductivity, and thermoelectric power.* Journal of Solid State Chemistry, 1990. **87**(1): p. 55-63.
273. Staykov, A., et al., *Oxygen Activation and Dissociation on Transition Metal Free Perovskite Surfaces.* Chemistry of Materials, 2015. **27**(24): p. 8273-8281.
274. Falcón, H., et al., *Large enhancement of the catalytic activity for CO oxidation on hole doped (Ln,Sr)NiO3 (Ln=Pr, Sm, Eu) Perovskites.* Solid State Ionics, 2000. **131**(3): p. 237-248.
275. Koch, G., et al., *Surface Conditions That Constrain Alkane Oxidation on Perovskites.* ACS Catalysis, 2020. **10**(13): p. 7007-7020.
276. Curtarolo, S., et al., *Predicting Crystal Structures with Data Mining of Quantum Calculations.* Physical Review Letters, 2003. **91**(13): p. 135503.
277. Greeley, J., et al., *Computational high-throughput screening of electrocatalytic materials for hydrogen evolution.* Nature Materials, 2006. **5**: p. 909.
278. Cerqueira, T.F.T., et al., *Identification of Novel Cu, Ag, and Au Ternary Oxides from Global Structural Prediction.* Chemistry of Materials, 2015. **27**(13): p. 4562-4573.
279. Hong, W.T., R.E. Welsch, and Y. Shao-Horn, *Descriptors of Oxygen-Evolution Activity for Oxides: A Statistical Evaluation.* The Journal of Physical Chemistry C, 2016. **120**(1): p. 78-86.
280. Pilania, G., et al., *Accelerating materials property predictions using machine learning.* Scientific Reports, 2013. **3**: p. 2810.
281. Elias, J.S., et al., *Elucidating the Nature of the Active Phase in Copper/Ceria Catalysts for CO Oxidation.* ACS Catalysis, 2016. **6**(3): p. 1675-1679.
282. Behler, J. and M. Parrinello, *Generalized Neural-Network Representation of High-Dimensional Potential-Energy Surfaces.* Physical Review Letters, 2007. **98**(14): p. 146401.
283. Kitchin, J.R., *Machine learning in catalysis.* Nature Catalysis, 2018. **1**(4): p. 230-232.
284. V., K.M., K.A. M., and P.A.J. L., *Mild, Single-Pot Hydrocarboxylation of Gaseous Alkanes to Carboxylic Acids in Metal-Free and Copper-Promoted Aqueous Systems.* Chemistry – A European Journal, 2010. **16**(31): p. 9485-9493.
285. V., K.M., K.A. M., and P.A.J. L., *Metal-Free and Copper-Promoted Single-Pot Hydrocarboxylation of Cycloalkanes to Carboxylic Acids in Aqueous Medium.* Advanced Synthesis & Catalysis, 2009. **351**(17): p. 2936-2948.

286. Brands, D.S., E.K. Poels, and A. Bliek, *Ester hydrogenolysis over promoted Cu/SiO2 catalysts.* Applied Catalysis A: General, 1999. **184**(2): p. 279-289.
287. Han, Y., et al., *Influence of metal ions on the selective catalytic oxidation properties of isostructural MOFs.* Inorganica Chimica Acta, 2018. **471**: p. 176-179.
288. Xuan, L., et al., *Selective Alkane Oxidation by Manganese Oxide: Site Isolation of MnOx Chains at the Surface of MnWO4 Nanorods.* Angewandte Chemie International Edition, 2016. **55**(12): p. 4092-4096.
289. Kılıç, Y. and İ. Kani, *Selective catalytic oxidation of alkenes employing homobinuclear manganese(II) catalysts with TBHP.* Polyhedron, 2018. **141**: p. 352-359.
290. Kraus, P., et al., *Towards automation of operando experiments: a case study in contactless conductivity measurements.* Digital Discovery, 2022.
291. Pechini, M.P., *Method of preparing lead and alkaline earth titanates and niobates and coating method using the same to form a capacitor*. 1967, Google Patents.
292. Yeh, J.J. and I. Lindau, *Atomic subshell photoionization cross sections and asymmetry parameters: 1 ⩽Z ⩽103.* Atomic Data and Nuclear Data Tables, 1985. **32**(1): p. 1-155.
293. Tanuma, S., C.J. Powell, and D.R. Penn, *Calculations of electron inelastic mean free paths (IMFPS). IV. Evaluation of calculated IMFPs and of the predictive IMFP formula TPP-2 for electron energies between 50 and 2000 eV.* Surface and interface analysis, 1993. **20**(1): p. 77-89.
294. Biesinger, M.C., et al., *Resolving surface chemical states in XPS analysis of first row transition metals, oxides and hydroxides: Cr, Mn, Fe, Co and Ni.* Applied Surface Science, 2011. **257**(7): p. 2717-2730.
295. Sunding, M.F., et al., *XPS characterisation of in situ treated lanthanum oxide and hydroxide using tailored charge referencing and peak fitting procedures.* Journal of Electron Spectroscopy and Related Phenomena, 2011. **184**(7): p. 399-409.
296. Biesinger, M.C., *Advanced analysis of copper X-ray photoelectron spectra.* Surface and Interface Analysis, 2017. **49**(13): p. 1325-1334.
297. Ogasawara, H., et al., *Praseodymium 3d-and 4d-core photoemission spectra of Pr 2 O 3.* Physical Review B, 1991. **44**(11): p. 5465.
298. Galakhov, V.R., et al., *Mn 3 s exchange splitting in mixed-valence manganites.* Physical Review B, 2002. **65**(11): p. 113102.
299. Salmeron, M. and R. Schlögl, *Ambient pressure photoelectron spectroscopy: A new tool for surface science and nanotechnology.* Surface Science Reports, 2008. **63**(4): p. 169-199.
300. Hwang, C.-C., et al., *Combustion synthesis of Ni–Zn ferrite powder—influence of oxygen balance value.* Journal of Solid State Chemistry, 2005. **178**(1): p. 382-389.
301. Epherre, R., et al., *Manganite perovskite nanoparticles for self-controlled magnetic fluid hyperthermia: about the suitability of an aqueous combustion synthesis route.* Journal of Materials Chemistry, 2011. **21**(12): p. 4393-4401.
302. Gabal, M.A., et al., *Auto-combustion synthesis and characterization of perovskite-type LaFeO3 nanocrystals prepared via different routes.* Ceramics International, 2019. **45**(13): p. 16530-16539.
303. Durrani, S.K., S. Naz, and K. Hayat, *Thermal analysis and phase evolution of nanocrystalline perovskite oxide materials synthesized via hydrothermal and self-combustion methods.* Journal of Thermal Analysis and Calorimetry, 2014. **115**(2): p. 1371-1380.
304. Doroftei, C., P.D. Popa, and F. Iacomi, *Synthesis of nanocrystalline La–Pb–Fe–O perovskite and methanol-sensing characteristics.* Sensors and Actuators B: Chemical, 2012. **161**(1): p. 977-981.
305. Chiu, T.-W., W.-R. Wang, and J.-S. Wu, *Synthesis of Pr2CuO4 powders by using a glycine–nitrate combustion method for cathode application in intermediate-temperature solid oxide fuel cells.* Ceramics International, 2015. **41**: p. S675-S679.

306. Rida, K., et al., *Effect of calcination temperature on structural properties and catalytic activity in oxidation reactions of LaNiO3 perovskite prepared by Pechini method.* Journal of Rare Earths, 2012. **30**(3): p. 210-216.
307. Wu, Y., et al., *Influence of calcination temperature on the catalytic properties of LaCu0.25Co0.75O3 catalysts in NOx reduction.* Applied Surface Science, 2019. **481**: p. 1277-1286.
308. Abdolrahmani, M., M. Parvari, and M. Habibpoor, *Effect of Copper Substitution and Preparation Methods on the LaMnO3±δ Structure and Catalysis of Methane Combustion and CO Oxidation.* Chinese Journal of Catalysis, 2010. **31**(4): p. 394-403.
309. Mizuno, N., Y. Fujiwara, and M. Misono, *Pronounced synergetic effect in the catalytic properties of LaMn 1–x Cu x O 3.* Journal of the Chemical Society, Chemical Communications, 1989(5): p. 316-318.
310. Yasuda, H., et al., *Oxidation of carbon monoxide on LaMn1 –CuO3 perovskite-type mixed oxides.* Journal of the Chemical Society, Faraday Transactions, 1994. **90**(8): p. 1183-1189.
311. Rojas, M.L., et al., *Preparation and characterization of LaMn1− xCuxO3+ λ perovskite oxides.* Journal of Catalysis, 1990. **124**(1): p. 41-51.
312. Bourzutschky, J.A.B., N. Homs, and A.T. Bell, *Conversion of synthesis gas over LaMn1− xCUx03+ λ perovskites and related copper catalysts.* Journal of Catalysis, 1990. **124**(1): p. 52-72.
313. Niwa, E., et al., *Dependence of crystal symmetry, electrical conduction property and electronic structure of LnFeO3 (Ln: La, Pr, Nd, Sm) on kinds of Ln3+.* Journal of the Ceramic Society of Japan, 2015. **123**(1438): p. 501-506.
314. Brown Bourzutschky, J.A., N. Homs, and A.T. Bell, *Conversion of synthesis gas over LaMn1−xCUx03+λ perovskites and related copper catalysts.* Journal of Catalysis, 1990. **124**(1): p. 52-72.
315. Zhan, H., et al., *Performance of the La–Mn–Zn–Cu–O based perovskite precursors for methanol synthesis from CO 2 hydrogenation.* Catalysis Letters, 2015. **145**(5): p. 1177-1185.
316. Zhong, H. and R. Zeng, *Structure of LaSrMO4 (M= Mn, Fe, Co, Ni, Cu) and their catalytic properties in the total oxidation of hexane.* Journal of the Serbian Chemical Society, 2006. **71**(10): p. 1049-1059.
317. Tabata, K., Y. Hirano, and E. Suzuki, *XPS studies on the oxygen species of LaMn1−xCuxO3+λ.* Applied Catalysis A: General, 1998. **170**(2): p. 245-254.
318. Andana, T., et al., *CO and Soot Oxidation over Ce-Zr-Pr Oxide Catalysts.* Nanoscale Research Letters, 2016. **11**.
319. Yamada, I., et al., *Control of bond-strain-induced electronic phase transitions in iron perovskites.* Inorganic chemistry, 2013. **52**(23): p. 13751-13761.
320. Mizokawa, T., et al., *Electronic structure of tetragonal LaCuO 3 studied by photoemission and x-ray-absorption spectroscopy.* Physical Review B, 1998. **57**(16): p. 9550.
321. Akizuki, Y., et al., *Rattling in the quadruple perovskite CuCu3V4O12.* Angewandte Chemie International Edition, 2015. **54**(37): p. 10870-10874.
322. McGuinness, C., et al., *X-ray spectroscopic study of the electronic structure of the high-dielectric-constant material Ca Cu 3 Ti 4 O 12.* Physical Review B, 2005. **71**(19): p. 195111.
323. Zhang, S., et al., *Solid Solutions of Pauli-Paramagnetic CaCu3V4O12 and Antiferromagnetic CaMn3V4O12.* Inorganic chemistry, 2013. **52**(18): p. 10610-10614.
324. Töpfer, J. and J.B. Goodenough, *$LaMnO_{3+\delta}$ Revisited.* Journal of Solid State Chemistry, 1997. **130**(1): p. 117-128.
325. Royer, S., et al., *Oxygen storage capacity of La1−xA'xBO3 perovskites (with A'=Sr, Ce; B=Co, Mn)—relation with catalytic activity in the CH4 oxidation reaction.* Applied Catalysis B: Environmental, 2005. **58**(3): p. 273-288.

326. Gaudin, E., F. Boucher, and M. Evain, *Some Factors Governing Ag^{+} and Cu^{+} Low Coordination in Chalcogenide Environments.* Journal of Solid State Chemistry, 2001. **160**(1): p. 212-221.
327. Miyoshi, S., et al., *Lattice expansion upon reduction of perovskite-type LaMnO3 with oxygen-deficit nonstoichiometry.* Solid State Ionics, 2003. **161**(3): p. 209-217.
328. Wilhelm, H., et al., *Pressure Induced Structural Phase Transitions in Pr2CuO4.*
329. Allan, N.L., J.M. Lawton, and W.C. Mackrodt, *A comparison of the calculated lattice and defect structures of La2CuO4, La2NiO4, Nd2CuO4, Pr2CuO4, Y2CuO4, Al2CuO4: Relationship to high-Tc superconductivity.* Philosophical Magazine B, 1989. **59**(2): p. 191-206.
330. Dharmadhikari, D.V., S.K. Nikam, and A.A. Athawale, *Template free hydrothermal synthesis and gas sensing application of lanthanum cuprate (La2CuO4): Effect of precursors on phase formation and morphology.* Journal of Alloys and Compounds, 2014. **590**: p. 486-493.
331. Burda, J.V., M. Zeizinger, and J. Leszczynski, *Activation barriers and rate constants for hydration of platinum and palladium square-planar complexes: An ab initio study.* The Journal of chemical physics, 2004. **120**(3): p. 1253-1262.
332. Zeizinger, M., et al., *A systematic ab initio study of the hydration of selected palladium square-planar complexes. A comparison with platinum analogues.* The Journal of Physical Chemistry A, 2001. **105**(34): p. 8086-8092.
333. Binici[1], E., et al., *Structural and Electrochemical Properties of LaMn1-xMxO3 (M= Ni, Co) Based Supercapacitor Electrodes.*
334. Hu, L., et al., *The effects of Jahn–Teller distortion changes on transport properties in LaMn1− xZnxO3.* Journal of Physics: Condensed Matter, 2003. **15**(12): p. 2033.
335. Sun, Y., et al., *Possible double-exchange interaction between manganese and chromium in LaMn 1− x Cr x O 3.* Physical Review B, 2001. **63**(17): p. 174438.
336. Li, C.-L., et al., *The effect of Pd content in LaMnO3 for methanol partial oxidation.* Catalysis Communications, 2011. **16**(1): p. 165-169.
337. Kundu, P., et al., *ZnO-Au nanohybrids by rapid microwave-assisted synthesis for CO oxidation.* Dalton transactions (Cambridge, England : 2003), 2012. **41**: p. 8762-6.
338. Amor, S.B., et al., *XPS characterisation of plasma treated and zinc oxide coated PET.* Applied Surface Science, 2009. **255**(9): p. 5052-5061.
339. Hou, Y.-C., et al., *Ni-substituted LaMnO 3 perovskites for ethanol oxidation.* RSC advances, 2014. **4**(11): p. 5329-5338.
340. Silva, R.C., et al., *Electronic Structure, Morphological Aspects, Optical and Electrochemical Properties of RuO2 Nanocrystals.* Electronic Materials Letters, 2019. **15**(5): p. 645-653.
341. Biabani-Ravandi, A., M. Rezaei, and Z. Fattah, *Low-temperature CO oxidation over nanosized Fe–Co mixed oxide catalysts: Effect of calcination temperature and operational conditions.* Chemical Engineering Science, 2013. **94**: p. 237-244.
342. Yang, J., et al., *Oxygen Vacancy Promoted O2 Activation over Perovskite Oxide for Low-Temperature CO Oxidation.* ACS Catalysis, 2019. **9**(11): p. 9751-9763.
343. Tejuca, L.G., et al., *Infrared spectroscopic study of the adsorption of pyridine, carbon monoxide and carbon dioxide on the perovskite-type oxides LaMO 3.* Journal of the Chemical Society, Faraday Transactions 1: Physical Chemistry in Condensed Phases, 1984. **80**(5): p. 1089-1099.
344. Levasseur, B. and S. Kaliaguine, *Effect of the rare earth in the perovskite-type mixed oxides AMnO3 (A=Y, La, Pr, Sm, Dy) as catalysts in methanol oxidation.* Journal of Solid State Chemistry, 2008. **181**(11): p. 2953-2963.
345. Hwang, J., et al., *Tuning perovskite oxides by strain: Electronic structure, properties, and functions in (electro)catalysis and ferroelectricity.* Materials Today, 2019. **31**: p. 100-118.

346. Yamazoe, N. and Y. Teraoka, *Oxidation catalysis of perovskites --- relationships to bulk structure and composition (valency, defect, etc.).* Catalysis Today, 1990. **8**(2): p. 175-199.
347. Freund, H.J. and R.P. Messmer, *On the bonding and reactivity of CO2 on metal surfaces.* Surface Science, 1986. **172**(1): p. 1-30.
348. Libby, W.F., *Promising catalyst for auto exhaust.* Science, 1971. **171**(3970): p. 499-500.
349. Voorhoeve, R.J.H., et al., *Perovskite oxides: materials science in catalysis.* Science, 1977. **195**(4281): p. 827-833.
350. Ziaei-Azad, H., et al., *Effects of Pd on enhancement of oxidation activity of LaBO3 (B=Mn, Fe, Co and Ni) pervoskite catalysts for pollution abatement from natural gas fueled vehicles.* Applied Catalysis B: Environmental, 2011. **102**(1): p. 62-70.
351. Kothari, M., et al., *Platinum incorporation into titanate perovskites to deliver emergent active and stable platinum nanoparticles.* Nature Chemistry, 2021. **13**(7): p. 677-682.
352. Kremenić, G., et al., *Chemisorption and catalysis on LaMO3 oxides.* Journal of the Chemical Society, Faraday Transactions 1: Physical Chemistry in Condensed Phases, 1985. **81**(4): p. 939-949.
353. Zheng, S., et al., *Catalytic oxidation of CO on LaMn1−xFexO3 perovskites solid solution.* Journal of Molecular Catalysis A: Chemical, 2014. **391**: p. 7-11.
354. Freund, H.-J., et al., *CO Oxidation as a Prototypical Reaction for Heterogeneous Processes.* 2011. **50**(43): p. 10064-10094.
355. Cheng, W., et al., *Nanoscale Hydration in Layered Manganese Oxides.* Langmuir, 2021. **37**(2): p. 666-674.
356. Risch, M., et al., *Structural Changes of Cobalt-Based Perovskites upon Water Oxidation Investigated by EXAFS.* The Journal of Physical Chemistry C, 2013. **117**(17): p. 8628-8635.
357. Mierwaldt, D., et al., *In situ XANES/XPS investigation of doped manganese perovskite catalysts.* Catalysts, 2014. **4**(2): p. 129-145.
358. Kang, J.-Y., et al., *Perovskite La 0.75 Sr 0.25 Cr 0.5 Mn 0.5 O 3− δ sensitized SnO 2 fiber-in-tube scaffold: highly selective and sensitive formaldehyde sensing.* Journal of Materials Chemistry A, 2018. **6**(22): p. 10543-10551.
359. Hu, Z., et al., *Total Oxidation of Propane over a Ru/CeO2 Catalyst at Low Temperature.* Environmental Science & Technology, 2018. **52**(16): p. 9531-9541.
360. Baranowska, K. and J. Okal, *Performance and Stability of the Ru–Re/γ-Al 2 O 3 Catalyst in the Total Oxidation of Propane: Influence of the Order of Impregnation.* Catalysis Letters, 2016. **146**(1): p. 72-81.
361. Baranowska, K. and J. Okal, *Bimetallic Ru-Re/γ-Al2O3 catalysts for the catalytic combustion of propane: Effect of the Re addition.* Applied Catalysis A: General, 2015. **499**: p. 158-167.
362. Okal, J., M. Zawadzki, and W. Tylus, *Microstructure characterization and propane oxidation over supported Ru nanoparticles synthesized by the microwave-polyol method.* Applied Catalysis B: Environmental, 2011. **101**(3-4): p. 548-559.
363. Okal, J. and M. Zawadzki, *Influence of Catalyst Pretreatments on Propane Oxidation Over Ru/γ-Al2O3.* Catalysis Letters, 2009. **132**(1): p. 225-234.
364. Zhang, C., et al., *LaMnO3 perovskites via a facile nickel substitution strategy for boosting propane combustion performance.* Ceramics International, 2020. **46**(5): p. 6652-6662.
365. Zhu, W., et al., *Insight into the Effect of Cobalt Substitution on the Catalytic Performance of LaMnO3 Perovskites for Total Oxidation of Propane.* The Journal of Physical Chemistry C, 2020. **124**(27): p. 14646-14657.
366. Merino, N.A., et al., *Synthesis, characterisation, catalytic activity and structural stability of LaCo1−yFeyO3±λ perovskite catalysts for combustion of ethanol and propane.* Journal of Catalysis, 2006. **240**(2): p. 245-257.

367. O'Brien, C.P. and I.C. Lee, *A detailed spectroscopic analysis of the growth of oxy-carbon species on the surface of Pt/Al2O3 during propane oxidation.* Journal of Catalysis, 2017. **347**: p. 1-8.
368. Taylor, M.N., et al., *Synergy between tungsten and palladium supported on titania for the catalytic total oxidation of propane.* Journal of Catalysis, 2012. **285**(1): p. 103-114.
369. Wang, S., et al., *Mesoporous Perovskite Nanotube-Array Enhanced Metallic-State Platinum Dispersion for Low Temperature Propane Oxidation.* ChemCatChem, 2018. **10**(10): p. 2184-2189.
370. Schlögl, R., *Heterogeneous Catalysis.* Angewandte Chemie International Edition, 2015. **54**(11): p. 3465-3520.
371. Kube, P., et al., *Isotope Studies in Oxidation of Propane over Vanadium Oxide.* ChemCatChem, 2017. **9**(18): p. 3446-3455.
372. Ulissi, Z.W., et al., *To address surface reaction network complexity using scaling relations machine learning and DFT calculations.* Nature Communications, 2017. **8**(1): p. 14621.
373. Ghiringhelli, L.M., et al., *Big Data of Materials Science: Critical Role of the Descriptor.* Physical Review Letters, 2015. **114**(10): p. 105503.
374. al., F.L.e., *Materials genes of heterogeneous catalysis from clean experiments and artificial intelligence.* submitted.
375. Ouyang, R., et al., *SISSO: A compressed-sensing method for identifying the best low-dimensional descriptor in an immensity of offered candidates.* Physical Review Materials, 2018. **2**(8): p. 083802.
376. Fujishiro, F., et al., *Effects of the Crystal Host Structure on the Oxygen Desorption Behavior in Perovskite-Type AeFe0.9In0.1O3−δ (Ae = Sr and Ba).* The Journal of Physical Chemistry C, 2021. **125**(24): p. 13283-13290.
377. Li, Z., L.E.K. Achenie, and H. Xin, *An Adaptive Machine Learning Strategy for Accelerating Discovery of Perovskite Electrocatalysts.* ACS Catalysis, 2020. **10**(7): p. 4377-4384.
378. Lu, S., et al., *Rapid Discovery of Ferroelectric Photovoltaic Perovskites and Material Descriptors via Machine Learning.* Small Methods, 2019. **3**(11): p. 1900360.
379. Lu, S., et al., *Accelerated discovery of stable lead-free hybrid organic-inorganic perovskites via machine learning.* Nature Communications, 2018. **9**(1): p. 3405.
380. Tao, Q., et al., *Machine learning for perovskite materials design and discovery.* npj Computational Materials, 2021. **7**(1): p. 23.
381. Liu, Y., et al., *Materials discovery and design using machine learning.* Journal of Materiomics, 2017. **3**(3): p. 159-177.
382. Weng, B., et al., *Simple descriptor derived from symbolic regression accelerating the discovery of new perovskite catalysts.* Nature Communications, 2020. **11**(1): p. 3513.
383. Ouyang, R., et al., *Simultaneous learning of several materials properties from incomplete databases with multi-task SISSO.* Journal of Physics: Materials, 2019. **2**(2): p. 024002.
384. Candès, E.J., J. Romberg, and T. Tao, *Robust uncertainty principles: Exact signal reconstruction from highly incomplete frequency information.* IEEE Transactions on information theory, 2006. **52**(2): p. 489-509.
385. Candès, E.J. and M.B. Wakin, *An introduction to compressive sampling.* IEEE signal processing magazine, 2008. **25**(2): p. 21-30.
386. Donoho, D.L., *Compressed sensing.* IEEE Transactions on information theory, 2006. **52**(4): p. 1289-1306.
387. Foppa, L., et al., *Materials genes of heterogeneous catalysis from clean experiments and artificial intelligence.* MRS Bulletin, 2021.
388. Engel, T. and G. Ertl, *A molecular beam investigation of the catalytic oxidation of CO on Pd (111).* The Journal of Chemical Physics, 1978. **69**(3): p. 1267-1281.

389. Sitja, G., H. Tissot, and C.R. Henry, *Particle size effect on the Langmuir-Hinshelwood barrier for CO oxidation on regular arrays of Pd clusters supported on ultrathin alumina films.* The Journal of chemical physics, 2019. **151**(17): p. 174703.
390. Singh, U.G., et al., *A Pd-doped perovskite catalyst, BaCe1−xPdxO3−δ, for CO oxidation.* Journal of Catalysis, 2007. **249**(2): p. 349-358.
391. Zhang-Steenwinkel, Y., et al., *Step response and transient isotopic labelling studies into the mechanism of CO oxidation over La0.8Ce0.2MnO3 perovskite.* Applied Catalysis B: Environmental, 2004. **54**(2): p. 93-103.
392. Tascón, J.M.D., J.L.G. Fierro, and L.G. Tejuca, *Kinetics and Mechanism of CO Oxidation on LaCoO3.* Zeitschrift für Physikalische Chemie, 1981. **124**(2): p. 249-257.
393. Rhee, C.K. and H.-I. Lee, *Co oxidation on LaCoO3 perovskite.* Korean Journal of Chemical Engineering, 1994. **11**(1): p. 48-54.
394. H.S.Taylor, J. Phys Chem., 1926. **30**: p. 145.
395. Kuznetsova, T., et al., *Effect of the surface/bulk doping of lanthanum manganite on the oxygen mobility, reactivity and catalytic activity in the CO oxidation.* Reaction Kinetics and Catalysis Letters, 2005. **86**(2): p. 257-265.
396. Zhang-Steenwinkel, Y., J. Beckers, and A. Bliek, *Surface properties and catalytic performance in CO oxidation of cerium substituted lanthanum–manganese oxides.* Applied Catalysis A: General, 2002. **235**(1): p. 79-92.
397. Fierro, J.L.G., J.M.D. Tascón, and L.G. Tejuca, *Surface properties of LaNiO3: Kinetic studies of reduction and of oxygen adsorption.* Journal of Catalysis, 1985. **93**(1): p. 83-91.
398. Li, H., et al., *Comparison of the nickel addition patterns on the catalytic performances of LaCoO3 for low-temperature CO oxidation.* Catalysis Today, 2017. **281**: p. 534-541.
399. Xiao, P., et al., *Effect of Textural Structure on the Catalytic Performance of LaCoO3 for CO Oxidation.* ChemCatChem, 2014. **6**(6): p. 1774-1781.
400. Ren, Z., et al., *Monolithically integrated spinel MxCo3− xO4 (M= Co, Ni, Zn) nanoarray catalysts: scalable synthesis and cation manipulation for tunable low-temperature CH4 and CO oxidation.* Angewandte Chemie, 2014. **126**(28): p. 7351-7355.
401. Zhong, S.-L., et al., *Uniform and Porous Ce1–x Zn X O2− δ Solid Solution Nanodisks: Preparation and Their CO Oxidation Activity.* The Journal of Physical Chemistry C, 2012. **116**(24): p. 13127-13132.
402. Rybarczyk, P., et al., *The Structure of Active Sites in Me–V–O Catalysts (Me = Mg, Zn, Pb) and Its Influence on the Catalytic Performance in the Oxidative Dehydrogenation (ODH) of Propane.* Journal of Catalysis, 2001. **202**(1): p. 45-58.
403. Wu, X., et al., *Enhanced catalytic performance of PtSn catalysts for propane dehydrogenation by a Zn-modified Mg(Al)O support.* Fuel Processing Technology, 2020. **198**: p. 106222.
404. Li, X., et al., *How to control selectivity in alkane oxidation?* Chemical science, 2019. **10**(8): p. 2429-2443.
405. Carrettin, S., et al., *Increasing the Number of Oxygen Vacancies on TiO2 by Doping with Iron Increases the Activity of Supported Gold for CO Oxidation.* Chemistry – A European Journal, 2007. **13**(27): p. 7771-7779.
406. Yang, J., et al., *Oxygen Vacancies and Lewis Acid Sites Synergistically Promoted Catalytic Methane Combustion over Perovskite Oxides.* Environmental Science & Technology, 2021. **55**(13): p. 9243-9254.
407. Zhang, S., et al., *Bi-active sites of stable and highly dispersed platinum and oxygen vacancy constructed by reducing a loaded perovskite-type oxide for CO oxidation.* Applied Surface Science, 2020. **532**: p. 147455.
408. Roberts, F.S., et al., *Oxygen activation and CO oxidation over size-selected Ptn/alumina/Re(0001) model catalysts: correlations with valence electronic structure,*

physical structure, and binding sites. Physical Chemistry Chemical Physics, 2014. **16**(48): p. 26443-26457.

409. Haber, J. and W. Turek, *Kinetic studies as a method to differentiate between oxygen species involved in the oxidation of propene.* Journal of Catalysis, 2000. **190**(2): p. 320-326.
410. Zhang, W., et al., *Real-space observation of surface termination of a complex metal oxide catalyst.* Angewandte Chemie International Edition, 2010. **49**(35): p. 6084-6089.
411. Merino, N.A., et al., *La1− xCaxCoO3 perovskite-type oxides: preparation, characterisation, stability, and catalytic potentiality for the total oxidation of propane.* Journal of Catalysis, 2005. **231**(1): p. 232-244.
412. Doshi, R., C.B. Alcock, and J.J. Carberry, *Effect of surface area on CO oxidation by the perovskite catalysts La 1− x Sr x MO 3-δ (M= Co, Cr).* Catalysis letters, 1993. **18**(4): p. 337-343.
413. Silva, P.R.N. and A.B. Soares, *Lanthanum based high surface area perovskite-type oxide and application in CO and propane combustion.* Eclética Química, 2009. **34**(1): p. 31-38.
414. Toniolo, F.S. and M. Schmal, *Improvement of catalytic performance of perovskites by partial substitution of cations and supporting on high surface area materials*, in *Perovskite Materials-Synthesis, Characterisation, Properties, and Applications*. 2016, InTechOpen.
415. Kim, Y.-K., et al., *Catalytic activity and activation mechanism of potassium carbonate supported on perovskite oxide for coal char combustion.* Fuel, 2012. **94**: p. 516-522.
416. Milt, V.G., et al., *The nature of active sites for the oxidation of methane on La-based perovskites.* Catalysis Letters, 1996. **42**(1): p. 57-63.